COLLOIDS, DIAGNOSTICS, AND 3D-PRINTED HYDROGELS

by

Thomas Brian LeFevre

A dissertation submitted in partial fulfillment
of the requirements for the degree

of

Doctor of Philosophy

in

Engineering

MONTANA STATE UNIVERSITY
Bozeman, Montana

December 2021

©COPYRIGHT

by

Thomas Brian LeFevre

2021

All Rights Reserved

DEDICATION

To my parents Brian and Jeanne, and my brothers Jim, Matt, and Joe.

ACKNOWLEDGEMENTS

Funding for this dissertation was provided by the National Science Foundation (DMR-1455247) and ULTSafety.

First, I thank Dr. Jim Wilking, my advisor, for being an all-around great person, giving me the freedom to pursue my interests in my research, always giving me the encouragement and support I needed, and just letting me be myself.

Thanks to my committee, Dr. Phil Stewart, Dr. Joe Seymour, and Dr. Mike Franklin for their guidance, advice, and encouragement.

Thanks to all the other graduate students and postdocs I worked with, especially Dr. Reha Abbasi, Isaak Thornton, and Dr. Dimitri Bikos.

And special thanks to my family, for giving me a sense of curiosity, honesty, and hard work.

TABLE OF CONTENTS

1. INTRODUCTION 1

Colloids 1
Significance 1
Colloidal Interactions 1
Interparticle Interaction Forces 4
Van der Waals Forces 4
Electrostatic Forces 9
Adding VDW and ES Forces 14
Measuring DLVO Interactions 15
Pathogen Detection 16
Significance 16
Loop-mediated Isothermal Amplification (LAMP) 19
Loop Structure Formation 20
Exponential Replication 21
Detection 21
Saliva as a Diagnostic Sample 24
Design For Injection Molding 25
References Cited 32

2. MEASURING COLLOID-SURFACE INTERACTION FORCES IN PARALLEL USING FLUORESCENCE CENTRIFUGE FORCE MICROSCOPY 47

Contribution of Authors and Co-Authors 47
Manuscript Information 48
Abstract 49
Introduction 50
Methods 52
Instrument 52
Fabrication 55
Experimental Protocol 56
Safety Considerations 60
Results & Discussion 61
Image Quality 61
Force Range 63
Force Validation 63
Validation of Centrifuge Rotational Frequency with Audio Signal Analysis 66
Colloid Detachment Force Measurements 68

TABLE OF CONTENTS CONTINUED

Conclusion 74
Supplementary Information 74
Measuring the Swinging Bucket Angle as a Function of Centrifuge Rotational Velocity 74
F-CFM Assembly 75
Cutting the Annular Tape Rings 76
Derivation of Microsphere Settling Velocity 76
Manual Image Counting Analysis of Microsphere Detachments 76
Assumptions for the Gregory Model of Predicted Detachment Force 77
Acknowledgements 79
Funding 80
References Cited 87

3. SPOC-LAMP: SALIVA POINT-OF-CARE LOOP-MEDIATED AMPLIFICATION – A LOW-COST, HAND-HELD, MANUALLY-OPERATED DEVICE FOR POINT-OF-CARE PATHOGEN DETECTION 92

Contribution of Authors and Co-Authors 92
Manuscript Information 94
Abstract 95
Introduction 96
Results & Discussion 97
Conclusion 104
Methods 105
Fabrication 106
Assay Formulation 106
Force Measurements 106
Design Considerations 107
Supplementary Information 108
Funding 109
References Cited 110

4. COUPLING FLUID FLOW TO HYDROGEL FLUIDIC DEVICES WITH REVERSIBLE “POP-IT” CONNECTIONS 113

Contribution of Authors and Co-Authors 113
Manuscript Information 114
Abstract 115
Introduction 116

TABLE OF CONTENTS CONTINUED

Results & Discussion 117
Conclusion 130
Methods 131
Hydrogel 3D Printing 131
Connector 3D Printing 131
Liquid Flow 132
Hydrostatic Pressure Measurements 132
Flow Rate Estimates 133
Rheology and Force Measurements 133
Measuring Contact Area of the Connector 134
Growth of 3D Printed Bacteria 134
Supplementary Information 136
Hydrostatic Pressure Measurements 136
Estimating Contact Area Between Connector and Gel 136
Evidence of Hysteresis in Normal Forces Associated with Connector Insertion and Removal 137
Funding 138
References Cited 143

5. LIGHT-BASED 3D PRINTING OF HYDROGELS WITH HIGH-RESOLUTION CHANNELS 147

Contribution of Authors and Co-Authors 147
Manuscript Information 148
Abstract 149
Introduction 150
Background 152
Results & Discussion 155
Conclusion 170
Methods 171
Chemicals 171
Resin Formulation 171
SLA Printer 171
Print Head Silanation 172
Print Control 172
Cure Depth Measurements 173
OCT Measurements 174
Absorbance Measurements 174
Supplementary Information 176
Cumulative Bleedthrough 176
Funding 178

TABLE OF CONTENTS CONTINUED

References Cited 185

6. AN INEXPENSIVE, VERSATILE, COMPACT PROGRAMMABLE TEMPERATURE CONTROLLER AND THERMOCYCLER FOR SIMULTANEOUS ANALYSIS AND VISUALIZATION WITHIN A MICROSCOPE 188

Contribution of Authors and Co-Authors 188
Manuscript Information 189
Abstract 190
Introduction 191
Materials and Methods 193
3D Design of the Device Holder and Control Device 193
Fabrication of the Device Holder 195
Fabrication of the Control Device 196
Temperature Control System Software 197
Smartphone Application Development 198
Rhodamine B Temperature Validation 198
PCR Validation Experiments 199
Results & Discussion 200
Analysis of Temperature Control Performance 200
External Validation of Temperature Control 203
Rhodamine B Temperature Dependence Measured Inside a PDMS/Glass Microfluidic Device 204
qPCR Amplification within the Temperature Control System 205
Conclusion 206
Supplementary Information 207
Initial Endpoint PCR Amplification Setup 209
Endpoint PCR Amplification Within the Temperature Control System 209
Calibration of the MAX6675 Thermocouple Temperature Sensor 210
Acknowledgements/Funding 213
References Cited 214

7. SARS-COV-2 DETECTION IN THE NASOPHARYNGEAL SWABS AND SALIVA OF COLLEGE STUDENTS USING RT-QPCR AND RT-LAMP 216

Contribution of Authors and Co-Authors 216
Manuscript Information 219

TABLE OF CONTENTS CONTINUED

Abstract 220
Background 220
Methods 220
Results 220
Conclusions 221
Introduction 222
Methods 223
Participants 223
Self-Reported Questionnaire 223
Sample Collection 223
Viral Inactivation – NP Swab 224
Viral Inactivation – Saliva 224
CDC-approved RT-qPCR from NP Swab 224
SalivirDetect – RT-qPCR in Saliva 225
SLAMP – RT-LAMP in Saliva 226
Statistical Analysis 227
Results 227
Comparing Testing Methods: SLAMP, SalivirDetect and NP RT-qPCR 227
Demographics 228
Clinical Presentation 228
Potential Saliva Contamination 229
Testing Outcomes – Performance of the Three Methods 231
Comparing Positive Samples – Two Sample Matrices and Three Testing Methods 232
Test Outcomes and Viral Titers by Age 233
Self-reported Clinical Presentations and Test Results 234
Consumption of Potential Inhibitors – Effect on SalivirDetect Ct Values 234
Site Comparison: Nasopharynx versus Saliva 235
Statistical Predictions for SLAMP Tests at Triplicate, Duplicate, or as a Single Replicate 235
Safety 238
Discussion 239
Supplementary Information 243
Methods 243
Results 248
Funding 261
Acknowledgements 261
References Cited 262

TABLE OF CONTENTS CONTINUED

8. CONCLUSION.....265

CUMULATIVE REFERENCES CITED 267

LIST OF FIGURES

Figure Page

1.1. DLVO model geometry 5

1.2. Example DLVO curve 15

1.3. Loop-mediated isothermal amplification (LAMP) process schematic 22

1.4. Concatamer formation during the exponential replication phase of LAMP 24

1.5. Injection molding process overview 26

1.6. Illustration of the molten plastic filling front 28

2.1. Fluorescence CFM construction and assembly 53

2.2. F-CFM image quality 59

2.3. CFM force validation using colloidal sedimentation 65

2.4. Audio waveforms indicate centrifuge speed 67

2.5. Colloid detachment force distributions as functions of electrolyte concentrations 70

3.1. SPOC-LAMP device overview 98

3.2. SPOC-LAMP device operation 99

3.3. Saliva transfer from swab to SPOC-LAMP device. 101

3.4. Blister compression forces and dynamics. 102

3.5. Device validation 105

4.1. Friction-based connections developed for traditional microfluidic devices fail when applied to hydrogels 118

LIST OF FIGURES CONTINUED

Figure Page

4.2. Plastic 3D printed connector secures fluidic tubing to 3D printed hydrogel. 120

4.3. Connector insertion into gel socket is governed by gel elasticity. 122

4.4. Seal between connector and gel socket improves as the connector head diameter increases relative to the gel neck diameter. 125

4.5. Double-sided pop-it connectors can be used to build interconnected assemblies from modular gels. 127

4.6. Pop-it connector advantages and potential applications. 129

5.1. Light-based stereolithographic 3D printing 152

5.2. Chlorophyllin as a photoblocker 156

5.3. Determining optimal layer-layer adhesion conditions for printing 3D objects. 160

5.4. Modeling and measuring channel bleedthrough. 163

5.5. Printed hydrogels with submillimeter channels 168

6.1. Schematics of the temperature control system 194

6.2. Device holder prototype overview. 196

6.3. Control device overview. 197

6.4. Heating and cooling rates 202

6.5. External validation of temperature accuracy. 203

6.6. Average relative fluorescence of rhodamine B in a microfluidic device during heating and cooling. 204

LIST OF FIGURES CONTINUED

Figure Page

6.7. Real-time PCR amplification using the temperature control system..... 206

7.1. Sample collection and testing workflow..... 228

7.2. Positive sample results compared between three tests..... 233

7.3. Study results and statistical predictions. 238

ABSTRACT

Colloidal suspensions are dispersions of microscopic particles in liquid. Their properties have broad impacts in industry, medicine, and biology. In Chapter 2, we focus on measuring the interactions between colloidal particles suspended in water and a glass surface. We measure these interactions using a custom-built fluorescence centrifuge force microscope (F-CFM). This is the first CFM built with fluorescence capability, the first CFM used to measure colloidal interaction forces, and the first CFM capable of operating at speeds above 2000 RPM – and up to 5000 RPM – in a centrifuge. The F-CFM enables colloidal scale objects to be discriminated by fluorescence, which opens potential applications for biological samples that fluoresce under different phenotypic states.

In Chapter 3, we focus on designing a point-of-care (POC) saliva collection, metering, and mixing system for detecting viral pathogens. The device was designed for the specific purpose of testing for the presence of SARS-CoV-2 in saliva using molecular amplification methods but could be applied to any pathogen whose constituents can be detected in saliva. The design to prioritizes ease of use, low cost, and scalability in order to facilitate massively widespread testing, which was absent during the first years since the emergence of SARS-CoV-2,

In Chapter 4, we describe a method of formulating and printing hydrogel resins with high resolution channels using light-based 3D printing. In Chapter 5, we describe a leak-resistant, pressurized connector platform for connecting modular hydrogels that can be used to create complex assemblies of hydrogel components. In Chapter 6, we describe a microscope sample temperature control platform that fits into standard upright microscope stages in order to heat and cool samples in a controlled manner under the microscope in order to observe temperature dependent reactions like polymerase chain reaction (PCR) and loop-mediated isothermal amplification (LAMP). In Chapter 7, we describe a LAMP formulation that can be used to detect the presence of SARS-CoV-2 RNA in saliva despite the inhibitory components present in saliva and demonstrate its comparable accuracy to the gold standard of pathogenic testing: nasopharyngeal PCR testing.

CHAPTER ONE

INTRODUCTION

Colloids

Significance

Colloidal dispersions are mixtures of nanometer- to micrometer-scale particles or liquid droplets distributed in a liquid[1-3]. Colloidal dispersions are widespread in food[4], medicine[5-13], biology[14-17], coatings[18], wastewater treatment[19-21], industry[22-24], and daily life. Common examples include milk, blood, microbial bioreactors, industrial water slurries, and environmental water systems[25, 26] such as lakes, rivers, and oceans. The physical properties of colloids and the interactions between colloids govern the behavior, function, and appearance of colloidal dispersions and thus are important for many environmental, industrial, and biological processes.

Colloidal Interactions

The macroscopic behavior of colloidal suspensions is a manifestation of the microscopic behavior of their colloidal particle constituents. In turn, the behavior of colloidal particles is determined by inter-particle interactions and extra-particle interactions with the suspension media and interfaces. Chapter 2 of this dissertation focuses on inter-particle interactions and colloid-interface interactions. These interactions between colloidal particles govern two important micro-scale phenomena: resistance to inter-particle aggregation, referred to as colloidal "stability"[3, 27-30], and particle adhesion[31-34] to substrates such as vessel walls and filter media. In many cases, this stability or adhesion is crucial for the proper function of the suspension or process. For example, our blood would not perform its life-sustaining nutrient delivery functions if blood cells aggregated

together and failed to flow as a dispersed phase. Similarly, microbial bioreactors[35-38] do not operate efficiently to produce bioproducts like antibiotics[39-41], fermented foods[42, 43] and drinks[44-46], fuels[47-52], and – increasingly – synthetic fabrics[53, 54] and materials[55-57], when the suspended planktonic microorganisms or their products clump together and foul functional reactor interfaces such as membranes and filters. Conversely, wastewater treatment[58-61] relies on the flocculation of waste particles for efficient[62, 63] separation of water and waste. Furthermore, colloidal particle interactions govern the properties and function of many other soft condensed matter systems including gels[64-66], which are discussed in Chapters 4 and 5 of this dissertation, emulsions[67-71], and biological tissues[72-74]. Thus, knowledge of colloidal behavior is necessary for controlling and predicting the behaviors of many systems. To properly predict and control the behavior of colloidal suspensions, we must understand the physical mechanisms behind their interactions.

Colloids dispersed in liquid experience random fluctuations in their position. This random "Brownian" motion[75] was first[76] described by Robert Brown[77] in 1827 upon observing the motion of pollen grains in water and was described theoretically in the early 1900s by Albert Einstein[78] and Jean Baptiste Perrin[79]. This motion is due to the kinetic (thermal) energy of the solvent molecules, kT where k is the Boltzmann constant and T is absolute temperature. Thermal energy drives the motion of the colloidal particles and is the relevant energy scale for colloidal systems[3, 80]; thus, it is useful to consider the interaction energy in terms of kT[81, 82]. For example, if the repulsive energy barrier between two particles is on the order of kT, thermal fluctuations will drive particles to aggregate. If the repulsion between two particles is many times kT, then it is unlikely that thermal fluctuations will overcome particle-particle repulsion and the particles will remain

dispersed. The diffusion coefficient that quantifies Brownian motion-induced diffusion of a colloidal sphere through a viscous liquid is described by the Stokes-Einstein equation[83-85],

$$D = \frac{kT}{6\pi\eta r}$$

where η is the viscosity of the liquid medium and r is the radius of the particle.

Interparticle interaction forces When colloidal particles approach each other or a surface, their interactions are governed by two electromagnetic forces[80]: the electrostatic (ES) force and the van der Waals (vdW) force. These electromagnetic forces between colloidal particles were first described by Derjaguin and Landau[86] and separately by Verwey and Overbeek[87] in the 1940s and have hence been termed Derjaguin, Landau, Verwey, and Overbeek (DLVO) forces. The following section of this dissertation focuses on the theory and experimental measurement of the forces described by DLVO theory. Other interaction forces such as steric and solvation forces can play an important role in many colloidal systems but are not described here. We choose as our model geometry a sphere interacting with a flat surface because our experimental system consists of suspended microspheres interacting with a glass coverslip surface (Chapter 2).

Van der Waals Forces Van der Waals forces originate from fluctuating dipole moments in the molecules that make up interacting objects[88]. Thus, vdW forces are electrostatic in nature, with the interaction arising from the reflection of the dipole on one molecule reflecting back from the dipole imposed on the other. vdW forces are short range, so objects must be close together, on the order of nanometers apart, for vdW forces to be significant. Transmission of vdW forces requires

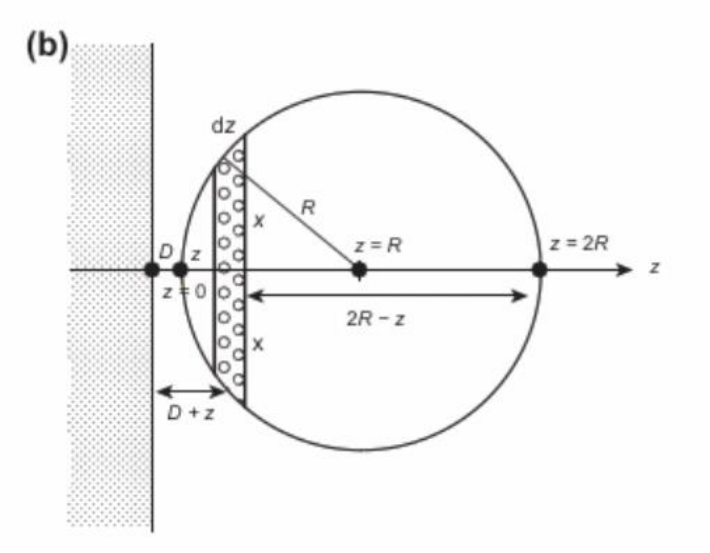


Figure 1.1: *DLVO model geometry*. Our chosen colloidal particle model geometry shows a spherical particle interacting with a flat substrate surface. Illustration from Israelachvili 2011[80].

transmission of electromagnetic radiation through the medium that separates the two objects, and thus the permittivity of the medium in which the objects are suspended governs the magnitude of the vdW forces.

The derivation of the van der Waals interaction energy is described by Israelachvili[88]. First, the interaction energy between a single molecule and flat bulk surface must be derived. Then, the energy can be integrated through the geometry of interest, in this case a sphere (**Fig. 1.1**), to determine the total energy between a sphere and a flat surface. The energy $w(r)$ between two atoms as a function of separation distance r is assumed to be attractive and equal to

$$w(r) = -\frac{C}{r^n}$$

where $n = 6$ for vdW forces. This is integrated through the volume of the sphere and, assuming the sphere and wall are very close together and therefore the region of the sphere closest to the surface dominates the integral, yields

$$W(D) = -\frac{\pi^2 C \rho^2 R}{6D}.$$

Therefore, the total force between the sphere and the flat surface can be found by integrating the individual molecule energy through the effective contact area of the sphere.

The pair-wise interaction energy between a single molecule at distance D from another molecule in a flat surface is again

$$w(r) = -\frac{C}{r^n}$$

where C is the interaction constant and $n = 6$ for vdW forces. The energy between the lone molecule and all the molecules in the flat surface can be found by integrating this pair-wise energy through a series of concentric rings extending outward radially in direction x and through the surface in direction z. The volume of any given ring (**Fig. 1.1**) is

$$dV = 2\pi x \, dx \, dz$$

which can be multiplied by the molecular density ρ to get the number of molecules n in the ring:

$$n = 2\pi\rho x \, dx \, dz \, .$$

Thus, by integrating the pairwise energy $w(r)$ through all the molecules present in any given ring of the flat substrate, one obtains for $n > 3$

$$w(r) = -\frac{2\pi C \rho}{(n-2)(n-3)D^{(n-3)}} \, .$$

For vdW forces $n = 6$ the previous equation becomes

$$w(D) = -\frac{\pi C \rho}{6D^3}.$$

Now that the interaction energy between a single molecule and a planar substrate is known, it is possible to integrate this energy throughout the volume of the entire sphere, similar in manner to integrating the pairwise molecular energy through the planar substrate. Using the Chord Theorem to determine the area of effective contact between a sphere and a flat surface that excludes solvent molecules from entering between the sphere and the surface, the contact geometry is described by

$$x^2 = (2R - z)z$$

where *x* is the diameter of the disc cross section of the sphere being integrated through, *z* is the distance from the surface of the sphere, and *R* is the radius of the sphere. Now it is possible to determine that the number of molecules *n* in any given disc is

$$n = \pi\rho(2R - Z)z\, dz$$

and by integrating the molecular pairwise energy through all the discs in the sphere to show that

$$W(D) = -\frac{2\pi C \rho^2}{(n-2)(n-3)} \int \frac{(2R - Z)z dz}{(D + z)^{n-3}}.$$

If one assumes the gap distance *D* is much smaller than the sphere radius *R* and thus only small values of *z*, on the order of $z \approx D$, dominate the integral, then the interaction energy is

$$W(D) = \frac{4\pi^2 C \rho^2 R}{(n-2)(n-3)(n-4)D^{n-5}}$$

which for vdW forces $n = 6$ and the above equation becomes

$$W(D) = -\frac{\pi^2 C \rho^2}{6D}.$$

For simplicity, it is common practice to define the Hamaker constant [89] as

$$A = -\pi^2 C \rho^2.$$

And now one can describe the interaction energy between a sphere and a flat surface as

$$W(D) = -\frac{AR}{6D}.$$

For our experiments, we want to know the force between the sphere and the flat substrate, which is the derivative of the interaction energy with respect to *D*,

$$F(D) = \frac{dW}{dD} = -\frac{AR}{6D^2}.$$

The negative sign here indicates that the force is attractive. These equations were derived assuming the sphere and flat substrate are of the same material and in a vacuum. For our experiments, the sphere and flat substrate are of unlike materials suspended in water. It is straightforward to calculate the Hamaker constant of any particular material by substituting the interaction constant and the molecular density into the Hamaker constant equation; but, for our experimental system discussed in Chapter 2, we need to know the Hamaker constant for a system of three different materials: (1) polystyrene mixed with iron oxide, (2) glass, and (3) water. The Hamaker constants of the materials cannot simply be added together, and we must use the Lifshitz theory of vdW forces which considers quantum effects to yield

$$A = \frac{3}{4} kT \left(\frac{\varepsilon_1 - \varepsilon_3}{\varepsilon_1 + \varepsilon_3}\right)\left(\frac{\varepsilon_2 - \varepsilon_3}{\varepsilon_2 + \varepsilon_3}\right) + \frac{\frac{3h\nu_e}{8\sqrt{2}}(n_1^2 - n_3^2)(n_2^2 - n_3^2)}{(n_1^2 + n_3^2)^{\frac{1}{2}}(n_2^2 + n_3^2)^{\frac{1}{2}}\left\{(n_1^2 + n_3^2)^{\frac{1}{2}} + (n_2^2 + n_3^2)^{\frac{1}{2}}\right\}}.$$

Electrostatic Forces The electrostatic (ES) force[80] between two objects is entropic in nature[90]. When two particles dispersed in a liquid approach each other to a distance that excludes ions from between them, then the total population of ions has lost some of its available configurational states and have thus become more organized or less entropic. This reduction in

entropy[91-98] is thermodynamically unfavorable and the particles tend to be repulsed from each other.

The characteristic thickness of the cloud of counterions surrounding a particle in suspension is the Debye length, κ^{-1}. Debye length is a critical parameter to calculate when trying to model particle behavior and is defined by

$$\kappa = \left(\sum_i \frac{\rho_{\infty i} e^2 z_i^2}{\varepsilon \varepsilon_0 kT} \right)^{\frac{1}{2}}.$$

A shorter Debye length allows particles to get closer together, which allows the shorter-range vdW forces to take effect, whereas a longer Debye length prevents particles from getting closer together and allows the repulsive ES forces to dominate. Thus, the Debye length greatly affects the predictive DLVO curve. One way to control the Debye length of a system is to control the ionic strength, or number of counterions, in the system.

The Debye length decreases when additional ions such those from dissolved salts are added to the suspension[90]. By increasing the density of ions in the suspension, the added salt increases the number of configurational states for the population of ions in the suspension and thus make the exclusion of ions between two approaching particles less thermodynamically unfavorable.

The full derivation and explanation of the various equation forms that govern ES force models is outside the scope of this dissertation; however, there are several fundamental relationships that lead to the quantitative predictions and are worth mentioning. This section focuses on the derivation method detailed in Israelachvili 1985[88].

The chemical potential μ of any given counterion in solution is defined by

$$\mu = ze\varphi + kT\log\rho$$

where z is the ion valence number, e is the charge of an electron, φ is the electrical potential, and ρ is the number density of ions in suspension.

From there, the Boltzmann distribution can be derived from the setting $s = 0$ at the midplane and $p = p_o$ and $ds/dx_o = 0$ where

$$\rho = \rho_0 \mathrm{e}^{\left(-\frac{ze\varphi}{kT}\right)}.$$

One can then take the Poisson equation,

$$ze\rho = -\varepsilon\varepsilon_0 \left(\frac{d^2\varphi}{dx^2}\right),$$

and combine the Poisson equation with the Boltzmann distribution to get the Poisson-Boltzmann (PB) equation,

$$\frac{d^2\varphi}{dx^2} = -\frac{ze\rho}{\varepsilon\varepsilon_0} = -\left(\frac{ze\rho_0}{\varepsilon\varepsilon_0}\right) \mathrm{e}^{-\left(\frac{ze\varphi}{kT}\right)}.$$

There are two boundary conditions that can be used to solve the PB equation:

$$E_0 = \left(\frac{d\varphi}{dx}\right)_0 = 0$$

$$E_s = \frac{\sigma}{\varepsilon\varepsilon_0}.$$

Differentiating the Boltzmann Distribution and combining with the PB equation leads to

$$\frac{d\rho}{dx} = -\frac{ze\rho_0}{kT} \mathrm{e}^{-\frac{ze\varphi}{kT}} \left(\frac{d\varphi}{dx}\right) = \frac{\varepsilon\varepsilon_0}{kT}\left(\frac{d\varphi}{dx}\right)\left(\frac{d^2\varphi}{dx^2}\right) = \frac{\varepsilon\varepsilon_0}{2kT}\frac{d}{dx}\left(\frac{d\varphi}{dx}\right)^2,$$

which can be solved to determine that

$$\rho_x = \rho_0 + \frac{\varepsilon\varepsilon_0}{2kT}\left(\frac{d\varphi}{dx}\right)_x^2.$$

Solving for the specific value ρ_s from the second boundary condition results in

$$\rho_s = \rho_0 + \frac{\sigma^2}{2\varepsilon\varepsilon_0 kT}.$$

Another important equation is the Grahame Equation, which will not be derived here, but describes the relation between surface charge density and surface potential assuming a low surface potential, typically below 25 mV, as

$$\sigma = \varepsilon\varepsilon_0 \kappa \varphi_0.$$

Now, utilizing the Contact Value Theorem, which describes the pressure between two surfaces at close contact, leads to

$$P_x(D) - P_x(\infty) = -\frac{1}{2}\varepsilon\varepsilon_0 \left[\left(\frac{d\varphi}{dx}\right)^2_{x(D)} - \left(\frac{d\varphi}{dx}\right)^2_{x(\infty)}\right] + kT\left[\sum_i \rho_{xi}(D) - \sum_i \rho_{xi}(\infty)\right].$$

Using the equation for the PB equation solution with sums added results in

$$\sum_i \rho_{xi} = \sum_i \rho_{mi} + \frac{\varepsilon\varepsilon_0}{2kT}\left(\frac{d\varphi}{dx}\right)^2_x$$

Combining these two equations determines the pressure across the gap between two surfaces

$$P_x(D) = kT\left[\sum_i \rho_{mi}(D) - \sum_i \rho_{mi}(\infty)\right]$$

which is the entropic or osmotic pressure active across the gap in relation to the bulk pressure.

For 1:1 electrolytes like NaCl,

$$P = kT\rho_\infty\left[\left(\mathrm{e}^{-\frac{e\varphi m}{kT}} - 1\right) + \left(\mathrm{e}^{\frac{e\varphi m}{kT}} - 1\right)\right] \approx \frac{e^2\varphi_m^2\rho_\infty}{kT}.$$

Now utilizing Gouy-Chapman theory, which is derived from the Graham equation, leads to

$$P = 64kT\rho_\infty\gamma^2\mathrm{e}^{-\kappa D}$$

where $\gamma = \tanh\left(\frac{ze\varphi}{4kT}\right)$.

By integrating the above pressure equation with respect to *D* to find the free energy per unit area, one can find that

$$W = \left(\frac{64kT\rho_{\infty}\gamma^2}{\kappa}\right)\mathrm{e}^{-\kappa D}.$$

The Derjaguin approximation, an alternate method to describe the effective contact area between two spheres, shows that

$$F = \pi R W(D)$$

where *W* is the interaction energy. This approximation can be used with the Gouy-Chapman theory to find

$$W = \left(\frac{64\pi kTR\rho_{\infty}\gamma^2}{\kappa^2}\right)\mathrm{e}^{-\kappa D}.$$

This is a general equation for the ES interaction that comes from solving the PB Equation. It assumes constant surface potential at the sphere and substrate, as opposed to constant surface charge density. However, it is likely that neither surface charge nor surface potential are truly constant in a real system, and oftentimes the principle of linear superposition, which states that two solutions to a differential equation can be added together, is used to generate analytical approximations, such as the form that we have chosen to use:

$$F_{es} = \kappa 64\varepsilon a\left(\frac{kT}{ze}\right)^2\gamma_1\gamma_2\mathrm{e}^{-\kappa h}$$

where κ is the inverse Debye length $\kappa = \sum\sqrt{(n_i e^2 z_i^2/\varepsilon kT)}$, n_i is the number density of the ith ion species, ε is the permittivity of the solution, *a* is the particle radius, *k* is the Boltzmann constant, *T* is the absolute temperature, z_i is the valence of the ith ion species, *e* is the charge of an electron, and $\gamma_1 = \tanh(ze\psi/4kT)$ where ψ is the surface potential and *h* is the separation distance.

This model was developed by Gregory [99] and has been used for approximating practical conditions where a middle ground between the constant charge and constant potential boundary conditions used in deriving these conditions is considered more appropriate [31, 100, 101].

Adding vdW and ES Forces to predict Colloid Detachment Forces In Chapter 2 of this dissertation, we sum the vdW and ES equations to find the total interaction force between the particle and the surface. Colloidal interactions are commonly characterized by their interaction energy, but here for comparison with our experimental force measurements we calculate and plot the total interaction force F_I as a function of h. For our system, the modified DLVO model predicts two minima: a deep primary minimum at small separation distances ($h < 0.5$ nm) and a shallower secondary minimum at intermediate distances ($h \approx 2$ nm). A representative $F_I(h)$ curve for one solution condition (0.5 M NaCl + 0.25× PBS) is shown in **Figure 1.2**. During loading, as the microspheres are drawn to the glass surface by gravity, they will be drawn into the secondary minimum; however, they are unlikely to overcome the barrier to enter the primary minimum. Thus, we assume the force F_d, required to remove the colloids from the surface of the glass at a separation distance h is equal to the depth of the secondary minimum (**Fig. 1.2**, dashed lines and inset).

Measuring DLVO Interactions A variety of tools exist for directly measuring colloidal interaction forces, which are both small and wide-ranging, from 10^{-2} to 10^{4} pN [102-104]. With optical trapping, colloids are brought close to one another and the magnitude of the attractive or repulsive forces between them measured as a function of separation distance [105-107]. Tools like atomic force

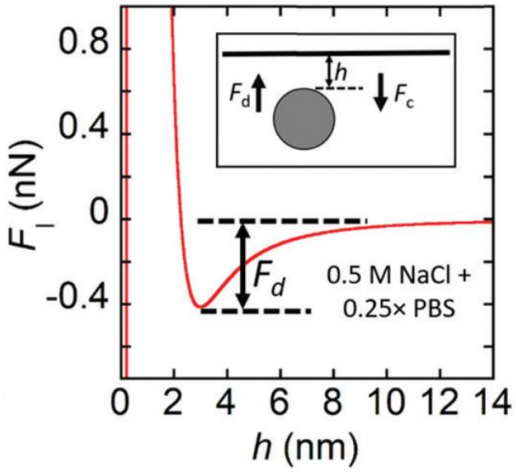


Figure 1.2: Example DLVO curve. The electrostatic and van der Waals forces add together to determine the overall interaction force between a sphere and a flat surface in specific aqueous suspension conditions. Shown here is the estimated interaction force F_I as function of gap distance h calculated using DLVO theory. This interaction force predicts a detachment force F_d = 0.040 nN for 0.5 M NaCl + 0.25× PBS. Chosen y-axis range does not allow the depth of primary minimum or height of energy barrier to be seen. Inset: Schematic of a bead at distance h from glass slide surface subjected to centrifugal force F_c and detachment force F_d. Taken from LeFevre et al. 2021 [108].

microscopy (AFM) [109, 110] measure interactions between colloids and a fixed surface. Both optical trapping and AFM provide high-resolution force information, but measurements are typically performed one at a time, and are not ideal for quantifying heterogeneous systems, which require many measurements to construct statistically significant force distributions. Instead, techniques like magnetic tweezers[104, 111] and centrifugal force microscopy (CFM)[112-117], which can perform multiple force measurements in parallel are better suited for characterizing heterogenous systems. CFM is a particularly attractive technique because it is capable of multiple simultaneous measurements (i.e. force multiplexing) and does not require significant device calibration or user training. A CFM instrument is composed of a miniaturized microscope housed inside a swinging bucket centrifuge. As the centrifuge spins, colloids suspended in liquid and interacting with a

coverslip are subjected to an effective gravitational force drawing them away from the surface. By controlling the rotational speed of the centrifuge, well-defined forces can be applied to 100s of individual colloids simultaneously; however, current CFM instruments rely on brightfield optical microscopy to identify and track colloidal objects [112-117]. This illumination technique is adequate for measuring colloidal interaction forces but is limited with regard to spatial resolution and sample characterization. Fluorescence microscopy offers enhanced spatial resolution and access to a wide variety of sample labelling techniques, but the incorporation of fluorescence imaging into a CFM has not yet been reported. Such an instrument would provide significant benefits for characterizing complex soft and biological materials.

Pathogen Detection

Significance

Infectious pathogens such as influenzas and coronaviruses are a threat to public health – they kill or permanently harm many people, cause large losses in productivity, disrupt normal public life and business, and harm the global economy. Diagnostic testing reduces mortality and disruption by informing infected people to quarantine and/or seek medical attention and by allowing uninfected people to continue their daily lives.

For example, the SARS-CoV-2 virus emerged in late 2019 and quickly became a worldwide pandemic. Prevention measures such as vaccines, social distancing, and masks work well; however, diagnostic testing can and should be an integral tool for preventing viral spread in vaccinated and unvaccinated people. Frequent testing is already an important cornerstone in the re-opening plans of many institutions, but inexpensive, accurate, rapid testing is still not widely

available at large scales even in wealthy countries, and tests are much less available in developing countries due to cost and scalability issues.

There are two common biomarkers for detecting the presence of virus in patient samples. Antigen tests detect the presence of viral proteins, and “molecular” tests detect the presence of viral genetic material. Both methods have their place in a comprehensive testing plan. Antigen tests are less accurate but easier to produce at scale. Molecular tests, in particular reverse transcription polymerase chain reaction (RT-PCR) tests, are considered the “gold standard” of diagnostic pathogen testing and are a better predictor of the patient’s current instantaneous viral load. Molecular tests have historically been more expensive and difficult to produce at scale; but a cheaper, scalable molecular test would provide the accuracy of molecular testing with the widespread distribution of antigen testing.

RT-PCR is the “gold standard” for molecular testing, but requires large reagent volumes, specialized expensive equipment, and trained technicians. One alternative to RT-PCR is RT-LAMP, which provides a level of sensitivity similar to PCR but with a simpler method of conducting the test without expensive equipment.

Molecular testing reagents like LAMP reagents are expensive, so affordable tests need to use a small amount of reagent. The requirement for small reagent volumes requires that a small, predictable amount of patient saliva sample be introduced to the test so as to not dilute the reagents and render them useless. Therefore, inexpensive POC tests require a simple way for the user to meter a small, repeatable amount of their saliva to the test without requiring training or the use of specialized equipment like pipettes.

While patient samples can be collected almost anywhere, the actual test processing is commonly carried out in laboratories. This laboratory processing often increases the amount of time required for the results to be reported to the patients, often taking days, even though many tests require only hours to conduct. More POC testing is a logical way to speed up the reporting time to less than one hour in order to make testing more convenient and provide feedback to the patients sooner – allowing them to go about their business sooner if tested negative, or to quarantine sooner if tested positive.

Without low-cost scalable molecular testing, the proper amount and frequency of accurate pathogen diagnostic testing will not take place, and the populace will not be equipped to make sound health decisions for themselves and their community, and our society will not be properly equipped to handle existing and new epidemics and pandemics, especially during the pre-deployment stages of vaccine development.

Here, we describe a low-cost, hand-held, manually operated device for POC molecular pathogen detection. The device includes a two-pronged fork geometry which enables metering and transfer of small volumes of saliva from flocked collection swabs and contains all reagents needed for isothermal nucleic acid amplification and fluorescence detection. The simple, injection moldable design facilitates easy scale-up and is designed to work with swabs and vials that already exist on the market. The test requires only a simple, inexpensive processing system that allows the test to be set up in a variety of institutions at low cost.

Loop-mediated isothermal amplification (LAMP)

Loop-mediated isothermal amplification (LAMP) is a method utilized in Chapters 3 and 7 of this dissertation for replicating a target nucleic acid sequence in order to determine the presence

or absence of that target sequence in a solution. Similar in concept to the more widely known polymerase chain reaction (PCR)[118-122] but using a different strategy of molecular mechanisms, LAMP was invented in the 1990s by Tsugunori Notomi[123]. In its simplest form, LAMP works by introducing four short segments of single-stranded DNA, called primers[124-126], to a targeted section of double stranded DNA. These four primers, usually 15 – 45 bp in length, are forward inner primer (FIP), forward outer primer (FOP), backward inner primer (BIP), and backward outer primer (BOP). These primers, in tandem with DNA polymerase, execute a chain reaction that produces a variety of nucleic acid structures, called concatamers, from the original target DNA sequence. Broadly speaking, the primers work by annealing to complementary target sequences on the available nucleic acid strands and then initiating complementary DNA production using a DNA polymerase enzyme with strand displacing activity[127]. The strand-displacing activity of the polymerase is a critical factor because it removes the requirement for thermal cycling to melt the DNA, making LAMP an isothermal process. These concatamer structures are detectable in a variety of ways, although they are not exact replicates of the original DNA, like PCR would produce, and thus are not as particularly useful for downstream genetic analysis. However, the effects of the amplification are easily detectable, and the occurrence of amplification indicates that the original target sequence of DNA or RNA was present in the sample. The LAMP reaction is gaining popularity as a diagnostic technique for a variety of nucleic acid biomarkers because it takes place at a constant temperature, unlike PCR which requires a temperature cycle between 65° C and 95° C – a temperature at which the DNA strands will certainly melt or dissociate[128, 129] – for every doubling of the reaction products. LAMP does require a heater to heat the sample to around 65° C to optimize the activity of the chosen DNA polymerase and to lower the binding energy

between the strands of DNA, although the exact temperature varies slightly depending on the exact sequence of base pairs in the system[128, 129]. Adenine and thymine have a slightly lower melting temperature than cytosine and guanine. The primers are designed to bind to specific base pairs in the target genetic sequence, so they have a different base pair sequence in every system, but they always have the same mechanistic functions from system to system which is described below. LAMP can be used with DNA or RNA. If the target sequence is an RNA, the process is called reverse transcription LAMP (RT-LAMP); in this method, a reverse transcriptase enzyme included in the formulation to produce complementary DNA (cDNA) from the RNA, after which the process proceeds as normal. There are two fundamental stages in the standard DNA replication process: loop structure formation and exponential replication.

Loop Structure Formation First, the FIP primer inserts itself into the target DNA strand and anneals to its target sequence (**Fig. 1.3 i**). A DNA polymerase with strand-displacing activity, for example Bst DNA polymerase derived from *Bacillus stearothermophilus*, then forms from the FIP primer a new DNA strand that displaces the original strand. Then the FOP primer inserts just behind the FIP primer (**Fig. 1.3 ii**) and DNA Polymerase starts from the FOP primer to create a new strand that displaces the strand generated from FIP. This displaced strand now interacts with the backward primers. The BIP primer binds to the displaced strand (**Fig. 1.3 iii**) and DNA polymerase starts from BIP to create a new strand. Now BOP attaches just behind the BIP primer (**Fig. 1.3 iv**) and DNA polymerase generates from BOP a new strand that displaces the BIP strand. This displaced BIP strand, due to the design of the primers, now has complementary tags at both ends, and these complementary tag ends loop around and attach to itself, forming the dumbbell structure (**Fig. 1.3 v**) that will undergo exponential replication.

Exponential Replication Now the FIP primer attaches to the outside of the dumbbell structure and DNA polymerase creates a new dumbbell structure. At this point there is a dumbbell structure and a complementary dumbbell structure, so FIP can work on the dumbbell structure (**Fig. 1.3 vi**) and BIP can work on the complementary dumbbell structure (**Fig. 1.3 vii**). Now new dumbbell structures are being generated on an exponential scale, and side effects of this process create additional more complex concatamer structures (**Fig. 1.4 i-ii**) typically constructed from integer multiples of the original dumbbell structure.

Detection The exponential generation of concatamers can be detected in several ways. A byproduct of DNA polymerization is pyrophosphate, a phosphorus oxyanion that upon encountering excess Mg^{2+} present in the reaction mix forms an insoluble complex which makes the suspension more turbid after the replication process has taken place, thereby indicating that the target sequence was present[125, 126]. Another method of detection is colorimetric[130, 131]: pH indicators can be added to the solution to cause a color change when the replication process has taken place due to the increase in hydronium ions as a result of DNA polymerization. One of the increasingly common methods is fluorometric [132] detection, suitable for detection in a qPCR machine or other fluorimeter. An intercalating or DNA binding fluorescent dye is included in the solution, and the fluorescence of the dye greatly increases when it is able to intercalate or bind into nucleic acid sequences; thus, increased fluorescence indicates that the replication process has taken place and therefore that the target sequence was present in the original sample.

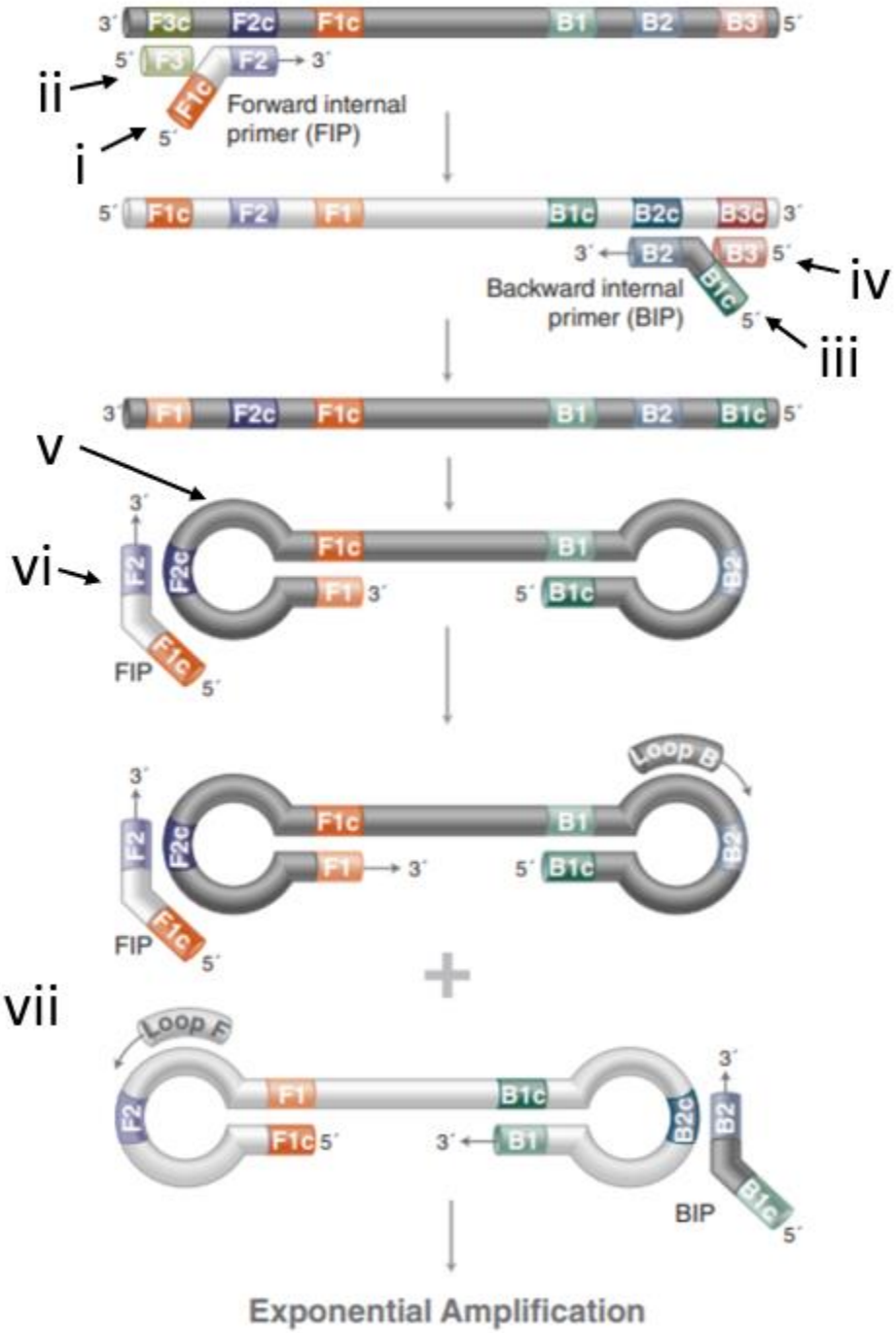


Figure 1.3: *Loop-mediated isothermal amplification (LAMP) process schematic*. The FIP, F3 (a.k.a. FOP), BIP, and B3 (a.k.a. BOP) primers initiate formation of the dumbbell concatamer structure. Once the first dumbbell structure is fully formed, the same four primers initiate exponential concatamer amplification to create more dumbbells as well as additional concatamers. Schematic taken from Gibson 2020 [133].

Saliva as a diagnostic sample Saliva is excreted from several glands in the mouth. It is composed [134-136] of about 98-99% water, with the remaining 2% composed of enzymes, polysaccharides, mucus, electrolytes, epithelial cells, and antibodies. Its main physiological purposes[135] are to lubricate the mucous membranes, start the digestion process of food, and lubricate the bolus of food when swallowing. It can also contain a number of biomarkers[137-140] valuable for diagnostics, including viruses[141-146].

Viruses can enter the saliva *via* three primary mechanisms[147, 148]: 1) transfer from blood to saliva through blood/saliva contact in infected mouth salivary glands; 2) transfer from infected lung tissue to mucus in the respiratory tract; and 3) direct production of virus-infected saliva in infected salivary glands. Saliva is a desirable sample medium for diagnostics because it is very non-invasive and convenient to collect compared to blood draws or nasopharyngeal swabs. However, most saliva-based tests are performed in a lab because the saliva contains enzymes called ribonucleases[149] that degrade RNA and thus can prevent viral RNA from being detected. The saliva must first be treated to deactivate the nucleases and to rupture the viral envelopes to make the viral RNA available to the LAMP reagents. An exact amount of saliva must be mixed with the LAMP reagents – not so much saliva that the saliva water content dilutes the LAMP reagents or that the saliva ribonucleases degrade the exposed viral RNA before it can be amplified, but also not so small of a volume that the sensitivity of the assay is diminished by a lower initial concentration of viruses. Thus, in Chapter 3 we create a method for collecting and pre-treating a specific amount of saliva and introduce the saliva to a specific volume of finely tuned RT-LAMP reagents that are

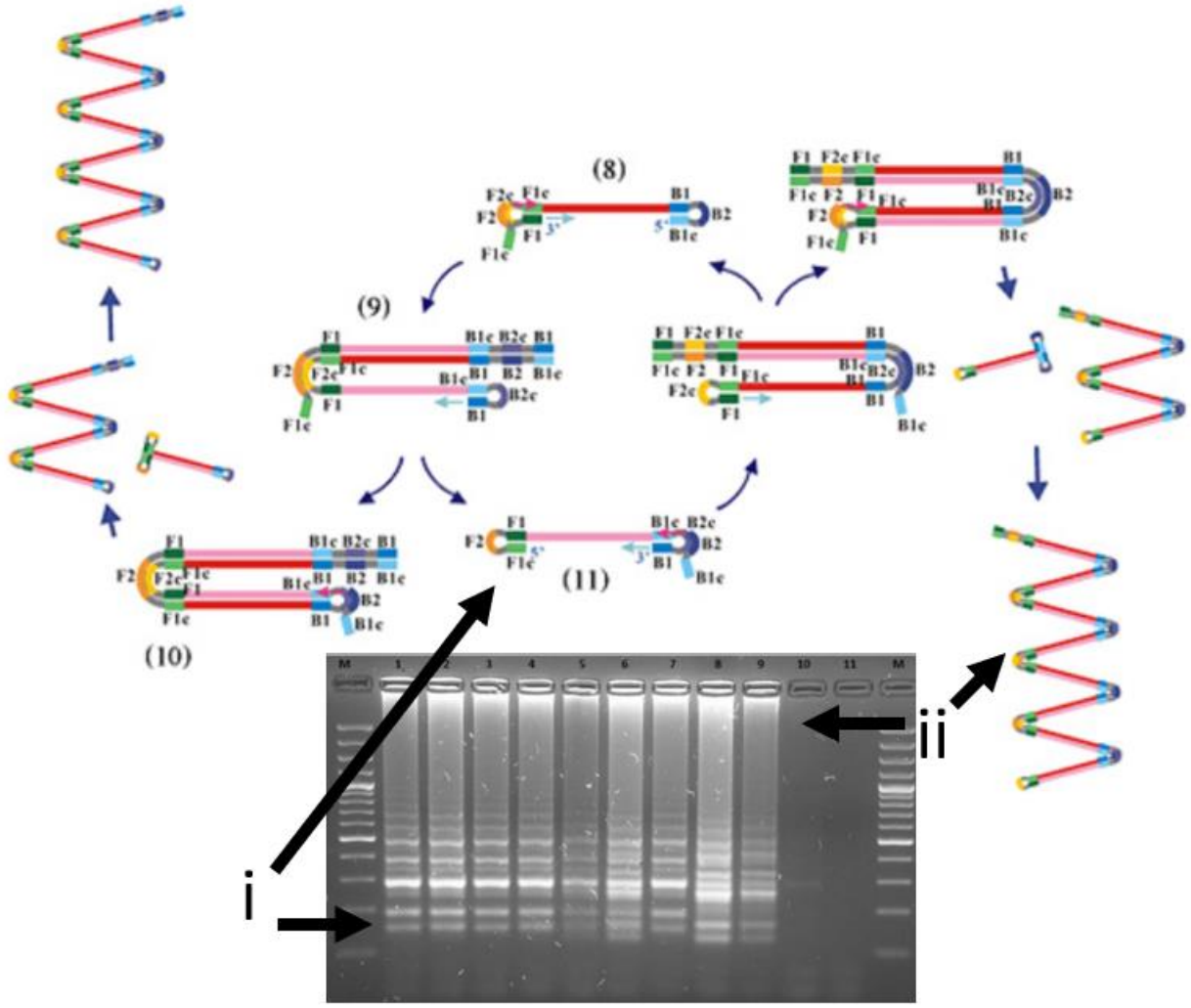


Figure 1.4: *Concatamer formation during the exponential replication phase of LAMP*. A variety of additional complex structures are formed from the initial dumbbell structures. The variety of structures is shown in a gel electrophoresis run (inset). The smaller concatamers (i) are more easily separated by the gel and thus form distinct bands, whereas the largest concatamers (ii) are not well separated by the gel and do not form distinct bands. Concatamer schematic taken from Eichen Chemical Co., Ltd. 2005 [150]. Gel image taken from Mugambi et al. 2015 [151].

developed in Chapter 7. This process must be relatively straightforward and not require specialized tools so that it can be done with minimal training in a POC setting rather than in a lab. After the collection, treatment, and mixing is complete, the sample is then placed in a heater at 65°C for 30

minutes, and the presence or absence of increased fluorescence is detected in a matter of seconds in our inexpensive custom detection box.

Design for Injection Molding

As previously discussed above and detailed in Chapters 3 and 7 of this dissertation, widespread diagnostic testing is an important cornerstone in strategies to mitigate the health, social, and economical effects of pathogenic diseases. To enable widespread testing, diagnostic devices must be easily scaled to high volume production. Our device was designed with high volume sourcing in mind for all components, including injection moldability of the syringe portion.

Injection Molding Concepts Injection molding[152-159] works by forcing melted plastic through a nozzle into a cavity between two mold halves. First, solid millimeter-scale plastic pellets are gravity fed (**Fig. 1.5 i**) into the back end of a rotating screw that fits tightly inside a heated barrel. The flights of the rotating screw[160-163] perform two functions: 1) to push the plastic forward towards the nozzle of the screw, and 2) to shear and mix the plastic pellets, heating them through friction at the same time. When the melted pellets reach the front of the screw and barrel, they are pushed past a check ring located on the front of the screw and into a reservoir in front of the screw. The size of the reservoir can be adjusted by moving the screw forward or backward. Thus, the screw and barrel form an adjustable plunger and syringe mechanism that can inject heated plastic into a mold. The check ring prevents plastic from traveling backward into the screw flights after it has passed forward of the check ring.

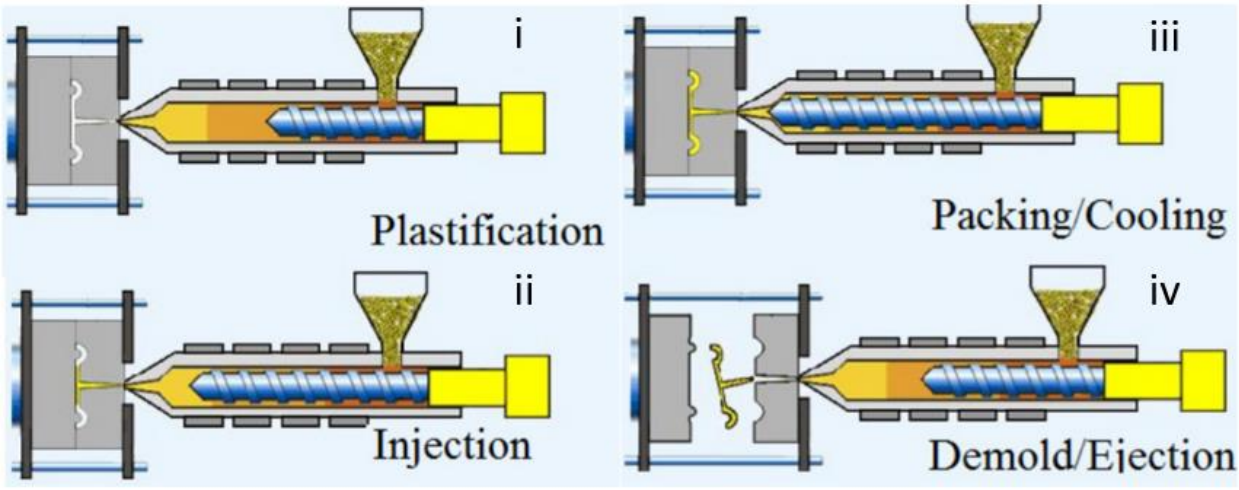


Figure 1.5: *Injection molding process overview*. i) Plastification: the plastic pellets gravity feed into the back of the screw. As the screw turns, the pellets are pushed forward and sheared by the flights of the screw. The shear force melts the pellets by the time they reach the front of the screw in preparation for injection. ii) Injection: The screw pushes forward to inject the plastic into the mold. A check ring prevents backflow of the molten plastic. iii) Packing/Cooling: The molding machine injects plastic to a defined pressure level in order to pack the polymer molecules tightly together and fill the mold completely. Then the machine sits idle for several seconds to allow the plastic to cool and solidify before ejection. iv) Demold/Ejection: The mold opens and ejector pins push the molded part off the core side of the mold. Schematic taken from Xie et al. 2011 [164].

Once the reservoir is filled to its capacity, the screw is pushed linearly forward (**Fig. 1.5 ii**). This forward motion pushes the plastic through a nozzle and into the cavity formed by the two mold halves. Each of the mold halves are held in the molding machine, in front of the screw and barrel, independently. Hydraulic pumps provide the huge clamping pressure[165] necessary to hold the mold shut during the injection process, which can create pressures on the order of tens of MPa [166, 167]. The plastic is pushed into the mold at a controlled rate. The molten plastic forms a curved flow front (**Fig. 1.6**), often termed fountain flow[168-174], as it flows into the cavity and experiences shear along the walls of the cavity. Then, as the part is almost completely full of plastic, the machine switches to pressure control and fills, or "packs"[166] (**Fig. 1.5 iii**), the cavity until a certain pressure is filled. This switch[175] from speed-control to pressure-control is often called "scientific

molding" because it removes some of the guess work involved in packing the polymer molecules adequately so as to reduce sink marks and warpage without increasing the risk of mold damage or flash[176]. Flash is the inadvertent leakage of plastic outside the mold cavity at the parting line[177] or at the vents, resulting in a thin feature that does not belong on the part.

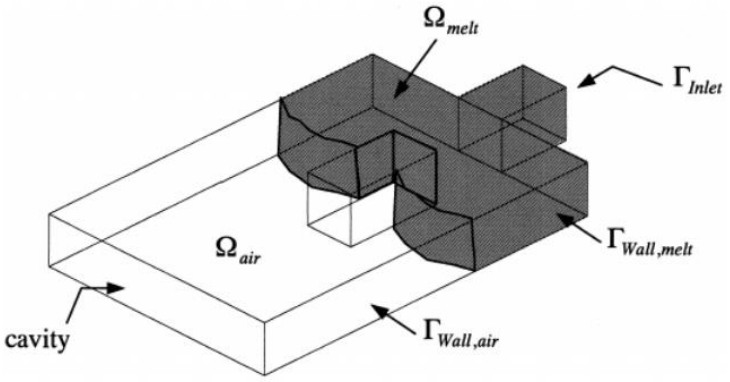


Figure 1.6: *Illustration of the molten plastic filling front*. The classic fountain flow geometry at the leading edge of the molten plastic is shown. Taken from Chang 2001[153].

As the molten plastic is rapidly injected into the mold cavity, it experiences high shear stress[178]. This stress forces the polymer molecules to align and thus lowers the viscosity of the molten plastic, a phenomenon known as shear thinning[179, 180]. The viscosity of molten plastic at low shear rates is very high; however, the shear generated by the injection process and corresponding shear thinning lowers the viscosity enough to make injection of the plastic possible[181-183]. Air that was originally inside the mold evacuates through vent channels[184] that are strategically placed throughout the mold, often along ejector pins that are thick enough to allow air to escape but thin enough to prevent molten plastic from entering the vent channel. Each plastic has a different viscosity at molding temperature and thus the vent channel dimensions are designed

with the specific plastic in mind. The mold geometry must be designed to facilitate proper flow and packing of the plastic inside the cavity.

After the plastic has been injected and packed into the cavity, the plastic is allowed to cool (**Fig. 1.5 iii**). The cooling process[185-188] can only take place properly if cooling channels are built into the mold. Cooling channels circulate fluid near the cavity so as to remove heat from the plastic during the molding process. Without cooling channels, the mold would keep heating up with every injection cycle and eventually the plastic would stop cooling in the mold. The fluid is circulated at a rate sufficient to generate turbulent flow, because turbulent flow transfers[189, 190] heat faster than laminar flow. The fluid is usually water for plastics with lower melting temperatures, like polypropylene, and is usually oil for plastics with higher melting temperatures, like polyetherimides such as Ultem.

After the part has cooled, the mold opens and ejector pins on the core side of the mold push the part off the mold (**Fig. 1.5 iv**). The part may simply fall into a bin under the mold, or it may be grasped by a robotic arm that places the part on a conveyor belt for controlled cooling or may engage the part with secondary processes like ink pad printing or sprue removal. The sprue is the plastic channel that leads from the screw nozzle and into the mold cavity. For multi-cavity molds, the sprue leads into runners that enter into each identical cavity. The cavities must be carefully laid out to ensure the plastic shear is identical in each cavity so that each cavity experiences the same plastic flow and pressure. The entrance from the runner into the cavity is called the gate, and the gate is carefully designed[191-195] in accordance with the specific plastic being used and the exact ejection method being used for the part. Different gate types include cashew gate, edge gate, submarine gate, and hot runner valve and thermal gates.

An important design parameter is wall thickness[196-198] and its uniformity. Different plastics have different ideal wall thicknesses[199], usually on the order of millimeters. Most injection molded parts are designed with millimeter-scale wall thicknesses in order to facilitate faster cooling, reduce sink marks, and save plastic. “Sink” is the defect that can occur when the plastic is not adequately packed into a region of the molded part. As the plastic cools, the polymer molecules try to curl back into their original non-linear shape[159]. If the polymer molecules are not adequately packed tightly enough together, then this curling up of polymers will result the surface of the part caving in and exhibiting depressions that align with the thickest area of the part, called sink marks, because the thickest area of the part has the most loosely packed polymer molecules. The uniformity of the wall thickness is crucial because the plastic will not pack into the part features uniformly if the walls are very non-uniform; thus, the thicker wall sections will exhibit sink marks.

Another important design factor is draft angle[200-202]. Draft is the angle applied to what would normally be a vertical surface in order to facilitate removal of the molded part from the mold. For example, if you are molding a plastic cup, the original cup design may contain perfectly vertical walls for aesthetic or functional purposes. However, the inside and outside of the vertical walls of the cup will scrape against the mold during part removal – first, as the molded opens, the cavity side of the mold will scrape against the outside of the cup; then, as the cup is pushed off the core side of the mold by ejector pins, the inside of the cup will scrap against the outside of the core feature on the core side of the mold. This scraping makes it more difficult to remove the part and could result in mold damage or in the part getting stuck in the mold, which is then time consuming and laborious to get out. Instead, the cup would be designed with a small angle on the inside and

outside of the walls – usually only 1° or 2° – so that the cup separates cleanly from the mold as soon as the part removal process begins.

The part must also be designed with mold fabrication techniques [203, 204] in mind. Molds are typically fabricated out of hardened steel or, for prototyping purposes, aluminum. The part must be designed in a way that allows the mold to be fabricated using traditional toolmaking techniques and with minimal risk of breakage or other problems during molding. Molds are fabricated using highly specialized equipment like heavy-duty lathes, computer numerical control (CNC) milling machines, and electro-discharge machines[205-207] (EDM). CNC machines mill features using specialized milling bits and a computer controlled milling head. EDM utilizes a graphite electrode that has been milled with a CNC machine. An electric potential is applied to the graphite electrode and the steel block while they are submerged into a conductive drilling fluid, causing plasma to effectively "burn" the shape of the electrode into the steel. More simple methods of EDM include wire-shaped copper electrodes, called "hole-poppers," that simply drill holes through large blocks of steel in preparation for other fabrication processing.

Each mold half is a complex mechanical assembly of tightly fitting moving parts. Mold complexity varies greatly from part to part, with the simplest molds having only the two static mold halves and a few ejector pins, and the most complex molds also including laterally moving sliders to create undercut features, rotating platens and double barrels for multi-material molding, and multiple stages of robotically and manually executed secondary processes after molding.

The physical geometry of the device must be designed in order to facilitate the fabrication of the mold and ensure mold longevity over many injection mold cycles. Furthermore, the physics of plastic flow and heat transfer must be considered in order to help ensure the molded parts are

produced consistently and to the required design specifications. Our device was designed with these requirements in mind and then further adjusted for manufacturing with the help of a contract injection molding company, Natech Plastics. Good contract manufacturers utilize their collective toolmaking and molding experience to implement design guidelines in order to reduce the risk of future productivity or quality problems and can help balance this risk management process with the functionality requirements for the device. This design process is called design for injection molding (DFIM) and more generally design for manufacturing[208] (DFM).

References cited

1. Jones, R. A. L., *Soft Condensed Matter*. Oxford University Press Inc.: 2002.

2. Witten, T. A. a. P., Phillip A., *Structured fluids: polymers, colloids, surfactants*, . Oxford University Press Inc.: 2004.

3. Russel, W. B.; Russel, W. B.; Saville, D. A.; Schowalter, W. R., *Colloidal Dispersions*. Cambridge University Press: 1991.

4. Nishinari, K., Rheological and DSC study of sol-gel transition in aqueous dispersions of industrially important polymers and colloids. *Colloid and Polymer Science* **1997,** *275* (12), 1093-1107.

5. Freundlich, H., Colloidal structures in biology. *Journal of Physical Chemistry* **1937,** *41* (9), 1151-1161.

6. Krogh, A.; Landis, E. M.; Turner, A. H., The movement of fluid through the human capillary wall in relation to venous pressure and to the colloid osmotic pressure of the blood. *Journal of Clinical Investigation* **1932,** *11* (1), 63-95.

7. Geoghegan, W. D.; Ackerman, G. A., ADSORPTION OF HORSERADISH-PEROXIDASE, OVOMUCOID AND ANTIIMMUNOGLOBULIN TO COLLOIDAL GOLD FOR INDIRECT DETECTION OF CONCANAVALIN-A, WHEAT-GERM AGGLUTININ AND GOAT ANTIHUMAN IMMUNOGLOBULIN-G ON CELL-SURFACES AT ELECTRON-MICROSCOPIC LEVEL - NEW METHOD, THEORY AND APPLICATION. *Journal of Histochemistry & Cytochemistry* **1977,** *25* (11), 1187-1200.

8. Dobrovolskaia, M. A.; Patri, A. K.; Zheng, J.; Clogston, J. D.; Ayub, N.; Aggarwal, P.; Neun, B. W.; Hall, J. B.; McNeil, S. E., Interaction of colloidal gold nanoparticles with human blood: effects on particle size and analysis of plasma protein binding profiles. *Nanomedicine-Nanotechnology Biology and Medicine* **2009,** *5* (2), 106-117.

9. Chi, E. Y.; Krishnan, S.; Kendrick, B. S.; Chang, B. S.; Carpenter, J. F.; Randolph, T. W., Roles of conformational stability and colloidal stability in the aggregation of recombinant human granulocyte colony-stimulating factor. *Protein Science* **2003,** *12* (5), 903-913.

10. Shaldon, S.; Caesar, J.; Chiandussi, L.; Sherlock, S.; Guevara, L., ESTIMATION OF HEPATIC BLOOD FLOW AND INTRAHEPATIC SHUNTED BLOOD FLOW BY COLLOIDAL HEAT-DENATATURED HUMAN SERUM ALBUMIN LABELED WITH I131. *Journal of Clinical Investigation* **1961,** *40* (7), 1346-&.

11. Pertoft, H.; Back, O.; Lindahlk.K, SEPARATION OF VARIOUS BLOOD CELLS IN COLLOIDAL SILICA-POLYVINYLPYRROLIDONE GRADIENTS. *Exp Cell Res* **1968,** *50* (2), 355-&.

12. Matejtschuk, P.; Dash, C. H.; Gascoigne, E. W., Production of human albumin solution: a continually developing colloid. *British Journal of Anaesthesia* **2000,** *85* (6), 887-895.

13. Hoeft, A.; Korb, H.; Mehlhorn, U.; Stephan, H.; Sonntag, H., PRIMING OF CARDIOPULMONARY BYPASS WITH HUMAN ALBUMIN OR RINGER LACTATE - EFFECT ON COLLOID OSMOTIC-PRESSURE AND EXTRAVASCULAR LUNG WATER. *British Journal of Anaesthesia* **1991,** *66* (1), 73-80.

14. Toyofuku, M.; Tashiro, Y.; Hasegawa, Y.; Kurosawa, M.; Nomura, N., Bacterial membrane vesicles, an overlooked environmental colloid: Biology, environmental perspectives and applications. *Advances in Colloid and Interface Science* **2015,** *226*, 65-77.

15. Edwards, S. A.; Williams, D. R. M., Hofmeister effects in colloid science and biology explained by dispersion forces: analytic results for the double layer interaction. *Current Opinion in Colloid & Interface Science* **2004,** *9* (1-2), 139-144.

16. Dholakia, K.; MacDonald, M. P.; Zemanek, P.; Cizmar, T., Cellular and colloidal separation using optical forces. In *Laser Manipulation of Cells and Tissues*, Berns, M. W.; Greulich, K. O., Eds. 2007; Vol. 82, pp 467-495.

17. Bostrom, M.; Williams, D. R. M.; Ninham, B. W., Specific ion effects: why colloid science has failed to contribute to biology. *Trends in Colloid and Interface Science Xvi* **2004,** *123*, 110-113.

18. Delabouret, A.; Thioune, O.; Fessi, H.; Devissaguet, J. P.; Puisieux, F., APPLICATION OF AN ORIGINAL PROCESS FOR OBTAINING COLLOIDAL DISPERSIONS OF SOME COATING POLYMERS - PREPARATION, CHARACTERIZATION, INDUSTRIAL SCALE-UP. *Drug Development and Industrial Pharmacy* **1995,** *21* (2), 229-241.

19. Kang, S. K.; Choo, K. H., Use of MF and UF membranes for reclamation of glass industry wastewater containing colloidal clay and glass particles. *Journal of Membrane Science* **2003,** *223* (1-2), 89-103.

20. Komesvarakul, N.; Scamehorn, J. F.; Gecol, H., Purification of phenolic-laden wastewater from the pulp and paper industry by using colloid-enhanced ultrafiltration. *Separation Science and Technology* **2003,** *38* (11), 2465-2501.

21. Chuang, S. H.; Chang, T. C.; Ouyang, C. F.; Leu, J. M., Colloidal silica removal in coagulation processes for wastewater reuse in a high-tech industrial park. *Water Science and Technology* **2007,** *55* (1-2), 187-195.

22. Quinson, J.; Neumann, S.; Wannmacher, T.; Kacenauskaite, L.; Inaba, M.; Bucher, J.; Bizzotto, F.; Simonsen, S. B.; Kuhn, L. T.; Bujak, D.; Zana, A.; Arenz, M.; Kunz, S., Colloids for Catalysts: A Concept for the Preparation of Superior Catalysts of Industrial Relevance. *Angewandte Chemie-International Edition* **2018,** *57* (38), 12338-12341.

23. Pendse, H. P.; Sharma, A., PARTICLE-SIZE DISTRIBUTION ANALYSIS OF INDUSTRIAL COLLOIDAL SLURRIES USING ULTRASONIC SPECTROSCOPY. *Particle & Particle Systems Characterization* **1993,** *10* (5), 229-233.

24. Huang, J. S.; Varadaraj, R., Colloid and interface science in the oil industry. *Current Opinion in Colloid & Interface Science* **1996,** *1* (4), 535-539.

25. Whitehouse, B. G.; Yeats, P. A.; Strain, P. M., Cross-flow filtration of colloids from aquatic environments. *Limnology and Oceanography* **1990,** *35* (6), 1368-1375.

26. Neal, C.; Jarvie, H.; Rowland, P.; Lawler, A.; Sleep, D.; Scholefield, P., Titanium in UK rural, agricultural and urban/industrial rivers: Geogenic and anthropogenic colloidal/sub-colloidal sources and the significance of within-river retention. *Sci Total Environ* **2011,** *409* (10), 1843-1853.

27. Verwey, E. J. W.; Overbeek, J. T. G., Theory of the stability of lyophobic colloids. *Elsevier Publishing Company* **1948**.

28. Moore, T. L.; Rodriguez-Lorenzo, L.; Hirsch, V.; Balog, S.; Urban, D.; Jud, C.; Rothen-Rutishauser, B.; Lattuada, M.; Petri-Fink, A., Nanoparticle colloidal stability in cell culture media and impact on cellular interactions. *Chemical Society Reviews* **2015,** *44* (17), 6287-6305.

29. Joanny, J. F.; Leibler, L.; Degennes, P. G., EFFECTS OF POLYMER-SOLUTIONS ON COLLOID STABILITY. *Journal of Polymer Science Part B-Polymer Physics* **1979,** *17* (6), 1073-1084.

30. Heurtault, B.; Saulnier, P.; Pech, B.; Proust, J. E.; Benoit, J. P., Physico-chemical stability of colloidal lipid particles. *Biomaterials* **2003,** *24* (23), 4283-4300.

31. Elimelech, M.; Gregory, J.; Jia, X.; Williams, R., Particle Deposition & Aggregation. *Butterworth-Heinemann Ltd* **1995**.

32. Tufenkji, N.; Elimelech, M., Breakdown of colloid filtration theory: Role of the secondary energy minimum and surface charge heterogeneities. *Langmuir* **2005,** *21* (3), 841-852.

33. Tufenkji, N.; Elimelech, M., Deviation from the classical colloid filtration theory in the presence of repulsive DLVO interactions. *Langmuir* **2004,** *20* (25), 10818-10828.

34. Harvey, R. W.; Garabedian, S. P., USE OF COLLOID FILTRATION THEORY IN MODELING MOVEMENT OF BACTERIA THROUGH A CONTAMINATED SANDY AQUIFER. *Environ Sci Technol* **1991,** *25* (1), 178-185.

35. Zhou, Z.; Tao, Y.; Zhang, S.; Xiao, Y.; Meng, F.; Stuckey, D. C., Size-dependent microbial diversity of sub-visible particles in a submerged anaerobic membrane bioreactor (SAnMBR): Implications for membrane fouling. *Water Res* **2019,** *159*, 20-29.

36. Kunacheva, C.; Soh, Y. N. A.; Stuckey, D. C., Effect of feed pH on reactor performance and production of soluble microbial products (SMPs) in a submerged anaerobic membrane bioreactor. *Chem Eng J* **2017,** *320*, 135-143.

37. Zhou, Z.; Meng, F.; Chae, S.-R.; Huang, G.; Fu, W.; Jia, X.; Li, S.; Chen, G.-H., Microbial Transformation of Biomacromolecules in a Membrane Bioreactor: Implications for Membrane Fouling Investigation. *Plos One* **2012,** *7* (8).

38. Song, W.; Lee, L. Y.; You, H.; Shi, X.; Ng, H. Y., Microbial community succession and its correlation with reactor performance in a sponge membrane bioreactor coupled with fiber-bundle anoxic bio-filter for treating saline mariculture wastewater. *Bioresource Technology* **2020,** *295*.

39. Elander, R. P., Industrial production of beta-lactam antibiotics. *Appl Microbiol Biot* **2003,** *61* (5-6), 385-392.

40. Takiguchi, Y.; Mishima, H.; Okuda, M.; Terao, M., MILBEMYCINS, A NEW FAMILY OF MACROLIDE ANTIBIOTICS - FERMENTATION, ISOLATION AND PHYSICOCHEMICAL PROPERTIES. *Journal of Antibiotics* **1980,** *33* (10), 1120-1127.

41. Sehgal, S. N.; Baker, H.; Vezina, C., RAPAMYCIN (AY-22,989), A NEW ANTIFUNGAL ANTIBIOTIC .2. FERMENTATION, ISOLATION AND CHARACTERIZATION. *Journal of Antibiotics* **1975,** *28* (10), 727-732.

42. Erguder, T. H.; Tezel, U.; Guven, E.; Demirer, G. N., Anaerobic biotransformation and methane generation potential of cheese whey in batch and UASB reactors. *Waste Management* **2001,** *21* (7), 643-650.

43. Castello, E.; Garcia y Santos, C.; Iglesias, T.; Paolino, G.; Wenzel, J.; Borzacconi, L.; Etchebehere, C., Feasibility of biohydrogen production from cheese whey using a UASB reactor: Links between microbial community and reactor performance. *International Journal of Hydrogen Energy* **2009,** *34* (14), 5674-5682.

44. Smogrovicova, D.; Domeny, Z.; Gemeiner, P.; Malovikova, A.; Sturdik, E., Reactors for continuous primary beer fermentation using immobilised yeast. *Biotechnology Techniques* **1997,** *11* (4), 261-264.

45. Parawira, W.; Kudita, I.; Nyandoroh, M. G.; Zvauya, R., A study of industrial anaerobic treatment of opaque beer brewery wastewater in a tropical climate using a full-scale UASB reactor seeded with activated sludge. *Process Biochemistry* **2005,** *40* (2), 593-599.

46. Branyik, T.; Silva, D. P.; Vicente, A. A.; Lehnert, R.; Silva, J. B. A. E.; Dostalek, P.; Teixeira, J. A., Continuous immobilized yeast reactor system for complete beer fermentation using spent grains and corncobs as carrier materials. *Journal of Industrial Microbiology & Biotechnology* **2006,** *33* (12), 1010-1018.

47. Najafpour, G.; Younesi, H.; Ismail, K. S. K., Ethanol fermentation in an immobilized cell reactor using Saccharomyces cerevisiae. *Bioresource Technology* **2004,** *92* (3), 251-260.

48. Ren, N. Q.; Wang, B. Z.; Huang, J. C., Ethanol-type fermentation from carbohydrate in high rate acidogenic reactor. *Biotechnology and Bioengineering* **1997,** *54* (5), 428-433.

49. Pan, X.; Fan, Z.; Chen, W.; Ding, Y.; Luo, H.; Bao, X., Enhanced ethanol production inside carbon-nanotube reactors containing catalytic particles. *Nature Materials* **2007,** *6* (7), 507-511.

50. Wargacki, A. J.; Leonard, E.; Win, M. N.; Regitsky, D. D.; Santos, C. N. S.; Kim, P. B.; Cooper, S. R.; Raisner, R. M.; Herman, A.; Sivitz, A. B.; Lakshmanaswamy, A.; Kashiyama, Y.; Baker, D.; Yoshikuni, Y., An Engineered Microbial Platform for Direct Biofuel Production from Brown Macroalgae. *Science* **2012,** *335* (6066), 308-313.

51. Peralta-Yahya, P. P.; Zhang, F.; del Cardayre, S. B.; Keasling, J. D., Microbial engineering for the production of advanced biofuels. *Nature* **2012,** *488* (7411), 320-328.

52. Li, Q.; Du, W.; Liu, D., Perspectives of microbial oils for biodiesel production. *Appl Microbiol Biot* **2008,** *80* (5), 749-756.

53. Heidebrecht, A.; Scheibel, T., Recombinant Production of Spider Silk Proteins. *Advances in Applied Microbiology, Vol 82* **2013,** *82*, 115-153.

54. Fahnestock, S. R.; Yao, Z.; Bedzyk, L. A., Microbial production of spider silk proteins. *Journal of biotechnology* **2000,** *74* (2), 105-19.

55. Singh, R. S.; Saini, G. K.; Kennedy, J. F., Pullulan: Microbial sources, production and applications. *Carbohydrate Polymers* **2008,** *73* (4), 515-531.

56. Jonas, R.; Farah, L. F., Production and application of microbial cellulose. *Polymer Degradation and Stability* **1998,** *59* (1-3), 101-106.

57. Chawla, P. R.; Bajaj, I. B.; Survase, S. A.; Singhal, R. S., Microbial Cellulose: Fermentative Production and Applications. *Food Technology and Biotechnology* **2009,** *47* (2), 107-124.

58. Suopajarvi, T.; Liimatainen, H.; Hormi, O.; Niinimaki, J., Coagulation-flocculation treatment of municipal wastewater based on anionized nanocelluloses. *Chem Eng J* **2013,** *231*, 59-67.

59. Hargreaves, A. J.; Vale, P.; Whelan, J.; Alibardi, L.; Constantino, C.; Dotro, G.; Cartmell, E.; Campo, P., Impacts of coagulation-flocculation treatment on the size distribution and bioavailability of trace metals (Cu, Pb, Ni, Zn) in municipal wastewater. *Water Res* **2018,** *128*, 120-128.

60. Chan, Y. J.; Chong, M. F.; Law, C. L.; Hassell, D. G., A review on anaerobic-aerobic treatment of industrial and municipal wastewater. *Chem Eng J* **2009,** *155* (1-2), 1-18.

61. Beltran-Heredia, J.; Sanchez-Martin, J., Municipal wastewater treatment by modified tannin flocculant agent. *Desalination* **2009,** *249* (1), 353-358.

62. Tu, X.; Song, Y.; Yu, H.; Zeng, P.; Liu, R., Fractionation and characterization of dissolved extracellular and intracellular products derived from floccular sludge and aerobic granules. *Bioresource Technology* **2012,** *123*, 55-61.

63. Shak, K. P. Y.; Wu, T. Y., Coagulation-flocculation treatment of high-strength agro-industrial wastewater using natural Cassia obtusifolia seed gum: Treatment efficiencies and flocs characterization. *Chem Eng J* **2014,** *256*, 293-305.

64. Peppas, N. A., *Hydrogels in Medicine and Pharmacy: Fundamentals*. CRC Press: 2019.

65. Menut, P.; Seiffert, S.; Sprakel, J.; Weitz, D. A., Does size matter? Elasticity of compressed suspensions of colloidal- and granular-scale microgels. *Soft Matter* **2012,** *8* (1), 156-164.

66. Benjamin, A. D.; Abbasi, R.; Owens, M.; Olsen, R. J.; Walsh, D. J.; LeFevre, T. B.; Wilking, J. N., Light-based 3D printing of hydrogels with high-resolution channels. *Biomedical Physics & Engineering Express* **2019,** *5* (2).

67. Farjami, T.; Madadlou, A., An overview on preparation of emulsion-filled gels and emulsion particulate gels. *Trends Food Sci. Technol.* **2019,** *86*, 85-94.

68. Mason, T. G.; Bibette, J.; Weitz, D. A., Elasticity of Compressed Emulsions. *Physical Review Letters* **1995,** *75* (10), 2051-2054.

69. Mason, T. G., New fundamental concepts in emulsion rheology. *Current Opinion in Colloid & Interface Science* **1999,** *4* (3), 231-238.

70. Brummer, R., *Rheology Essentials of Cosmetic and Food Emulsions*. Springer Berlin Heidelberg: 2006.

71. Fryd, M. M.; Mason, T. G., Advanced Nanoemulsions. In *Annual Review of Physical Chemistry, Vol 63*, Johnson, M. A.; Martinez, T. J., Eds. Annual Reviews: Palo Alto, 2012; Vol. 63, pp 493-518.

72. Lee, G.; Han, S.-B.; Lee, J.-H.; Kim, H.-W.; Kim, D.-H., Cancer Mechanobiology: Microenvironmental Sensing and Metastasis. *ACS Biomaterials Science & Engineering* **2019,** *5* (8), 3735-3752.

73. Verbruggen, S., *Mechanobiology in Health and Disease*. Elsevier Science: 2018.

74. Hu, R. Q.; Li, F.; Lv, J. Q.; He, Y.; Lu, D. T.; Yamada, T.; Ono, N., Microfluidic analysis of pressure drop and flow behavior in hypertensive micro vessels. *Biomedical Microdevices* **2015,** *17* (3).

75. von Smoluchowski, M., Experiments on a mathematical theory of kinetic coagulation of coloid solutions. *Zeitschrift Fur Physikalische Chemie--Stochiometrie Und Verwandtschaftslehre* **1917,** *92* (2), 129-168.

76. Doob, J. L., The Brownian movement and stochastic equations. *Annals of Mathematics* **1942,** *43*, 351-369.

77. Brown, R., A brief account of microscopical observations on the particles contained in the pollen of plants. 1827.

78. Einstein, A., The theory of the Brownian Motion. *Annalen Der Physik* **1906,** *19* (2), 371-381.

79. Perrin, J., Brownian motion and molecular reality. *Annales De Chimie Et De Physique* **1909,** *18*, 5-114.

80. Israelachvili, J. N., Intermolecular and Surface Forces, 3rd Edition. *Intermolecular and Surface Forces, 3rd Edition* **2011**, 1-674.

81. Duncan, G. A.; Gerecht, S.; Fairbrother, D. H.; Bevan, M. A., Diffusing Colloidal Probes of kT-Scale Biomaterial-Cell Interactions. *Langmuir* **2016,** *32* (46), 12212-12220.

82. Bevan, M. A.; Eichmann, S. L., Optical microscopy measurements of kT-scale colloidal interactions. *Current Opinion in Colloid & Interface Science* **2011,** *16* (2), 149-157.

83. Sutherland, W., A dynamical theory of diffusion for non-electrolytes and the molecular mass of albumin. *Philosophical Magazine* **1905,** *9* (49-54), 781-785.

84. Langevin, M. P., Sur la the´orie du mouvement brownien. *C. R. Acad. Sci.* **1908,** *146*, 530–533.

85. Einstein, A., Über die von der molekularkinetischen Theorie der Wärme geforderte Bewegung von in ruhenden Flüssigkeiten suspendierten Teilchen. *Annalen der Physik* **1905,** *322* (8), 549-560.

86. Derjaguin, B.; Landau, L., THEORY OF THE STABILITY OF STRONGLY CHARGED LYOPHOBIC SOLS AND OF THE ADHESION OF STRONGLY CHARGED-PARTICLES IN SOLUTIONS OF ELECTROLYTES. *Prog. Surf. Sci.* **1993,** *43* (1-4), 30-59.

87. Verwey, E. J. W., THEORY OF THE STABILITY OF LYOPHOBIC COLLOIDS. *Journal of Physical and Colloid Chemistry* **1947,** *51* (3), 631-636.

88. Israelachvilli, J. N., Intermolecular & Surface Forces, 2nd Edition. **1985**, 1-674.

89. Hamaker, H. C., The London - Van Der Waals attraction between spherical particles. *Physica* **1937,** *4*, 1058-1072.

90. Lipomi, D., Van der Waals forces between surfaces, Derjaguin approximation. In *NANO 202*, YouTube: University of California San Diego, 2017.

91. Mo, S.; Shao, X.; Chen, Y.; Cheng, Z., Increasing entropy for colloidal stabilization. *Sci Rep-Uk* **2016,** *6*.

92. van Roij, R., Defying gravity with entropy and electrostatics: sedimentation of charged colloids. *Journal of Physics-Condensed Matter* **2003,** *15* (48), S3569-S3580.

93. Swendsen, R. H., Statistical mechanics of colloids and Boltzmann's definition of the entropy. *American Journal of Physics* **2006,** *74* (3), 187-190.

94. Speck, T.; Blickle, V.; Bechinger, C.; Seifert, U., Distribution of entropy production for a colloidal particle in a nonequilibrium steady state. *Epl* **2007,** *79* (3).

95. Royall, C. P.; van Roij, R.; van Blaaderen, A., Extended sedimentation profiles in charged colloids: the gravitational length, entropy, and electrostatics. *Journal of Physics-Condensed Matter* **2005,** *17* (15), 2315-2326.

96. Manoharan, V. N., Colloidal matter: Packing, geometry, and entropy. *Science* **2015,** *349* (6251).

97. Overbeek, J. T. G., THE ROLE OF ENERGY AND ENTROPY IN THE ELECTRICAL DOUBLE-LAYER. *Colloids and Surfaces* **1990,** *51*, 61-75.

98. Frenkel, D., Why colloidal systems can be described by statistical mechanics: some not very original comments on the Gibbs paradox. *Molecular Physics* **2014,** *112* (17), 2325-2329.

99. Gregory, J., Interaction of Unequal Double Layers at Constant Charge. *J Colloid and Interface Sci* **1974,** *51*, 44-51.

100. Assemi, S.; Nalaskowski, J.; Johnson, W. P., Direct force measurements between carboxylate-modified latex microspheres and glass using atomic force microscopy. *Colloid Surf. A-Physicochem. Eng. Asp.* **2006,** *286* (1-3), 70-77.

101. Chen, C.; Liu, K. S.; Shang, J. Y., Effects of ionic strength, electrolyte type, pH, and flow rate on transport and retention of atmospheric deposition particles in saturated porous media. *Journal of Soils and Sediments* **2018,** *18* (3), 1066-1075.

102. Liang, Y.; Hilal, N.; Langston, P.; Starov, V., Interaction forces between colloidal particles in liquid: Theory and experiment. *Advances in Colloid and Interface Science* **2007,** *134-35*, 151-166.

103. Trefalt, G.; Palberg, T.; Borkovec, M., Forces between colloidal particles in aqueous solutions containing monovalent and multivalent ions. *Current Opinion in Colloid & Interface Science* **2017,** *27*, 9-17.

104. Gosse, C.; Croquette, V., Magnetic tweezers: Micromanipulation and force measurement at the molecular level. *Biophys. J.* **2002,** *82* (6), 3314-3329.

105. Wilson, L.; Matsudaira, P. T.; Sheetz, M. P., *Laser Tweezers in Cell Biology*. Elsevier Science: 1997.

106. Grier, D. G., Optical tweezers in colloid and interface science. *Current Opinion in Colloid & Interface Science* **1997,** *2* (3), 264-270.

107. Kegler, K.; Salomo, M.; Kremer, F., Forces of Interaction between DNA-Grafted Colloids: An Optical Tweezer Measurement. *Physical Review Letters* **2007,** *98* (5), 058304.

108. LeFevre, T. B.; Bikos, D. A.; Chang, C. B.; Wilking, J. N., Measuring colloid-surface interaction forces in parallel using fluorescence centrifuge force microscopy. *Soft Matter* **2021,** *17* (26), 6326-6336.

109. Butt, H. J.; Berger, R.; Bonaccurso, E.; Chen, Y.; Wang, J., Impact of atomic force microscopy on interface and colloid science. *Advances in Colloid and Interface Science* **2007,** *133* (2), 91-104.

110. Butt, H. J.; Cappella, B.; Kappl, M., Force measurements with the atomic force microscope: Technique, interpretation and applications. *Surf. Sci. Rep.* **2005,** *59* (1-6), 1-152.

111. van Oene M, D. L., Cross B, Pedaci F, Lipfert J, Dekker N, Applying torque to the Escherichia coli flagellar motor using magnetic tweezers. *Nature Scientific Reports* **2017,** *7*, 1-11.

112. Halvorsen, K.; Wong, W. P., Massively Parallel Single-Molecule Manipulation Using Centrifugal Force. *Biophys. J.* **2010,** *98* (11), L53-L55.

113. Hoang, T.; Patel, D. S.; Halvorsen, K., A wireless centrifuge force microscope (CFM) enables multiplexed single-molecule experiments in a commercial centrifuge. *Rev Sci Instrum* **2016,** *87* (8), 083705.

114. Yang, D.; Ward, A.; Halvorsen, K.; Wong, W. P., Multiplexed single-molecule force spectroscopy using a centrifuge. *Nat. Commun.* **2016,** *7*, 7.

115. Kou, L.; Jin, L.; Lei, H.; Hu, C.; Li, H.; Hu, X., Real-time parallel 3D multiple particle tracking with single molecule centrifugal force microscopy. *J. Microsc.* **2019,** *273* (3), 178-188.

116. Punnoose, J. A.; Hayden, A.; Zhou, L. F.; Halvorsen, K., Wi-Fi Live-Streaming Centrifuge Force Microscope for Benchtop Single-Molecule Experiments. *Biophys. J.* **2020,** *119* (11), 2231-2239.

117. Kirkness, M. W. H.; Forde, N. R., Single-Molecule Assay for Proteolytic Susceptibility: Force-Induced Collagen Destabilization. *Biophys. J.* **2018,** *114* (3), 570-576.

118. Saiki, R. K.; Scharf, S.; Faloona, F.; Mullis, K. B.; Horn, G. T.; Erlich, H. A.; Arnheim, N., ENZYMATIC AMPLIFICATION OF BETA-GLOBIN GENOMIC SEQUENCES AND RESTRICTION SITE ANALYSIS FOR DIAGNOSIS OF SICKLE-CELL ANEMIA. *Science* **1985,** *230* (4732), 1350-1354.

119. Saiki, R. K.; Gelfand, D. H.; Stoffel, S.; Scharf, S. J.; Higuchi, R.; Horn, G. T.; Mullis, K. B.; Erlich, H. A., PRIMER-DIRECTED ENZYMATIC AMPLIFICATION OF DNA WITH A THERMOSTABLE DNA-POLYMERASE. *Science* **1988,** *239* (4839), 487-491.

120. Mullis, K. B.; Faloona, F. A., SPECIFIC SYNTHESIS OF DNA INVITRO VIA A POLYMERASE-CATALYZED CHAIN-REACTION. *Methods in Enzymology* **1987,** *155*, 335-350.

121. Mullis, K. B., THE UNUSUAL ORIGIN OF THE POLYMERASE CHAIN-REACTION. *Scientific American* **1990,** *262* (4), 56-&.

122. Mullis, K.; Faloona, F.; Scharf, S.; Saiki, R.; Horn, G.; Erlich, H., SPECIFIC ENZYMATIC AMPLIFICATION OF DNA INVITRO - THE POLYMERASE CHAIN-REACTION. *Cold Spring Harbor Symposia on Quantitative Biology* **1986,** *51*, 263-273.

123. Notomi, T.; Okayama, H.; Masubuchi, H.; Yonekawa, T.; Watanabe, K.; Amino, N.; Hase, T., Loop-mediated isothermal amplification of DNA. *Nucleic Acids Research* **2000,** *28* (12).

124. Parida, M.; Sannarangaiah, S.; Dash, P. K.; Rao, P. V. L.; Morita, K., Loop mediated isothermal amplification (LAMP): a new generation of innovative gene amplification technique; perspectives in clinical diagnosis of infectious diseases. *Reviews in Medical Virology* **2008,** *18* (6), 407-421.

125. Mori, Y.; Kitao, M.; Tomita, N.; Notomi, T., Real-time turbidimetry of LAMP reaction for quantifying template DNA. *Journal of Biochemical and Biophysical Methods* **2004,** *59* (2), 145-157.

126. Mori, Y.; Nagamine, K.; Tomita, N.; Notomi, T., Detection of loop-mediated isothermal amplification reaction by turbidity derived from magnesium pyrophosphate formation. *Biochemical and Biophysical Research Communications* **2001,** *289* (1), 150-154.

127. Ignatov, K. B.; Barsova, E. V.; Fradkov, A. F.; Blagodatskikh, K. A.; Kramarova, T. V.; Kramarov, V. M., A strong strand displacement activity of thermostable DNA polymerase markedly improves the results of DNA amplification. *Biotechniques* **2014,** *57* (2), 81-87.

128. Ririe, K. M.; Rasmussen, R. P.; Wittwer, C. T., Product differentiation by analysis of DNA melting curves during the polymerase chain reaction. *Anal Biochem* **1997,** *245* (2), 154-160.

129. Owen, R. J.; Hill, L. R.; Lapage, S. P., DETERMINATION OF DNA BASE COMPOSITIONS FROM MELTING PROFILES IN DILUTE BUFFERS. *Biopolymers* **1969,** *7* (4), 503-&.

130. Viet Loan Dao, T.; Herbst, K.; Boerner, K.; Meurer, M.; Kremer, L. P. M.; Kirrmaier, D.; Freistaedter, A.; Papagiannidis, D.; Galmozzi, C.; Stanifer, M. L.; Boulant, S.; Klein, S.; Chlanda, P.; Khalid, D.; Miranda, I. B.; Schnitzler, P.; Kraeusslich, H.-G.; Knop, M.; Anders, S., A colorimetric RT-LAMP assay and LAMP-sequencing for detecting SARS-CoV-2 RNA in clinical samples. *Science Translational Medicine* **2020,** *12* (556).

131. Chow, F. W.-N.; Chan, T. T.-Y.; Tam, A. R.; Zhao, S.; Yao, W.; Fung, J.; Cheng, F. K.-K.; Lo, G. C.-S.; Chu, S.; Aw-Yong, K. L.; Tang, J. Y.-M.; Tsang, C.-C.; Luk, H. K.-H.; Wong, A. C.-P.; Li, K. S.-M.; Zhu, L.; He, Z.; Tam, E. W. T.; Chung, T. W.-H.; Wong, S. C. Y.; Que, T.-L.; Fung, K. S.-C.; Lung, D. C.; Wu, A. K.-L.; Hung, I. F.-N.; Woo, P. C.-Y.; Lau, S. K.-P., A Rapid, Simple, Inexpensive, and Mobile Colorimetric Assay COVID-19-LAMP for Mass On-Site Screening of COVID-19. *Int. J. Mol. Sci.* **2020,** *21* (15).

132. Clune, T.; Anstey, S.; Kasimov, V.; Jacobson, C.; Jelocnik, M., Real-Time Fluorometric Isothermal LAMP Assay for Detection of Chlamydia pecorum in Rapidly Processed Ovine Abortion Samples: A Veterinary Practitioner's Perspective. *Pathogens* **2021,** *10* (9).

133. Gibson, J., Loop-mediated isothermal amplification (LAMP) - a fast-growing technology with a wide range of applications [white paper]. *New England Biolabs, Inc.* **2020**.

134. Schenkels, L.; Veerman, E. C. I.; Amerongen, A. V. N., BIOCHEMICAL-COMPOSITION OF HUMAN SALIVA IN RELATION TO OTHER MUCOSAL FLUIDS. *Critical Reviews in Oral Biology and Medicine* **1995,** *6* (2), 161-175.

135. Humphrey, S. P.; Williamson, R. T., A review of saliva: Normal composition, flow, and function. *Journal of Prosthetic Dentistry* **2001,** *85* (2), 162-169.

136. Iorgulescu, G., Saliva between normal and pathological. Important factors in determining systemic and oral health. *Journal of medicine and life* **2009,** *2* (3), 303-7.

137. Oncescu, V.; O'Dell, D.; Erickson, D., Smartphone based health accessory for colorimetric detection of biomarkers in sweat and saliva. *Lab on a Chip* **2013,** *13* (16), 3232-3238.

138. Michael, A.; Bajracharya, S. D.; Yuen, P. S. T.; Zhou, H.; Star, R. A.; Illei, G. G.; Alevizos, I., Exosomes from human saliva as a source of microRNA biomarkers. *Oral Diseases* **2010,** *16* (1), 34-38.

139. Kinney, J. S.; Morelli, T.; Braun, T.; Ramseier, C. A.; Herr, A. E.; Sugai, J. V.; Shelburne, C. E.; Rayburn, L. A.; Singh, A. K.; Giannobile, W. V., Saliva/Pathogen Biomarker

Signatures and Periodontal Disease Progression. *Journal of Dental Research* **2011,** *90* (6), 752-758.

140. Jokerst, J. V.; Raamanathan, A.; Christodoulides, N.; Floriano, P. N.; Pollard, A. A.; Simmons, G. W.; Wong, J.; Gage, C.; Furmaga, W. B.; Redding, S. W.; McDevitt, J. T., Nano-bio-chips for high performance multiplexed protein detection: Determinations of cancer biomarkers in serum and saliva using quantum dot bioconjugate labels. *Biosens Bioelectron* **2009,** *24* (12), 3622-3629.

141. Musso, D.; Roche, C.; Tu-Xuan, N.; Robin, E.; Teissier, A.; Cao-Lormeau, V.-M., Detection of Zika virus in saliva. *Journal of Clinical Virology* **2015,** *68*, 53-55.

142. Groopman, J. E.; Salahuddin, S. Z.; Sarngadharan, M. G.; Markham, P. D.; Gonda, M.; Sliski, A.; Gallo, R. C., HTLV-III IN SALIVA OF PEOPLE WITH AIDS-RELATED COMPLEX AND HEALTHY HOMOSEXUAL MEN AT RISK FOR AIDS. *Science* **1984,** *226* (4673), 447-449.

143. Dubrulle, M.; Mousson, L.; Moutailler, S.; Vazeille, M.; Failloux, A.-B., Chikungunya Virus and Aedes Mosquitoes: Saliva Is Infectious as soon as Two Days after Oral Infection. *Plos One* **2009,** *4* (6).

144. Wyllie, A. L.; Fournier, J.; Casanovas-Massana, A.; Campbell, M.; Tokuyama, M.; Vijayakumar, P.; Warren, J. L., Saliva or Nasopharyngeal Swab Specimens for Detection of SARS-CoV-2. *New England Journal of Medicine* **2020,** *383* (13), 1283-1286.

145. To, K. K.-W.; Tsang, O. T.-Y.; Leung, W.-S.; Tam, A. R.; Wu, T.-C.; Lung, D. C.; Yip, C. C.-Y.; Cai, J.-P.; Chan, J. M.-C.; Chik, T. S.-H.; Lau, D. P.-L.; Choi, C. Y.-C.; Chen, L.-L.; Chan, W.-M.; Chan, K.-H.; Ip, J. D.; Ng, A. C.-K.; Poon, R. W.-S.; Luo, C.-T.; Cheng, V. C.-C.; Chan, J. F. W.; Hung, I. F.-N.; Chen, Z.; Chen, H.; Yuen, K.-Y., Temporal profiles of viral load in posterior oropharyngeal saliva samples and serum antibody responses during infection by SARS-CoV-2: an observational cohort study. *Lancet Infectious Diseases* **2020,** *20* (5), 565-574.

146. Azzi, L.; Carcano, G.; Gianfagna, F.; Grossi, P.; Dalla Gasperina, D.; Genoni, A.; Fasano, M.; Sessa, F.; Tettamanti, L.; Carinci, F.; Maurino, V.; Rossi, A.; Tagliabue, A.; Baj, A., Saliva is a reliable tool to detect SARS-CoV-2. *Journal of Infection* **2020,** *81* (1), E45-E50.

147. Pedrosa, M. d. S.; Sipert, C. R.; Nogueira, F. N., Salivary Glands, Saliva and Oral Findings in COVID-19 Infection. *Pesquisa Brasileira Em Odontopediatria E Clinica Integrada* **2020,** *20*.

148. Fini, M. B., Oral saliva and COVID-19. *Oral Oncology* **2020,** *108*.

149. Eichel, H. J.; Conger, N.; Chernick, W. S., ACID + ALKALINE RIBONUCLEASES OF HUMAN PAROTID SUBMAXILLARY + WHOLE SALIVA. *Archives of Biochemistry and Biophysics* **1964,** *107* (2), 197-&.

150. Eichen Chemical Co., L. The principle of LAMP method.

151. Mugambi, R. M.; Agola, E. L.; Mwangi, I. N.; Kinyua, J.; Shiraho, E. A.; Mkoji, G. M., Development and evaluation of a Loop Mediated Isothermal Amplification (LAMP) technique for the detection of hookworm (Necator americanus) infection in fecal samples. *Parasites & Vectors* **2015,** *8*.

152. Isayev, A. I.; Hieber, C. A., TOWARD A VISCOELASTIC MODELING OF THE INJECTION-MOLDING OF POLYMERS. *Rheologica Acta* **1980,** *19* (2), 168-182.

153. Chang, R. Y.; Yang, W. H., Numerical simulation of mold filling in injection molding using a three-dimensional finite volume approach. *International Journal for Numerical Methods in Fluids* **2001,** *37* (2), 125-148.

154. Kamal, M. R.; Kenig, S., INJECTION MOLDING OF THERMOPLASTICS .1. THEORETICAL MODEL. *Polymer Engineering and Science* **1972,** *12* (4), 294-&.

155. Huang, M. C.; Tai, C. C., The effective factors in the warpage problem of an injection-molded part with a thin shell feature. *Journal of Materials Processing Technology* **2001,** *110* (1), 1-9.

156. Ozcelik, B.; Erzurumlu, T., Comparison of the warpage optimization in the plastic injection molding using ANOVA, neural network model and genetic algorithm. *Journal of Materials Processing Technology* **2006,** *171* (3), 437-445.

157. Fujiyama, M.; Wakino, T.; Kawasaki, Y., STRUCTURE OF SKIN LAYER IN INJECTION-MOLDED POLYPROPYLENE. *Journal of Applied Polymer Science* **1988,** *35* (1), 29-49.

158. Chiang, H. H.; Hieber, C. A.; Wang, K. K., A UNIFIED SIMULATION OF THE FILLING AND POSTFILLING STAGES IN INJECTION-MOLDING .1. FORMULATION. *Polymer Engineering and Science* **1991,** *31* (2), 116-124.

159. Tadmor, Z., MOLECULAR-ORIENTATION IN INJECTION MOLDING. *Journal of Applied Polymer Science* **1974,** *18* (6), 1753-1772.

160. Lipshitz, S. D.; Lavie, R.; Tadmor, Z., MELTING MODEL FOR RECIPROCATING SCREW INJECTION-MOLDING MACHINES. *Polymer Engineering and Science* **1974,** *14* (8), 553-559.

161. Donovan, R. C.; Thomas, D. E.; Leversen, L. D., EXPERIMENTAL STUDY OF PLASTICATING IN A RECIPROCATING-SCREW INJECTION MOLDING MACHINE. *Polymer Engineering and Science* **1971,** *11* (5), 353-&.

162. Donovan, R. C., THEORETICAL MELTING MODEL FOR A RECIPROCATING-SCREW INJECTION MOLDING MACHINE. *Polymer Engineering and Science* **1971,** *11* (5), 361-&.

163. Bi, C.; Jiang, B., Study of residence time distribution in a reciprocating single-screw pin-barrel extruder. *Journal of Materials Processing Technology* **2009,** *209* (8), 4147-4153.

164. Xie, L.; Shen, L.; Jiang, B.-y. In *Modelling and Simulation for Micro Injection Molding Process*, 2011.

165. Chen, J. Y.; Liu, C. Y.; Huang, M. S., Enhancement of Injection Molding Consistency by Adjusting Velocity/Pressure Switching Time Based on Clamping Force. *International Polymer Processing* **2019,** *34* (5), 564-572.

166. Pantani, R.; Coccorullo, I.; Speranza, V.; Titomanlio, G., Morphology evolution during injection molding: Effect of packing pressure. *Polymer* **2007,** *48* (9), 2778-2790.

167. Kurt, M.; Kamber, O. S.; Kaynak, Y.; Atakok, G.; Girit, O., Experimental investigation of plastic injection molding: Assessment of the effects of cavity pressure and mold temperature on the quality of the final products. *Mater Design* **2009,** *30* (8), 3217-3224.

168. Mavridis, H.; Hrymak, A. N.; Vlachopoulos, J., THE EFFECT OF FOUNTAIN FLOW ON MOLECULAR-ORIENTATION IN INJECTION-MOLDING. *Journal of Rheology* **1988,** *32* (6), 639-663.

169. Mavridis, H.; Hrymak, A. N.; Vlachopoulos, J., FINITE-ELEMENT SIMULATION OF FOUNTAIN FLOW IN INJECTION-MOLDING. *Polymer Engineering and Science* **1986,** *26* (7), 449-454.

170. Lafleur, P. G.; Kamal, M. R., A STRUCTURE-ORIENTATED COMPUTER-SIMULATION OF THE INJECTION-MOLDING OF VISCOELASTIC CRYSTALLINE POLYMERS .1. MODEL WITH FOUNTAIN FLOW, PACKING, SOLIDIFICATION. *Polymer Engineering and Science* **1986,** *26* (1), 92-102.

171. Kamal, M. R.; Goyal, S. K.; Chu, E., SIMULATION OF INJECTION MOLD FILLING OF VISCOELASTIC POLYMER WITH FOUNTAIN FLOW. *Aiche Journal* **1988,** *34* (1), 94-106.

172. Gogos, C. G.; Huang, C. F.; Schmidt, L. R., THE PROCESS OF CAVITY FILLING INCLUDING THE FOUNTAIN FLOW IN INJECTION-MOLDING. *Polymer Engineering and Science* **1986,** *26* (20), 1457-1466.

173. Coyle, D. J.; Blake, J. W.; Macosko, C. W., THE KINEMATICS OF FOUNTAIN FLOW IN MOLD-FILLING. *Aiche Journal* **1987,** *33* (7), 1168-1177.

174. Kamal, M. R.; Chu, E.; Lafleur, P. G.; Ryan, M. E., COMPUTER-SIMULATION OF INJECTION MOLD FILLING FOR VISCOELASTIC MELTS WITH FOUNTAIN FLOW. *Polymer Engineering and Science* **1986,** *26* (3), 190-196.

175. Chang, Y. H.; Wei, T. H.; Chen, S. C.; Lou, Y. F., The investigation onPVTcontrol method establishment for scientific injection molding parameter setting and its quality control. *Polymer Engineering and Science* **2020,** *60* (11), 2895-2907.

176. Chen, Z. B.; Giacomin, A. J.; Turng, L. S., Flash. *Polymer Engineering and Science* **2006,** *46* (3), 241-247.

177. Weinstein, M.; Manoochehri, S., Optimum parting line design of molded and cast parts for manufacturability. *Journal of Manufacturing Systems* **1997,** *16* (1), 1-12.

178. Schmidt, L. R., SPECIAL MOLD AND TRACER TECHNIQUE FOR STUDYING SHEAR AND EXTENSIONAL FLOWS IN A MOLD CAVITY DURING INJECTION MOLDING. *Polymer Engineering and Science* **1974,** *14* (11), 797-800.

179. Zhou, Y.; Yu, F.; Deng, H.; Huang, Y.; Li, G.; Fu, Q., Morphology Evolution of Polymer Blends under Intense Shear During High Speed Thin-Wall Injection Molding. *Journal of Physical Chemistry B* **2017,** *121* (25), 6257-6270.

180. Zhang, S. X.; Khayat, R. E., A low-dimensional description of transient shear-thinning free-surface flow in thin cavities, as applied to injection molding. *International Journal for Numerical Methods in Fluids* **2004,** *44* (1), 91-114.

181. Li, Y.; Huang, B.; Qu, X., Viscosity and melt rheology of metal injection moulding feedstocks. *Powder Metallurgy* **1999,** *42* (1), 86-90.

182. Koszkul, J.; Nabialek, J., Viscosity models in simulation of the filling stage of the injection molding process. *Journal of Materials Processing Technology* **2004,** *157*, 183-187.

183. Hieber, C. A.; Chiang, H. H., SHEAR-RATE-DEPENDENCE MODELING OF POLYMER MELT VISCOSITY. *Polymer Engineering and Science* **1992,** *32* (14), 931-938.

184. Sorgato, M.; Babenko, M.; Lucchetta, G.; Whiteside, B., Investigation of the influence of vacuum venting on mould surface temperature in micro injection moulding. *Int J Adv Manuf Tech* **2017,** *88* (1-4), 547-555.

185. Yao, D. G.; Kim, B., Development of rapid heating and cooling systems for injection molding applications. *Polymer Engineering and Science* **2002,** *42* (12), 2471-2481.

186. Sachs, E.; Wylonis, E.; Allen, S.; Cima, M.; Guo, H. L., Production of injection molding tooling with conformal cooling channels using the three dimensional printing process. *Polymer Engineering and Science* **2000,** *40* (5), 1232-1247.

187. Xu, X. R.; Sachs, E.; Allen, S., The design of conformal cooling channels in injection molding tooling. *Polymer Engineering and Science* **2001,** *41* (7), 1265-1279.

188. Dimla, D. E.; Camilotto, M.; Miani, F., Design and optimisation of conformal cooling channels in injection moulding tools. *Journal of Materials Processing Technology* **2005,** *164*, 1294-1300.

189. Gnielinski, V., NEW EQUATIONS FOR HEAT AND MASS-TRANSFER IN TURBULENT PIPE AND CHANNEL FLOW. *International Chemical Engineering* **1976,** *16* (2), 359-368.

190. Ahlers, G.; Grossmann, S.; Lohse, D., Heat transfer and large scale dynamics in turbulent Rayleigh-Benard convection. *Rev. Mod. Phys.* **2009,** *81* (2), 503-537.

191. Shen, Y.-K.; Wu, C.-W.; Yu, Y.-F.; Chung, H.-W., Analysis for optimal gate design of thin-walled injection molding. *International Communications in Heat and Mass Transfer* **2008,** *35* (6), 728-734.

192. Pandelidis, I.; Zou, Q., OPTIMIZATION OF INJECTION-MOLDING DESIGN .1. GATE LOCATION OPTIMIZATION. *Polymer Engineering and Science* **1990,** *30* (15), 873-882.

193. Lee, B. H.; Kim, B. H., Automated selection of gate location based on desired quality of injection-molded part. *Polymer-Plastics Technology and Engineering* **1996,** *35* (2), 253-269.

194. Kim, I. H.; Park, S. J.; Chung, S. T.; Kwon, T. H., Numerical modeling of injection/compression molding for center-gated disk: Part I. Injection molding with viscoelastic compressible fluid model. *Polymer Engineering and Science* **1999,** *39* (10), 1930-1942.

195. Cabrera-Rios, M.; Zuyev, K. S.; Chen, X.; Castro, J. M.; Straus, E. J., Optimizing injection gate location and cycle time for the in-mold coating (IMC) process. *Polymer Composites* **2002,** *23* (5), 723-738.

196. Lee, B. H.; Kim, B. H., OPTIMIZATION OF PART WALL THICKNESSES TO REDUCE WARPAGE OF INJECTION-MOLDED PARTS BASED ON THE MODIFIED COMPLEX METHOD. *Polymer-Plastics Technology and Engineering* **1995,** *34* (5), 793-811.

197. Injection molding design guidelines. In *Stratasys*.

198. Wall Thickness Guide For Plastic Part Design. https://www.xcentricmold.com/how-wall-thickness-impacts-injection-mold-part-design/.

199. How to Improve Injection Molding Design With Uniform Wall Thickness.

200. Harris, R.; Hopkinson, N.; Newlyn, H.; Hague, R.; Dickens, P., Layer thickness and draft angle selection for stereolithography injection mould tooling. *International Journal of Production Research* **2002,** *40* (3), 719-729.

201. Draft Angle Guidelines for Injection Molding. https://www.protolabs.com/resources/design-tips/improving-part-moldability-with-draft/.

202. Draft Angles in Injection Molded Plastics. https://www.natechplastics.com/draft_angles/.

203. Ho, K. H.; Newman, S. T., State of the art electrical discharge machining (EDM). *International Journal of Machine Tools & Manufacture* **2003,** *43* (13), 1287-1300.

204. Abbas, N. M.; Solomon, D. G.; Bahari, M. F., A review on current research trends in electrical discharge machining (EDM). *International Journal of Machine Tools & Manufacture* **2007,** *47* (7-8), 1214-1228.

205. Lin, J. L.; Lin, C. L., The use of the orthogonal array with grey relational analysis to optimize the electrical discharge machining process with multiple performance characteristics. *International Journal of Machine Tools & Manufacture* **2002,** *42* (2), 237-244.

206. Ho, K. H.; Newman, S. T.; Rahimifard, S.; Allen, R. D., State of the art in wire electrical discharge machining (WEDM). *International Journal of Machine Tools & Manufacture* **2004,** *44* (12-13), 1247-1259.

207. Dibitonto, D. D.; Eubank, P. T.; Patel, M. R.; Barrufet, M. A., THEORETICAL-MODELS OF THE ELECTRICAL-DISCHARGE MACHINING PROCESS .1. A SIMPLE CATHODE EROSION MODEL. *J Appl Phys* **1989,** *66* (9), 4095-4103.

208. Boothroyd, G., PRODUCT DESIGN FOR MANUFACTURE AND ASSEMBLY. *Computer-Aided Design* **1994,** *26* (7), 505-520.

CHAPTER TWO

MEASURING COLLOID-SURFACE INTERACTIONS IN PARALLEL USING FLUORESCENCE CENTRIFUGE FORCE MICROSCOPY

Contribution of Authors and Co-Authors

Manuscript in Chapter 2

Author: Thomas B. LeFevre

Contributions: Planned and performed the experiments, analyzed the data, and wrote the manuscript.

Co-Author: Dimitri A. Bikos

Contributions: Performed the experiments, analyzed the data, and wrote the manuscript.

Co-Author: Connie B. Chang

Contributions: Analyzed the data and wrote the manuscript.

Co-Author: James N. Wilking

Contributions: Planned and oversaw the experiments, analyzed the data, and wrote the manuscript.

Manuscript Information

Thomas B. LeFevre, Dimitri A. Bikos, Connie B. Chang, and James N. Wilking

Soft Matter

Status of Manuscript:
___ Prepared for submission to a peer-reviewed journal
___ Officially submitted to a peer-reviewed journal
___ Accepted by a peer-reviewed journal
_X_ Published in a peer-reviewed journal

DOI: 10.1039/d1sm00461a

Royal Society of Chemistry

Abstract

Interactions between colloidal-scale structures govern the physical properties of soft and biological materials, and knowledge of the forces associated with these interactions is critical for understanding and controlling these materials. A common approach to quantify colloidal interactions is to measure the interaction forces between colloids and a fixed surface. The centrifuge force microscope (CFM), a miniaturized microscope inside a centrifuge, is capable of performing hundreds of force measurements in parallel over a wide force range (10^{-2} to 10^{4} pN), but CFM instruments are not widely used to measure colloid-surface interaction forces. In addition, current CFM instruments rely on brightfield illumination and are not capable of fluorescence microscopy. Here we present a fluorescence CFM (F-CFM) that combines both fluorescence and brightfield microscopy and demonstrate its use for measuring microscale colloidal-surface interaction forces. The F-CFM operates at speeds up to 5000 RPM, 2.5× faster than those previously reported, yielding a 6.25× greater maximum force than previous instruments. A battery-powered GoPro video camera enables real-time viewing of the microscopy video on a mobile device, and frequency analysis of the audio signal correlates centrifuge rotational speed with the video signal. To demonstrate the capability of the F-CFM, we measure the force required to detach hundreds of electrostatically-stabilized colloidal microspheres attached to a charged glass surface as a function of ionic strength and compare the resulting force distributions with an approximated DLVO theory. The F-CFM will enable microscale force measurements to be correlated with fluorescence imaging in soft and biological systems.

Introduction

Soft materials are widespread in nature and industry.[1-8] Examples include food,[9, 10] personal care products,[11] biomedical supplies,[12] and biological tissues.[13] These materials are characterized by colloidal-scale structures such as drops,[14] particles,[15-17] and polymers,[4, 18, 19] which range in size from nanometers to micrometers, and the behavior of these structures govern material properties.[2, 3, 20, 21] A defining attribute of soft materials is their mechanical properties, and knowledge of these properties is valuable for both fundamental and applied research. For example, products like toothpaste must be formulated to achieve desired flow properties and the mechanics of tissues and bio-gels play critical roles in diseases like cancer[22, 23] and osteoarthritis.[24, 25] These properties are governed by interactions between colloidal constituents;[21, 26, 27] thus, characterizing colloidal interaction forces is important for understanding and controlling soft material mechanical properties.[28, 29]

A variety of tools exist for directly measuring colloidal interaction forces, which are both small and wide-ranging, from 10^{-2} to 10^{4} pN.[30-32] With optical trapping, colloids are brought close to one another and the magnitude of the attractive or repulsive forces between them measured as a function of separation distance.[33-35] Tools like atomic force microscopy (AFM)[36, 37] measure interactions between colloids and a fixed surface. Both optical trapping and AFM provide high-resolution force information, but measurements are typically performed one at a time, and are not ideal for quantifying heterogeneous systems, which require many measurements to construct statistically significant force distributions. Instead, techniques like magnetic tweezers[32, 38] and centrifugal force microscopy (CFM),[39-44] which can perform multiple force measurements in parallel are better suited for characterizing heterogenous systems. CFM is a particularly attractive

technique because it is capable of multiple simultaneous measurements (i.e. force multiplexing) and does not require significant device calibration or user training. A CFM instrument is composed of a miniaturized microscope housed inside a swinging bucket centrifuge. As the centrifuge spins, colloids suspended in liquid and interacting with a coverslip are subjected to an effective gravitational force drawing them away from the surface. By controlling the rotational speed of the centrifuge, well-defined forces can be applied to 100s of individual colloids simultaneously; however, current CFM instruments rely on brightfield optical microscopy to identify and track colloidal objects.[39-44] This illumination technique is adequate for measuring colloidal interaction forces but is limited with regard to spatial resolution and sample characterization. Fluorescence microscopy offers enhanced spatial resolution and access to a wide variety of sample labelling techniques, but the incorporation of fluorescence imaging into a CFM has not yet been reported. Such an instrument would provide significant benefits for characterizing complex soft and biological materials.

Here we present a fluorescence CFM (F-CFM) capable of performing both fluorescence and brightfield microscopy in combination with microscale force measurements. The F-CFM can perform 100s of interaction force measurements simultaneously. The F-CFM operates at speeds up to 5000 RPM, 2.5× faster than those previously reported, yielding a 6.25× greater maximum force for any given colloid and a resulting force range of 10^{-2} to 10^{5} pN. Additionally, use of a battery-powered GoPro video camera enables real-time transfer of microscopy video to a mobile device during operation, and frequency analysis of the audio signal provided by on-camera microphones correlates centrifuge rotational speed with the video signal. Wireless streaming video allows observation and control of experiments in real time, similar to previous CFM iterations.[43,

[44] Audio verification of speed, also not reported in previous iterations, allows determination of centrifuge speed profiles in standard unmodified benchtop centrifuges to be controlled through an external computer user interface. We validate the accuracy of the instrument by measuring, at various effective gravities, the time required for fluorescent colloidal microspheres to sediment from one imaging plane to another. To demonstrate the capability of the F-CFM for performing multiple measurements in parallel, we measure the forces required to detach 100s of electrostatically-stabilized colloidal microspheres attached to a charged glass surface as a function of ionic strength and compare the resulting force distributions to a modified Derjaguin-Landau-Verwey-Overbeek (DLVO) theory. The F-CFM will enable microscale force measurements to be correlated with fluorescence markers in soft and biological systems.

Methods

Instrument

The F-CFM design is based on a brightfield CFM developed for single-molecule force multiplexing.[41] Optical hardware and supporting electronics are housed in a cylindrical 3D-printed clamshell enclosure that splits into two pieces, bisected by a plane parallel to the long axis (**Fig. 2.1A**). Supporting electronics include a white brightfield light-emitting diode (LED) (**Fig. 2.1A, i and ii**), a blue fluorescent excitation LED (**Fig. 2.1A, iii and iv**), and a lithium polymer (LiPo) battery (**Fig. 2.1A, v**). For brightfield illumination, a diffuse white LED is soldered to a customized circuit board (PCB) along with a 10-kΩ resistor and Japanese solderless terminal (JST) male

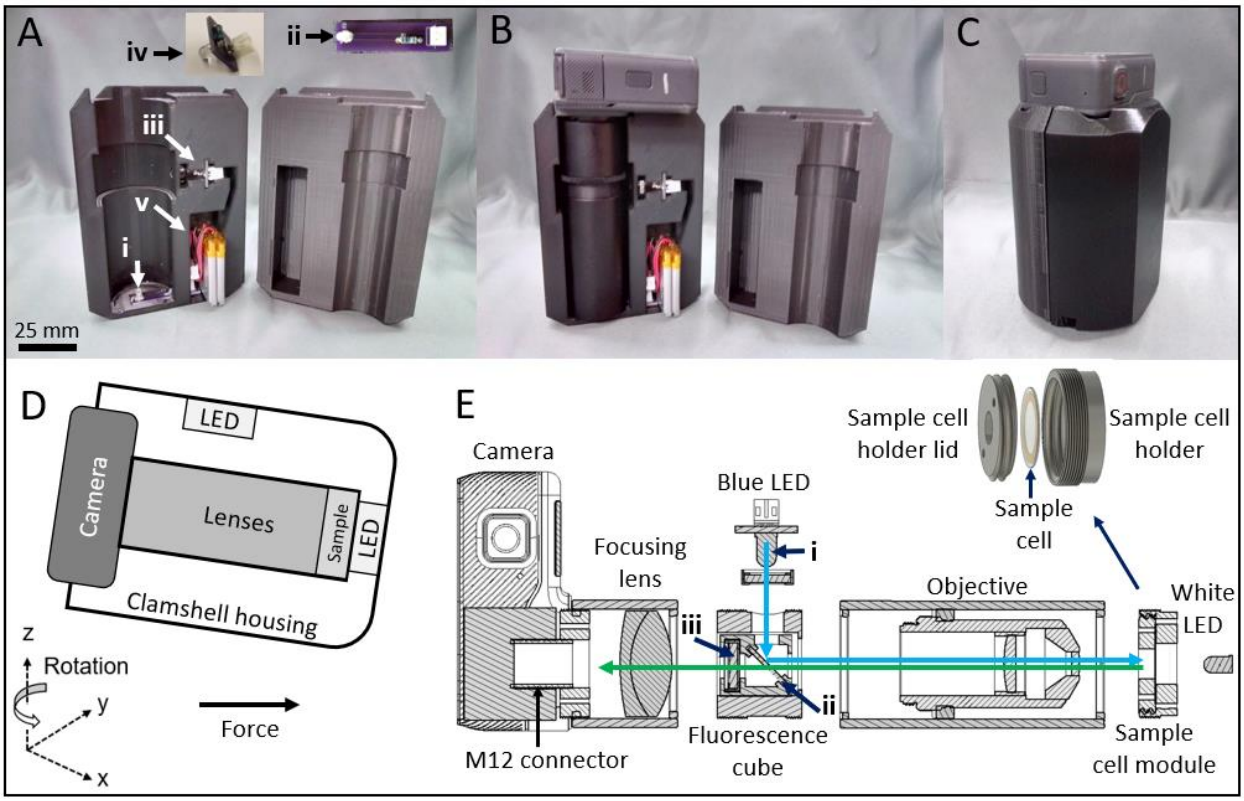


Figure 2.1: *Fluorescence CFM construction and assembly.* (**A**) Two-part clamshell housing for F-CFM module. Brightfield LED (i and ii), fluorescence LED (iii and iv), and lithium polymer (LiPo) battery (v) are built into the housing. Inset: custom printed circuit board for brightfield operation. (**B**) The F-CFM module fits inside the clamshell housing during assembly. (**C**) Clamshell housing closes around F-CFM module. Assembly is ready to be lowered into centrifuge bucket. Two camera microphones are visible as small holes to the right and left of the power button (square with red circle). (**D**) Orientation of the F-CFM components, axis of rotation, and centrifugal force vector during operation. (**E**) Optical components of the F-CFM module. Fluorescence excitation light (blue) travels from the blue LED and through the excitation filter (i) before reflecting off the dichroic mirror (ii) and reaching the sample. Fluorescence emission light (green) travels from the sample, through the dichroic mirror, the emission filter (iii), and the focusing lens, and into the camera sensor. Brightfield illumination light (not shown) follows same path as fluorescence emission light. Inset: Sample cell holder components. Sample cell holder lid screws into sample cell holder, clamping sample cell in place.

connector socket (**Fig. 2.1A, right inset**). For fluorescent illumination, a blue LED is soldered to another customized PCB along with a 10-Ω resistor and JST male connector socket (**Fig. 2.1A, left inset**). The battery can be connected to the brightfield LED, the blue fluorescent LED, or both

– resulting in three available illumination modes. When both LEDs are operational, two batteries are used, and a piece of neutral density filter film (ND = 1.2) is placed over the brightfield LED to reduce the reflection of the fluorescence optical beam off the brightfield LED. The F-CFM is operated in any of these modes by connecting the appropriate LiPo battery to the desired LED during instrument assembly. The camera and optical hardware fit into a custom-designed recess within the clamshell housing (**Fig. 2.1B**). After the F-CFM module is assembled and battery wiring harness connected, the second clamshell piece closes around the module (**Fig. 2.1C**) and the entire module with housing is inserted into the bucket of a commercially available centrifuge (ThermoFisher Sorvall Legend X1R).

During operation, the centrifuge swinging buckets do not fully extend 90° to the rotational axis *z* during operation, resulting in a non-normal force vector acting on the sample cell. This is illustrated in **Fig. 2.1D**. The force vector is 76.6° from perpendicular at 300 RPM and 80.7° from perpendicular at 1000 to 5000 RPM (see **SI Note 2.1** and **SI Fig. 2.1**) The objective tube, containing the sample cell module and objective, connects to a 3D-printed fluorescence cube, containing a 495-nm dichroic mirror and 520-nm bandpass emission filter, which connects to the focusing lens tube to form a tubular microscope which is attached to a camera (**Fig. 2.1E**). The 472-nm bandpass excitation filter fits inside the blue LED housing. The sample cell, constructed from two circular glass coverslips separated by a spacer to create a sealed shallow sample well, is contained in a two-part 3D-printed housing constructed from a sample cell holder and lid that screws into the objective microscope tube (**Fig. 2.1E, inset**). Mounting the sample cell on the interior of the objective tube rather than the exterior end of the tube reduces deformation of the sample cell during centrifugation because the thick walls of the objective tube resist deformation

better than the thin threads connecting an exterior sample cell holder to the objective tube. This provides less change in focus throughout the experiment, even at 5000 RPM, the highest RPM for which our buckets are rated. A complete exploded-view diagram and parts ordering information are listed in **SI Fig. 2.2**. CAD files in STEP format for all 3D-printed components are included as supplemental files as well.

Recent advances in camera technology enable the F-CFM. Here, we use a compact, wireless GoPro Hero 5 action camera. The compact form factor of the camera allows more room for fluorescence optical components than previous CFM designs.[39-41] The wireless feature allows the video to be viewed in real time through an application on a smartphone, which also allows the user to start and stop recording remotely. The live video feed is clear up to 4000 RPM and exhibits only minor interference up to 5000 RPM. The GoPro camera has a 6.17 mm × 4.55 mm CMOS 12-megapixel sensor capable of 4K video at 30 frames per second (fps) and 1080p video at 120 fps, stores video on an SD card and requires no electronics knowledge to operate. Here, we use a shorter optical path (≈ 40 mm) than previous designs (≈ 90 mm), which require turning mirrors.[39-41] This configuration leads to aberrative vignetting and optical distortion in the corners of the image but offers an acceptable compromise by providing room for important optical components.

Fabrication

Construction of F-CFM components is straight-forward and does not require extensive fabrication, programming, or electronics knowledge. The M12 threaded connector that attaches the camera to the focusing tube is made by threading a plain aluminum tube (12 mm O.D. × 10 mm I.D.) using an M12 die along with a die wrench, pipe cutter, and vise. The brightfield LED is soldered to a simple customized PCB (oshpark.com) along with a JST connector and 10-kΩ

resistor. The fluorescence LED is soldered to a different customized PCB along with a JST connector and 10-Ω resistor. The brightfield LED requires a strong resistor to prevent oversaturation of the brightfield images, and the fluorescence LED requires a weak resistor to generate enough light to excite the fluorescent dye in the sample. All other components are purchased from optics companies or 3D-printed with a Stanley Model 1 fused deposition modeling (FDM) printer with poly-lactic acid (PLA) 1.75-mm diameter filament. See **SI Note 2.2** for assembly information.

Experimental Protocol

Circular glass coverslips (Thomas Scientific, diameter 18 mm, No. 2 thickness) are cleaned by sonicating for 15 min in each of the following: acetone, isopropanol, 2.0 M NaOH, and pure distilled water, in that order. Prior to the final distilled water sonication step, the coverslips are rinsed several times in pure distilled water to remove excess NaOH. After the final sonication step, the slides are dried with nitrogen. Donut-shaped annular spacers (I.D. = 7 mm, O.D. = 15 mm) are cut from 102.5 μm ± 3.6 μm thickness Kapton tape using a craft cutter (Silhouette CAMEO 2) and adhered to one slide (see **SI Note 2.3** and **SI Fig. 2.3**). An annular bead of UV-curing optical adhesive (Norland 61) is deposited inside the annular tape ring on the slide. This bead of adhesive protects the central region of interest on the slide from being disturbed by air bubbles that form on the edge of the tape during centrifugation, likely due to compression of the tape. After curing the bead of UV adhesive under UV light until hardened (20 – 300 s depending on the light source), 25 μL of the colloid suspension is pipetted into the shallow well created by the annular spacer and slide. Another cleaned slide is then placed on top of the tape spacer, sealing the sample inside. The

inadvertent incorporation of air bubbles must be avoided as their movement during measurements leads to undesired liquid flows.

Once the sample cell is prepared, it is loaded into the sample cell holder which screws into the objective tube. The distance from the sample cell to the objective is adjusted by screwing in the sample cell holder until the interior surface of interest is in focus. This is accomplished by looking at the built-in camera display screen or by attaching the camera to a monitor with the camera mini-USB connection. The sample cell must be illuminated manually, independent of the housing during the focusing adjustment before the F-CFM is placed inside the clamshell holder.

After focus is achieved, the F-CFM module is enclosed in the clamshell housing and loaded into a centrifuge bucket. The two sides of the housing are held together by the snug fit within the centrifuge bucket. The weight of the counterbalance at the opposing bucket is verified using an electronic scale, the lid is closed, and the centrifuge is started. When the run is complete, the centrifuge is allowed to come to rest and opened, the camera recording is stopped, and the video files are downloaded to a computer. The onset of centrifuge rotation is distinctly audible in the recorded video, providing a reference point for video image data to be synced with speed data.

The centrifuge used in this study is a swinging bucket ThermoFisher Sorvall Legend X1R with 400-mL buckets (TX-400, p/n 75003655), custom-ordered for PC-control. Operation is controlled by PC instead of the front control pad and records the RPM profile by reporting speed values every 0.5 s. The RPM is measured using a built-in Hall effect sensor and magnets in the rotor base. Detailed speed profiles can be programmed from the included PC control software. A centrifuge without PC control could also be used by manually increasing the centrifuge speed in a stepwise fashion using the centrifuge control pad.

Video files (.mp4) are downloaded from the GoPro SD card onto a PC. Using the FFmpeg toolbox in MATLAB, the .mp4 files are converted into .tiff stacks. Here, for ease of analysis, only one out of every hundred frames is kept for analysis. The frame is cropped from its original 1280 × 720 px to a central 320 × 300 px rectangle in the region of best focus (**Fig. 2.2**). These frames are then corrected for drift in Imaris 9.2.1 software. The resulting drift-corrected frames are analyzed one-by-one manually by counting the number of colloids in each frame and recording the colloid counts in a spreadsheet. The frame numbers are synchronized with the reported centrifuge speed to determine the RPM and effective gravity g_{eff} associated with each colloid count. The centrifugal force acting on each microsphere is defined by $F_c = m\omega^2 r$ where r is the moment arm of the centrifuge (0.15 m), ω is the rotational velocity, and m is the effective mass of the colloid. Here, $m = V_c(\rho_c - \rho_f)$, where V_c is the volume of the colloid, ρ_c is the density of the colloid and ρ_f is the density of the fluid.

Independent verification of the reported centrifuge speeds is performed by audio analysis of the .mp4 video files. Using a custom MATLAB R2019b routine, we extract the 48000 Hz stereo samples recorded by the left channel of the audio track. The GoPro provides two channels of audio (right and left) which capture similar audio information. Here, we have chosen the left channel for analysis. To match the centrifuge reporting frequency of 0.5 s^{-1}, we fit audio signal clips of 0.5 s duration using a sum-of-sines routine found within the MATLAB Curve Fitting Toolbox. Thus, we can associate each video frame, taken at 25 fps in PAL format, to a corresponding audio clip

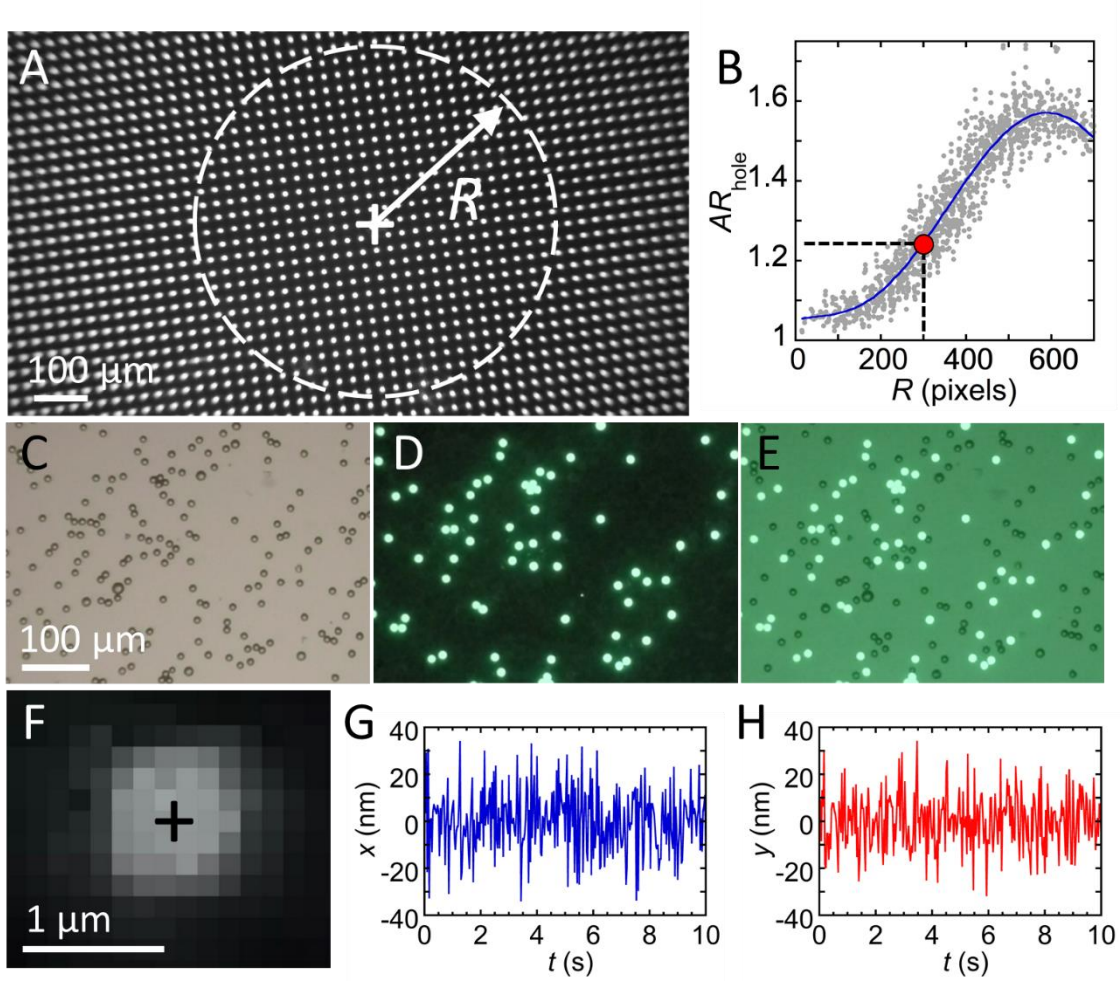


Figure 2.2: *F-CFM image quality*. (**A**) Brightfield F-CFM image of photomask grid of uniform circular holes (d = 10 µm) reveals optical aberrations near edges. White cross represents center of focus around which white dashes define circle of radius R. (**B**) Plot of apparent hole aspect ratios AR_{hole} as functions of R for all holes in part A (solid gray circles) fit with a polynomial regression (blue line) to guide the eye (see **SI Table 1** for fitting form). This can be used to quantify a region of defined image quality. For example, white dashed line in (A) corresponding to R = 300 px encloses holes with $AR_{hole} \leq 1.25$ (red dot). (**C-E**) F-CFM images (350 × 250 px) of a mixed suspension of green and red fluorescent polystyrene/iron oxide microspheres ($\bar{d}$ = 8.3 µm) captured using (C) brightfield, (D) fluorescence, and (E) concurrent brightfield and fluorescence imaging modes. Red fluorescent microspheres do not fluoresce under these imaging conditions. (**F**) Digitally zoomed grayscale fluorescence F-CFM image of a small microsphere ($\bar{d}$ = 1.0 µm) fixed by drying to the surface of a glass slide. (**G** and **H**) Tracking x- and y-positions of sphere from part (F) over time t = 10 s using the radial symmetry method.

containing 2000 samples. After fitting the resulting audio waveform using the sum-of-sines fitting routine, frequency information is extracted from the fit parameters, associating an RPM with each 0.5 s time interval. It is convenient to record in PAL format rather than NTSC format to ensure an integer number of video frames per second; this option is available in the "Preferences" menu of the GoPro.

Safety Considerations

Care must be taken to properly balance the centrifuge. To accomplish this, we set opposing bucket weights to within 1 g of each other. Larger mass imbalances will lead to centrifuge vibration during operation. More importantly, the centers of mass of opposing buckets must match closely as small differences will lead to centrifuge vibration. Given the low cost of a F-CFM module and housing (see **SI Fig. 2.2**), we counterbalance the F-CFM with a second, identical complete F-CFM module and housing in the opposing bucket. We find this approach is simpler than attempting to replicate the F-CFM module mass distribution with an assembly of similarly weighted objects, and it provides the option of running two different experiments simultaneously.

Care must also be taken to avoid LiPo battery leakage and fire. LiPo batteries should be inspected for damage after each run. If the batteries become dented or smashed, they should be stored in a fireproof LiPo battery bag (e.g. Suncentech 180 × 230 mm LiPo Guard battery storage bags) and brought to an electronics retailer for recycling. In initial testing, some of our large batteries (1000 mAh) did leak fluid after extended operation at high speeds; thus, we prefer to use small batteries (40 - 400 mAh) to reduce the risk of rupture, leakage, and fire. These small batteries provide more than enough current to operate the LED for hours, and we have not observed any damage or leakage due to centrifugation. The centrifuge and buckets are capable of speeds up to

5000 RPM. However, in most cases we prefer to limit our experiments to a maximum speed of 4700 RPM to reduce stress on the camera, batteries, and LEDs.

The F-CFM is housed within a custom-built guarding enclosure composed of an extruded aluminum frame (80/20 brand) and 1/4-in. polycarbonate (8020.net) (**SI Fig. 2.4**). Although our centrifuge was custom-ordered, it contains standard safety features such as thick steel plates surrounding the centrifugation chamber and an automatic override stop when excess vibration is detected. Since our centrifuge buckets are well-balanced and still within the weight threshold for which the buckets are rated, this polycarbonate guarding is simply meant to help contain debris in the unlikely event of centrifuge failure.

Results and Discussion

Image Quality

To assess the image quality provided by the F-CFM, we image a photomask printed with a grid of uniform circular dots (d = 10 μm) (**Fig. 2.2A**). This video frame image measures 1280 × 720 px. The image edges are out-of-focus because we use a short focal length focusing lens. The out-of-focus area is likely due to comatic and spherical aberrations. To quantify the aberration, we measure the aspect ratio (AR) of each dot using ImageJ and plot the aspect ratio as a function of radius R from the center of focus (**Fig. 2.2B**). A perfect circle has an aspect ratio of 1, and the aspect ratio increases as aberration increases. The peak of the curve, with an aspect ratio of 1.6, occurs ~575 px from the center of focus. The aspect ratio then dips slightly at the outer edges of the image due to refraction of the light rays that reach the photomask at the highest angle. The center of focus was determined by defining all the dots with AR = 1 and then finding the center of that circle. The center of focus is near, but not directly aligned with the center of the image because

the objective, focusing lens, and camera sensor are not perfectly aligned. Fig. 2B provides a measure of aberration across the image, and this information can be used to characterize a region of acceptable image quality. For example, a circle (white dashed line) with R = 300 px enclosing average hole aspect ratios $AR_{hole} \leq 1.25$ is shown in Fig. 2A. Different experiments will require different ranges of acceptable image quality.

To demonstrate the capability of the F-CFM in differentiating two distinct but identically-sized colloid populations using fluorescence, we image an aqueous suspension of microspheres containing green and red fluorescent microspheres (Bangs Laboratories; green: $\bar{d}$ = 8.3 ± 0.224 μm (UMDG003) and red: $\bar{d}$ = 8.3 ± 0.28 μm (UMFR003)). The microspheres are nearly identical in size and thus indistinguishable with brightfield imaging alone (**Fig. 2.2C**). The red fluorescent microspheres are not excited by the blue LED illumination, and thus are effectively non-fluorescent under these imaging conditions; thus, the two microsphere populations are clearly distinguishable when imaged by the F-CFM in fluorescence mode (**Fig. 2.2D, E**).

Fluorescence biophysical force measurements (e.g. single-molecule) comprise a potentially important application for the F-CFM. Single-molecule force measurements require high-precision, sub-pixel particle tracking within 10s of nm, which can be performed using the F-CFM. To demonstrate, we adhere fluorescently-labelled, polystyrene colloids ($\bar{d}$ = 1.0 μm, 1 wt%, Thermo Scientific, G0100) to the inner surface of a water-filled sample cell, place the F-CFM module on an optical table to reduce vibrations, and record individual beads for 10 s (**Fig. 2.2F**). A radial symmetry particle tracking method records the center of each colloid as a function of time with a maximum resolution of ± 0.027 px corresponding to ~2.7 nm. The x (**Fig. 2.2G**) and y (**Fig. 2.2H**) positions of a single representative bead fluctuates by ± 20 nm. We chose a radial symmetry

particle tracking method[45] over alternatives (e.g. centroid, Gaussian) for its accuracy, speed, and MATLAB graphical user interface.

Force Range

The F-CFM can apply a broad range of forces to colloidal particles. The force range is set by r, ω, and m. Here, our r and minimum ω_{min} are comparable to other commercial centrifuges; thus, the minimum force that can be applied practically is comparable to that reported for other CFMs ($F_{c,min} \approx 10^{-2}$ pN). However, our ω_{max} = 5000 RPM is 2.5× greater than values reported for other CFMs (ω_{max} = 2000 RPM). Since $F_c \propto \omega^2$, this provides a 6.25× increase in the maximum force, compared to other CFMs.[39-41] For a polystyrene microsphere with d = 1 μm and ρ_c = 1.06 g/cm^3 suspended in water and run at 2000 RPM, the centrifugal force acting on the microsphere, $F_{c,max} \approx 0.2$ pN, while at 5000 RPM, $F_{c,max} \approx 1.3$ pN. The maximum force can be increased by increasing d or ρ_c, which increases m. For example, from a practical perspective, the largest, most dense colloid would likely be a silica microsphere with $d \approx 20$ μm and ρ_c = 2.6 g/cm^3. At ω_{max} = 5000 RPM, this colloid would experience $F_{c,max} \approx 10^5$ pN. Thus, here we report the force range of the F-CFM to be 10^{-2} to 10^5 pN.

Force Validation

Most experiments with the F-CFM will subject colloidal suspensions to a well-defined centrifugal force field. While this force is straightforward to calculate from known parameters and should not require calibration, here we offer a simple sedimentation experiment to validate our force predictions. We measure the time required for monodisperse, fluorescently-labelled, polystyrene colloidal microspheres ($\bar{d}$ = 4.19 ± 0.27 μm, 0.97 wt %, ρ_c = 1.06 g/cm^3, Bangs Laboratories, FSDG006) to sediment from the top of the sample cell to the bottom at different

rotational velocities, convert these times to sedimentation velocities, and compare the experimentally-measured velocities to theoretical predictions.

With the F-CFM module focused on the colloids at the bottom inside of the sample cell, the F-CFM module is turned upside down to let the microspheres sediment to the inner surface of the coverslip nearest the camera (i.e. "top") (**Fig. 2.3A**). The total time required for the microspheres to sediment the thickness of the sample cell under gravity g is about 2 min, so the F-CFM module is allowed to sit upside down for 5 min to ensure the microspheres have reached the top of the sample cell before the measurement is started. Then we centrifuge the sample in the F-CFM and measure the time required for the microspheres to sediment to the bottom of the sample cell.

For each measurement, the centrifuge rotation is quickly ramped up to a fixed rotational speed and held at that speed until the colloids reach the inner surface of the coverslip farthest from the camera (i.e. "bottom") (**Fig. 2.3B**). The centrifuge routine is systematically varied for a range of average rotational speeds, from 150-400 RPM, corresponding to accelerations ranging from 49-216 m/s^2 and a g_{eff} range of 5-22 g. Effective gravity, or relative centrifugal force (RCF), is calculated using $g_{\text{eff}} = 11.18r\left(\frac{Q}{1000}\right)^2$ where r is the moment arm of the centrifuge (here, r = 15.0 cm) and Q is the RPM.

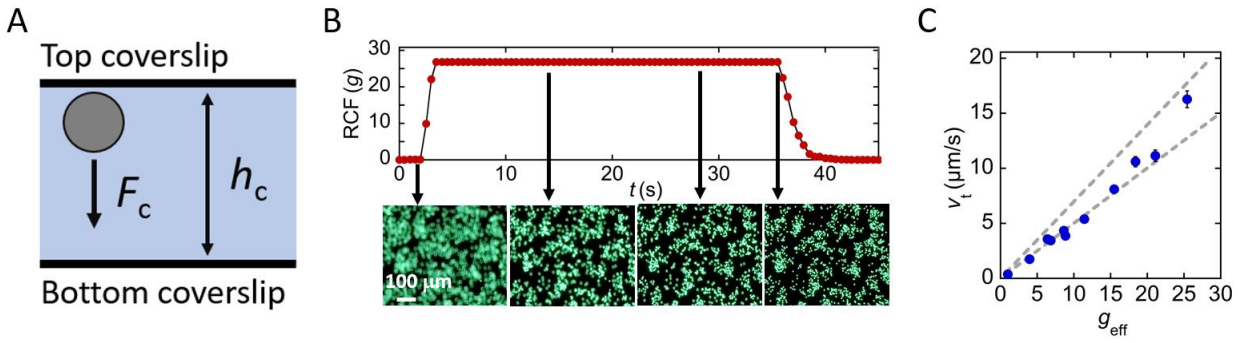


Figure 2.3: *CFM force validation using colloidal sedimentation.* (**A**) Sample cell cross-section. Gray circle represents microsphere at t = 0 near top coverslip. Not to scale. (**B**) Plot of relative centrifugal force (RCF) as a function of time t (s) for a representative sedimentation measurement. Sedimentation of green polystyrene fluorescent microspheres ($\bar{d}$ = 4.19 µm) is shown below in representative frames of an optical microscopy movie. (**C**) Plot of sedimentation terminal velocity v_t (solid blue circles) as a function of effective gravity g_{eff}. Bounding lines represent expected range.

The terminal velocity v_t is determined by dividing the settling distance by the measured sedimentation time. The settling distance is set by the thickness of the sample cell h_c which is set by the thickness of the Kapton tape (102.5 ± 3.6 µm). Loading and initiating the centrifuge takes 30 ± 5 s, during which time the colloids sediment 19.7 ± 2.5 µm; so, for our validation, the settling distance under g_{eff} is the modified thickness h_m = 82.8 ± 6.2 µm. Even at the low colloid concentrations used here (< 1.0 wt %), many of the microspheres interact with one another hydrodynamically, settle together and arrive at the bottom of the sample cell sooner than those that sediment individually (**SI Video 2.1**). Thus, the sedimentation time is defined as the time from the start of the centrifuge rotation to the time at which all the individual microspheres have reached the bottom surface and are fully in focus. A plot of the measured v_t as a function of g_{eff} is shown in **Fig. 2.3C**.

To compare these velocity results with expected values, we balance the force due to g_{eff} with the Stokes' drag force on a sphere and solve for the terminal velocity of a sinking sphere:

$v_t = \frac{2}{9}\frac{(\rho_c - \rho_f)}{\eta} g_{eff} a^2$. Here, η is the dynamic viscosity of the medium, ρ_c is the density of the colloid, ρ_f is the density of the fluid medium, g_{eff} is the effective gravitational acceleration (RCF), and a is the radius of the colloid (see **SI Note 2.4** for more details). For each experiment, we calculate the average g_{eff} over the time frame provided by the observed settling time and plot the predicted v_t as a function of g_{eff}. The predicted v_t plotted as a function of g_{eff} agrees well with our measurements (**Fig. 2.3C**)**.** The two gray dashed lines in Fig. 3C indicate the upper and lower predictions for v_t based on uncertainty in h_m, a, and sample temperature (20 °C ≤ T ≤ 23 °C), with the latter dictating the water viscosity (0.9321 cP ≤ η ≤ 1.0016 cP). The measurements fall almost entirely within the two bounds, confirming that we are accurately reporting g_{eff} acting on colloids in the F-CFM. The few points lying below the lower bound can be attributed to potential variations in tape thickness (i.e. sedimentation distance) and colloid density, and the fact that we wait for all colloids to reach the lower surface, thus effectively excluding the fastest settling colloids, which are likely interacting hydrodynamically, from our measurements.

Validation of Centrifuge Rotational Frequency with Audio Signal Analysis

Instantaneous rotational frequencies, reported as centrifuge speed RPMs, may be independently validated by analysis of the audio signal recorded by the GoPro microphone during F-CFM operation (**Fig. 2.4**). Audio sample waveforms are a record of the sounds produced by the physical motion of the rotor, effectively providing a sinusoidal signal wherein rotational frequency information is encoded. To illustrate this, we record an audiovisual movie of a linear ramp of

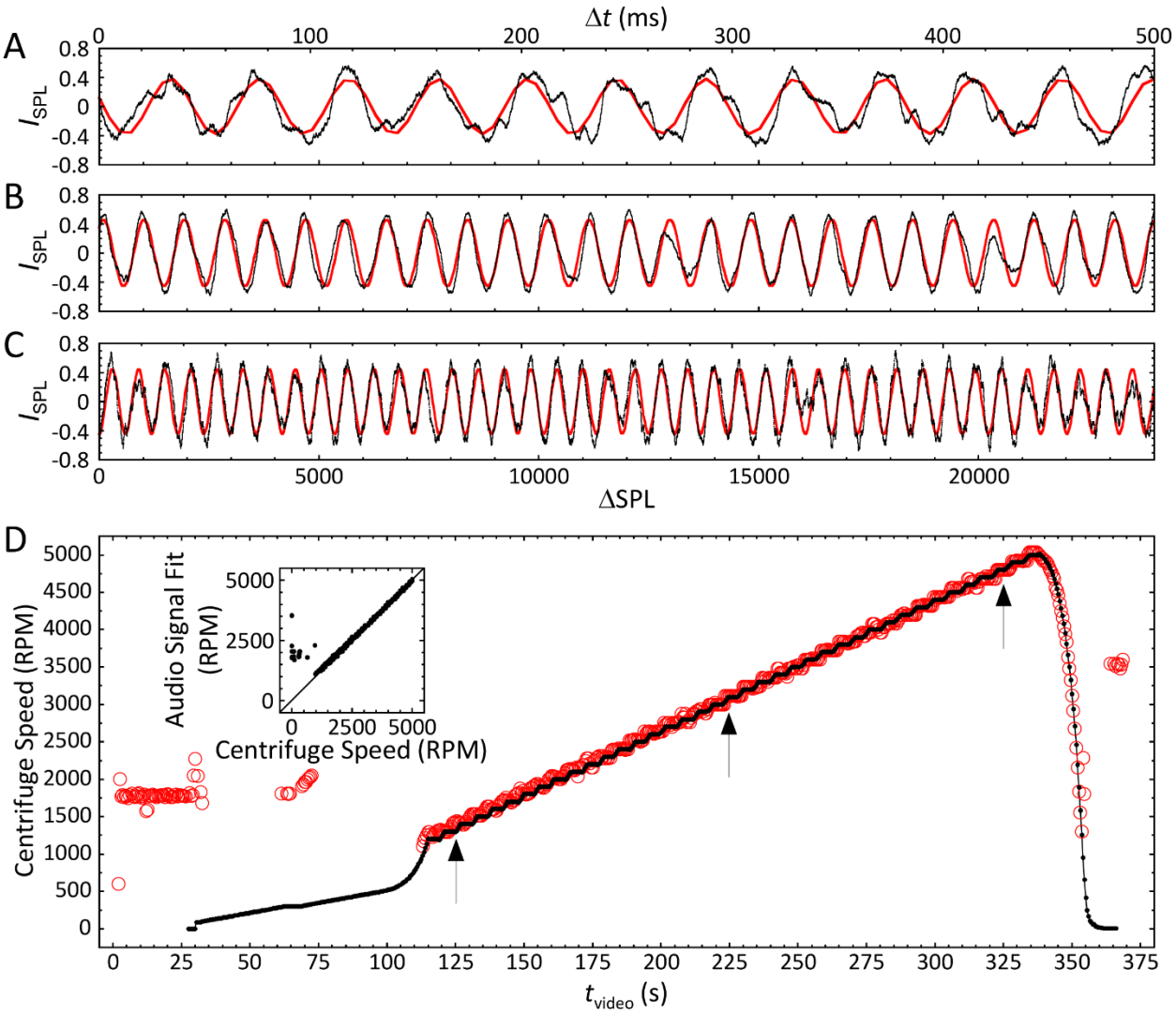


Figure 2.4: *Audio waveforms indicate centrifuge speed.* (**A-C**) Sections of 48000 Hz audio samples (black traces) recorded during the beginning, middle, and end of a linearly accelerating F-CFM run. Audio sample (SPL) traces as functions of increments of time (Δ*t*, upper *x*-axis) and sample number (ΔSPL, lower *x*-axis) are fit using equation, $I_{\mathrm{SPL}} = A\sin(ft + \varphi)$ (solid red lines) where I_{SPL} represents recorded sample intensity (arbitrary units), *A* amplitude, *f* frequency (rad), *t* time (s), and φ offset. Fit parameter *f* is used to calculate centrifuge speed values of (A) 1429, (B) 3114, and (C) 4800 RPM operation. (**D**) Centrifuge speed (RPM) reported by instrument (solid black circles, solid black line guides the eye) plotted alongside audio-calculated RPM (open red circles) fit to intervals of 0.5 s (24000 samples at 48000 Hz). Arrows indicate locations of parts A-C. Inset: Centrifuge speed values (RPM) from both audio signal fits and magnetic encoder at corresponding times show excellent agreement when RPM > 1000.

centrifuge speed from 0 to 5000 RPM during which audio is recorded at a sampling rate of 48 kHz. For the case of a F-CFM movie taken at 25 fps, each image frame represents a duration of 0.04 s. To compare the data obtained using audio signals with the data reported by the centrifuge magnetic encoder, we divide the audio samples into 0.5-s intervals, each corresponding to 24 kHz samples (**Fig. 2.4A-C**, black lines). Using a customized MATLAB routine (see **Experimental Protocol**), we fit these sample traces to a sinusoidal function, $I = A\sin(ft + \varphi)$ where I is the recorded sample intensity (arbitrary units), A is the amplitude, f is the frequency in rad s^{-1}, t is time, and φ is the offset (**Fig. 2.4A-C**, red lines) which tracks the waveforms. Every 0.5 s interval in the movie is given a sine fit, and fitting parameter frequency f is used to determine the RPM value (**Fig. 2.4D**). At centrifuge speeds < 1000 RPM, cumulative acoustic effects mask the waveform frequency information, but for values > 1000 RPM, any harmonic effects are minimized, and values track with those reported by the on-board magnetic encoder (**Fig. 2.4D**, inset). Individual measurements in this range routinely differ by < 3.0% from the magnetically-encoded values.

Colloid Detachment Force Measurements

To demonstrate the capability of the F-CFM for performing multiple force measurements in parallel, we induce attractive interactions between electrostatically-stabilized colloids with a negative net surface charge and a negatively charged-glass coverslip and measure the forces required to remove these colloids from the coverslip. We explore a range of attractive forces by suspending monodisperse polystyrene/iron oxide microbeads (Sigma-Aldrich, 49664, 5.0 wt %, $\bar{d}$ = 10.41 ± 0.13 μm, ρ_c = 1.71 g/cm^3) in 0.25× (ionic strength I = 0.053 M) phosphate buffered saline (PBS) solution and varying the concentration of NaCl (0.1 M, 0.5 M, 1.25 M, and 2.5 M). The interactions between a charged microsphere and like-charged wall are described by DLVO

theory as the sum of a van der Waals attraction and an electrostatic repulsion. The addition of salt to the colloidal suspension screens the electrostatic repulsion, thus increasing the relative contribution of the van der Waals attraction. PBS is added to buffer the pH to mitigate changes in surface charge with changes in ionic strength.[46] For experiments with 0.25× PBS, the pH decreases from 7.6 to 6.6 as the concentration of added NaCl increases from 0.1 M to 2.5 M.

For each measurement, the suspension is loaded into the sample cell, and the colloids settled and adhered to the interior glass surface of the coverslip. The cell is then oriented such that the g_{eff} acts to draw the colloids away from the surface, and the centrifuge rotational speed is ramped up at 8.9 RPM/s from 0 - 4700 RPM, corresponding to 1 - 3458 RCF. The applied centrifugal force F_c, depends on the effective mass of the particle and the centrifuge RPM (**SI Note 2.4**), enabling a broad range of forces for colloids of different sizes and densities. Colloids detach with increasing rotational speed (**Fig. 2.5A**, **SI Video 2.2**, and **SI Video 2.3**). Colloid detachment between sequential frames is determined using a manual image analysis process (**Fig. 2.5B** and **SI Note 2.5**). Detachment counts are normalized to the initial number of attached colloids to determine the fraction of colloids detached f_d, averaged across three runs per condition with 100-189 colloids tracked per run, and plotted as a function of F_c (**Fig. 2.5C**). We observe that most colloids detach within the range of applied forces. In addition, the force required to detach colloids increases with increasing ionic strength. To better visualize the dependence of colloid attachment strength as a function of ionic strength, we plot bead-detachment events for each of the four different conditions as probability distributions (**Fig. 2.5F**). We find that the data are fit well by a log-normal probability distribution (see **SI Table 2.3**), with the mode of the distribution increasing with increasing ionic strength.

To calculate the expected strength of the colloidal interaction with the glass surface, we use a modified DLVO model.[47] Colloidal interactions are commonly characterized by an interaction potential where the interaction energy U is plotted as a function of the gap between the two surfaces h; here, instead, for comparison with our experimental force measurements, we calculate and plot the total interaction force F_I as a function of h. For our system, the modified DLVO model predicts two minima: a deep primary minimum at small separation distances ($h < 0.5$ nm) and a shallower secondary minimum at intermediate distances ($h \approx 2$ nm). A representative F_I (h) curve for one solution condition (0.5 M NaCl + 0.25× PBS) is shown in **Fig. 2.5D** (see **SI Note 2.6** for DLVO equations and assumptions). During loading, as the microspheres are drawn to the glass surface by gravity, they will be drawn into the secondary minimum; however, they are unlikely to overcome the barrier to enter the primary minimum. Thus, we assume the force F_d required to remove the colloids from the surface of the glass at a separation distance h is equal to the depth of the secondary minimum (**Fig. 2.5D**, dashed lines and inset).

To compare our results with expected values, we co-plot the force values associated with the mode of each distribution from Fig. 5F as a function of ionic strength (**Fig. 2.5E**, solid blue circles) together with predictions from the modified DLVO model (**Fig. 2.5E**, gray dashed lines).

To represent the uncertainty in surface charge potential[48] of the glass surface ψ_g and colloid surface ψ_{cs} (see **SI Note 2.6**) we include two limiting cases as bounding lines: a high surface charge case (ψ_g = 300 mV, ψ_{cs} = 100 mV) represented by the lower gray dashed line in Fig. 5E, and a low surface charge case (ψ_g = 150 mV, ψ_{cs} = 30 mV) represented by the upper gray dashed line in Fig.

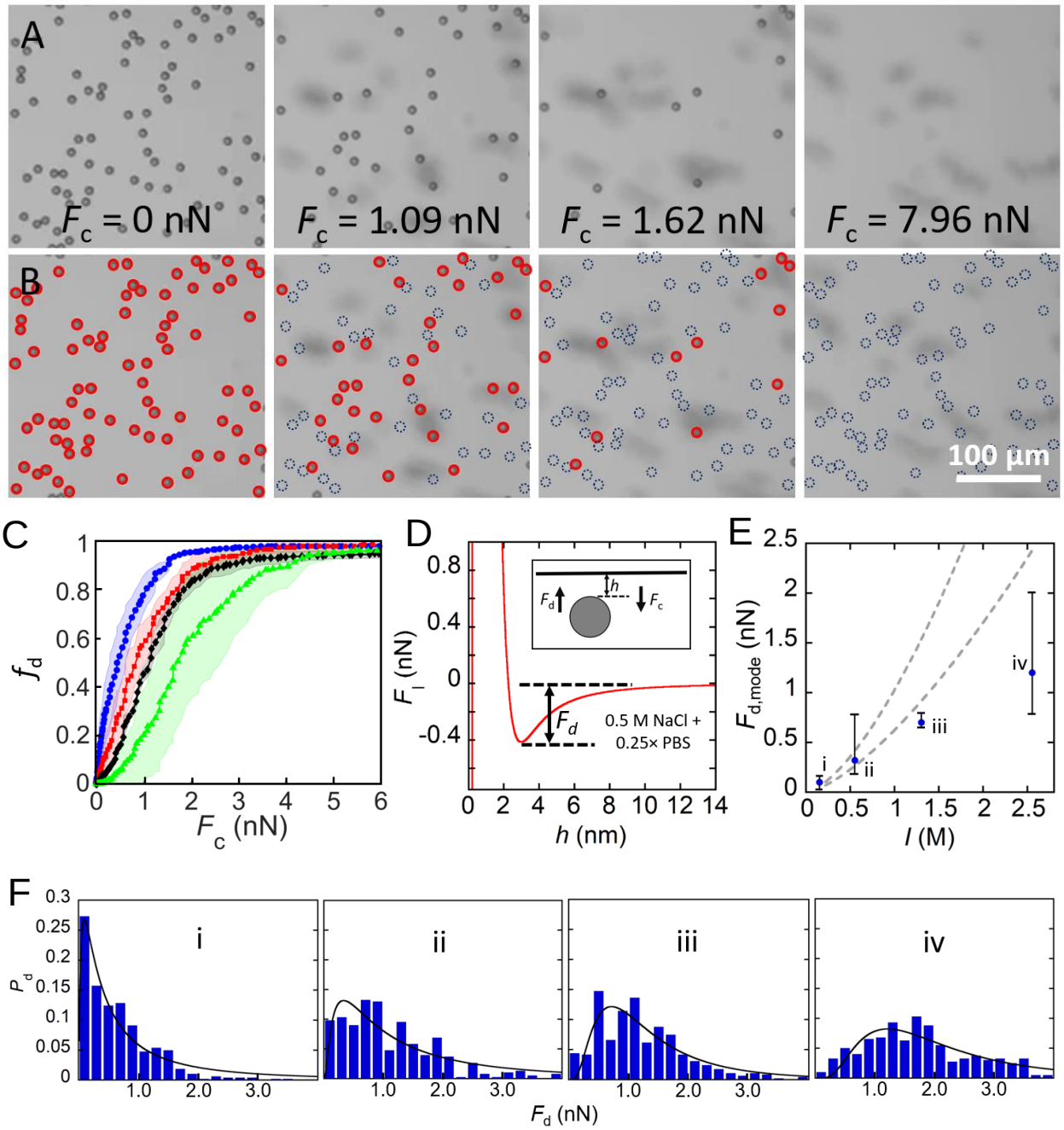


Figure 2.5: *Colloid detachment force distributions as functions of electrolyte concentrations.* (**A**) Representative optical microscopy images (cropped for better visualization) recorded by the F-CFM show electrostatically-stabilized polystyrene/iron oxide colloidal microspheres ($\bar{d}$ = 10.4 µm) being detached from a glass coverslip surface during a force ramp from 1 - 283 relative centrifugal force (RCF). Images are cropped to represent the area of best focus. (**B**) Images from (A) indicating attached, in-focus bead locations (solid open red circles) and former locations (dashed open blue circles) of now detached, out-of-focus beads. Scale bar = 100 µm (**A** and **B**) (**C**)

Fractions of total colloids detached f_d as a function of applied centrifugal force F_c for NaCl concentrations 0.1 M (solid blue circles), 0.5 M (solid red squares), 1.25 M (solid black diamonds), and 2.5 M (solid green triangles). Solid lines represent the averages of three runs and transparent envelopes indicate one standard deviation. (**D**) Estimated interaction force F_I as function of gap distance h calculated using DLVO theory predicts a detachment force F_d = 0.040 nN for 0.5 M NaCl + 0.25× PBS. Chosen y-axis range does not allow the depth of primary minimum or height of energy barrier to be seen. Inset: Schematic of a bead at distance h from glass slide surface subjected to centrifugal force F_c and detachment force F_d. (**E**) Average detachment force $F_{d,mode}$ (solid blue circles) from the distribution peaks in (F) as a function of ionic strength I. Bounding lines represent expected range (see **SI Note 6** for parameter assumptions and **SI Table 3** for upper and lower fit parameters). (**F**) Normalized probability distributions of detachment forces for each experimental condition (i) 0.1 M, (ii) 0.5 M, (iii) 1.25 M, and (iv) 2.5 M, each with 0.25× PBS. Solid lines represent fits to log-normal distribution function (**SI Table 2**).

5E. We find good agreement between experimental and expected detachment force values at low ionic strength, but deviation at higher ionic strengths, with the calculated detachment force F_d higher than the observed values. These differences could be attributed to surface charge uncertainty,[49-56] spatial heterogeneities of the glass substrate surface potential,[57-60] and surface roughness.[31, 37, 61-64] Despite the disagreement at high ionic strength, our results reflect the capability of the F-CFM to perform 10s to 100s of force measurements in parallel.

The F-CFM could be used to perform a variety of other parallel force measurements including measurement of other colloidal interaction potentials (e. g. depletion and steric), single molecule forces[39-41], microbial adhesion[41, 65] and emulsion stability under compression in real time. Future iterations of the F-CFM design could benefit from additional modifications. For example, a second camera sensor could be added below the sample cell to allow transmitted light imaging separately and concurrently with fluorescence imaging. This would improve the image quality for both the transmitted and fluorescence image compared to the current combined “two-in-one” fluorescence and brightfield image. A motorized sample holder that can move in the z-axis could be incorporated for precise real-time mechanical image focusing. Currently, the sample is focused

manually at the start of the experiment and cannot be adjusted during the experiment. The ability to move the sample in the *z*-axis while the centrifuge is spinning would allow focusing on samples as they change position in the sample cell. Real-time focusing could also prevent the reduction in clarity caused by flexing of the sample cell out of the focal plane inherent in high-speed experiments. A second fluorescence cube could be integrated to allow for multiple fluorophores to be imaged in a single run. This would require additional miniaturization of some components or a larger swinging bucket. Mirrors could be added to directly image the bottom of the surface of interest, allowing non-transparent substrates to be characterized. Other mirror configurations could also allow the sample to be imaged from the side in order to track colloid motion after detachment, although this would limit the number of in-focus colloids. Further miniaturization and ruggedization would also allow the F-CFM to be incorporated into a fixed rotor ultracentrifuge, enabling detachment force measurements on colloids such as bacteria and viruses. Fluidic pumps could also be integrated into the empty remaining centrifuge buckets to alter solution conditions during centrifugation, for example, enabling the concentration of electrolytes in the suspension to be tuned until the point of colloid detachment. Biological samples could be characterized by functionalizing the glass cover slips with treatments such as silane followed by ligands of interests. Alternatively, a different transparent material such as PMMA or polypropylene could be used in place of cover slips if the functionalization is better suited to that material.

Conclusion

To our knowledge, the F-CFM is the first CFM to incorporate fluorescence microscopy. Additionally, the F-CFM is the first CFM used for colloid interaction force measurements and the first CFM to operate up to 5000 RPM. This F-CFM is easy to assemble, requiring only basic

knowledge of electronics and fabrication. Additionally, the audio microphone provides highly accurate rotational speed information for CFM configurations that lack a centrifuge with a computer interface or on-board magnetic encoder. The wireless F-CFM provides high resolution video with acceptable levels of aberrative vignetting to perform nm-scale, sub-pixel particle tracking. Three illumination modes are available: brightfield, fluorescence, and combined brightfield and fluorescence. Using the F-CFM, we induce attractive interactions between 100s of colloids and a glass coverslip, measure their adhesion force as a function of ionic strength, and show excellent correspondence with prediction at low ionic strength using a modified DLVO model.

Supplemental Information

Measuring the swinging bucket angle as a function of centrifuge rotational velocity

A hole was drilled in the bottom of one of the swinging buckets. The brightfield LED was soldered upside down into the PCB so that it pointed down through the bucket hole instead of up towards the sample (**SI Fig. 2.2A**). A new F-CFM clamshell holder was printed to accommodate the LED pointing downwards. A piece of photosensitive cyanotype paper (stevespanglerscience.com) was taped to the wall of the centrifuge. The centrifuge was closed and allowed to run at a constant speed for 20 min, with the LED light creating a line in the photosensitive paper. The centrifuge was then opened, and the bucket held such that the LED pointed at the line it created. Then a digital angle finder was held against the bucket to determine its angle in that position (**SI Fig. 2.2B**). This process was repeated throughout the speed range of

the centrifuge. The visibility of the line created by the LED on the photosensitive paper was improved slightly after developing in water (**SI Fig. 2.2C**).

F-CFM Assembly

The F-CFM is assembled as follows. The camera (**SI Fig. 2.1a**) is prepared using pliers to unscrew the commercial lens from the camera. The camera is attached to the microscope via a hand-fabricated M12 externally threaded aluminum tube (**SI Fig. 2.1b**) which is connected to a Thorlabs M12-SM1 adapter (**SI Fig. 2.1c**) screwed into a 1-in long Thorlabs SM1 lens tube (**SI Fig. 2.1d**). Retaining rings (**SI Fig. 2.1e**) hold a focusing lens (**SI Fig. 2.1f**) in this same tube. The fluorescence cube (**SI Fig. 2.1g**) contains the emission filter (**SI Fig. 2.1h**) and dichroic mirror (**SI Fig. 2.1i**). The fluorescence LED (**SI Fig. 2.1j**) is soldered to a PCB with a male 2-pin JST connector and 10-Ω resistor; this PCB assembly slides into a slot in the CFM clamshell holder aligned to the excitation filter (**SI Fig. 2.1k**) in an adjacent slot, pointing towards the fluorescence cube adapter (**SI Fig. 2.1l**) that holds the fluorescence cube. The adapter screws into the tube above it and the tube below it. The tube below it (**SI Fig. 2.1m**) holds an RMS-SM1 adapter (**SI Fig. 2.1n**) that holds the objective (**SI Fig. 2.1o**). The sample cell holder (**SI Fig. 2.1p and 2.1q**) screws into this objective tube until the sample inside the holder is in focus. The sample is backlit by the brightfield LED (**SI Fig. 2.1r**) soldered to a PCB with a male 2-pin JST connector and 10-kΩ resistor.

Cutting the annular tape rings

A 3" wide strip of 3M double sided masking tape (uline.com) was adhered to an 8.5” × 11” sheet of heavy weight cardstock printer paper. The 3M tape cover paper was removed and saved. Then a three-inch-wide strip of double-sided Kapton polyimide tape (kaptontape.com) was placed,

cover paper down, onto the 3M tape adhering the 3M cover paper on top of the Kapton tape. The tape assembly was then loaded into a craft cutter (Silhouette Cameo 2) with the blade at the deepest cut position (#10) and the pressure and speed set at the factory settings. The annular circle dimensions (I.D. = 7 mm, O.D. = 15 mm) were drawn in the Silhouette software in a repeating pattern and sent to the Silhouette cutter for cutting. After the cutting is finished, the tape assembly was removed from the cutter.

Derivation of microsphere settling velocity

For a spherical microbead settling through a Newtonian liquid, the drag force acting on the particle is $F_{\mathrm{d}} = 6\pi\eta a v$, where F_{d} is the frictional force, η is the dynamic viscosity of the fluid, a is the radius of the particle, and v is the settling velocity of the particle. The gravitational force acting on this particle is $F_{\mathrm{g}} = (\rho_{\mathrm{c}} - \rho_{\mathrm{f}}) g \frac{4}{3}\pi a^3$, where ρ_{c} is the density of the particle, ρ_{f} is the density of the fluid, and g is the acceleration due to gravity. Balancing the two force equations and solving for the velocity v, provides terminal velocity v_{t} of the particle. We assume v_{t} is reached in a very short time, much less than the settling time.

Manual Image Counting Analysis of Microsphere Detachments

MATLAB image analysis was performed manually frame-by-frame (for every one out of 100 frames) to count the number of particles that detach in each frame. The number of particles detached from each frame to the next was recorded in a spreadsheet. The frame-by-frame particle counts were added together across three runs at each experimental condition, synced with the speed data to determine the effective gravity acting on the particles in each frame, and then binned as a function of effective gravitational force in MATLAB The “histogram” command was used to

generate the normalized probability distribution according to predefined bin limits, and the "counts" command was used to retrieve the bin *y*-axis values so they could be plotted and fitted in a plotting software (**Fig. 2.5F**).

Assumptions for the Gregory model of predicting detachment force

The theoretical van der Waals force was calculated using $F_{vdw} = Aa/(6h(1+14h/\lambda))$ where A is the Hamaker constant, a is the particle radius, h is the separation distance, and λ is the characteristic wavelength of retardation, typically assumed to be 100 nm. This model of F_{vdw} is similar to the simpler model derived by Hamaker[66] and by Israelachvili,[67] but is more accurate for very small separation distances and up to about 0.2× the particle radius.[68, 69]

The Van der Waals force F_{vdw} at a given separation distance h is largely dependent on the Hamaker constant A_{132}, which is dependent on the refractive indices (n_i) and relative permittivities (ε_i) of the two objects (materials 1 and 2) and the medium separating them (material 3) as $A_{132} = 3kT((\varepsilon_1 - \varepsilon_3)/(\varepsilon_1 + \varepsilon_3))((\varepsilon_2 - \varepsilon_3)/(\varepsilon_2 + \varepsilon_3))/4 + 3h\nu((n_1^2 - n_3^2)(n_2^2 - n_3^2)/\sqrt{((n_1^2 + n_3^2)(n_2^2 + n_3^2)(\sqrt{(n_1^2 + n_3^2)} + \sqrt{(n_2^2 + n_3^2)})/8\sqrt{2}}$. Glass (material 1) and aqueous electrolyte (material 3) are well characterized,[67] as is polystyrene, but polystyrene/iron oxide is not well characterized. These microspheres are a homogeneous mixture of iron oxide nanoparticles in a polystyrene polymer matrix, with at least 20% composition iron oxide by mass. Thus, to determine the Hamaker constant of the microsphere composite material, we used the mass average of the refractive indices and relative permittivities of polystyrene and iron oxide ($n_{ps} = 1.557$, $n_{iro} = 1.97$, $\varepsilon_{ps} = 2.55$, $\varepsilon_{iro} = 14.2$), assuming an iron oxide mass fraction of 0.2, and arrived at a Hamaker constant for our system of $A_{132} = 13.2 \times 10^{-21}$ J. The Hamaker constant is, however, screened in aqueous

electrolytes,[70] so we multiplied the Hamaker constant by a factor of 2/3 to arrive at a value of A_{132} = 8.77 × 10^{-21} J.

The theoretical electrostatic force is calculated by $F_{el} = \kappa 64\pi\varepsilon a(kT/ze)^2\gamma_1\gamma_2\exp[-\kappa h]$ where κ is the inverse Debye length $\kappa = \sum\sqrt{(n_i e^2 z_i^2/\varepsilon kT)}$, n_i is the number density of the ith ion species, ε is the permittivity of the solution, a is the particle radius, k is the Boltzmann constant, T is the absolute temperature, z_i is the valence of the ith ion species, e is the charge of an electron, and $\gamma_1 = \tanh(ze\psi/4kT)$ where ψ is the surface potential and h is the separation distance. This model was also developed by Gregory[47] and has been used for approximating practical conditions where a middle ground between the constant charge and constant potential boundary conditions used in deriving these conditions is considered more appropriate.[48, 68, 71]

The electrostatic force F_{el} is largely dependent on the glass surface potential ψ_g, the polystyrene microsphere surface potential ψ_{cs}, and the inverse Debye length κ^{-1}. The Debye length is well defined based on the aqueous electrolyte concentration, but the surface potentials ψ_{cs} and ψ_g are quite uncertain. Polystyrene spheres are manufactured using emulsion polymerization and are stabilized by the negatively charged sulfate surface groups that result from the production process. Depending on the exact procedure used during production, polystyrene spheres can have a range[72] of surface charge densities from 0.002 - 0.025 C/m^2 (based on reference [14] and on reported data from Thermo Fisher carboxyl latex microspheres such as p/n C37281), and the zeta potential ζ is usually observed[17, 49, 50, 53, 56] to be 40 – 1000 mV in pure or low electrolyte water. The zeta potential is also reported to decrease with increasing electrolyte concentration, down to around 20 – 40 mV, but models also suggest that low ζ at high ionic strength solutions may represent significantly higher surface potentials than are observed.[73] In general, across most ionic

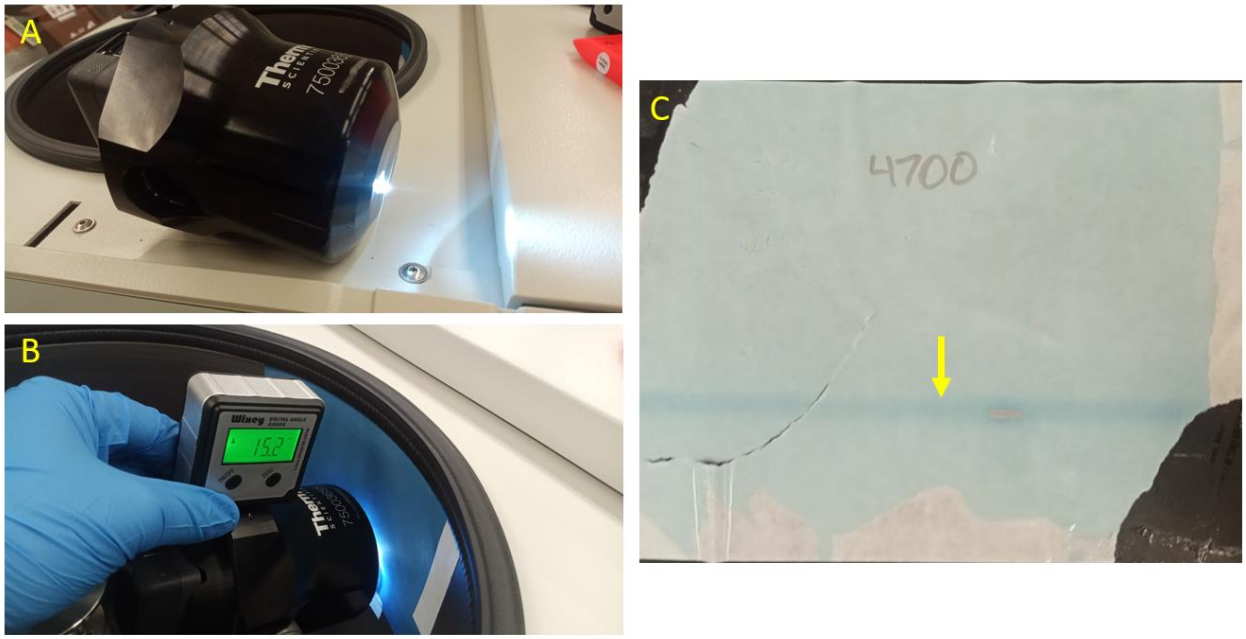
strengths, the true surface potential is assumed to be at least somewhat higher than ζ. The same issues apply for glass ψ_g. Our treatment process includes sonication in NaOH, which has been shown to make the glass highly negatively charged,[74] up to 0.76 C/m^2 at 1.0 M NaOH, which using the Gouy-Chapman model[53, 75] results in a surface potential of 350 mV. Glass has also been well characterized in aqueous electrolyte,[31, 76-78] but, to our knowledge, no one has reported how long NaOH treatment effects last and if they persist after drying and immersing in aqueous electrolyte. Therefore, we take ranges of values from the literature and assume the glass is relatively highly charged at ψ_g = 150 – 300 mV and the polystyrene microspheres are low to moderately charged at ψ_{cs} = 30 – 100 mV, keeping in mind that the true values may deviate even further than this range. The predicted detachment forces for these ranges are shown as the upper and lower gray dashed lines in **Figure 2.5E**. Our experimentally measured values at high ionic strength (Fig. 2.5E, blue circles) are lower than the predicted values (Fig. 2.5E, gray dashed lines). This is likely due to the aforementioned surface charge uncertainty[17, 49-51, 53-56] as well as surface roughness[31, 37, 61-64, 79] and spatial heterogeneities of the glass substrate surface potential.[57-60]

Acknowledgements

Special thanks to Wesley Wong and Darren Yang for generously showing us their CFM and explaining its construction and operation. We also thank Matthew Griffin and Mandy Rutherford from the Montana State University Makerspace for their help in the early design stages of this project, and Aaron D. Benjamin for useful discussions.

Funding

This work was supported by the National Science Foundation (DMR-1455247, DMR-1753352, and OIA-1736255).



Supplemental Figure 2.1: *Measuring the swinging bucket angle at different rotational velocities*. The bucket angle at different rotational velocities was measured using light sensitive cyanotype paper. (**A**) A hole was drilled in the bottom of a centrifuge bucket and an LED was installed to point downward out of the bucket. (**B**) A sheet of cyanotype paper was taped to the inside of the centrifuge. After the centrifuge run was complete, and a digital protractor was used to measure the angle required to create (**C**) the light-developed line in the cyanotype paper.

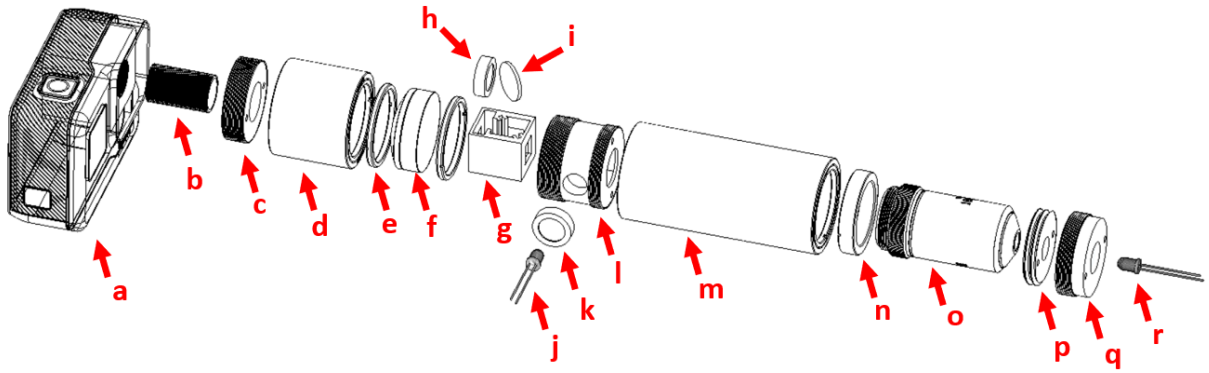
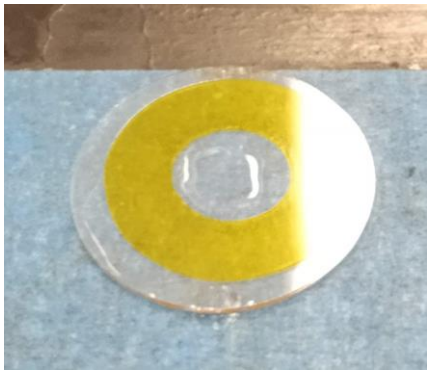


FIG. REF.	VENDOR	PART NUMBER	DESCRIPTION	PRICE
a	Gopro	n/a	Hero 5 Black action camera	$180.00
b*	n/a	n/a	M12 1-inch adapter, fabricated	$50.00
c	Thorlabs	SM1TM12	SM1 to M12 x 0.5 Lens Cell Adapter	$22.00
d	Thorlabs	SM1M10	SM1 Lens Tube Without External Threads, 1" Long	$13.87
e	Thorlabs	n/a	Retaining ring (included with lens tube)	$0.00
f	Thorlabs	AC254-030-A	f=30.0 mm, 1" Dia. Achromatic Doublet, ARC: 400-700 nm	$82.62
g	n/na	n/a	Fluorescence Cube, 3D Printed	$0.00
h	Edmund Optics	67016	Emission Filter 520NM x 36 NM BP 93T 12.5D	$185.00
i	Edmund Optics	67055	Filter Dichroic 495NM 12.5D	$140.00
j**	Adafruit		Diffused white LED	$5.00
k	Edmund Optics	67013	Excitation Filter 472NM x 30 NM BP 93T 12.5D	$185.00
l	n/a	n/a	Fluorescence Cube Adapter, 3D printed	$0.00
m	Thorlabs	SM1M25	SM1 Lens Tube Without External Threads, 2.5" Long	$17.44
n	Thorlabs	SM1A3	Adapter with External SM1 Threads and Internal RMS Threads	$17.44
o	Boli Optics	BM13063431	Objective 20X 5.1mm WD Infinity Plan Achromat	$89.98
p	n/a	n/a	Sample cell holder top, 3D printed	$0.00
q	n/a	n/a	Sample cell holder bottom, 3D printed	$0.00
r***	Mouser Electronics	C503B-BAN-CX0B0461	Standard LEDs - Through Hole Blue Round - 5mm dia - T-1 3.4 - 470 nm	$5.00
n/a	Amazon	EL-CK-004	Elegoo resistor kit 0 Ω - 1 MΩ (10 kΩ resistor)	$13.86
n/a	Digi-key	B2B-PH-K-S(LF)(SN)	JST 2-pin male connector	$0.17
n/a	Amazon	EL-CK-004	Elegoo resistor kit 0 Ω - 1 MΩ (10 Ω resistor)	$0.00
n/a	Amazon		Neutral Density Filter, ND1.2, 4 F-Stop, Rosco E Colour 299	$9.00
				$1,016.38

Supplemental Figure 2.2: *Exploded F-CFM diagram and parts information.*
*Fabricated using M12 × 0.5 metric right-hand thread die, manual die holder, manual pipe cutter, and 12-mm OD aluminum tubing, all purchased from Amazon.
**Soldered to PCB with 10-kΩ resistor and through-hole male JST PH 2-pin connector (Digi-Key p/n 455-1704-ND). PCB is designed in Eagle CAD and ordered from OshPark.
*** Soldered to PCB with 10-Ω resistor and through-hole male JST PH 2-pin connector (Digi-Key p/n 455-1704-ND). PCB is designed in Eagle CAD and ordered from OshPark. Powered by LiPo battery (Sparkfun p/n PRT-13813).



Supplemental Figure 2.3: *Assembled sample cell.* The adhesive bead “bubble barrier” is visible as the square shape inside the annular golden colored Kapton tape ring sandwiched between two glass cover slips.



Supplemental Figure 2.4: *Images of the F-CFM unit and centrifuge.* (**A**) The F-CFM module can be seen in the centrifuge buckets at the 6:00 o'clock and 12:00 o'clock positions. (**B**, **C**) Images of the polycarbonate enclosure.

Supplemental Table 2.1: Fitting form and parameters for Figure 2B (main text).
Fit equation: $AR_{\text{hole}} = a + bR + cR^2 + dR^3 + eR^4 + fR^5$

Fit parameter	Value
a	1.06
b	0.000135
c	-2.54e-6
d	2.60e-8,
e	4.80e-11
f	2.49e-14
R	0.876

Supplemental Table 2.2: Log-normal fit parameters for detachment force probability distributions in Figure 5F (main text). Fit equation: $P_d(F_d) = d(\exp[-\ln(F_d)/c]^2)/(2b^2))/(F_d b\sqrt{\pi})$.

Fit Parameter	NaCl concentration (M)							
	0.1	0.1 error	0.5	0.5 error	1.25	1.25 error	2.5	2.5 error
b	1.350	0.06666	1.113	0.05990	0.6925	0.04231	0.6366	0.03254
c	0.5931	0.04765	1.143	0.1133	1.154	0.05916	1.824	0.07036
d	0.2156	0.01076	0.2260	0.01592	0.1919	0.01170	0.1960	0.009828
R	0.9825		0.9306		0.9286		0.9427	

Supplemental Table 2.3: Power fit parameters for predicted detachment force curves in Figure 5E (main text).

Fit equation: $F_{d,mode}(I) = p(I)^q$

Fit Parameter	Lower Curve	Upper Curve
p	0.6254	1.029
q	1.448	1.521
R	0.9999	0.9998

References Cited

1. Daoud, M.; Lyle, S. N.; Williams, C. E., *Soft Matter Physics*. Springer Berlin Heidelberg: 2013.

2. Chaikin, P. M.; Lubensky, T. C., *Principles of Condensed Matter Physics*. Cambridge University Press: 2000.

3. Russel, W. B.; Russel, W. B.; Saville, D. A.; Schowalter, W. R., *Colloidal Dispersions*. Cambridge University Press: 1991.

4. Rubinstein, M. C., Ralph *Polymer Physics*. Oxford University Press: 2003.

5. Farjami, T.; Madadlou, A., An overview on preparation of emulsion-filled gels and emulsion particulate gels. *Trends Food Sci. Technol.* **2019,** *86*, 85-94.

6. Kokubo, T.; Kim, H. M.; Kawashita, M., Novel bioactive materials with different mechanical properties. *Biomaterials* **2003,** *24* (13), 2161-2175.

7. Marchetti, M. C.; Joanny, J. F.; Ramaswamy, S.; Liverpool, T. B.; Prost, J.; Rao, M.; Simha, R. A., Hydrodynamics of soft active matter. *Rev. Mod. Phys.* **2013,** *85* (3), 47.

8. Fryd, M. M.; Mason, T. G., Advanced Nanoemulsions. In *Annual Review of Physical Chemistry, Vol 63*, Johnson, M. A.; Martinez, T. J., Eds. Annual Reviews: Palo Alto, 2012; Vol. 63, pp 493-518.

9. Mezzenga, R.; Schurtenberger, P.; Burbidge, A.; Michel, M., Understanding foods as soft materials. *Nature Materials* **2005,** *4* (10), 729-740.

10. Donald, A., Food for thought. *Nature Materials* **2004,** *3* (9), 579-581.

11. Brummer, R., *Rheology Essentials of Cosmetic and Food Emulsions*. Springer Berlin Heidelberg: 2006.

12. Peppas, N. A., *Hydrogels in Medicine and Pharmacy: Fundamentals*. CRC Press: 2019.

13. Fung, Y. C., *Biomechanics: Mechanical Properties of Living Tissues*. Springer New York: 2013.

14. Mason, T. G., New fundamental concepts in emulsion rheology. *Current Opinion in Colloid & Interface Science* **1999,** *4* (3), 231-238.

15. Lu, P. J.; Weitz, D. A., Colloidal Particles: Crystals, Glasses, and Gels. *Annual Review of Condensed Matter Physics* **2013,** *4* (1), 217-233.

16. Vlassopoulos, D.; Cloitre, M., Tunable rheology of dense soft deformable colloids. *Current Opinion in Colloid & Interface Science* **2014,** *19* (6), 561-574.

17. Adamczyk, Z.; Warszynski, P., Role of electrostatic interactions in particle adsorption. *Advances in Colloid and Interface Science* **1996,** *63*, 41-149.

18. Wilking, J. N.; Angelini, T. E.; Seminara, A.; Brenner, M. P.; Weitz, D. A., Biofilms as complex fluids. *MRS Bull.* **2011,** *36* (5), 385-391.

19. Benjamin, A. D.; Abbasi, R.; Owens, M.; Olsen, R. J.; Walsh, D. J.; LeFevre, T. B.; Wilking, J. N., Light-based 3D printing of hydrogels with high-resolution channels. *Biomedical Physics & Engineering Express* **2019,** *5* (2).

20. Larson, R. G., *The Structure and Rheology of Complex Fluids*. OUP USA: 1999.

21. Mason, T. G.; Bibette, J.; Weitz, D. A., Elasticity of Compressed Emulsions. *Physical Review Letters* **1995,** *75* (10), 2051-2054.

22. Lee, G.; Han, S.-B.; Lee, J.-H.; Kim, H.-W.; Kim, D.-H., Cancer Mechanobiology: Microenvironmental Sensing and Metastasis. *ACS Biomaterials Science & Engineering* **2019,** *5* (8), 3735-3752.

23. Verbruggen, S., *Mechanobiology in Health and Disease*. Elsevier Science: 2018.

24. Erhart-Hledik, J. C.; Chehab, E. F.; Asay, J. L.; Favre, J.; Chu, C. R.; Andriacchi, T. P., Longitudinal changes in tibial and femoral cartilage thickness are associated with baseline ambulatory kinetics and cartilage oligomeric matrix protein (COMP) measures in an asymptomatic aging population. *Osteoarthritis and cartilage* **2021**.

25. Zignego, D. L.; Hilmer, J. K.; June, R. K., Mechanotransduction in primary human osteoarthritic chondrocytes is mediated by metabolism of energy, lipids, and amino acids. *Journal of biomechanics* **2015,** *48* (16), 4253-61.

26. Mason, T. G.; Weitz, D. A., Linear Viscoelasticity of Colloidal Hard Sphere Suspensions near the Glass Transition. *Physical Review Letters* **1995,** *75* (14), 2770-2773.

27. Menut, P.; Seiffert, S.; Sprakel, J.; Weitz, D. A., Does size matter? Elasticity of compressed suspensions of colloidal- and granular-scale microgels. *Soft Matter* **2012,** *8* (1), 156-164.

28. Leite, F. L.; Bueno, C. C.; Da Roz, A. L.; Ziemath, E. C.; Oliveira, O. N., Theoretical Models for Surface Forces and Adhesion and Their Measurement Using Atomic Force Microscopy. *Int. J. Mol. Sci.* **2012,** *13* (10), 12773-12856.

29. Meyers, M. A.; Chen, P. Y.; Lin, A. Y. M.; Seki, Y., Biological materials: Structure and mechanical properties. *Progress in Materials Science* **2008,** *53* (1), 1-206.

30. Liang, Y.; Hilal, N.; Langston, P.; Starov, V., Interaction forces between colloidal particles in liquid: Theory and experiment. *Advances in Colloid and Interface Science* **2007,** *134-35*, 151-166.

31. Trefalt, G.; Palberg, T.; Borkovec, M., Forces between colloidal particles in aqueous solutions containing monovalent and multivalent ions. *Current Opinion in Colloid & Interface Science* **2017,** *27*, 9-17.

32. Gosse, C.; Croquette, V., Magnetic tweezers: Micromanipulation and force measurement at the molecular level. *Biophys. J.* **2002,** *82* (6), 3314-3329.

33. Wilson, L.; Matsudaira, P. T.; Sheetz, M. P., *Laser Tweezers in Cell Biology*. Elsevier Science: 1997.

34. Grier, D. G., Optical tweezers in colloid and interface science. *Current Opinion in Colloid & Interface Science* **1997,** *2* (3), 264-270.

35. Kegler, K.; Salomo, M.; Kremer, F., Forces of Interaction between DNA-Grafted Colloids: An Optical Tweezer Measurement. *Physical Review Letters* **2007,** *98* (5), 058304.

36. Butt, H. J.; Berger, R.; Bonaccurso, E.; Chen, Y.; Wang, J., Impact of atomic force microscopy on interface and colloid science. *Advances in Colloid and Interface Science* **2007,** *133* (2), 91-104.

37. Butt, H. J.; Cappella, B.; Kappl, M., Force measurements with the atomic force microscope: Technique, interpretation and applications. *Surf. Sci. Rep.* **2005,** *59* (1-6), 1-152.

38. van Oene M, D. L., Cross B, Pedaci F, Lipfert J, Dekker N, Applying torque to the Escherichia coli flagellar motor using magnetic tweezers. *Nature Scientific Reports* **2017,** *7*, 1-11.

39. Halvorsen, K.; Wong, W. P., Massively Parallel Single-Molecule Manipulation Using Centrifugal Force. *Biophys. J.* **2010,** *98* (11), L53-L55.

40. Hoang, T.; Patel, D. S.; Halvorsen, K., A wireless centrifuge force microscope (CFM) enables multiplexed single-molecule experiments in a commercial centrifuge. *Rev Sci Instrum* **2016,** *87* (8), 083705.

41. Yang, D.; Ward, A.; Halvorsen, K.; Wong, W. P., Multiplexed single-molecule force spectroscopy using a centrifuge. *Nat Commun* **2016,** *7*, 11026.

42. Kou, L.; Jin, L.; Lei, H.; Hu, C.; Li, H.; Hu, X., Real-time parallel 3D multiple particle tracking with single molecule centrifugal force microscopy. *J. Microsc.* **2019,** *273* (3), 178-188.

43. Punnoose, J. A.; Hayden, A.; Zhou, L. F.; Halvorsen, K., Wi-Fi Live-Streaming Centrifuge Force Microscope for Benchtop Single-Molecule Experiments. *Biophys. J.* **2020,** *119* (11), 2231-2239.

44. Kirkness, M. W. H.; Forde, N. R., Single-Molecule Assay for Proteolytic Susceptibility: Force-Induced Collagen Destabilization. *Biophys. J.* **2018,** *114* (3), 570-576.

45. Parthasarathy, R., Rapid, accurate particle tracking by calculation of radial symmetry centers. *Nat. Methods* **2012,** *9* (7), 724-U291.

46. Behrens, S. H.; Grier, D. G., The charge of glass and silica surfaces. *J. Chem. Phys.* **2001,** *115* (14), 6716-6721.

47. Gregory, J., Interaction of Unequal Double Layers at Constant Charge. *J Colloid and Interface Sci* **1974,** *51*, 44-51.

48. Elimelech, M.; Gregory, J.; Jia, X.; Williams, R., Particle Deposition & Aggregation. *Butterworth-Heinemann Ltd* **1995**.

49. Folkersma, R.; van Diemen, A. J. G.; Stein, H. N., Electrophoretic properties of polystyrene spheres. *Langmuir* **1998,** *14* (21), 5973-5976.

50. Ohsawa, K. M., M.; and Ohshima, H., Zeta potential and surface charge density of polystyrene-latex; comparison with synaptic vesicle and brush border membrane vesicle. *Colloid & Polymer Science* **1986,** *264*, 1005-1009.

51. Garg, A.; Cartier, C. A.; Bishop, K. J. M.; Velegol, D., Particle Zeta Potentials Remain Finite in Saturated Salt Solutions. *Langmuir* **2016,** *32* (45), 11837-11844.

52. Adamczyk, Z.; Bratek-Skicki, A.; Dabrowska, P.; Nattich-Rak, M., Mechanisms of Fibrinogen Adsorption on Latex Particles Determined by Zeta Potential and AFM Measurements. *Langmuir* **2012,** *28* (1), 474-485.

53. Yan, E. C. Y.; Liu, Y.; Eisenthal, K. B., New method for determination of surface potential of microscopic particles by second harmonic generation. *Journal of Physical Chemistry B* **1998,** *102* (33), 6331-6336.

54. El-Gholabzouri, O.; Cabrerizo, M. A.; Hidalgo-Alvarez, R., The surface charge density influence on the electrokinetic properties of model colloids: Solvent composition effect. *Journal of Colloid and Interface Science* **1999,** *214* (2), 243-250.

55. Tabata, Y.; Ikada, Y., Effect of the size and surface-charge of polymer microspheres on their phagocytosis by macrophage. *Biomaterials* **1988,** *9* (4), 356-362.

56. Brouwer, W. M.; Zsom, R. L. J., Polystyrene latex particle surface characteristics. *Colloids and Surfaces* **1987,** *24* (2-3), 195-208.

57. Luthi, Y.; Ricka, J.; Borkovec, M., Colloidal particles at water-glass interface: Deposition kinetics and surface heterogeneity. *Journal of Colloid and Interface Science* **1998,** *206* (1), 314-321.

58. Schrader, A. M.; Monroe, J. I.; Sheil, R.; Dobbs, H. A.; Keller, T. J.; Li, Y. X.; Jain, S.; Shell, M. S.; Israelachvili, J. N.; Han, S. G., Surface chemical heterogeneity modulates silica surface hydration. *PNAS* **2018,** *115* (12), 2890-2895.

59. Cras, J. J.; Rowe-Taitt, C. A.; Nivens, D. A.; Ligler, F. S., Comparison of chemical cleaning methods of glass in preparation for silanization. *Biosens Bioelectron* **1999,** *14* (8-9), 683-688.

60. Warszynski, P. a. A., Z, Calculations of Double-Layer Electrostatic Interactions for the Sphere/Plane Geometry. *J Colloid and Interface Sci* **1996,** *1878*, 283-295.

61. Pashley, R. M.; McGuiggan, P. M.; Ninham, B. W.; Evans, D. F., Attractive forces between uncharged hydrophobic surfaces - direct measurements in aqueous-solution. *Science* **1985,** *229* (4718), 1088-1089.

62. Rabinovich, Y. I.; Adler, J. J.; Ata, A.; Singh, R. K.; Moudgil, B. M., Adhesion between nanoscale rough surfaces - I. Role of asperity geometry. *Journal of Colloid and Interface Science* **2000,** *232* (1), 10-16.

63. Cooper, K.; Ohler, N.; Gupta, A.; Beaudoin, S., Analysis of contact interactions between a rough deformable colloid and a smooth substrate. *Journal of Colloid and Interface Science* **2000,** *222* (1), 63-74.

64. Cooper, K.; Gupta, A.; Beaudoin, S., Substrate morphology and particle adhesion in reacting systems. *Journal of Colloid and Interface Science* **2000,** *228* (2), 213-219.

65. Wu, L.; Feng, H.; Guo, D.; Zheng, B., Measuring the adhesion strength of a thin film to a substrate by centrifugation. *RSC Adv.* **2014,** *4* (104), 60002-60006.

66. Hamaker, H. C., The London - Van Der Waals attraction between spherical particles. *Physica* **1937,** *4*, 1058-1072.

67. Israelachvilli, J., Intermolecular & Surface Forces. **1985**.

68. Assemi, S.; Nalaskowski, J.; Johnson, W. P., Direct force measurements between carboxylate-modified latex microspheres and glass using atomic force microscopy. *Colloid Surf. A-Physicochem. Eng. Asp.* **2006,** *286* (1-3), 70-77.

69. Gregory, J., Approximate expressions for retarded vanderwaals interaction. *Journal of Colloid and Interface Science* **1981,** *83* (1), 138-145.

70. Bevan, M. A. a. P., D. C., Direct Measurement of Retarded van der Waals Attraction. *Langmuir* **1999,** *15*, 7925-7936.

71. Chen, C.; Liu, K. S.; Shang, J. Y., Effects of ionic strength, electrolyte type, pH, and flow rate on transport and retention of atmospheric deposition particles in saturated porous media. *Journal of Soils and Sediments* **2018,** *18* (3), 1066-1075.

72. Tsaur, S. L.; Fitch, R. M., Preparation and properties of polystyrene model colloids .1. Preparation of surface-active monomer and model colloids derived therefrom. *Journal of Colloid and Interface Science* **1987,** *115* (2), 450-462.

73. Lyklema, J.; Overbeek, J. T., On interpretation of electrokinetic potentials. *Journal of Colloid Science* **1961,** *16* (5), 501-&.

74. Rimsza, J. M.; Jones, R. E.; Criscenti, L. J., Interaction of NaOH solutions with silica surfaces. *Journal of Colloid and Interface Science* **2018,** *516*, 128-137.

75. Elassy, K. S.; Rahman, M. A.; Yama, N. S.; Shiroma, W. A.; Ohta, A. T., Complex Permittivity of NaOH Solutions Used in Liquid-Metal Circuits. *IEEE Access* **2019,** *7*, 150150-150156.

76. Gu, Y. G.; Li, D. Q., The zeta-potential of glass surface in contact with aqueous solutions. *Journal of Colloid and Interface Science* **2000,** *226* (2), 328-339.

77. Kirby, B. J.; Hasselbrink, E. F., Zeta potential of microfluidic substrates: 1. Theory, experimental techniques, and effects on separations. *Electrophoresis* **2004,** *25* (2), 187-202.

78. Erickson, D.; Li, D. Q.; Werner, C., An improved method of determining the zeta-potential and surface conductance. *Journal of Colloid and Interface Science* **2000,** *232* (1), 186-197.

79. Rabinovich, Y. I.; Adler, J. J.; Ata, A.; Singh, R. K.; Moudgil, B. M., Adhesion between nanoscale rough surfaces - II. Measurement and comparison with theory. *Journal of Colloid and Interface Science* **2000,** *232* (1), 17-24.

CHAPTER THREE

SPOC-LAMP: SALIVA POINT-OF-CARE LAMP DEVICE FOR DETECTION OF SARS-COV-2

Contribution of Authors and Co-Authors

Manuscript in Chapter 3

Author: Thomas B. LeFevre

Contributions: Planned and performed the experiments, analyzed the data, and wrote the manuscript.

Co-Author: Isaak J. Thornton

Contributions: Planned and performed the experiments and analyzed the data.

Co-Author: Dimitri A. Bikos

Contributions: Planned and performed the experiments and analyzed the data.

Co-Author: Perry Ellis

Contributions: Planned and performed the experiments.

Co-Author: Connie B. Chang

Contributions: Secured funding.

Co-Author: Michael R. Pavia

Contributions: Planned the experiments.

Co-Author: David A. Weitz

Contributions: Planned the experiments, analyzed the data, and secured funding.

Co-Author: James N. Wilking

Contributions: Planned and oversaw the experiments, analyzed the data, secured funding, and wrote the manuscript.

Manuscript Information

Thomas B. LeFevre, Isaak J. Thornton, Dimitri A. Bikos, Perry Ellis, Connie B. Chang, Michael R. Pavia, David A. Weitz, and James N. Wilking,

Analyst

Status of Manuscript:
_X_ Prepared for submission to a peer-reviewed journal
___ Officially submitted to a peer-reviewed journal
___ Accepted by a peer-reviewed journal
___ Published in a peer-reviewed journal

DOI:

Royal Society of Chemistry

Abstract

Human microbial pathogens including viruses, bacteria, and fungi pose a profound threat to human health, as evidenced by the SARS-CoV-2 global pandemic. To limit the spread of infectious disease, frequent, widespread diagnostic testing is critical. Specifically, there is a need for low-cost, accurate point-of-care (POC) molecular assays. Isothermal amplification methods offer a potential solution, and molecular-based POC tests offer tremendous potential for rapid, accurate POC testing, but to keep reagent costs low, methods for aliquoting exact volumes of specimen sample onto the assay device are needed. Here, we describe a low-cost, hand-held, manually operated device for rapid POC pathogen detection. The device includes a two-pronged fork geometry which enables transfer of small volumes of saliva from flocked collection swabs and contains all reagents needed for isothermal nucleic acid amplification and fluorescence detection. We describe the design and operation of the device and demonstrate use of the device for isothermal nucleic acid amplification and fluorescence detection using loop-mediated isothermal amplification of the SARS-CoV-2 virus in saliva.

Introduction

Human microbial pathogens pose a profound threat to human health, as evidenced by the SARS-CoV-2 global pandemic[1]. To limit the spread of infectious disease, control measures like handwashing, respiratory masks, social distancing, contact tracing, and vaccination have been shown to be highly effective. Another critical control measure is diagnostic testing[2]. Frequent, widespread testing for infection has been shown to mitigate pathogen spread; yet, diagnostic tests for human microbial pathogen infections remain underdeveloped.

Diagnostic tests can be classified in several different ways. One defining attribute is the location where the test is performed. Laboratory-based tests[3-6] are performed in a laboratory separate from the sample collection site, whereas point-of-care[7-14] (POC) tests are performed directly at the collection site. Laboratory-based tests are generally more accurate and sensitive than POC tests, but more costly and time-intensive. Another defining attribute is the choice of infection marker. Molecular[15-18] tests detect pathogen genomic material, whereas antigen[19-22] tests detect the presence of pathogen proteins. Molecular tests are generally more accurate than antigen tests, but require genomic amplification, and thus are more costly and time intensive to perform.

Benchmark molecular diagnostic tests are based on the polymerase chain reaction (PCR)[23-27]. While these molecular tests have traditionally been laboratory based[28-31], a number of POC PCR-based tests have recently been developed[32-34]. Yet, these POC tests still require temperature cycling to amplify pathogen genomic material. A promising alternative is isothermal amplification[35-38], which achieves amplification at a constant temperature and does not require thermocycling equipment, allowing them to be performed with minimal training in a POC environment. These isothermal, molecular-based POC tests offer tremendous potential for rapid,

accurate POC testing. However, the cost of each assay remains high, largely because of the cost of isothermal amplification enzymes. To minimize the cost of POC isothermal molecular assays, methods for aliquoting exact volumes of specimen samples onto the assay device are required. Without this, the cost of POC assays will limit frequent, widespread diagnostic testing.

Here, we describe a low-cost, hand-held, manually operated device for rapid point-of-care pathogen detection. The device includes a two-pronged fork geometry which enables transfer of small volumes of saliva from flocked collection swabs and contains all reagents needed for isothermal nucleic acid amplification and fluorescence detection. We describe the design and operation of the device, including a geometry for optimal transfer of saliva from a sample collection swab to device, a one-step actuation that requires minimal forces and provides tactile user feedback. Finally, we demonstrate use of the device for isothermal nucleic acid amplification and fluorescence detection using loop-mediated isothermal amplification of the SARS-CoV-2 virus in saliva.

Results & Discussion

The device consists of two main portions, an upper syringe-type portion, and a microcentrifuge tube, as illustrated in **Fig. 3.1A**. The syringe-type portion contains a plunger and a liquid-filled blister pack adhered to the inside floor of the syringe cylinder. Before device actuation, the plunger is positioned inside the syringe cylinder in a raised position (**Fig. 3.1B**, left). Depression of the plunger compresses the blister and presses the foil-sealed underside of the blister against spikes (**Fig. 3.1B**, middle). This action pierces the foil, driving liquid into the tube beneath. Liquid expelled from the blister carries the saliva sample with it and mixes with lyophilized

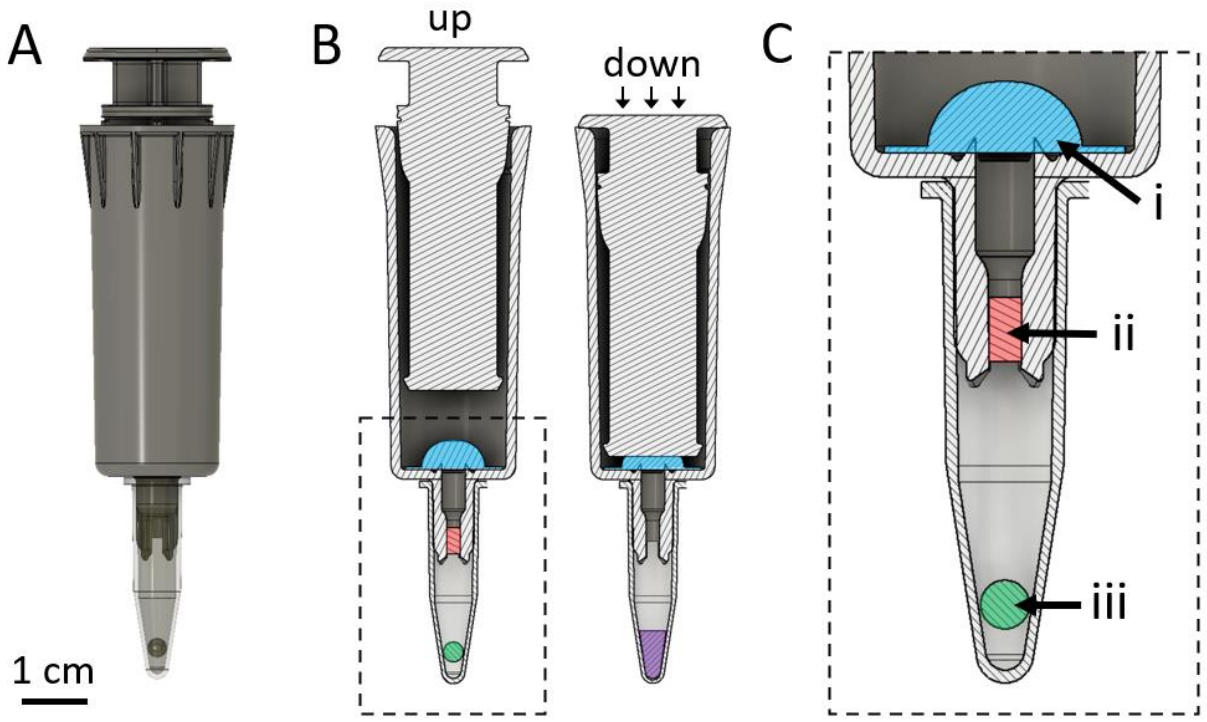


Figure 3.1: *Device overview*. (**A**) Illustration of assembled device consisting of an upper syringe-type portion and lower microcentrifuge tube. (**B**) Cross-sectional view of device with plunger in the "up" and "down" positions. Pressing the plunger compresses and ruptures the blister (blue), driving liquid and saliva (pink) into the tube with the lyophilized reagent (green), resulting in a mixture (purple). Region enclosed by dashed line is expanded view of the lower portion of device: (i) liquid filled blister, (ii) saliva sample and (iii) lyophilized reagents.

reagent. An expanded view of the lower portion of the device highlights the blister pack, spikes, and sample fork features (**Fig. 3.1B**, dashed line).

To conduct the assay, three components are required: the syringe-type device containing a liquid-filled blister pack with the plunger in the "up" position, a flocked specimen swab, and a microcentrifuge tube (**Fig. 3.2A**). The tube contains lyophilized reagent and is sealed with a laminate foil seal to protect the lyophilized reagent. Test operation steps are as follows. First, to collect saliva, the swab is removed from its packaging and the flocked end of the swab placed in the mouth for 10-20 s (**Fig. 3.2B**). To transfer saliva from the swab to device, the swab is then

drawn through the forks of the device (**Fig. 3.2C**). The foil-sealed microcentrifuge tube is then pressed onto the forks with the beveled fork points piercing the foil until the rim of the tube fits snugly over the base of the forks (**Fig. 3.2D**). Finally, the device is gripped in one hand and the

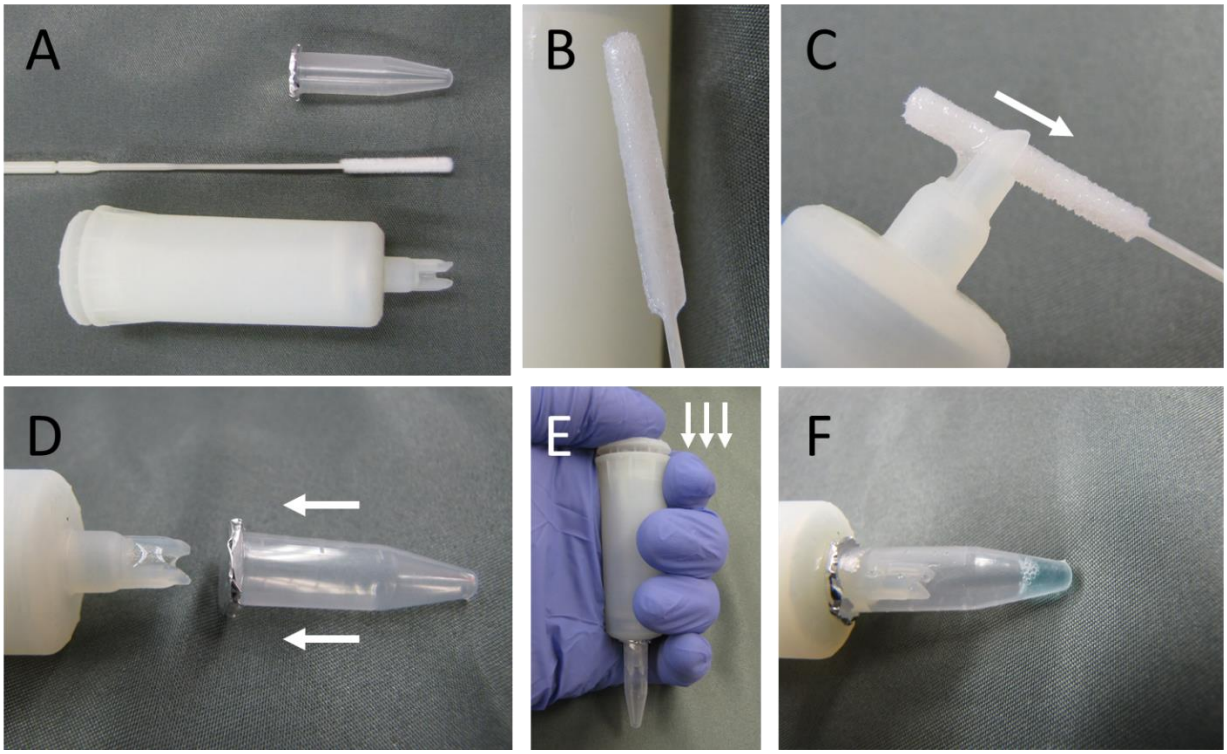


Figure 3.2: *Device operation*. (**A**) Components of the test include syringe-type device, flocked specimen swab, and vial. Lyophilized reagent in vial not shown. (**B**) Saliva is collected by soaking the swab in the mouth for 10 – 20 s. (**C**) Saliva is then transferred to the device by drawing the swab through device forks. (**D**) The tube is attached to the device by pushing the forks through the foil seal. (**E**) The plunger is depressed to express blister contents through the forks into the vial. (**F**) Saliva, blister contents, and lyophilized reagents are now combined at the bottom of the tube. Blue dye is included for visualization.

plunger depressed by thumb until the plunger top is fully seated in the device tube (**Fig. 3.2E**). Saliva, blister contents, and lyophilized reagents are now combined at the bottom of the vial (**Fig. 3.2F**).

A critical feature of the device are the device forks, which enable small volumes of saliva to be transferred from the collection swab to the device. The forks are composed of two prongs separated by a gap distance *d* as illustrated in **Fig. 3.3A**. As a swab is drawn between the forks, a combination of surface wetting, swab fiber compression, and gravity draws saliva from the swab to the device and the trough beneath, as shown by the series of high-speed images in **Fig. 3.3B**. To determine an ideal *d*, we measure the saliva transfer volume V_F from a flocked swab with a flock tip outer diameter d_{swab} from devices over the range 1.3 mm $\leq d \leq$ 2.3 mm. The data does not show a strong correlation between *d* and V_F. The experiments resulted in an average V_F of approximately 13 – 20 uL. However, there was an apparent optimal *d* based on usability. We chose *d* = 1.7 mm. At *d* < 1.7 mm, it became difficult to draw the swab through the forks, which is undesirable from a user standpoint and resulted in greater variance in V_F. At *d* > 1.7 mm, it was more difficult to tell if the swab drag had been done correctly because there was less frictional tactile feedback as the swab was drawn through the forks, and anecdotally it seemed that a low volume swab with V_S < 60 µL had a higher risk of depositing a very low trace amount of saliva when *d* was significantly above 1.7 mm. That being said, it was also clear that other *d* would have likely worked but *d* = 1.7 mm seemed to be a reasonable choice. Primarily, we didn't want to risk getting zero saliva and that risk seemed greater at higher *d*.

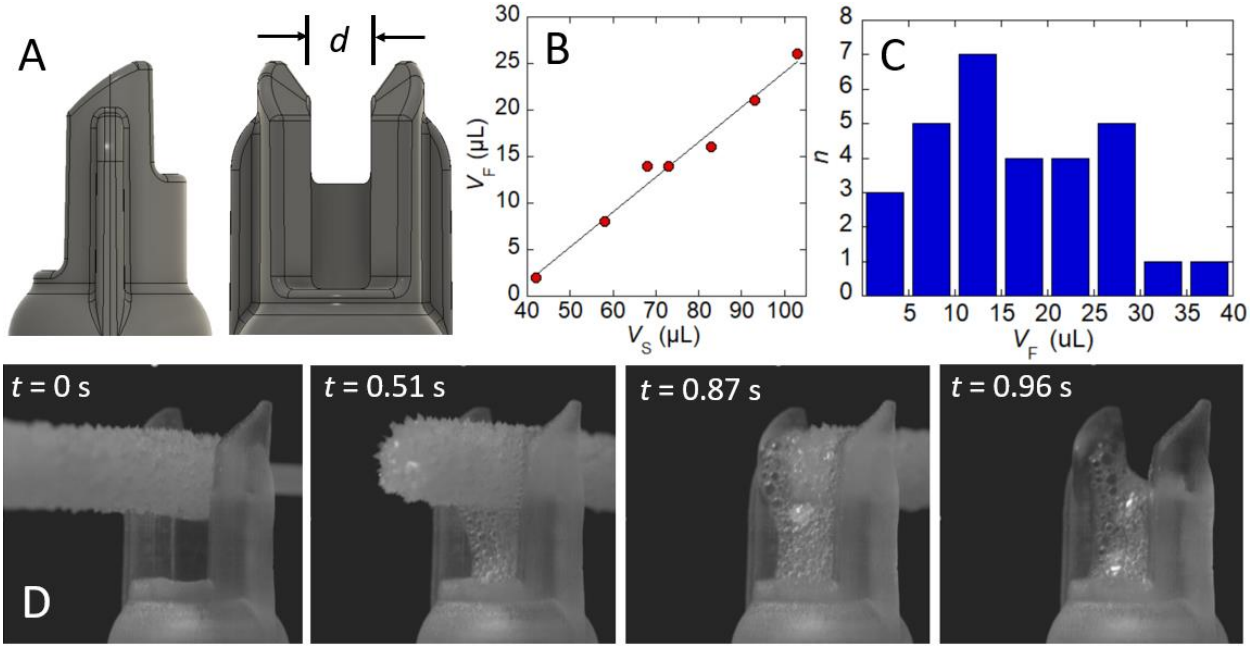


Figure 3.3: *Saliva transfer from swab to device*. (**A**) Geometry of device forks. Forks beveled to pierce tube foil seal. (**B**) Saliva volume transferred between device forks V_F plotted as a function of saliva volume in swab V_S. Line is linear fit. (**C**) Histogram of V_F for multiple individuals. (**D**) Time-lapse image series of saliva transfer process captured at 3000 fps.

We find that V_F is proportional to the volume of saliva contained in the collection swab V_S, as shown by the plot in **Fig. 3.3C**. To get a measure of the variability in V_F between individuals, we recruit ten individuals to collect and transfer their own saliva from swab to device (n = 3 each). Plotting the data, we find a distribution in V_F with a peak near 10-15 µL (**Fig. 3.3D**) with an average of 16.3 µL. This volume of saliva is sufficient to detect low pathogen counts while keeping reagent costs low.

For most molecular diagnostic assays, delivery of exact volumes of aqueous media to the reaction tube is critical. To accomplish this, we design the plunger to translate by a well-defined

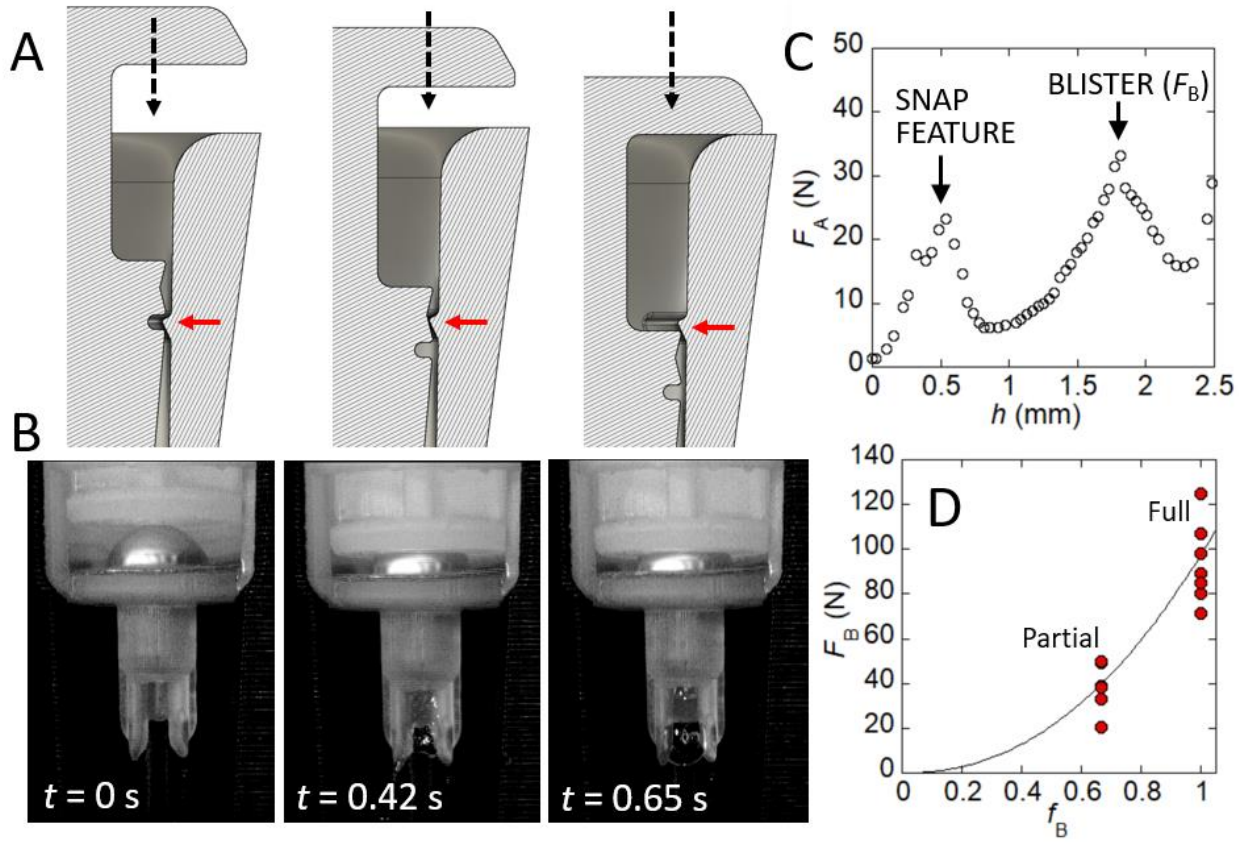


Figure 3.4: *Blister compression forces and dynamics.* (**A**) Series of illustrations depicting position of snap features inside plunger and syringe tube during depression of plunger. Red arrows indicate position of internal snap ring. (**B**) Series of high-speed images depict plunger depression, blister compression, and expulsion of blister liquid. (**C**) Representative measurement of force required to depress the syringe plunger, F_A as a function of plunger displacement, h. (**D**) Force required to compress a 130 µL blister in the device, F_B plotted as a function of blister compression fraction, f_B. Curve is a fit to $F_B = 97.549 f_B^{2.2092}$.

distance and compress the blister by an exact amount. The initial position of the plunger is held in place by a positive snap ring in the syringe which seats within a negative feature in the plunger (**Fig. 3.4A**). The mirror symmetry of the negative feature also resists removal of the plunger from the tube. The final position of the plunger is set by contact between the underside of the plunger rim and the top rim of the syringe tube (**Fig. 3.4A**). Compression of the blister and the corresponding expulsion of liquid is shown in the series of images in **Fig. 3.4B**. Actuation of the

device is easily achieved by grasping the device in a single hand and depressing the plunger by thumb. Actuation is accompanied by a tactile snap, which provides the user feedback of successful actuation.

Useability studies recommend that hand-actuated devices require less than xx N to actuate. The force required to complete the compression of a blister within our device is F_b = 39.8 N ± 10.9 N. Partial compression of the blister requires significantly less force than full compression; thus, we design the device such that plunger actuation does not fully compress the blister. To measure the force profile required to actuate the device, we perform blister device actuation measurements using a normal force transducer. We observe two peaks in the force profile. The first peak in the normal force corresponds to displacement of the negative feature in the plunger from the positive snap feature. Following this peak, the normal force drops but then increases again as the plunger begins to compress the blister (**Fig 3.4C**). We define this second, larger peak as the maximum force required to actuate the blister F_b. Device actuation during these measurements is performed with a fixed plunger translation velocity, v = 0.1 – 0.5 mm/s. By contrast, manual actuation is accomplished in a less controlled manner and at a significantly higher velocity. So, while this does not directly characterize the forces required when the plunger is actuated manually by hand because the rate of actuation is slower with a rheometer, it does provide some measure of the profile of resistance that the plunger is overcoming. That is because this force results in an acceleration of both the plunger and the user's thumb that results in enough kinetic energy to help compress the blister dome without requiring additional effort from the user. We want the user to continue pressing on the plunger until it bottoms out, but not to have to exert extra force after the initial "snap" as the plunger disc moves past the snap ring of the syringe.

We plot the distribution of F_B as a function of blister compression distance given our chosen partial compression compared to full compression of a blister (**Fig. 3.4E**). There is a squared relationship between blister compression distance (normalized by the blister height) and the force required to actuate the blister, which indicates that a partial compression is much easier for the user that a full compression. Since the blister is being pierced in both cases, we assume the greater force in the full compression is coming from the structural element of the blister dome and thus would be present even if the blister were not completely filled with water (as was observed anecdotally with half-filled blisters).

We test our device using a common RT-LAMP formulation to show that it successfully captures the accurate amount of saliva, punctures the water-filled blister, delivers the water and saliva to the vial, and adequately mixes the water, saliva, and lyophilized reagents in the vial. Then we place the device in a dry bath vial heater at 65° C for 30 minutes. We use saliva that has been spiked with synthetic viral RNA. We lyophilize the LAMP reagents in individual PCR vials using a lyophilizer. The sample that did not have viral RNA does not show an increased fluorescence (**Fig. 3.5 i**) whereas the sample spiked with viral RNA exhibits increased fluorescence (**Fig. 3.5 ii**).

Conclusion

Here, we describe a low-cost, hand-held, manually operated device for point-of-care molecular pathogen detection. The device includes a two-pronged fork geometry which enables metering and transfer of small volumes of saliva from flocked collection swabs and contains all reagents needed for isothermal nucleic acid amplification and fluorescence detection. The simple,

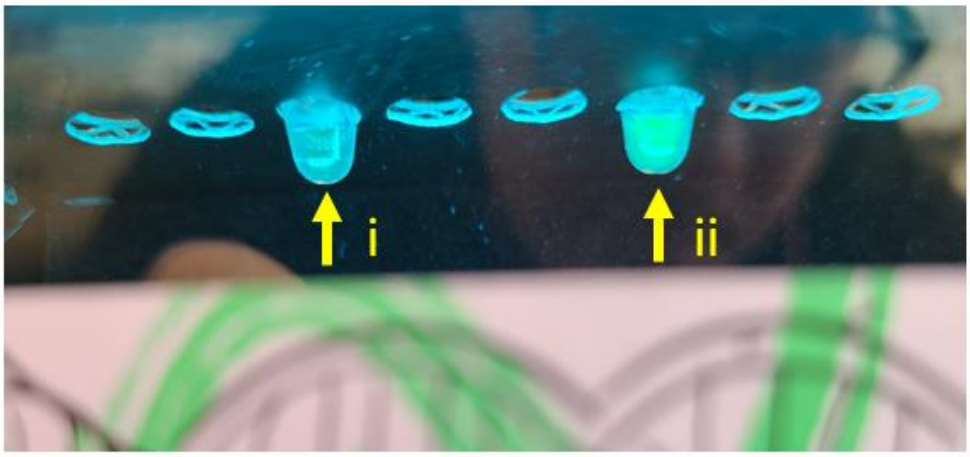


Figure 3.5: *Device validation*. The sample with no viral RNA present (i) exhibits less fluorescence intensity than the sample with viral RNA present (ii). Both samples were heating at 65° C for 30 minutes. The injection moldable design facilitates easy scale-up and is designed to work with swabs and vials that already exist on the market. The test requires only a simple, inexpensive processing system that allows the test to be set up in a variety of institutions at low cost.

Methods

Fabrication

Devices were fabricated using a Formlabs 3D printer (Form 2) and Formlabs resin (Durable). Durable resin was chosen for its mechanical properties, which are similar to polypropylene, a polymer commonly used for injection molded diagnostic devices. Devices were cured in a Formlabs curing station (Form Cure) for 2 h following fabrication to ensure that the internal spike features were rigid enough to pierce the underside of the blister. Other materials included capless polypropylene microcentrifuge tubes (Sarstedt, 0.5 mL, 72.698.200), diagnostic reagent blisters (J-Pac Medical, 135 uL), and PCR sealing film (Southern Labware, P1001-Q). Lyobeads were produced by Evik Diagnostics.

Assay Formulation

For each reaction vial, the following LAMP formulation components were freeze dried using a commercial freeze-drier (Millrock LD85). Warm Start 2x Master Mix (12 uL, NEB), dUTP (0.175 uL), UDG (0.5 uL), SYTO 82 (0.5 uL, 25 uM solution; Invitrogen SYTO-9 Green Fluorescent Nucleic Acid Stain, cat no. S34854), nuclease free water (4.325 uL, NEB), 10x primers (2.5 uL), SARS-CoV-2 E-gene (10^5 c/uL, 2 uL).

Force Measurements

Partial blister compression measurements were performed using the normal force transducer on a mechanical rheometer (TA Instruments, AR-G2). The device was held vertically upright in a 3D printed holder which was centered on the lower plate of the rheometer. The normal force transducer was tared, and the upper plate of the rheometer lowered to contact the top of the plunger. To actuate the device and compress the blister, the upper plate was lowered 2.8 mm at a rate between 100 µm/s and 500 µm/s. Full blister compression measurements were performed on an electronic scale (brand and model here). The device was held vertically upright in a 3D printed holder A 3D printed holder was used to hold the device vertically, which was centered on the scale. The scale was tared and the device actuated manually by hand. The force required to actuate the device was read by eye.

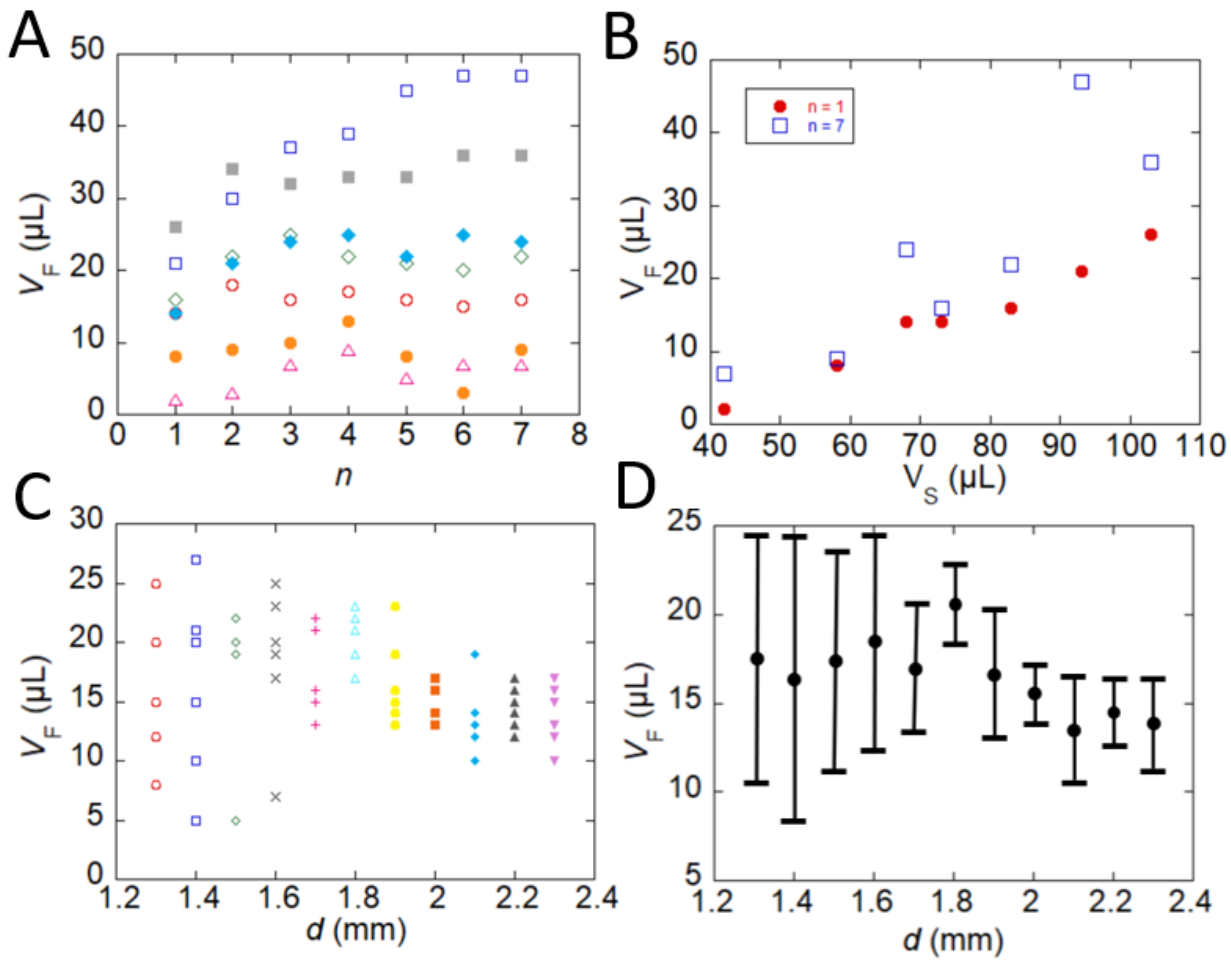
Design Considerations

General considerations The asymmetric fork geometry with a “trough” for saliva collection was designed to avoid trapping and compressing air in the channel between saliva and the blister pack. This design allows for consistent collection of saliva volumes (10-20 µl).

Injection molding considerations Wall thickness was kept as uniform as possible throughout the device to achieve proper plastic flow and packing during injection molding. Corners were rounded to standards[39] for injection molding for polypropylene, about 0.5 to 1.5 times the adjacent wall thickness. Snap features in the plunger and tube were designed with mold construction and device demolding in mind. Pinch points in the design that could restrict plastic flow were avoided.

Ease-of-use considerations The device was designed for the average adult hand. The average adult hand width[40] is 8.4 cm and the syringe portion of the device is 5.3 cm tall, which we found to be easily graspable by the average adult hand. The device was also designed so that plunger actuation can easily be performed by hand and provides tactile feedback. The average adult can easily exert 20-45 N using their thumb, which we achieved by designing partial compression of the blister. Snap features were added to provide tactile feedback to the user. The user does not experience two noticeable force maxima (**Fig. 3.4D**), but only feels the initial click of the snap features as the plunger moves past the snap ring in the tube. This is because the force required to overcome the first force peak is significant enough that the resulting momentum punctures and compresses the blister without any additional noticeable force. The minimum sample and blister liquid volumes were chosen based on the amount of total liquid visible to the user after expression from the blister. This provides additional confirmation to the user that the device has been successfully actuated. Additionally, we considered the minimum saliva volume that could be repeatably transferred from the swab to device; too little saliva could result in a false negative.

Supplementary Information



Supplementary Figure 3.1: Saliva collection volume data. We test the transfer of saliva from a loaded swab to the device forks. A) We test how the saliva transfer volume V_F is affected by the number of times n we drag the swab through the forks, using different initial saliva loading volumes. Open pink triangles 42 µL, closed orange circles = 58 µL, open red circles = 68 µL, closed blue diamonds = 73 µL, open green diamonds 83 = µL, open blue squares 93 = µL, closed gray squares = 103 µL. B) We plot the amount of saliva transferred based on the initial swab loading volume V_S. We show this data for two different drag numbers, n = 1 and n = 7. The plot shows there is not a noticeable improvement in performance when a higher n is used. C) We show effect of fork inner diameter d on the amount of saliva V_F transferred to the forks. D) We show the same data from (C) but showing the average and standard deviation.

Funding

This work was supported by ULTSafety, Inc.

References cited

1. Munster, V. J.; Koopmans, M.; van Doremalen, N.; van Riel, D.; de Wit, E., A novel coronavirus emerging in China — Key questions for impact assessment. *New England Journal of Medicine* **2020,** *382* (8), 692-694.

2. Mina, M. J.; Andersen, K. G., COVID-19 testing: One size does not fit all. **2021,** *371* (6525), 126-127.

3. Jain, K. K., Nanotechnology in clinical laboratory diagnostics. *Clin Chim Acta* **2005,** *358* (1-2), 37-54.

4. Janda, J. M.; Abbott, S. L., 16S rRNA gene sequencing for bacterial identification in the diagnostic laboratory: Pluses, perils, and pitfalls. *Journal of Clinical Microbiology* **2007,** *45* (9), 2761-2764.

5. Gao, Y.; Li, T.; Han, M.; Li, X.; Wu, D.; Xu, Y.; Zhu, Y.; Liu, Y.; Wang, X.; Wang, L., Diagnostic utility of clinical laboratory data determinations for patients with the severe COVID-19. *Journal of Medical Virology* **2020,** *92* (7), 791-796.

6. Chiappin, S.; Antonelli, G.; Gatti, R.; De Palo, E. F., Saliva specimen: A new laboratory tool for diagnostic and basic investigation. *Clin Chim Acta* **2007,** *383* (1-2), 30-40.

7. Yager, P.; Domingo, G. J.; Gerdes, J., Point-of-care diagnostics for global health. *Annual Review of Biomedical Engineering* **2008,** *10*, 107-144.

8. Hu, J.; Wang, S.; Wang, L.; Li, F.; Pingguan-Murphy, B.; Lu, T. J.; Xu, F., Advances in paper-based point-of-care diagnostics. *Biosens Bioelectron* **2014,** *54*, 585-597.

9. Gubala, V.; Harris, L. F.; Ricco, A. J.; Tan, M. X.; Williams, D. E., Point of Care Diagnostics: Status and Future. *Analytical Chemistry* **2012,** *84* (2), 487-515.

10. Craw, P.; Balachandran, W., Isothermal nucleic acid amplification technologies for point-of-care diagnostics: a critical review. *Lab on a Chip* **2012,** *12* (14), 2469-2486.

11. Chin, C. D.; Linder, V.; Sia, S. K., Commercialization of microfluidic point-of-care diagnostic devices. *Lab on a Chip* **2012,** *12* (12), 2118-2134.

12. Ahn, C. H.; Choi, J. W.; Beaucage, G.; Nevin, J. H.; Lee, J. B.; Puntambekar, A.; Lee, J. Y., Disposable Smart lab on a chip for point-of-care clinical diagnostics. *Proceedings of the Ieee* **2004,** *92* (1), 154-173.

13. Yetisen, A. K.; Akram, M. S.; Lowe, C. R., Paper-based microfluidic point-of-care diagnostic devices. *Lab on a Chip* **2013,** *13* (12), 2210-2251.

14. Wang, J., Electrochemical biosensors: Towards point-of-care cancer diagnostics. *Biosens Bioelectron* **2006,** *21* (10), 1887-1892.

15. Yang, S.; Rothman, R. E., PCR-based diagnostics for infectious diseases: uses, limitations, and future applications in acute-care settings. *Lancet Infectious Diseases* **2004,** *4* (6), 337-348.

16. Reed, G. H.; Kent, J. O.; Wittwer, C. T., High-resolution DNA melting analysis for simple and efficient molecular diagnostics. *Pharmacogenomics* **2007,** *8* (6), 597-608.

17. Huggett, J. F.; Cowen, S.; Foy, C. A., Considerations for Digital PCR as an Accurate Molecular Diagnostic Tool. *Clinical Chemistry* **2015,** *61* (1), 79-88.

18. Elnifro, E. M.; Ashshi, A. M.; Cooper, R. J.; Klapper, P. E., Multiplex PCR: Optimization and application in diagnostic virology. *Clin Microbiol Rev* **2000,** *13* (4), 559-+.

19. Porte, L.; Legarraga, P.; Vollrath, V.; Aguilera, X.; Munita, J. M.; Araos, R.; Pizarro, G.; Vial, P.; Iruretagoyena, M.; Dittrich, S.; Weitzel, T., Evaluation of a novel antigen-based rapid detection test for the diagnosis of SARS-CoV-2 in respiratory samples. *International Journal of Infectious Diseases* **2020,** *99*, 328-333.

20. Mak, G. C. K.; Cheng, P. K. C.; Lau, S. S. Y.; Wong, K. K. Y.; Lau, C. S.; Lam, E. T. K.; Chan, R. C. W.; Tsang, D. N. C., Evaluation of rapid antigen test for detection of SARS-CoV-2 virus. *Journal of Clinical Virology* **2020,** *129*.

21. Hirotsu, Y.; Maejima, M.; Shibusawa, M.; Nagakubo, Y.; Hosaka, K.; Amemiya, K.; Sueki, H.; Hayakawa, M.; Mochizuki, H.; Tsutsui, T.; Kakizaki, Y.; Miyashita, Y.; Yagi, S.; Kojima, S.; Omata, M., Comparison of automated SARS-CoV-2 antigen test for COVID-19 infection with quantitative RT-PCR using 313 nasopharyngeal swabs, including from seven serially followed patients. *International Journal of Infectious Diseases* **2020,** *99*, 397-402.

22. Dinnes, J.; Deeks, J. J.; Adriano, A.; Berhane, S.; Davenport, C.; Dittrich, S.; Emperador, D.; Takwoingi, Y.; Cunningham, J.; Beese, S.; Dretzke, J.; di Ruffano, L. F.; Harris, I. M.; Price, M. J.; Taylor-Phillips, S.; Hooft, L.; Leeflang, M. M. G.; Spijker, R.; Van den Bruel, A.; Cochrane, C.-D. T. A., Rapid, point-of-care antigen and molecular-based tests for diagnosis of SARS-CoV-2 infection (Review). *Cochrane Database of Systematic Reviews* **2020,** (8).

23. Saiki, R. K.; Scharf, S.; Faloona, F.; Mullis, K. B.; Horn, G. T.; Erlich, H. A.; Arnheim, N., ENZYMATIC AMPLIFICATION OF BETA-GLOBIN GENOMIC SEQUENCES AND RESTRICTION SITE ANALYSIS FOR DIAGNOSIS OF SICKLE-CELL ANEMIA. *Science* **1985,** *230* (4732), 1350-1354.

24. Saiki, R. K.; Gelfand, D. H.; Stoffel, S.; Scharf, S. J.; Higuchi, R.; Horn, G. T.; Mullis, K. B.; Erlich, H. A., PRIMER-DIRECTED ENZYMATIC AMPLIFICATION OF DNA WITH A THERMOSTABLE DNA-POLYMERASE. *Science* **1988,** *239* (4839), 487-491.

25. Mullis, K. B.; Faloona, F. A., SPECIFIC SYNTHESIS OF DNA INVITRO VIA A POLYMERASE-CATALYZED CHAIN-REACTION. *Methods in Enzymology* **1987,** *155*, 335-350.

26. Mullis, K. B., THE UNUSUAL ORIGIN OF THE POLYMERASE CHAIN-REACTION. *Scientific American* **1990,** *262* (4), 56-&.

27. Mullis, K.; Faloona, F.; Scharf, S.; Saiki, R.; Horn, G.; Erlich, H., SPECIFIC ENZYMATIC AMPLIFICATION OF DNA INVITRO - THE POLYMERASE CHAIN-REACTION. *Cold Spring Harbor Symposia on Quantitative Biology* **1986,** *51*, 263-273.

28. Mackay, I. M., Real-time PCR in the microbiology laboratory. *Clinical Microbiology and Infection* **2004,** *10* (3), 190-212.

29. Johnston, S. P.; Pieniazek, N. J.; Xayavong, M. V.; Slemenda, S. B.; Wilkins, P. P.; da Silva, A. J., PCR as a confirmatory technique for laboratory diagnosis of malaria. *Journal of Clinical Microbiology* **2006,** *44* (3), 1087-1089.

30. Geha, D. J.; Uhl, J. R.; Gustaferro, C. A.; Persing, D. H., MULTIPLEX PCR FOR IDENTIFICATION OF METHICILLIN-RESISTANT STAPHYLOCOCCI IN THE CLINICAL LABORATORY. *Journal of Clinical Microbiology* **1994,** *32* (7), 1768-1772.

31. Espy, M. J.; Uhl, J. R.; Sloan, L. M.; Buckwalter, S. P.; Jones, M. F.; Vetter, E. A.; Yao, J. D. C.; Wengenack, N. L.; Rosenblatt, J. E.; Cockerill, F. R.; Smith, T. F., Real-time PCR in clinical microbiology: Applications for a routine laboratory testing. *Clin Microbiol Rev* **2006,** *19* (1), 165-+.

32. Petralia, S.; Conoci, S., PCR Technologies for Point of Care Testing: Progress and Perspectives. *Acs Sensors* **2017,** *2* (7), 876-891.

33. Park, S.; Zhang, Y.; Lin, S.; Wang, T.-H.; Yang, S., Advances in microfluidic PCR for point-of-care infectious disease diagnostics. *Biotechnol Adv* **2011,** *29* (6), 830-839.

34. Lee, S. H.; Kim, S.-W.; Kang, J. Y.; Ahn, C. H., A polymer lab-on-a-chip for reverse transcription (RT)-PCR based point-of-care clinical diagnostics. *Lab on a Chip* **2008,** *8* (12), 2121-2127.

35. Tomita, N.; Mori, Y.; Kanda, H.; Notomi, T., Loop-mediated isothermal amplification (LAMP) of gene sequences and simple visual detection of products. *Nature Protocols* **2008,** *3* (5), 877-882.

36. Notomi, T.; Okayama, H.; Masubuchi, H.; Yonekawa, T.; Watanabe, K.; Amino, N.; Hase, T., Loop-mediated isothermal amplification of DNA. *Nucleic Acids Research* **2000,** *28* (12).

37. Nagamine, K.; Hase, T.; Notomi, T., Accelerated reaction by loop-mediated isothermal amplification using loop primers. *Molecular and Cellular Probes* **2002,** *16* (3), 223-229.

38. Mori, Y.; Nagamine, K.; Tomita, N.; Notomi, T., Detection of loop-mediated isothermal amplification reaction by turbidity derived from magnesium pyrophosphate formation. *Biochemical and Biophysical Research Communications* **2001,** *289* (1), 150-154.

39. Cutting Corners on Injection-Molded Parts. https://www.protolabs.com/resources/design-tips/cutting-corners-on-injection-molded-parts/.

40. What's the Average Hand Size for Men, Women, and Children? https://www.healthline.com/health/average-hand-size#adults.

CHAPTER FOUR

COUPLING FLUID FLOW TO HYDROGEL FLUIDIC DEVICES WITH REVERSIBLE "POP-IT" CONNECTIONS

Contribution of Authors and Co-Authors

Manuscript in Chapter 4

Author: Reha Abbasi

Contributions: Planned and performed the experiments, analyzed the data, and wrote the manuscript.

Author: Thomas B. LeFevre

Contributions: Performed the experiments, analyzed the data, and wrote the manuscript.

Co-Author: Aaron D. Benjamin

Contributions: Performed the experiments.

Co-Author: Isaak J. Thornton

Contributions: Performed the experiments, analyzed the data, and wrote the manuscript.

Co-Author: James N. Wilking

Contributions: Planned and oversaw the experiments, analyzed the data, and wrote the manuscript.

Manuscript Information

Reha Abbasi, Thomas B. LeFevre, Aaron D. Benjamin, Isaak J. Thornton, and James N. Wilking

Lab on a Chip

Status of Manuscript:
___ Prepared for submission to a peer-reviewed journal
___ Officially submitted to a peer-reviewed journal
___ Accepted by a peer-reviewed journal
_X_ Published in a peer-reviewed journal

DOI: 10.1039/D1LC00135C

Royal Society of Chemistry

Abstract

Hydrogels are soft, water-based polymer gels that are increasingly used to fabricate free-standing fluidic devices for tissue and biological engineering applications. In many of these applications, pressurized liquid must be driven through the hydrogel device. To couple pressurized liquid to a hydrogel device, a common approach is to insert tubing into a hole in the gel; however, this usually results in leakage and expulsion of the tubing, and other options for coupling pressurized liquid to hydrogels remain limited. Here, we describe a simple coupling approach where microfluidic tubing is inserted into a plastic, 3D-printed bulb-shaped connector, which "pops" into a 3D-printed socket in the gel. By systematically varying the dimensions of the connector relative to those of the socket entrance, we find an optimal head-socket ratio that provides maximum resistance to leakage and expulsion. The resulting connection can withstand liquid pressures on the order of several kilopascals, three orders of magnitude greater than traditional, connector-free approaches. We also show that two-sided connectors can be used to link multiple hydrogels to one another to build complex, reconfigurable hydrogel systems from modular components. We demonstrate the potential usefulness of these connectors by established long-term nutrient flow through a 3D-printed hydrogel device containing bacteria. The simple coupling approach outlined here will enable a variety of applications in hydrogel fluidics.

Introduction

Hydrogels are soft, water-based polymer gels[41-44] with widespread applications in medicine[45, 46] and bioengineering.[47, 48] While hydrogels have long been incorporated into fluidic devices[49, 50], the development of stand-alone hydrogel fluidic devices and other hydrogel fluidic elements with complex three-dimensional structures has historically been limited. However, recent advances in rapid fabrication are now enabling the creation of hydrogel-based fluidic elements and free-standing devices with complex, high-resolution structures.[51-54] For example, hydrogel-based photoreactors,[55] bioreactors,[56] and a variety of engineered tissues with intricate structures[57-60] and microscale vasculature[51, 55, 56, 60-64] have been created. As rapid fabrication technologies continue to advance, the use of hydrogel-based fluidic devices are expected to expand.[65]

To drive liquid through a fluidic device, tubing containing liquid must be coupled to the device. For devices composed of hydrogel, this presents a challenge.[65] A common solution, used in soft polydimethylsiloxane (PDMS)-based microfluidics, is to simply insert microfluidic tubing into a hole in the device.[66, 67] In a PDMS device, static friction between the tubing and PDMS prevents the tubing from slipping out of the device and allows the formation of a robust, high-pressure seal.[68] However, when this approach is attempted with hydrogel devices, a thin layer of water on the surface of the gel lubricates the interaction between the gel and tubing and allows the tubing to slip out under relatively low pressure. Adhesives and barb-type connectors have been shown to provide stable, high-pressure seals,[69] but simple, reversible connector solutions are still needed, and the lack of such technologies limits the development of hydrogel-based fluidics.

Here, we describe a simple, reversible, plug-based connector designed to couple microfluidic tubing to a hydrogel-based fluidic device, to allow for pressurized liquid flow through

the system. The connection consists of a 3D-printed plastic plug inserted into a matching spherical socket in a 3D-printed hydrogel, which is then held in place by the elasticity of the gel. We call this a “pop-it” connector. The connection can easily be removed and reinserted, allows for rotation around the long axis of the connector, and can also be used to link individual hydrogel modules to one another to build complex, reconfigurable fluidic hydrogel systems. To characterize the connection, we systematically vary the diameter of the connector head relative to the diameter of the gel socket entrance, measure both the force required for insertion and the liquid pressure the resulting seal can withstand, and find the head-socket ratio that provides the maximum resistance to leakage and expulsion. To demonstrate the usefulness of these connectors, we use them to deliver nutrient broth to a 3D printed hydrogel containing bacteria for over a day. The simple and robust connector design should enable a variety of hydrogel fluidic applications.

Results & Discussion

To illustrate the standard approach for driving liquid into soft microfluidic devices, we create a cylindrical, mm-scale hole in a PDMS-based microfluidic device using a biopsy punch and insert plastic tubing into the hole (**Fig. 4.1a**). The outer diameter of the tubing (OD = 1.09 mm) is larger than the inner diameter of the hole (ID = 1.05 mm) and is held in place by static friction. This friction is enough to withstand the pressure needed to drive liquids through the device, which can approach $\Delta P \approx 10^3$ Pa.[70, 71]

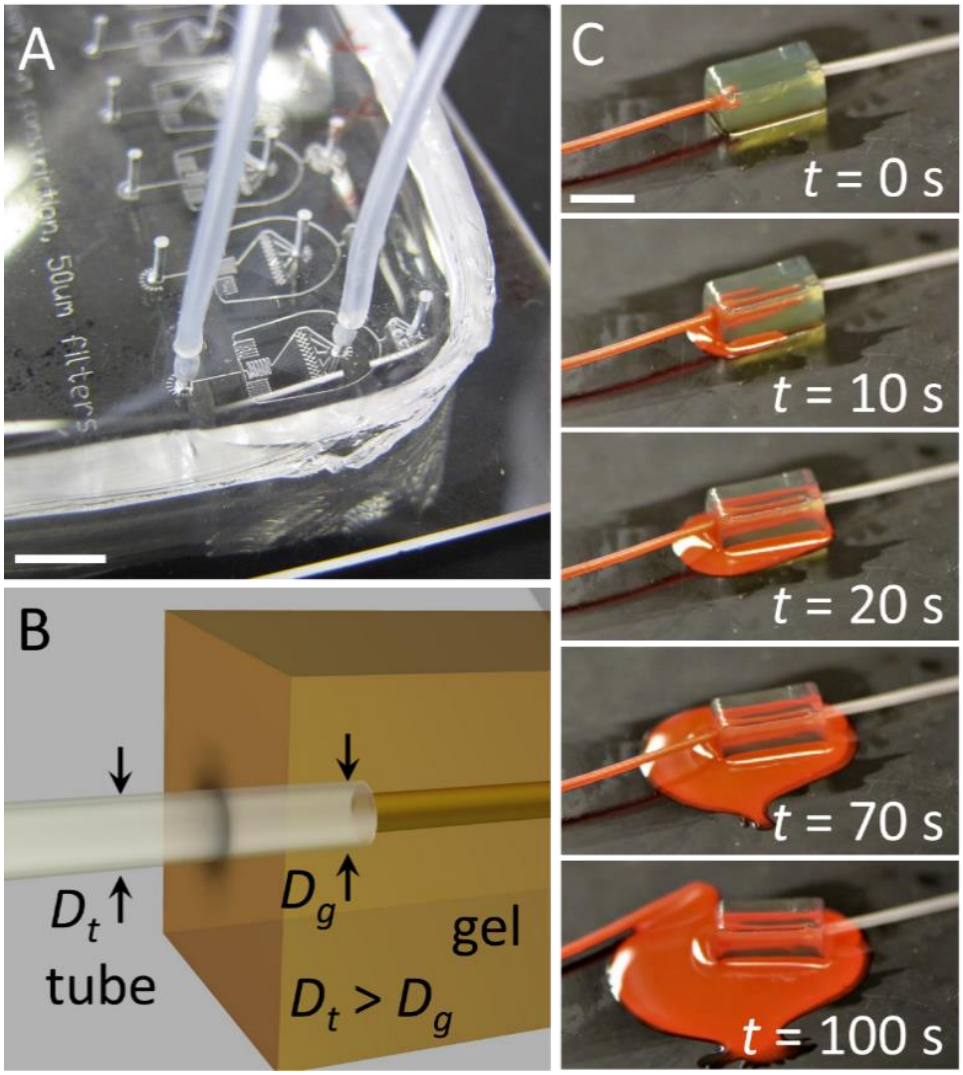


Figure 4.1. *Friction-based connections developed for traditional microfluidic devices fail when applied to hydrogels.* (**A**) Liquid is introduced into a soft microfluidic device by punching a hole in the PDMS and inserting larger diameter microfluidic tubing into the hole. Static friction prevents the tubing from being expelled even for liquid pressures as high as $\Delta P \approx 10^3$ Pa. When the same approach is applied to a 3D printed PEG-DA hydrogel, where (**B**) tubing is inserted into a smaller diameter hole in the surface of the gel to a depth of 3 mm, (**C**) the tubing is expelled from the hydrogel as liquid is forced into the gel at low pressure ($\Delta P \approx 1$ Pa). Scale bars in (A) and (C) correspond to 5 mm and 10 mm, respectively.

By contrast, when tubing is inserted into a hydrogel fluidic device, friction between the tubing and gel is insufficient to resist even very small pressures. To demonstrate this, we 3D print a cm-scale polyethylene glycol diacrylate (PEG-DA) hydrogel (10 w/w%) containing a single

straight channel of length, l = 12 mm and diameter, D = 0.8 mm and insert microfluidic tubing into the channel. The outer diameter of the tubing (OD = 1.32 mm) is larger than the inner diameter of the channel entrance (ID = 1.20 mm) corresponding to a gel strain of $\gamma \approx 0.1$, so the gel exerts a radial compressive stress on the tubing (**Fig. 4.1b**). When we drive water through the hydrogel using a syringe pump at a low flow rate (Q = 200 μL/min), we observe that the seal begins to leak in less than 10 seconds, and the tubing, with an inserted section length, $l \approx 3$ mm, is forced out of the hydrogel in less than 100 seconds. This is illustrated by the series of time-resolved images in **Fig. 4.1b**. While the failure rate depends on a variety of factors such as gel elasticity, surface moisture, surface roughness, and gel strain, leakage and tubing expulsion from hydrogel-based fluidic devices occurs consistently and at low flow rates. Failure occurs even more frequently when hydrogels with smaller channels and more complex vasculature are used due to the higher pressures required to drive flow.

To address this issue, we design and fabricate a plastic connector and gel socket pair that serves to secure fluidic tubing to the hydrogel. Our connector is plug-shaped, and 3D printed using a photopolymerizable plastic (see Methods). Microfluidic tubing is inserted into the connector and the two are held together with static friction (**Fig. 4.2a**). To couple the tubing and connector assembly to a hydrogel, a matching socket is printed at the channel inlet to the hydrogel, and the connector is inserted into the socket, as shown in **Fig. 4.2b-c**. The design is such that a lip of gel at the channel orifice is stretched during connector insertion and relaxes to form a tight seal around the connector after insertion. We call this a “pop-it” connection. These connectors are simple and easy to manufacture. For example, the batch of connectors shown in **Fig. 4.2d** ($n \approx 100$) can be

fabricated in less than two hours. A hydrogel with pop-it connectors inserted on both inlet and outlet ports is shown in the photograph in **Fig. 4.2e**.

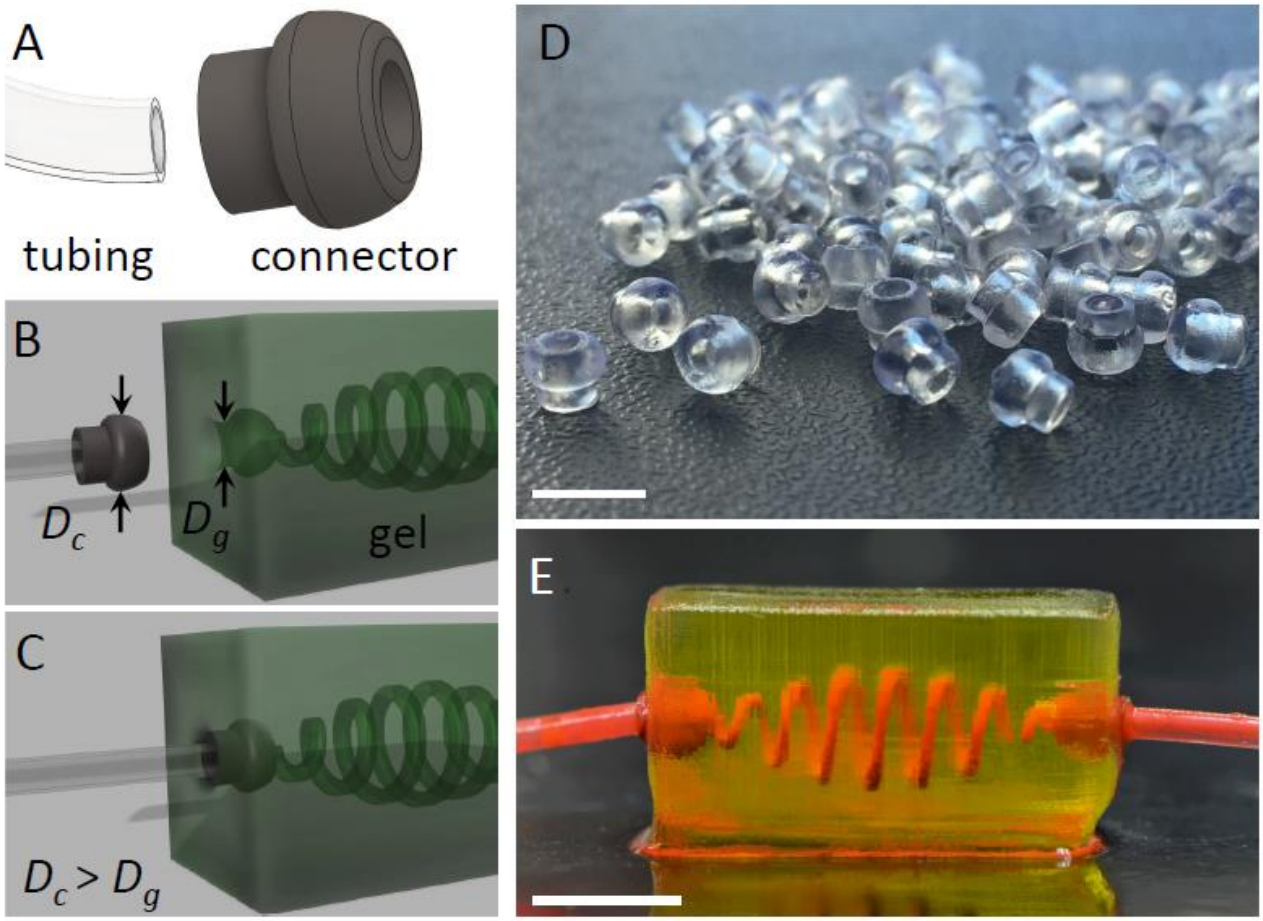


Figure 4.2. *Plastic 3D printed connector secures fluidic tubing to 3D printed hydrogel.* (**A**) CAD rendering of connector design. (**B, C**) Illustrations of connector insertion into 3D printed socket opening into a hydrogel channel. For a seal to form, the diameter of the connector head, D_c must be larger than the diameter of the gel socket neck, D_g. (**D**) Connectors can be rapidly printed and with high fidelity. (**E**) Connectors secure fluidic tubing to two ends of a 3D printed hydrogel. Channel is filled with an oil-based dye to highlight channel shape. Liquid beneath gel is not leaked oil, but residual water with color reflection from above. Scale bars in (D) and (E) correspond to 5 mm.

Provided a connector is matched with a smaller-diameter, appropriately sized gel socket, the gel will form a seal and the elasticity of the gel will resist removal. Appropriate sizing is based on the condition that the head of the connector, with diameter D_c, is larger than the inner neck

diameter D_g of the gel socket ($D_c/D_g \geq 1$; Fig. 4.2b, c). Intuitively, we expect the seal to improve as D_c/D_g increases; however, if D_c/D_g is too large, the gel will fracture during connector insertion. To determine the magnitude of the forces associated with connector insertion as well as the largest achievable D_c/D_g ratio without gel fracture, we systematically vary D_c/D_g and for each condition measure the force required for insertion as well as the maximum liquid pressure the seal can withstand. For these measurements, we fix the gel neck entrance size (D_g = 2.30 mm) and systematically vary the connector head size (2.70 mm $\leq D_c \leq$ 3.50 mm). In this way, we vary the D_c/D_g ratio from 1.17 to 1.52.

To measure the force required for connector insertion as a function of D_c/D_g, we use the normal force sensor of a mechanical rheometer (**Fig. 4.3a**). For each measurement, a connector with a defined D_c is mounted on the upper rheometer plate and brought down towards the gel at a fixed velocity (v = 10 μm/s). Before the connector and gel come into contact, the normal force F is zero. When the two contact, the normal force jumps, and increases as the connector is forced into the gel socket, deforming the gel. The normal force increases to a maximum, F_{max} and then drops back to a value close to zero as the connector locks into the gel socket. A representative measurement is shown in **Fig. 4.3b**. For each D_c, we measure multiple force-displacement curves (n = 3-7) and co-plot these data. We observe that F_{max} increases with increasing D_c (**Fig. 4.3c**). For connectors with D_c > 3.60 we observe that the gel fractures when the connector is inserted (data not shown). This sets an upper limit for D_c/D_g for this connector geometry and gel formulation.

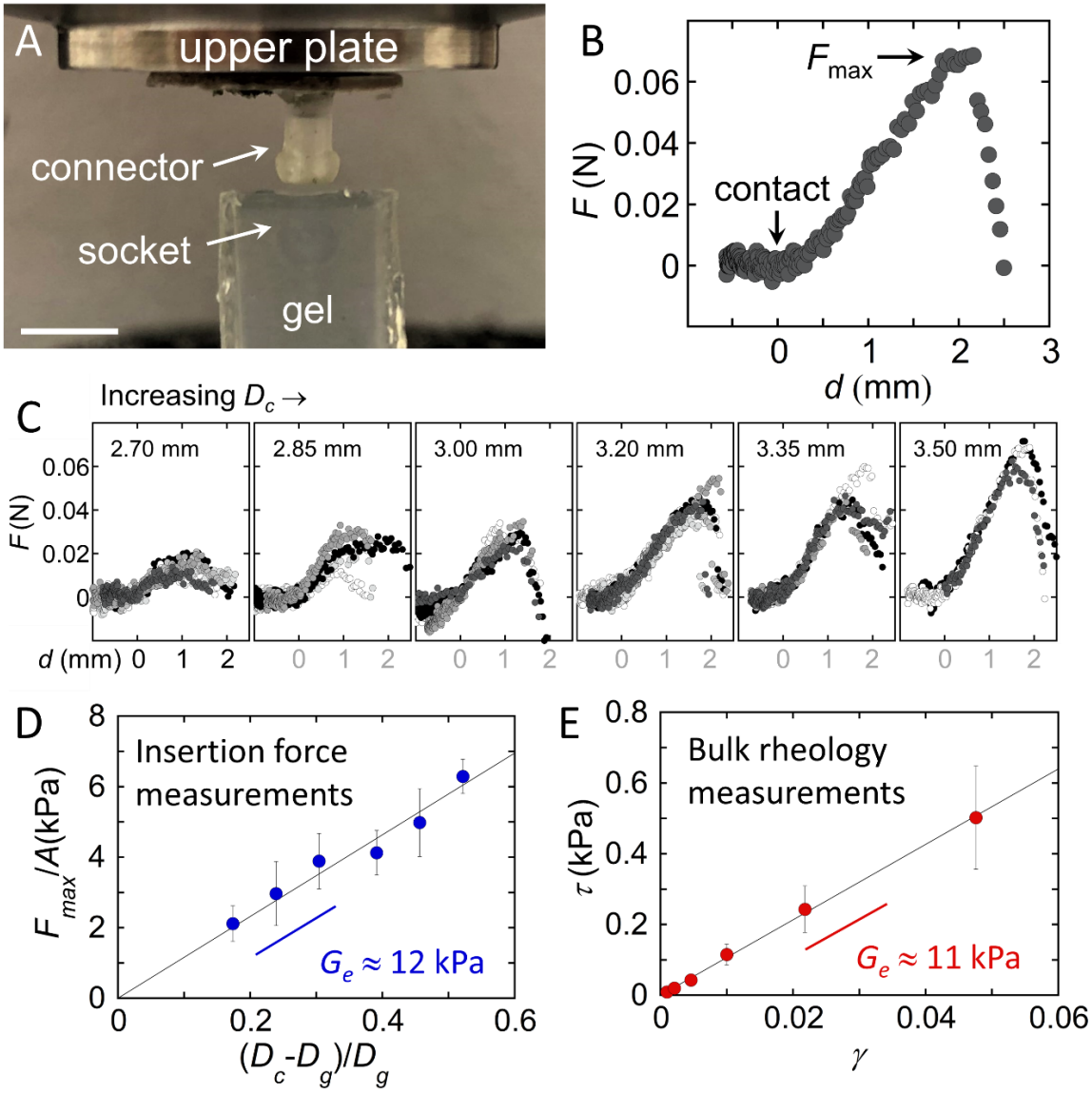


Figure 4.3. *Connector insertion into gel socket is governed by gel elasticity.* (**A**) Experimental setup for measuring the normal force resisting connector insertion into a gel socket. The upper plate of the rheometer brings the connector down into contact with the gel. The normal force, F is measured by a plate beneath the gel. Scale bar corresponds to 5 mm. (**B**) Representative plot of normal force F as a function of distance d for the experiment shown in (A) for D_c = 3.50 mm and D_g = 2.15 mm. (**C**) Force measurements for connectors of varying D_c and gels with fixed D_g = 2.15 mm. F_{max} increases with increasing D_c. Different colored symbols represent measurements on individual gels (n = 3-7 for each D_c). (**D**) Averaged F_{max} from (C) divided by the contact area A between the connector and gel provides a stress, which is plotted as a function of the maximum dimensionless strain: $(D_c - D_g)/D_g$. The slope of the curve provides the gel elastic modulus G_e. (**E**) Bulk rheology measurements on the gel provide a comparable value for G_e, confirming the role of gel elasticity.

To understand the forces resisting connector insertion, we convert the measured force to a stress τ by dividing the averaged F_{max} for each D_c by the maximum contact area between the connector and gel (see Methods and ESI). We then define the maximum gel strain during connector insertion to be $\gamma \approx (D_c - D_g)/ D_g$, and plot τ as a function of γ (**Fig. 4.3d**). We find that the data is fit well by a straight line, even for large $\gamma > 0.5$. This is consistent with elastic behavior, where $\tau = G_e\gamma$ and G_e is the elastic modulus of the gel.[72] From our fit, we find the elastic modulus to be G_e = 11.6 ± 1.1 kPa. To compare this result from insertion force measurements with bulk measurements, we perform shear rheometry on large hydrogels and find the elastic modulus of the gel to be G_e = 10.7 ± 0.2 kPa (**Fig. 4.3e**). This confirms that the gel is deformed elastically for this D_c/D_g range and that the elasticity of the gel resists connector insertion. Here, because there were no device design constraints, the overall dimensions of the hydrogel fluidic device were sized such that the printed socket did not interfere with the macroscale structure or functionality of the gel; however, socket size may become an issue for very small devices. For example, practical considerations like physical handling and insertion of the connector into the socket will limit the smallest connector and socket that can be used. For small socket sizes, the gel lip thickness may also become so thin that it is unable to withstand deformation without gel fracture. Also, in situations where important structural features of the gel device are in close proximity to the socket, gel deformation induced by connector insertion may impact these features.

Next, we test the maximum liquid pressure, P_{max} that the pop-it connections can withstand before connector leakage and expulsion. To apply a well-defined hydrostatic pressure, we attach the pop-it connector to a reservoir of water that can be raised and lowered in a controlled manner (see Methods and ESI). To apply static pressure without needing to account for pressure loss due

to liquid flow, we use hydrogel sockets with a closed inner surface that are not connected to open channels in the gel. For each experiment, we systematically increase the hydrostatic pressure, P in increments ranging from 0.025 Pa to 10 Pa until connection failure is observed. We do this over the range: $1.16 \leq D_c/D_g \leq 1.67$ by fixing the socket size (D_g = 2.15 mm) and systematically varying D_c. For each connector ratio, we measure P_{max} multiple times ($n \approx 12$) by performing up to 3 repeat measurements on 4 to 5 different hydrogels. Hydrogels are elastically deformed during insertion and removal, and we observe no statistically significant trend in P_{max} with repeated measurements on the same gel. While the gel formulation used in these experiments has a swelling ratio less than 1% in distilled water[73], we equilibrate the gels for 24 h in distilled water to mitigate any swelling effects.

We find that P_{max} increases with γ, approaching values as high as $P_{max} \approx 3$ kPa (**Fig. 4.4**). These pressures are three orders of magnitude greater than those we measure for connector-free couplings ($P_{max} \approx 2.5 \pm 1.5$ Pa, n = 3 hydrogels) and are equivalent to pressures generated in PDMS-based microfluidic devices. Pressure of this magnitude could be used to generate significant flow rates in large channels ($Q \approx 170$ mL/min, cylindrical channel with D = 0.8 mm and l = 12 mm, see Methods) and are large enough to drive flows through highly vascularized tissues.[74] Interestingly, though both connector insertion and expulsion require gel deformation, P_{max} increases exponentially with γ, while $[F_{max}/A]$ increases linearly with γ (**Fig. 4.3c**). This may be because for large D_c the connector head becomes asymmetric along the axis of the cylinder (see images in ESI); thus, the contact area between the connector and gel during insertion and removal may be quite different. In addition, the gel socket lip is asymmetric and may deform differently during insertion and removal. This apparent hysteresis is supported by preliminary normal force

measurements of connector insertion and removal (see ESI). While understanding this hysteresis is outside the scope of this paper, this warrants further investigation. Here, the liquids we flow through the gel are the same as the liquids used to equilibrate the gel; if liquids with different compositions and osmolalities are used, potential swelling or shrinkage may impact P_{max}.

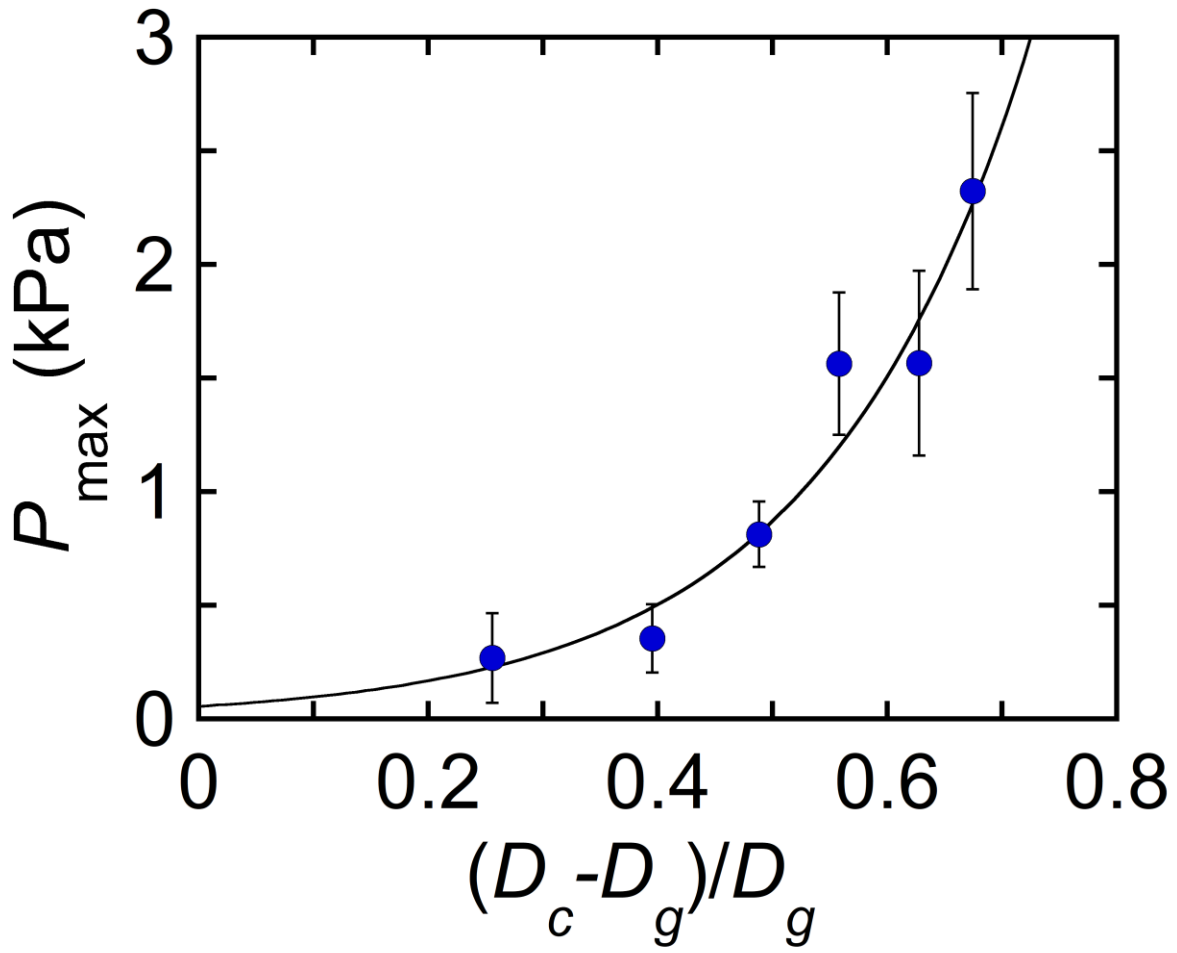


Figure 4.4. *Seal between connector and gel socket improves as the connector head diameter increases relative to the gel neck diameter.* Maximum hydrostatic pressure at failure, P_{max}, plotted as function of maximum gel neck strain during connector expulsion and fit to a simple exponential increase (see Methods). For the connector with the largest head, the connection can withstand pressures $\Delta P > 2.5$ kPa, three orders of magnitude greater than the pressures that standard, connector free approaches can withstand ($\Delta P \approx 1$ Pa).

Pop-it connectors can also be used to connect modular gels to one another. For example, two-sided, dumbbell-shaped connectors (**Fig. 4.5a**) matched to 3D printed sockets in opposing gels can be used to bring adjacent gel cubes into contact and hold them in place. For example, joining of two hydrogel cubes using a two-sided connector is shown in a series of images in **Fig. 4.5b, c**. To further demonstrate this modularity, we print four hydrogel cubes (edge length, l_c = 9 mm), three of which contain a straight cylindrical channel (D = 1.20 mm) running from one cube face to the opposing face, and one cube with three cylindrical channels running from three different cube faces and joining at a single intersection point. We dye these cubes with food coloring to highlight their individuality, connect them using two-sided pop-it connectors, and drive water through the assembly with one-sided pop-it connectors coupled to microfluidic tubing. Images of the gel modules and the assembly are shown in **Fig. 4.5d, e**. The connectors form an excellent seal between hydrogels, allowing for liquid flow. This approach could be used to build complex, reconfigurable hydrogel systems from simple modular components. We note that a variety of connector types exist for connecting modular microfluidic components to one another[75, 76] including self-aligning magnetic interconnects[77] and integrated microfabricated gaskets[78]; however, these technologies have not been demonstrated for use with hydrogels.

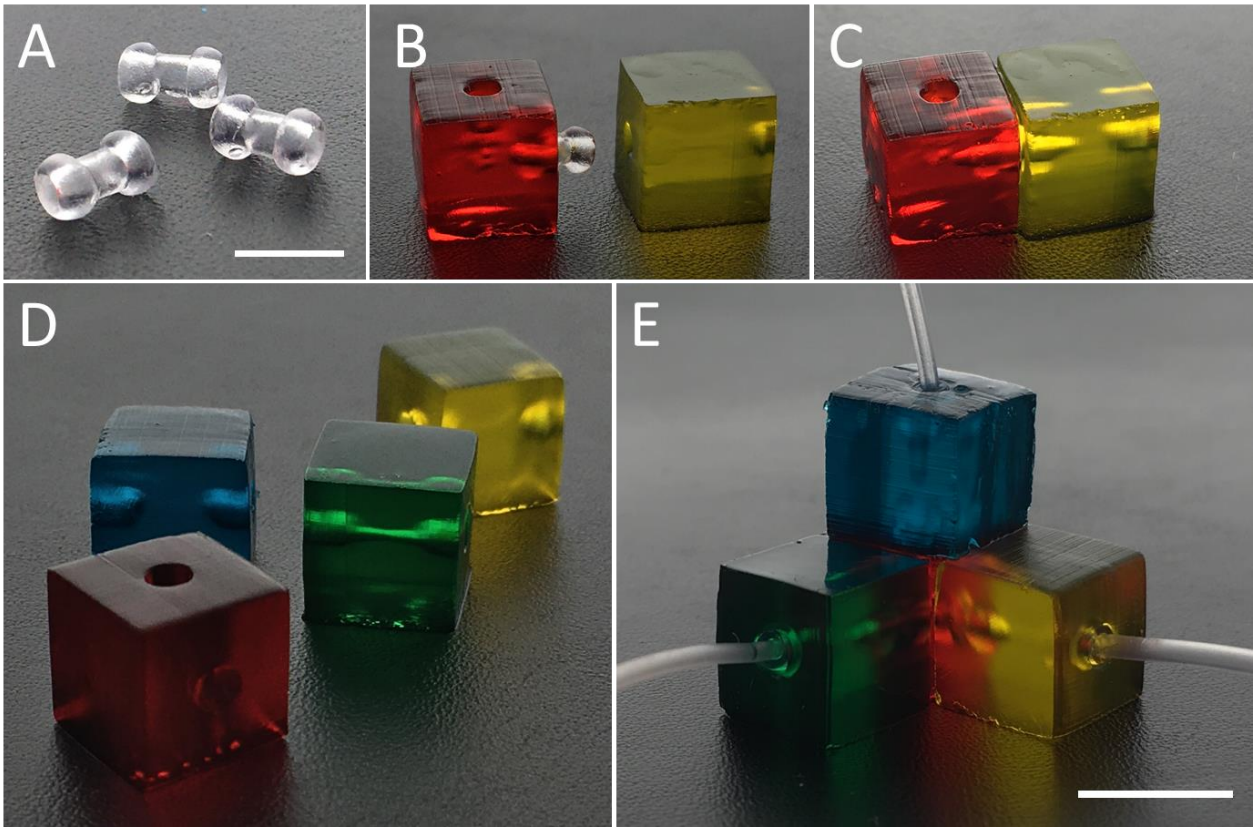


Figure 4.5. *Double-sided pop-it connectors can be used to build interconnected assemblies from modular gels.* (**A**) Photograph of two-sided connectors. (**B, C**) Image series of two 3D printed hydrogels joined using a two-sided connector. (**D, E**) Images of four 3D printed hydrogels joined together using multiple two-sided connectors. Gels were colored with food dye before assembly to illustrate modular nature of the assembly. The blue, green, and yellow cubes contain a single straight channel running from one cube face to another. The red gel contains channels running from three adjacent faces that connect in the center of the cube. The modular assembly does not leak when water is driven through the assembly. Scale bars in (A) and (E) correspond to 5 mm and 10 mm, respectively.

Pop-it connections offer additional advantages. First, pop-it connections allow for rotation around the long axis of the connector. To demonstrate this, we attach two hydrogels together with a two-sided connector and rotate the upper (blue) hydrogel by 45° around the *z*-axis without disturbing the connection (**Fig. 4.6a-c**). This rotational degree of freedom could be used for reconfigurable modular assemblies for structure-function studies and soft robotics. Second, two-sided connectors can be used to bring two hydrogel modules into contact together to allow for

molecular diffusion from one module to another. To demonstrate this, we bring two hydrogel cubes together with a dumbbell shaped connector and observe the diffusion of red dye from one cube into the other (**Fig. 4.6d-f**). This could be used to establish well-defined concentration gradients in engineered tissues. Third, the reversibility of the pop-it connection allows one to change the composition of the liquid driven through a given hydrogel during an experiment. To demonstrate this, we introduce one colored oil to a hydrogel module, followed by a second colored oil from a separate tubing source (**Fig. 4.6g, h)**. This approach could be used to alter the media conditions supplied to living cells embedded in hydrogel. This rapid exchange is not feasible for connections requiring adhesive.[69]

Finally, to demonstrate a clear application of the pop-it connection, we 3D-print a hydrogel cube containing *Pseudomonas aeruginosa* (pMF230; constitutively expressing GFP) with a single straight channel with connection sockets at both ends of the channel and use pop-it connections on either end to establish nutrient flow through the hydrogel. We use a plastic 3D-printed holder to stabilize the gel, connectors, and tubing (**Fig. 4.6i**). We store the entire assembly in an incubator at 37 °C and 100% relative humidity and drive tryptic soy broth (TSB) media at a flow rate of 2 mL/h through the gel. After 24 h, we cross-section the hydrogel and image the GFP intensity with confocal microscopy. A duplicate bacteria-laden hydrogel is cross-sectioned at $t = 0$ and imaged as well for comparison. The images in **Fig. 4.6j, k** show clear microbial growth in the hydrogel supplied with media.

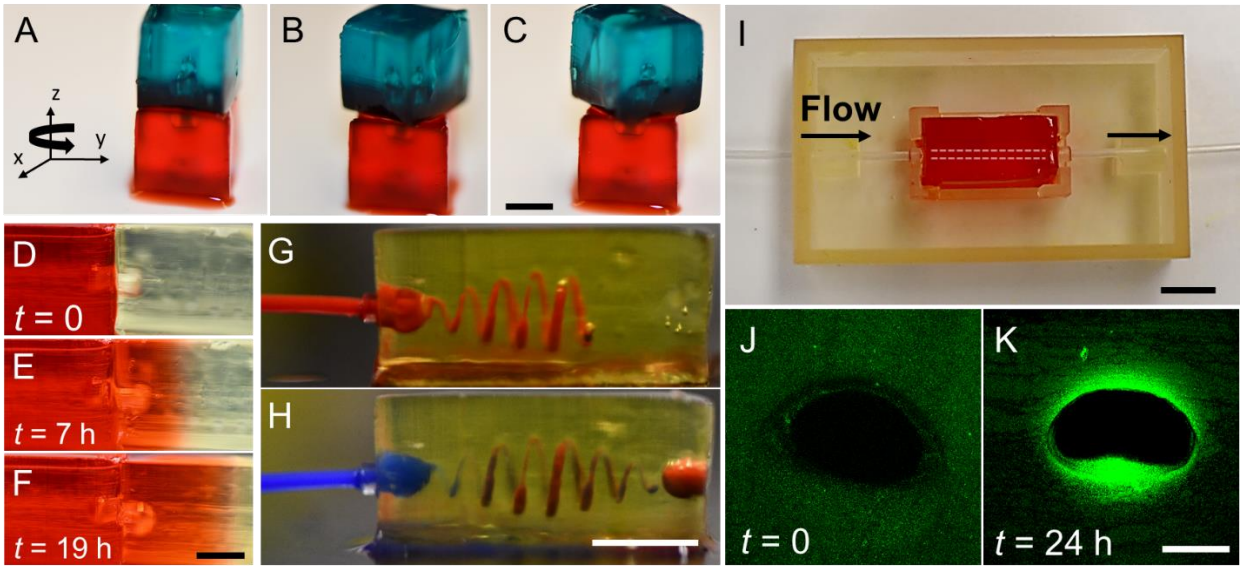


Figure 4.6. *Pop-it connector advantages and potential applications*. (**A-C**) Connectors allow for free rotation around the long z-axis of the connector. The two gels are colored with red and blue food dye for clarity. (**D-F**) Two hydrogels held in contact by a two-sided connector allows diffusion of material from one gel into the other. Here, red food dye is used. (**G, H**) Connector reversibility allows multiple fluid streams to be sequentially introduced into the same hydrogel. (**I-K**) Long-term flow of media through a hydrogel containing bacteria enabled by connectors maintains cell growth and viability, (I) Hydrogel and tubing are assembled and held in a plastic 3D-printed holder. Fresh media is driven from left to right through the hydrogel. The gel is dyed red here for clarity. (J, K) Fluorescence confocal microscopy cross-sectional images of gel containing *Pseudomonas aeruginosa* (pMF230; constitutive GFP) before (J) and after (K) growth for 24 hours. Dark center hole is the cross-section of a semi-cylindrical channel ($D \approx 1.20$ mm). Scale bars correspond to: (H) 10 mm; (C), (F), and (H) 5 mm; and (K) 500 μm

The connector design presented here could be modified in a variety of ways. For example, the shape of the connector and socket could be optimized for ease of insertion, for improved seal formation, or to better distribute stress in the hydrogel. Here, we use a bulb-shaped connector, but other connector geometries such as screw shapes and configurations with different rotational and axial symmetry could be explored. In addition, fabrication methods other than 3D printing could be used to structure the connector socket in the hydrogel. For example, a casting approach like that used in soft lithography-based could be used, [79-81] and, the creation of overhanging features in the negative mold could be achieved using two-photon polymerization techniques.[82, 83] Pop-it

connectors could also be integrated into hybrid hydrogel/PDMS systems.[50] Finally, a wide variety of hydrogel formulations could be explored to improve or optimize connector performance.[84] Gel mechanical properties could be varied by controlling monomer and crosslinker chemistries [85], molecular weight[86], gel concentration,[86] and by the addition of filler materials.[87] In addition, alginate,[88] agarose,[88] gelatin methacryloyl (GelMA),[89] poly(vinyl alcohol) (PVA),[90] and double-network hydrogels with enhanced strength and elasticity[87] could be explored.

Conclusion

In conclusion, the 3D printed "pop-it" connection presented here represents the first reported hydrogel connection mechanism for coupling tubing to hydrogel fluidic devices in a stable, reversible manner to allow for liquid flow. Pop-it connectors mount into well-defined 3D printed sockets by simple insertion and are held in place by the elasticity of the hydrogel, rather than static friction. Using this connection, we show that it is possible to drive fluid flow while sustaining pressures up to $\Delta P \approx 3$ kPa, which is three orders of magnitude greater than the standard connector-free approach and equivalent to the pressures required to drive flow through standard PDMS-based microfluidic devices. We demonstrate that a two-sided connector can be used to couple two hydrogels together to construct modular assemblies with intermodular diffusion. Lastly, we demonstrate that pop-it connectors can be used to establish long-term nutrient flow to hydrogels to sustain the growth and viability of bacteria in the gel. These pop-it connectors will enable a variety of hydrogel applications by allowing for reliable, leak-free flow.

Methods

Hydrogel 3D Printing

Hydrogels were designed using CAD software (Autodesk, Fusion 360) and 3D printed using a commercial stereolithography 3D printer (Formlabs, Form 1+). For the aqueous resin formulation, poly(ethylene glycol) diacrylate (PEG-DA) was used as a monomer (10 wt%, Sigma-Aldrich, M_n 700), lithium phenyl-2,4,6-trimethylbenzoylphosphinate (LAP) was used as a photoinitiator (0.1 wt%, Tokyo Chemical Industry), and tartrazine was used as a photoblocker (0.075 wt%, Alfa Aesar). Prepared resin solutions were poured into the printer resin tray. To fabricate gels with well-defined and open structures, resin formulation and light exposure conditions were selected for optimal printing.[51] To ensure adhesion of hydrogel to the print head, microscopy slides (Fisherbrand Colorfrost, 25 mm × 75 mm × 1 mm) were pretreated with Bind-Silane (2.0 vol%, GE Healthcare, 17-1330-01). Microscopy slides were submerged in the Bind-Silane solution for five minutes then baked at 100 °C for another five minutes. Treated slides were attached to the custom-made print head with a UV bonding adhesive (Norland Products).[91] Hydrogel CAD files are available in ESI. The printing process proceeds by photopolymerizing the object layer-by-layer as described elsewhere.[92]

Connector 3D Printing

Connectors were designed using CAD software (Autodesk, Fusion 360) and 3D printed with a commercial stereolithography 3D printer (Formlabs, Form 3) using a methacrylic acid ester-based resin (Formlabs, Clear Resin). After printing, connectors were washed with isopropyl alcohol and post-cured with a benchtop ultraviolet light. Formlabs resins are resistant to ethanol and UV light, both of which can be used for sterilization. As an alternative, Formlabs High-

Temperature resin could be used to create autoclavable connectors. Connector CAD files are available in ESI.

Liquid Flow

To drive water through a hydrogel, a plastic syringe (60 mL Soft-Ject Luer Lock, Henke Sass Wolf) was filled with water and mounted into a syringe pump (World Precision Instruments, Model AL-4000). A blunt, 20-gauge dispensing needle was attached to the syringe end with a luer lock fitting and polyethylene tubing (Scientific Commodities Inc., I.D. = 0.86 mm; O.D. = 1.32 mm). The other end of the tubing, with or without attached pop-it connector, was then inserted into the 3D printed hydrogel. For the hydrogels in Fig. 1 and 2, oil-based red and yellow paint diluted with silicone oil (AR20) was used to highlight the channels.

Hydrostatic Pressure Measurements

To determine the pressure required for connector failure, we constructed a custom experimental setup capable of applying well-defined hydrostatic pressures (**SI Fig. 4.1**). The mechanized system consisted of a microcontroller (Elegoo UNO R3), a stepper motor driver (TB6600), and two stepper motors with lead screws (NEMA 17 with 150 mm T8 lead Screws). The lead screws provided controlled linear movement with a minimum step size of 2.5 μm. A water reservoir was mounted to the stepper motor lead screws and connected to the hydrogel through tubing and a pop-it connector. The reservoir was incrementally raised using the stepper motors until the connection between the connector and the hydrogel failed. The height differential between the top of the water reservoir and the pop-it connector was then used to determine the maximum liquid pressure, $P_{\max}$ by calculating the hydrostatic pressure at that point using $P_h = \rho g h$, where ρ is density of the fluid, g is gravitational force and h is the height of the fluid. A video

of a representative experiment is shown in **Video S1**. The data in Fig. 4.4 is fit to the following function: $\Delta P = ae^{b\gamma}$ where $\gamma \approx (D_c - D_g)/ D_g$, a = 0.056, and b = 5.48.

Flow Rate Estimates

To estimate the flow rates that our pop-it connections are capable of withstanding, we calculate the volumetric flow rate, Q through a cylindrical channel of diameter, D = 0.8 mm and length l = 12 mm using the Hagen-Poiseuille equation: $Q = \frac{\Delta P \pi D^4}{128 \eta l}$

Here, η is the dynamic viscosity of the liquid and $\Delta P = \Delta P_{max}$. For water and ΔP_{max} = 3 kPa, we find Q = 170 mL/min.

Rheometry and Force Measurements

A mechanical rheometer (TA Instruments AR-G2) was used to perform two types of measurements: standard shear rheometry and non-standard normal force measurements. Small amplitude shear rheometry measurements over a range of frequencies, ω = 0.01 Hz – 1 Hz and strain amplitudes, γ = 0.001 – 0.05 were performed after mounting coin-shaped 3D-printed hydrogels (sample thickness, h = 3 mm; sample diameter, D_s = 20 mm) in a parallel plate geometry (plate diameter, D_p = 20 mm). Normal force measurements were performed by attaching individual connectors to the upper rheometer head with double-sided adhesive tape. Then, a spot in the center of the lower rheometer plate was marked, 3D printed hydrogel samples were mounted inside a 3D printed housing, and the housing placed on the lower plate in a well-defined position. To further ensure axial alignment of the connector with the socket, the z-position of the upper rheometer head was slowly lowered to approach the hydrogel allowing any necessary adjustments to be made. To measure the normal force required to remove the connector from a hydrogel socket, an inserted

connector was retracted by lifting the upper rheometer plate away from the gel. Each measurement took approximately 2-3 minutes in total; if the measurement was prolonged, the hydrogel was kept hydrated by the addition of a small amount of water. The pressure sensing unit of the rheometer is within the lower standing platform. Once the connector and gel are in contact, the integrity of the connector adhesion to the upper geometry should not impact the measurement. If this adhesion were to fail before contact, we would expect a sudden jump in the force. Adhesion of the holder to the lower platform is less likely to fail, would result in a shift in the xy-plane, and would easily be observed by visual inspection.

Measuring Contact Area of the Connector

The contact area, A used in Fig. 4.3d to calculate τ was estimated using the "Measure" function in Fusion 360. For this, each connector CAD drawing was used to estimate potential contact area of each connector on the inner walls of the hydrogel (See supplementary). Estimating A is done by assuming that the hydrogel socket is stretching into the shape of pop-it connector upon insertion. Also, since the surface area of the pop-it connector acting on the hydrogel during F_{max} should not change for insertion and removal of the connector, the same A values are valid to calculate pressure acting on the hydrogel during both insertion and removal of the connector.

Growth of 3D Printed Bacteria

Pseudomonas aeruginosa (pMF230) is cultured overnight in liquid TSB media with ampicillin (100 µg mL^{-1}). After 12+ h of growth, approximately 10^9 CFU/mL of planktonic bacteria is added to the bioink resin prior to the 3D printing. The pMF230 strain constitutively expresses GFP, so fluorescence intensity and colony size are used to measure growth and viability. The hydrogel holder in Fig. 4.6i is 3D printed (Formlabs, Form 3, High Temperature Resin) and

autoclaved prior to assembly. After growth for 24 h at 37 C, the gel is sectioned with a razor blade and imaged with a confocal microscope (Leica SP5; 5× air objective).

Supplementary Information

Hydrostatic pressure measurements

To determine the pressure required for connector failure, we constructed a custom experimental setup capable of applying well-defined hydrostatic pressures (**SI Fig. 4.1**). The mechanized system consisted of a microcontroller (Elegoo UNO R3), a stepper motor driver (TB6600), and two stepper motors with lead screws (NEMA 17 with 150mm T8 lead Screws). The lead screws provided controlled linear movement with a minimum step size of 2.5 μm. A water reservoir was mounted to the stepper motor lead screws and connected to the hydrogel through tubing and a pop-it connector. The reservoir was incrementally raised using the stepper motors until the connection between the pop-it connector and the hydrogel failed. The height of the reservoir at failure could then be calculated from the number of steps the stepper motors had taken. The height differential between the top of the water reservoir and the pop-it connector was used to determine the hydrostatic pressure P_h required for connection failure using the simple equation: $P_h = \rho g h$, where ρ is density of the fluid, g is gravitational force and h is the height of the fluid. A video of a representative experiment is shown in **Video S1**.

Estimating contact area between connector and gel

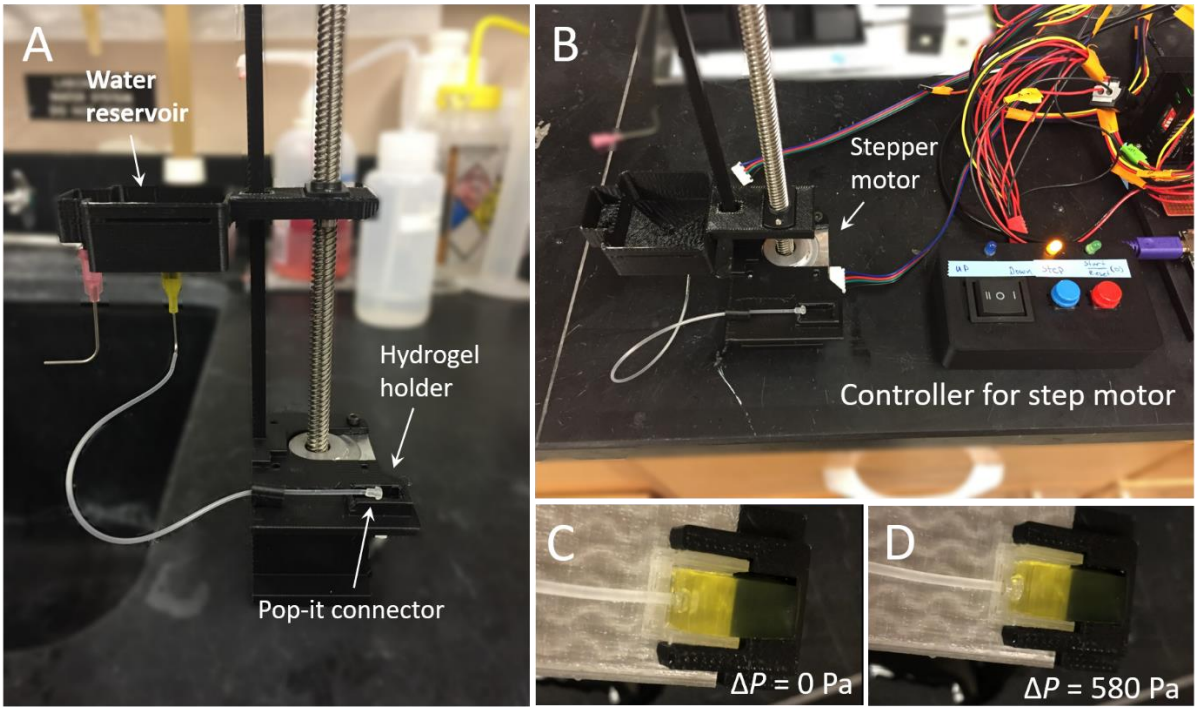
Method used to estimate the contact area, A between the connector and gel at maximum deformation during connector insertion (**SI Fig. 4.2**). These values of A were then used to calculate the stress, $\tau = F_{max}/A$, and the values plotted in Fig 4.3d.

Evidence of hysteresis in normal forces associated with connector insertion and removal

To compare the normal forces associated with insertion and removal of the pop-it connector, we 3D printed a PLA enclosure (dimensions: 8.5 mm x 8.5 mm x 15.5 mm; wall thickness: 0.50 mm; top hole diameter: 5.00 mm) to hold the hydrogel in place during retraction of the rheometer head (**SI Fig. 4.3a, b**). The pop-it connector and hydrogel holder were each taped to the rheometer head and platform, respectively as shown in **SI Fig. 4.3c**. For each measurement, the pop-it connector was inserted into the hydrogel in a manner similar to that described for Fig 4.3, and the rheometer head was then also retracted to remove the connector. A representative force measurement with clear hysteresis is plotted in **SI Fig. 4.4**.

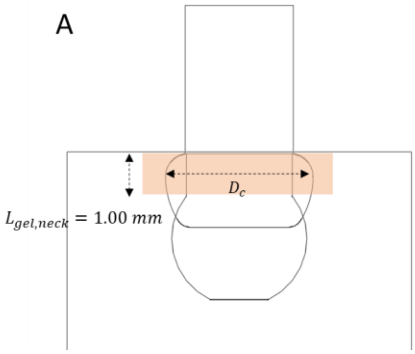
Funding

This work was supported by the National Science Foundation (DMR-1455247 and OIA-1736255).



Supplemental Figure 4.1. Hydrostatic pressure setup. (A) 3D printed parts were assembled together with a stepper motor and microcontroller to control the height of the water reservoir and generate a hydrostatic pressure on the hydrogel inlet. (B) Movement of the stepper motor was controlled by an Elegoo UNO R3 microcontroller and a TB6600 stepper motor driver to provide precise control of the height. (C) A hydrogel with an attached pop-it connector remains stable when no hydrostatic pressure is applied (ΔP = 0 Pa), and is (D) expelled from hydrogel when ΔP = 580 Pa

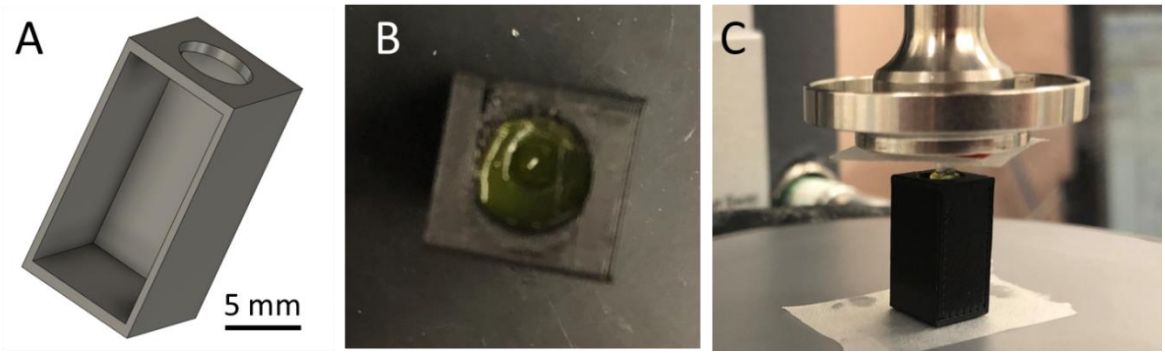
A



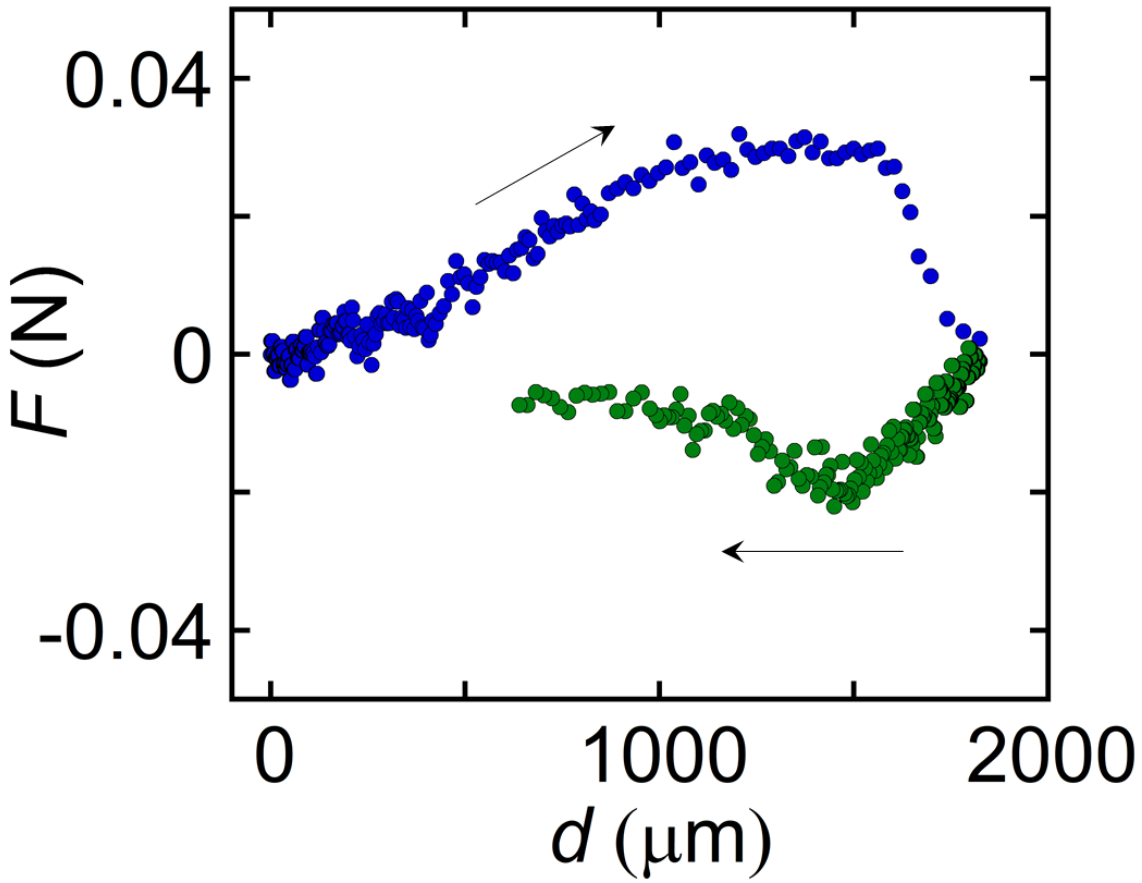
B

D_c [mm]	Contact Area, A [mm^2]
2.70	9.02
2.85	9.03
3.00	10.40
3.20	10.55
3.35	10.44
3.50	10.90

Supplemental Figure 4.2. Contact area, A when hydrogel is at $\boldsymbol{F_{max}}$ during the insertion of the pop-it connector. (A) Representative side view of connector and gel to shows the position of the connector in the hydrogel socket during insertion when force is at $\boldsymbol{F_{max}}$. Area of the roughly highlighted zone is extracted using the software Fusion 360. (B) Table of *A* values for each pop-it connector.



Supplemental Figure 4.3. Experimental setup for measuring normal forces associated with connector insertion and removal. (**A**) CAD design file of hydrogel holder. (**B**) Top-view of the hydrogel holder (**C**) Full experimental setup mounted on the rheometer.



Supplemental Figure 4.4. Representative measurement of normal force, *F* as a function of displacement, *d*, for a connector inserted into a gel socket (blue data points) and then removed from the socket (green data points). For the two data sets, the upper rheometer plate is moving in opposite directions, indicated by the arrows. The measurement reveals clear hysteresis in the forces associated with insertion and removal. The reason for this hysteresis is not clear.

References Cited

1. Munster, V. J.; Koopmans, M.; van Doremalen, N.; van Riel, D.; de Wit, E., A novel coronavirus emerging in China — Key questions for impact assessment. *New England Journal of Medicine* **2020,** *382* (8), 692-694.

2. Mina, M. J.; Andersen, K. G., COVID-19 testing: One size does not fit all. **2021,** *371* (6525), 126-127.

3. Jain, K. K., Nanotechnology in clinical laboratory diagnostics. *Clin Chim Acta* **2005,** *358* (1-2), 37-54.

4. Janda, J. M.; Abbott, S. L., 16S rRNA gene sequencing for bacterial identification in the diagnostic laboratory: Pluses, perils, and pitfalls. *Journal of Clinical Microbiology* **2007,** *45* (9), 2761-2764.

5. Gao, Y.; Li, T.; Han, M.; Li, X.; Wu, D.; Xu, Y.; Zhu, Y.; Liu, Y.; Wang, X.; Wang, L., Diagnostic utility of clinical laboratory data determinations for patients with the severe COVID-19. *Journal of Medical Virology* **2020,** *92* (7), 791-796.

6. Chiappin, S.; Antonelli, G.; Gatti, R.; De Palo, E. F., Saliva specimen: A new laboratory tool for diagnostic and basic investigation. *Clin Chim Acta* **2007,** *383* (1-2), 30-40.

7. Yager, P.; Domingo, G. J.; Gerdes, J., Point-of-care diagnostics for global health. *Annual Review of Biomedical Engineering* **2008,** *10*, 107-144.

8. Hu, J.; Wang, S.; Wang, L.; Li, F.; Pingguan-Murphy, B.; Lu, T. J.; Xu, F., Advances in paper-based point-of-care diagnostics. *Biosens Bioelectron* **2014,** *54*, 585-597.

9. Gubala, V.; Harris, L. F.; Ricco, A. J.; Tan, M. X.; Williams, D. E., Point of Care Diagnostics: Status and Future. *Analytical Chemistry* **2012,** *84* (2), 487-515.

10. Craw, P.; Balachandran, W., Isothermal nucleic acid amplification technologies for point-of-care diagnostics: a critical review. *Lab on a Chip* **2012,** *12* (14), 2469-2486.

11. Chin, C. D.; Linder, V.; Sia, S. K., Commercialization of microfluidic point-of-care diagnostic devices. *Lab on a Chip* **2012,** *12* (12), 2118-2134.

12. Ahn, C. H.; Choi, J. W.; Beaucage, G.; Nevin, J. H.; Lee, J. B.; Puntambekar, A.; Lee, J. Y., Disposable Smart lab on a chip for point-of-care clinical diagnostics. *Proceedings of the Ieee* **2004,** *92* (1), 154-173.

13. Yetisen, A. K.; Akram, M. S.; Lowe, C. R., Paper-based microfluidic point-of-care diagnostic devices. *Lab on a Chip* **2013,** *13* (12), 2210-2251.

14. Wang, J., Electrochemical biosensors: Towards point-of-care cancer diagnostics. *Biosens Bioelectron* **2006,** *21* (10), 1887-1892.

15. Yang, S.; Rothman, R. E., PCR-based diagnostics for infectious diseases: uses, limitations, and future applications in acute-care settings. *Lancet Infectious Diseases* **2004,** *4* (6), 337-348.

16. Reed, G. H.; Kent, J. O.; Wittwer, C. T., High-resolution DNA melting analysis for simple and efficient molecular diagnostics. *Pharmacogenomics* **2007,** *8* (6), 597-608.

17. Huggett, J. F.; Cowen, S.; Foy, C. A., Considerations for Digital PCR as an Accurate Molecular Diagnostic Tool. *Clinical Chemistry* **2015,** *61* (1), 79-88.

18. Elnifro, E. M.; Ashshi, A. M.; Cooper, R. J.; Klapper, P. E., Multiplex PCR: Optimization and application in diagnostic virology. *Clin Microbiol Rev* **2000,** *13* (4), 559-+.

19. Porte, L.; Legarraga, P.; Vollrath, V.; Aguilera, X.; Munita, J. M.; Araos, R.; Pizarro, G.; Vial, P.; Iruretagoyena, M.; Dittrich, S.; Weitzel, T., Evaluation of a novel antigen-based rapid detection test for the diagnosis of SARS-CoV-2 in respiratory samples. *International Journal of Infectious Diseases* **2020,** *99*, 328-333.

20. Mak, G. C. K.; Cheng, P. K. C.; Lau, S. S. Y.; Wong, K. K. Y.; Lau, C. S.; Lam, E. T. K.; Chan, R. C. W.; Tsang, D. N. C., Evaluation of rapid antigen test for detection of SARS-CoV-2 virus. *Journal of Clinical Virology* **2020,** *129*.

21. Hirotsu, Y.; Maejima, M.; Shibusawa, M.; Nagakubo, Y.; Hosaka, K.; Amemiya, K.; Sueki, H.; Hayakawa, M.; Mochizuki, H.; Tsutsui, T.; Kakizaki, Y.; Miyashita, Y.; Yagi, S.; Kojima, S.; Omata, M., Comparison of automated SARS-CoV-2 antigen test for COVID-19 infection with quantitative RT-PCR using 313 nasopharyngeal swabs, including from seven serially followed patients. *International Journal of Infectious Diseases* **2020,** *99*, 397-402.

22. Dinnes, J.; Deeks, J. J.; Adriano, A.; Berhane, S.; Davenport, C.; Dittrich, S.; Emperador, D.; Takwoingi, Y.; Cunningham, J.; Beese, S.; Dretzke, J.; di Ruffano, L. F.; Harris, I. M.; Price, M. J.; Taylor-Phillips, S.; Hooft, L.; Leeflang, M. M. G.; Spijker, R.; Van den Bruel, A.; Cochrane, C.-D. T. A., Rapid, point-of-care antigen and molecular-based tests for diagnosis of SARS-CoV-2 infection (Review). *Cochrane Database of Systematic Reviews* **2020,** (8).

23. Saiki, R. K.; Scharf, S.; Faloona, F.; Mullis, K. B.; Horn, G. T.; Erlich, H. A.; Arnheim, N., ENZYMATIC AMPLIFICATION OF BETA-GLOBIN GENOMIC SEQUENCES AND RESTRICTION SITE ANALYSIS FOR DIAGNOSIS OF SICKLE-CELL ANEMIA. *Science* **1985,** *230* (4732), 1350-1354.

24. Saiki, R. K.; Gelfand, D. H.; Stoffel, S.; Scharf, S. J.; Higuchi, R.; Horn, G. T.; Mullis, K. B.; Erlich, H. A., PRIMER-DIRECTED ENZYMATIC AMPLIFICATION OF DNA WITH A THERMOSTABLE DNA-POLYMERASE. *Science* **1988,** *239* (4839), 487-491.

25. Mullis, K. B.; Faloona, F. A., SPECIFIC SYNTHESIS OF DNA INVITRO VIA A POLYMERASE-CATALYZED CHAIN-REACTION. *Methods in Enzymology* **1987,** *155,* 335-350.

26. Mullis, K. B., THE UNUSUAL ORIGIN OF THE POLYMERASE CHAIN-REACTION. *Scientific American* **1990,** *262* (4), 56-&.

27. Mullis, K.; Faloona, F.; Scharf, S.; Saiki, R.; Horn, G.; Erlich, H., SPECIFIC ENZYMATIC AMPLIFICATION OF DNA INVITRO - THE POLYMERASE CHAIN-REACTION. *Cold Spring Harbor Symposia on Quantitative Biology* **1986,** *51,* 263-273.

28. Mackay, I. M., Real-time PCR in the microbiology laboratory. *Clinical Microbiology and Infection* **2004,** *10* (3), 190-212.

29. Johnston, S. P.; Pieniazek, N. J.; Xayavong, M. V.; Slemenda, S. B.; Wilkins, P. P.; da Silva, A. J., PCR as a confirmatory technique for laboratory diagnosis of malaria. *Journal of Clinical Microbiology* **2006,** *44* (3), 1087-1089.

30. Geha, D. J.; Uhl, J. R.; Gustaferro, C. A.; Persing, D. H., MULTIPLEX PCR FOR IDENTIFICATION OF METHICILLIN-RESISTANT STAPHYLOCOCCI IN THE CLINICAL LABORATORY. *Journal of Clinical Microbiology* **1994,** *32* (7), 1768-1772.

31. Espy, M. J.; Uhl, J. R.; Sloan, L. M.; Buckwalter, S. P.; Jones, M. F.; Vetter, E. A.; Yao, J. D. C.; Wengenack, N. L.; Rosenblatt, J. E.; Cockerill, F. R.; Smith, T. F., Real-time PCR in clinical microbiology: Applications for a routine laboratory testing. *Clin Microbiol Rev* **2006,** *19* (1), 165-+.

32. Petralia, S.; Conoci, S., PCR Technologies for Point of Care Testing: Progress and Perspectives. *Acs Sensors* **2017,** *2* (7), 876-891.

33. Park, S.; Zhang, Y.; Lin, S.; Wang, T.-H.; Yang, S., Advances in microfluidic PCR for point-of-care infectious disease diagnostics. *Biotechnol Adv* **2011,** *29* (6), 830-839.

34. Lee, S. H.; Kim, S.-W.; Kang, J. Y.; Ahn, C. H., A polymer lab-on-a-chip for reverse transcription (RT)-PCR based point-of-care clinical diagnostics. *Lab on a Chip* **2008,** *8* (12), 2121-2127.

35. Tomita, N.; Mori, Y.; Kanda, H.; Notomi, T., Loop-mediated isothermal amplification (LAMP) of gene sequences and simple visual detection of products. *Nature Protocols* **2008,** *3* (5), 877-882.

36. Notomi, T.; Okayama, H.; Masubuchi, H.; Yonekawa, T.; Watanabe, K.; Amino, N.; Hase, T., Loop-mediated isothermal amplification of DNA. *Nucleic Acids Research* **2000,** *28* (12).

37. Nagamine, K.; Hase, T.; Notomi, T., Accelerated reaction by loop-mediated isothermal amplification using loop primers. *Molecular and Cellular Probes* **2002,** *16* (3), 223-229.

38. Mori, Y.; Nagamine, K.; Tomita, N.; Notomi, T., Detection of loop-mediated isothermal amplification reaction by turbidity derived from magnesium pyrophosphate formation. *Biochemical and Biophysical Research Communications* **2001,** *289* (1), 150-154.

39. Cutting Corners on Injection-Molded Parts. https://www.protolabs.com/resources/design-tips/cutting-corners-on-injection-molded-parts/.

40. What's the Average Hand Size for Men, Women, and Children? https://www.healthline.com/health/average-hand-size#adults.

41. Mahinroosta, M.; Farsangi, Z. J.; Allahverdi, A.; Shakoori, Z., Hydrogels as intelligent materials: A brief review of synthesis, properties and applications. *Mater Today Chem* **2018,** *8*, 42-55.

42. Li, H. J.; Tan, C.; Li, L., Review of 3D printable hydrogels and constructs. *Mater Design* **2018,** *159*, 20-38.

43. Ahmed, E. M., Hydrogel: Preparation, characterization, and applications: A review. *J Adv Res* **2015,** *6* (2), 105-121.

44. Saroia, J.; Wang, Y. E.; Wei, Q. H.; Zhang, K.; Lu, T. L.; Zhang, B., A review on biocompatibility nature of hydrogels with 3D printing techniques, tissue engineering application and its future prospective. *Bio-Des Manuf* **2018,** *1* (4), 265-279.

45. Rosiak, J. M.; Yoshii, F., Hydrogels and their medical applications. *Nucl Instrum Meth B* **1999,** *151* (1-4), 56-64.

46. Saul, J. M.; Williams, D. F., Hydrogels in Regenerative Medicine. *Pdl Handb Ser* **2014**, 279-302.

47. Calo, E.; Khutoryanskiy, V. V., Biomedical applications of hydrogels: A review of patents and commercial products. *Eur Polym J* **2015,** *65*, 252-267.

48. Chai, Q. Y.; Jiao, Y.; Yu, X. J., Hydrogels for Biomedical Applications: Their Characteristics and the Mechanisms behind Them. *Gels-Basel* **2017,** *3* (1).

49. Sidar, B.; Jenkins, B. R.; Huang, S.; Spence, J. R.; Walk, S. T.; Wilking, J. N., Long-term flow through human intestinal organoids with the gut organoid flow chip (GOFlowChip). *Lab on a Chip* **2019,** *19* (20), 3552-3562.

50. Chueh, B. H.; Zheng, Y.; Torisawa, Y. S.; Hsiao, A. Y.; Ge, C. X.; Hsiong, S.; Huebsch, N.; Franceschi, R.; Mooney, D. J.; Takayama, S., Patterning alginate hydrogels using light-directed release of caged calcium in a microfluidic device. *Biomedical Microdevices* **2010,** *12* (1), 145-151.

51. Benjamin, A. D.; Abbasi, R.; Owens, M.; Olsen, R. J.; Walsh, D. J.; LeFevre, T. B.; Wilking, J. N., Light-based 3D printing of hydrogels with high-resolution channels. *Biomedical Physics & Engineering Express* **2019,** *5* (2).

52. Grigoryan, B.; Paulsen, S. J.; Corbett, D. C.; Sazer, D. W.; Fortin, C. L.; Zaita, A. J.; Greenfield, P. T.; Calafat, N. J.; Gounley, J. P.; Ta, A. H.; Johansson, F.; Randles, A.; Rosenkrantz, J. E.; Louis-Rosenberg, J. D.; Galie, P. A.; Stevens, K. R.; Miller, J. S., BIOMEDICINE Multivascular networks and functional intravascular topologies within biocompatible hydrogels. *Science* **2019,** *364* (6439), 458-+.

53. Goy, C. B.; Chaile, R. E.; Madrid, R. E., Microfluidics and hydrogel: A powerful combination. *React Funct Polym* **2019,** *145*.

54. Zhou, Y. F., The recent development and applications of fluidic channels by 3D printing. *J Biomed Sci* **2017,** *24*.

55. Koo, H. J.; Velev, O. D., Design and characterization of hydrogel-based microfluidic devices with biomimetic solute transport networks. *Biomicrofluidics* **2017,** *11* (2).

56. Xia, C. G.; Fang, N. X., 3D microfabricated bioreactor with capillaries. *Biomedical Microdevices* **2009,** *11* (6), 1309-1315.

57. Dhariwala, B.; Hunt, E.; Boland, T., Rapid prototyping of tissue-engineering constructs, using photopolymerizable hydrogels and stereolithography. *Tissue Eng* **2004,** *10* (9-10), 1316-1322.

58. Spicer, C. D., Hydrogel scaffolds for tissue engineering: the importance of polymer choice. *Polym Chem-Uk* **2020,** *11* (2), 184-219.

59. Schaffner, M.; Ruhs, P. A.; Coulter, F.; Kilcher, S.; Studart, A. R., 3D printing of bacteria into functional complex materials. *Sci Adv* **2017,** *3* (12).

60. Ogawa, M.; Higashi, K.; Miki, N., Microbial Production inside Microfabricated Hydrogel Microtubes. *2015 Transducers - 2015 18th International Conference on Solid-State Sensors, Actuators and Microsystems (Transducers)* **2015**, 1692-1694.

61. Bertassoni, L. E.; Cecconi, M.; Manoharan, V.; Nikkhah, M.; Hjortnaes, J.; Cristino, A. L.; Barabaschi, G.; Demarchi, D.; Dokmeci, M. R.; Yang, Y. Z.; Khademhosseini, A., Hydrogel bioprinted microchannel networks for vascularization of tissue engineering constructs. *Lab on a Chip* **2014,** *14* (13), 2202-2211.

62. Sooppan, R.; Paulsen, S. J.; Han, J.; Ta, A. H.; Dinh, P.; Gaffey, A. C.; Venkataraman, C.; Trubelja, A.; Hung, G.; Miller, J. S.; Atluri, P., In Vivo Anastomosis and Perfusion of a Three-Dimensionally-Printed Construct Containing Microchannel Networks. *Tissue Eng Part C Methods* **2016,** *22* (1), 1-7.

63. Kinstlinger, I. S.; Miller, J. S., 3D-printed fluidic networks as vasculature for engineered tissue. *Lab Chip* **2016,** *16* (11), 2025-43.

64. Miller, J. S.; Stevens, K. R.; Yang, M. T.; Baker, B. M.; Nguyen, D. H. T.; Cohen, D. M.; Toro, E.; Chen, A. A.; Galie, P. A.; Yu, X.; Chaturvedi, R.; Bhatia, S. N.; Chen, C. S., Rapid casting of patterned vascular networks for perfusable engineered three-dimensional tissues. *Nature Materials* **2012,** *11* (9), 768-774.

65. Nie, J.; Fu, J. Z.; He, Y., Hydrogels: The Next Generation Body Materials for Microfluidic Chips? *Small* **2020,** *16* (46).

66. Wong, A. P.; Perez-Castillejos, R.; Love, J. C.; Whitesides, G. M., Partitioning microfluidic channels with hydrogel to construct tunable 3-D cellular microenvironments. *Biomaterials* **2008,** *29* (12), 1853-1861.

67. Christensen, A. M.; Chang-Yen, D. A.; Gale, B. K., Characterization of interconnects used in PDMS microfluidic systems. *J Micromech Microeng* **2005,** *15* (5), 928-934.

68. Chang, W. J.; Akin, D.; Sedlak, M.; Ladisch, M. R.; Bashir, R., Poly(dimethylsiloxane) (PDMS) and silicon hybrid biochip for bacterial culture. *Biomedical Microdevices* **2003,** *5* (4), 281-290.

69. Faley, S. L.; Baer, B. B.; Larsen, T. S. H.; Bellan, L. M., Robust fluidic connections to freestanding microfluidic hydrogels. *Biomicrofluidics* **2015,** *9* (3).

70. Hu, R. Q.; Li, F.; Lv, J. Q.; He, Y.; Lu, D. T.; Yamada, T.; Ono, N., Microfluidic analysis of pressure drop and flow behavior in hypertensive micro vessels. *Biomedical Microdevices* **2015,** *17* (3).

71. Patel, J. N.; Kaminska, B.; Gray, B. L.; Gates, B. D., PDMS as a sacrificial substrate for SU-8-based biomedical and microfluidic applications. *J Micromech Microeng* **2008,** *18* (9).

72. Ravetz, J. R., The Rational Mechanics of Flexible or Elastic Bodies - Truesdell,C. *Isis* **1962,** *53* (172), 263-266.

73. Yanez-Soto, B.; Liliensiek, S. J.; Murphy, C. J.; Nealey, P. F., Biochemically and topographically engineered poly(ethylene glycol) diacrylate hydrogels with biomimetic characteristics as substrates for human corneal epithelial cells. *Journal of Biomedical Materials Research Part A* **2013,** *101* (4), 1184-1194.

74. Seymour, R. S.; Blaylock, A. J., The principle of laplace and scaling of ventricular wall stress and blood pressure in mammals and birds. *Physiol Biochem Zool* **2000,** *73* (4), 389-405.

75. Bhargava, K. C.; Thompson, B.; Malmstadt, N., Discrete elements for 3D microfluidics. *P Natl Acad Sci USA* **2014,** *111* (42), 15013-15018.

76. Loskill, P.; Marcus, S. G.; Mathur, A.; Reese, W. M.; Healy, K. E., mu Organo: A Lego (R)-Like Plug & Play System for Modular Multi-Organ-Chips. *Plos One* **2015,** *10* (10).

77. Ong, L. J. Y.; Ching, T.; Chong, L. H.; Arora, S.; Li, H.; Hashimoto, M.; DasGupta, R.; Yuen, P. K.; Toh, Y. C., Self-aligning Tetris-Like (TILE) modular microfluidic platform for mimicking multi-organ interactions. *Lab on a Chip* **2019,** *19* (13), 2178-2191.

78. Miserendino, S.; Tai, Y. C., Modular microfluidic interconnects using photodefinable silicone microgaskets and MEMS O-rings. *Sensor Actuat a-Phys* **2008,** *143* (1), 7-13.

79. Justin, A. W.; Brooks, R. A.; Markaki, A. E., Multi-casting approach for vascular networks in cellularized hydrogels. *J R Soc Interface* **2016,** *13* (125).

80. Golden, A. P.; Tien, J., Fabrication of microfluidic hydrogels using molded gelatin as a sacrificial element. *Lab on a Chip* **2007,** *7* (6), 720-725.

81. Nie, J.; Gao, Q.; Wang, Y. D.; Zeng, J. H.; Zhao, H. M.; Sun, Y.; Shen, J.; Ramezani, H.; Fu, Z. L.; Liu, Z. J.; Xiang, M. X.; Fu, J. Z.; Zhao, P.; Chen, W.; He, Y., Vessel-on-a-chip with Hydrogel-based Microfluidics. *Small* **2018,** *14* (45).

82. LaFratta, C. N.; Li, L. J., Making Two-Photon Polymerization Faster. *Micro Nano Technol* **2016**, 221-241.

83. LaFratta, C. N.; Baldacchini, T.; Farrer, R. A.; Fourkas, J. T.; Teich, M. C.; Saleh, B. E. A.; Naughton, M. J., Replication of two-photon-polymerized structures with extremely high aspect ratios and large overhangs. *Journal of Physical Chemistry B* **2004,** *108* (31), 11256-11258.

84. Markert, C. D.; Guo, X. Y.; Skardal, A.; Wang, Z.; Bharadwaj, S.; Zhang, Y. Y.; Bonin, K.; Guthold, M., Characterizing the micro-scale elastic modulus of hydrogels for use in regenerative medicine. *J Mech Behav Biomed* **2013,** *27*, 115-127.

85. Fairbanks, B. D.; Schwartz, M. P.; Bowman, C. N.; Anseth, K. S., Photoinitiated polymerization of PEG-diacrylate with lithium phenyl-2,4,6-trimethylbenzoylphosphinate: polymerization rate and cytocompatibility. *Biomaterials* **2009,** *30* (35), 6702-6707.

86. Della Sala, F.; Biondi, M.; Guarnieri, D.; Borzacchiello, A.; Ambrosio, L.; Mayol, L., Mechanical behavior of bioactive poly(ethylene glycol) diacrylate matrices for biomedical application. *J Mech Behav Biomed* **2020,** *110*.

87. Xu, C. C.; Dai, G. H.; Hong, Y., Recent advances in high-strength and elastic hydrogels for 3D printing in biomedical applications. *Acta Biomaterialia* **2019,** *95*, 50-59.

88. Ahearne, M.; Yang, Y.; El Haj, A. J.; Then, K. Y.; Liu, K. K., Characterizing the viscoelastic properties of thin hydrogel-based constructs for tissue engineering applications. *J R Soc Interface* **2005,** *2* (5), 455-463.

89. Sun, M. Y.; Sun, X. T.; Wang, Z. Y.; Guo, S. Y.; Yu, G. J.; Yang, H. Z., Synthesis and Properties of Gelatin Methacryloyl (GelMA) Hydrogels and Their Recent Applications in Load-Bearing Tissue. *Polymers-Basel* **2018,** *10* (11).

90. Stammen, J. A.; Williams, S.; Ku, D. N.; Guldberg, R. E., Mechanical properties of a novel PVA hydrogel in shear and unconfined compression. *Biomaterials* **2001,** *22* (8), 799-806.

91. Raman, R.; Bhaduri, B.; Mir, M.; Shkumatov, A.; Lee, M. K.; Popescu, G.; Kong, H.; Bashir, R., High-Resolution Projection Microstereolithography for Patterning of Neovasculature. *Adv Healthc Mater* **2016,** *5* (5), 610-9.

92. Jacobs, P. F., *Rapid Prototyping & Manufacturing: Fundamentals of StereoLithography*. 1992.

CHAPTER FIVE

LIGHT-BASED 3D PRINTING OF HYDROGELS WITH HIGH-RESOLUTION CHANNELS

Contribution of Authors and Co-Authors

Manuscript in Chapter 5

Author: Aaron D. Benjamin

Contributions: Planned and performed the experiments, analyzed the data, and wrote the manuscript.

Author: Reha Abbasi

Contributions: Performed the experiments, analyzed the data, and wrote the manuscript.

Co-Author: Madison Owens

Contributions: Performed the experiments, analyzed the data, and wrote the manuscript.

Co-Author: Robert J. Olsen

Contributions: Performed the experiments, analyzed the data, and wrote the manuscript.

Co-Author: Danica J. Walsh

Contributions: Performed the experiments.

Co-Author: Thomas B. LeFevre

Contributions: Performed the experiments and analyzed the data.

Co-Author: James N. Wilking

Contributions: Planned and oversaw the experiments, analyzed the data, and wrote the manuscript.

Manuscript Information

Aaron D. Benjamin*, Reha Abbasi*, Madison Owens, Robert J. Olsen, Danica J. Walsh, Thomas B. LeFevre, and James N. Wilking

Biomedical Physics & Engineering Express

*co-first author

Status of Manuscript:
____ Prepared for submission to a peer-reviewed journal
____ Officially submitted to a peer-reviewed journal
____ Accepted by a peer-reviewed journal
__X__ Published in a peer-reviewed journal

DOI: 10.1088/2057-1976/aad667

Published by IOP Publishing Ltd
Biomedical Physics & Engineering Express, Volume 5, Number 2

Abstract

Hydrogels are soft, water-based gels with widespread applications in personal care products, medicine and biomedical engineering. Many applications require structuring the hydrogel into complex three-dimensional (3D) shapes. For these applications, light-based 3D printing methods offer exquisite control over material structure. However, the use of these methods for structuring hydrogels is underdeveloped. In particular, the ability to print hydrogel objects containing internal voids and channels is limited by the lack of well-characterized formulations that strongly attenuate light and the lack of a theoretical framework for predicting and mitigating channel occlusion. Here we present a combined experimental and theoretical approach for creating well-defined channels with any orientation in hydrogels using light-based 3D printing. This is achieved by the incorporation of photoblocker and the optimization of print conditions to ensure layer-layer adhesion while minimizing channel occlusion. To demonstrate the value of this approach we print hydrogels containing individual spiral channels with centimeter-scale length and submillimeter-scale cross-section. While the channels presented here are relatively simple, this same approach could be used to achieve more complex channel designs mimicking, for example, the complex vasculature of living organisms. The low cytotoxicity of the gel makes the formulation a promising candidate for biological applications.

Introduction

Hydrogels are water-based gels comprised of polymer dissolved in water and crosslinked to form a solid[1-3]. Typically, hydrogels contain a low mass fraction of polymer; thus, they are soft and easily deformed. In addition, many hydrogels are compatible with biological systems[4] and have widespread applications in personal care products[5], medicine[6-9], and bioengineering[10, 11]. For many applications, the ability to form soft hydrogel into complex, three-dimensional structures is critical. For example, when hydrogel is used as a tissue scaffold[12] internal channels with high permeability to liquid flow must be incorporated to mimic tissue vasculature and maintain cell viability[13-16]. Likewise, in microfabrication, the ability to control hydrogel structure with high fidelity is important[7, 17, 18]. Applications such as these require methods and technologies for accurately and precisely building hydrogel objects with complex, sub-millimeter-scale structures.

Three-dimensional (3D) printing technologies provide exquisite control over material structure[19]. For example, in fused deposition modeling (FDM) printing, a three-dimensional object is built layer-by-layer by extruding thermoplastic from a nozzle, which is translated in the *xy*-plane. Modified versions of these extrusion-based printers have been used to print hydrogels[20, 21] but are limited by their resolution and speed. By contrast, light-based 3D printing methods can be used to form objects much faster and with finer spatial resolution than FDM printers[22, 23]. These printers rely on photopolymerization to initiate the polymerization of a liquid into a solid. This is achieved by projecting a 2D pattern of light (digital light processing (DLP))[24, 25] or by raster-scanning a beam of laser light (stereolithography (SLA))[22, 26] into a photocrosslinkable liquid. Yet, despite their tremendous potential, formulations and techniques for printing hydrogels using light-based printers remain limited.

A primary issue limiting light-based 3D printing of hydrogels is the lack of a generalized approach to create objects with high resolution internal channels and voids in any desired orientation while minimizing channel occlusion (e.g. “bleedthrough”). This requires proper attenuation of the light[26, 27] and a quantitative understanding of the relationship between formulation composition and light exposure conditions. Hydrogel structures containing submillimeter-scale voids that are constrained with axes oriented parallel or perpendicular to the light path (*z*-axis) have been reported[28, 29], and printed hydrogels containing submillimeter-scale channels with no orientation restrictions have recently been reported[27]; however, a generalizable approach for optimizing critical parameters such as layer resolution and light attenuation while mitigating channel occlusion is lacking. This is needed to optimize new photocrosslinkable liquid formulations (i.e. “resins”) for hydrogel printing and provide a framework for understanding the experimental limits of channel resolution. Complex internal channels are essential for a variety of bioengineering applications, but, without a clear optimization approach, the full potential of light-based printers cannot be met.

Here we present a generalizable method for light-based 3D printing of hydrogels containing well-defined, submillimeter-scale channels with any orientation. To characterize a new formulation, we begin by systematically measuring the single-layer cure depth as a function of light exposure and photoblocker concentration. Next, we determine the print conditions needed to adhere one layer to another by systematically varying single-layer cure depth and instrument-imposed layer thickness. Finally, we measure channel bleedthrough as a function of layer thickness, use this data to test bleedthrough models, and find that the effect of cumulative exposure contributes significantly to channel bleedthrough. To demonstrate the practicality of our approach,

we print hydrogels containing spiral channels with centimeter-scale length and submillimeter-scale cross-section and establish liquid flow through these channels.

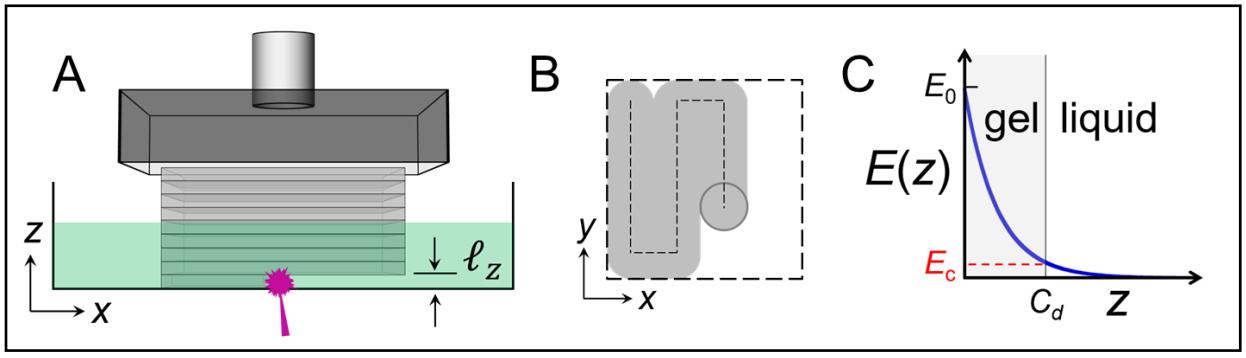


Figure 5.1. *Light-based stereolithographic 3D printing.* (**A**) Illustration of a stereolithography (SLA)-based 3D printer used to print hydrogel. An object is printed layer-by-layer by polymerization of a liquid resin (green) to a solid upon exposure to laser light (violet). Layer thickness, ℓ_z is set by the gap between the underside of the object and the bottom surface of the resin tray. (**B**) A single layer in the xy plane is formed by raster-scanning a focused laser light spot (circle) within the plane. (**C**) Light is attenuated by the liquid resin, and light exposure, E(z) decreases with depth, z. At a critical exposure value, E_c, the light is insufficient to induce polymerization and this defines the cure depth, $\boldsymbol{C_d}$ beyond which resin remains liquid.

Background

In stereolithography (SLA)-based 3D printing, a solid object is built layer-by-layer from a liquid resin using a focused laser spot. Photopolymerization occurs at the laser focal point, which is raster-scanned within the *xy*-plane of the resin bath to create a single layer which adheres to the print head (**Fig. 5.1a, b**). The print head is then moved upwards in the *z*-direction and the next layer is printed onto the previous layer. Polymerization typically occurs through free-radical transfer: a photoinitiator absorbs laser light to form a reactive species and initiates a reaction cascade by which low molecular weight monomers react to form high molecular weight polymers and eventually a crosslinked solid. The polymerization process terminates through free radical

combination or when free radicals become topologically constrained[26]; thus, the reaction does not propagate through the entire bath after polymerization is initiated by the laser light.

As each successive layer is added to a printed object, the laser light needed to polymerize a new layer passes into previously printed layers (**Fig. 5.1a**). This condition is necessary for the adhesion of one layer to the next but can be problematic if the printed object is meant to contain voids or overhangs and bleedthrough occurs in these regions. Light is attenuated as it propagates into the resin, so the intensity decreases with penetration depth, z. At some depth, the light becomes insufficient to induce polymerization; this is referred to as the cure depth, C_d, beyond which the resin remains liquid (**Fig. 5.1c**). For an object composed of multiple layers, the balance between necessary overlap and undesired curing can be determined by comparing two lengths: the layer thickness, ℓ_z, which is set by the incremental, vertical movement of the print head, and the cure depth, C_d, which is set by the composition of the resin. Thus, when formulating a new resin, knowledge of C_d is critical.

A variety of photopolymerizable hydrogel formulations for use with 3D printing have been reported, including polyethylene glycol-diacrylate (PEG-DA) gels[19, 30], polyethylene glycol-diacrylamide (PEG-DAAm) gels[31], and Pluronic monocarboxylate-gelatin methacrylate (Plu-GelMA) composite gels[32, 33]; however, knowledge of how formulation variables affect printing parameters such as C_d is lacking. As a result, it is difficult to quantify and compare advances in the spatial resolution of light-based hydrogel printing. Additionally, most studies focus on digital light projection (DLP) systems or SLA printers which use ultraviolet light, and, to our knowledge, no studies involving SLA printers that make use of violet (λ = 405 nm) light have been reported. This may be important if living cells are incorporated into the liquid resin and exposed to laser

light during the printing process as violet light is lower in energy than ultraviolet light, is not strongly absorbed by DNA[34], and has shown to be less cytotoxic for a variety of mammalian cells[35-38].

In this context, we focus on characterizing a photopolymerizable hydrogel resin formulation for use with violet laser light that can be used to generate hydrogels with high-resolution internal channels using components that are generally accepted as non-cytotoxic. Two primary components of any photopolymerizable formulation are a reactive monomer and a photoinitiator. For the hydrogel monomer, we choose PEG-DA to create PEG-based hydrogels, which are considered a benchmark for non-cytotoxic hydrogels[4, 39]. Mammalian cells do not adhere to PEG gels, so, for applications incorporating living cells, the gel would need to be functionalized[19, 30, 31]; however, for the purposes of this study, we use non-functionalized PEG. For the photoinitiator, we choose lithium phenyl-2,4,6-trimethylbenzoylphospinate (LAP)[40, 41]. LAP is freely soluble in water, has been shown to be biologically inert[40], and absorbs light in the UV and low visible range with high efficiency. This formulation pair is well-established for a variety of non-3D printing hydrogel applications; however, when printing is attempted using a light-based 3D-printer (Formlabs, Form 1+), the polymerized gel layers are very thick. Thus, a third formulation component, one that strongly attenuates the laser light, is required: a photoblocker. This component is critical for achieving high-resolution printing with any light-based 3D printer (e.g. SLA or DLP). Several photoblockers including Quinolone Yellow[27] and Sudan I[42] have been reported for use in photopolymerizable hydrogel applications. Here we explore the use of chlorophyllin and tartrazine. Chlorophyllin is a hydrolyzed version of chlorophyll that is soluble in water and strongly absorbs blue-violet light (Supplemental Information, SI Fig.1)[43]. Tartrazine

is yellow azo dye commonly found in food coloring, with strong absorbance at 405 nm[44]. To our knowledge, this is the first reported use of both these compounds as photoblockers for photopolymerization applications.

Results & Discussion

For the hydrogel formulations used here, light attenuation is dominated by the photoblocker. In the absence of photoblocker, the aqueous PEG-DA/LAP print formulation provides a cure depth on the order of centimeters (**Fig. 5.2a**; $C_d \approx 1.85$ cm) for moderate exposures on a commercially available 3D SLA printer (see Methods). By comparison, under identical print conditions, the addition of chlorophyllin at a concentration of only 0.01 wt% results in a striking reduction in cure depth (**Fig. 5.2b**; $C_d \approx 0.50$ mm). To quantify the capacity of chlorophyllin as a photoblocker, we systematically measure C_d as a function of light exposure and chlorophyllin concentration. We do this experimentally by removing the print head, printing a single layer, which adheres to the bottom surface of the resin tray, and measuring the thickness of that layer with optical coherence tomography (see Methods and SI Fig. 2). Light exposure is defined as the total integrated energy of laser light that passes through a given area. For an SLA printer, exposure is proportional to laser power and inversely proportional to the velocity at which the laser is scanned (see Methods). The exposure profile in z is expected to fall off exponentially as $E(z) = E_0 \exp(-z/D_p)$, where E_0 is the exposure at the bottom of the resin tray just as the laser light enters the resin ($z = 0$), and the penetration depth, D_p is the length scale that characterizes the exponential decay. Setting $z = C_d$, defining E at this depth as the critical exposure, E_c below which a gel does not form, and solving for C_d provides the following: $C_d = D_p \ln(E_0/E_c)$, as shown

elsewhere [26, 40, 45]. Thus, plotting C_d as a function of E_0 on a linear-log scale should provide a straight line with a slope of D_p and an *x*-intercept corresponding to E_c, as has been shown

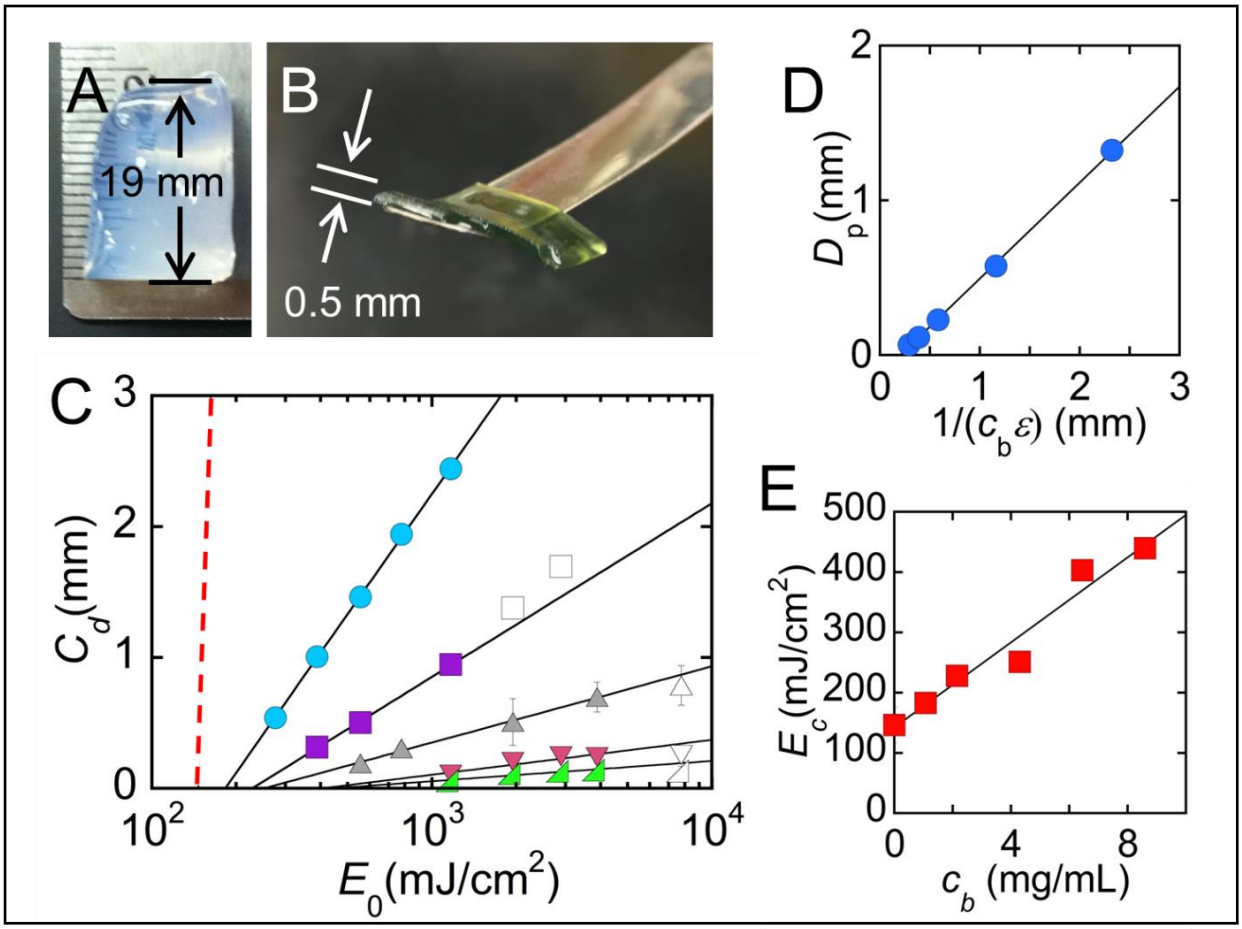


Figure 5.2. *Chlorophyllin as a photoblocker*. Photographs of PEG-DA hydrogel single layers printed (**A**) without photoblocker and (**B**) with 0.01 wt% chlorophyllin photoblocker using an SLA 3D printer with the same exposure conditions. Thickness of the gel represents the cure depth, C_d. (**C**) Single layer cure depth, C_d as a function of light exposure, E_0 for PEG-DA/LAP aqueous formulations with different chlorophyllin concentrations (c_b = 0.108 (•), 0.215 (■), 0.430 (▲), 0.645 (▼), 0.860 (right triangle) mg/mL). Lines are fits of solid symbols to $C_d = D_p \ln(E_0/E_c)$ (0.108 mg/mL, R^2 = 0.999; 0.215 mg/mL, R^2 = 0.999; 0.430 mg/mL, R^2 = 0.996; 0.645 mg/mL, R^2 = 0.876; 0.860 mg/mL, R^2 = 0.920). Open symbols not included in fit. Red, dashed line is fit to data for c_b = 0 mg/mL, which are out of scale (C_d > 3 mm) and thus not shown (see Methods). (**D**) Characteristic length scale associated with light attenuation, D_p as extracted from the slope of the fits in (C), and plotted as a function of $(c_b \varepsilon)^{-1}$ (R^2 = 0.999). (**E**) Critical exposure, E_c determined from the *x*-intercept of the fits in (C) and plotted as a function of c_b (R^2 = 0.880).

extensively in the light-based 3D printing literature[26, 28].

We find that our data obtained with low to moderate exposure values are described well by the theoretical prediction. Plots of C_d versus E_0 for five different chlorophyllin concentrations, c_b = 0.108, 0.215, 0.430, 0.645, and 0.860 mg/mL are shown in **Fig. 5.2c**, with fits to the solid symbols. As expected, the characteristic penetration depth, D_p, described by the slope of each fit, decreases with increasing chlorophyllin concentration; that is, more chlorophyllin results in more attenuation. For very high exposure values, the data diverges slightly from the fit. For the three highest concentrations (c_b = 0.430, 0.645, and 0.860 mg/mL) the data at high exposure values demonstrates sub-logarithmic behavior. This has been reported previously for non-hydrogel resins, and has been attributed to the potential development of inclusions in the gel at high exposures, which result in scattering[26]. The next lowest concentration (c_b = 0.215 mg/mL) exhibits super-logarithmic behavior at high exposures. This has been reported previously as well, and has been attributed to photobleaching and self-focusing[26]. These deviations are irrelevant for most 3D printing applications where exposure values $E_0 \leq 10^3$ mJ/cm^2 are sufficient.

To better understand the dependence of D_p on c_b, we consider the Beer-Lambert Law, $A = \varepsilon L c_b$, which relates the absorbance of light, A, to the absorptivity coefficient ε, the path length traveled by light L, and concentration c_b. Absorbance is commonly defined as $A = \log_{10}(I_0/I(L))$, where I_0 is the intensity of the incident light and $I(L)$ is the intensity of the light after passing through a sample of thickness L. Absorbance can also be expressed in terms of exposure: $A = \log_{10}(E_0/E(L))$. Setting $E(L) = E(C_d)$, combining with the Beer-Lambert relationship, and solving for C_d provides $C_d = (1/\varepsilon c_b)\log_{10}(E_0/E_c)$. Combining this equation with the previously described equation for C_d yields $D_p = a/(\varepsilon c_b)$, where the coefficient a, the

consequence of a change of base, should equal 0.4343. This provides a theoretical prediction of the relationship between D_p and c_b. To test this prediction, we plot D_p as a function of $1/(\varepsilon c_b)$, as shown in **Fig. 5.2d**. The linearity of the resulting plot is striking, and the data fits well to the following form: $D_p = [a/(\varepsilon c_b)] - b$, where $a = 0.6208$ and $b = 0.1265$. While the physical origin of the difference in the slope, a, and the presence of an offset, b is unclear, the $1/c_b$ scaling above b captures the basic physics of photoblocker attenuation. Preliminary results with photoblockers such as tartrazine, fast green FCF, and sunset yellow show better agreement with our theoretical prediction, a topic which warrants further study.

The minimum exposure required for gel formation is defined as the critical exposure E_c and can be determined from the *x*-intercept for each curve in **Fig. 5.2c** as the cure depth goes to zero. We plot E_c as a function of c_b and find that E_c increases proportionally with c_b from a constant value at c_b = 0 (**Fig. 5.2e**). In free-radical photopolymerization reactions, the presence of oxygen, which is a known scavenger of free radicals, has been shown to increase E_c[26]. Thus, it is not surprising that chlorophyllin, which is also known to react with free radicals, has a similar effect. The minimal increase in E_c due to chlorophyllin should not inhibit printing since the E_c values at the highest c_b are at least an order of magnitude below exposures easily achieved with available violet lasers on commercially available printers. However, the increase in E_c may become important when attempting to both maximize spatial resolution and minimize light exposure.

To move beyond single layers and print 3D objects containing internal voids, layer-layer adhesion must be ensured while minimizing bleedthrough. To find the optimal balance between these opposing factors, we design a test geometry: a hydrogel cube (dimensions: 6 mm × 6 mm × 6 mm) containing an internal, fully-enclosed rectangular channel with a square cross-section

(dimensions: 1.5 mm × 1.5 mm × 3 mm; see SI Fig. 2.3). The enclosed channel design prevents the exchange of liquid between the channel and resin bath and thus represents conditions which will result in maximal channel bleedthrough, h_e such as a channel printed deep within a hydrogel where liquid exchange is limited. Intuition suggests that layer-layer adhesion will be achieved by meeting the condition $C_d \geq \ell_z$. To test this, we print the test geometry under varied conditions of ℓ_z and C_d. We vary ℓ_z over the range 6.25 μm ≤ ℓ_z ≤ 300 μm by controlling the gap between the underside of the printed object and inner surface of the resin tray, and vary C_d from 100 μm, 150 μm, and 200 μm by selecting E_0 from the working curves in **Fig. 5.2c**. After printing, we evaluate each cube for layer-to-layer adherence and mechanical integrity using stereomicroscopy and classify the print as a success or failure.

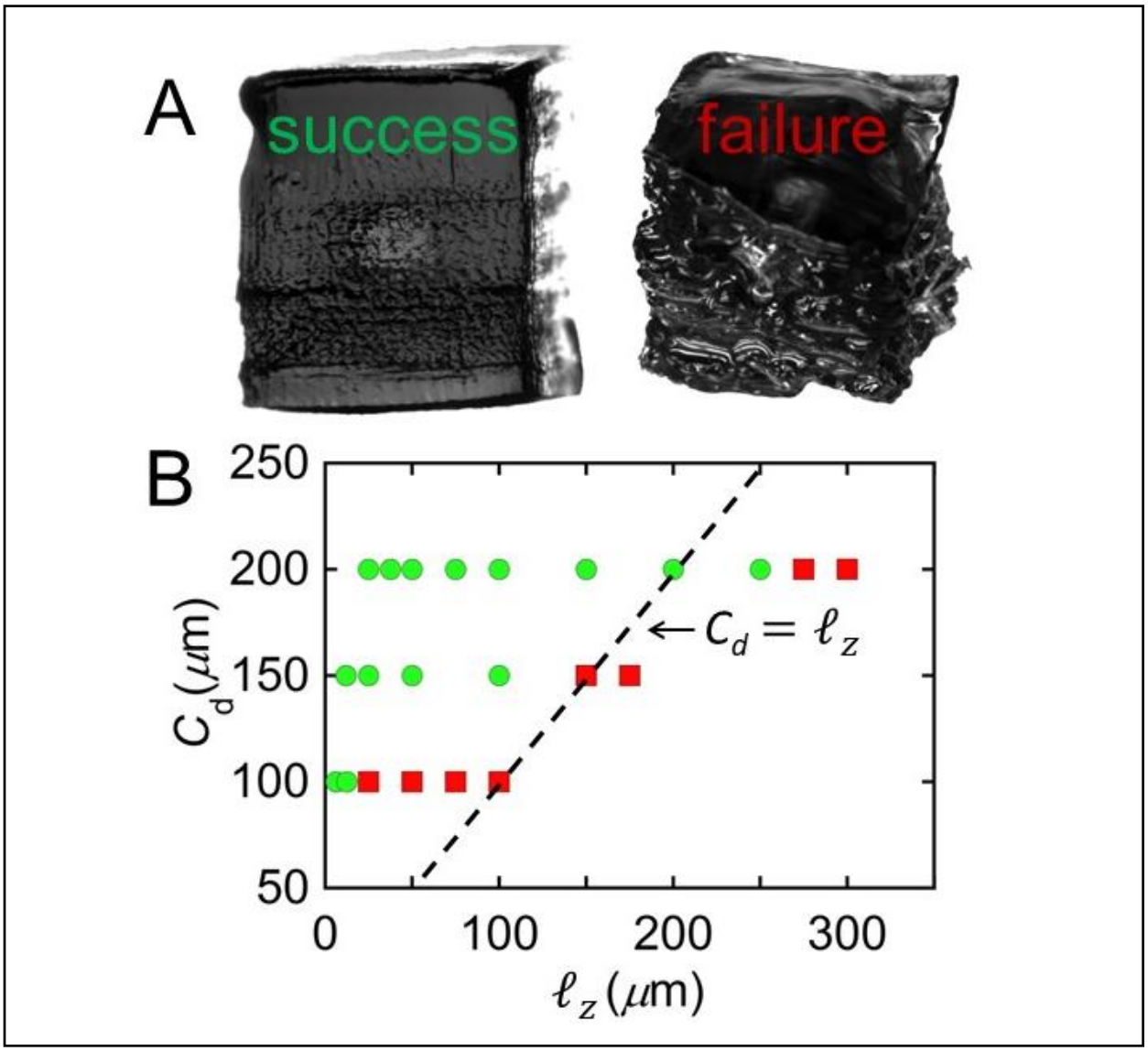


Figure 5.3. *Determining optimal layer-layer adhesion conditions for printing 3D objects.* (**A**) Stereomicroscopy images of hydrogel test cubes (outer dimensions: 6 mm × 6 mm × 6 mm) each printed under defined conditions (left: $\boldsymbol{C_d}$ = 150 μm, ℓ_z = 25 μm; right: $\boldsymbol{C_d}$ = 150 μm, ℓ_z = 150 μm) then imaged and classified as a success or failure. The success-failure criterion was based on mechanical integrity and not surface irregularities, which are an aesthetic issue that is straightforward to address. (**B**) Plot of $\boldsymbol{C_d}$ versus ℓ_z generated from the classification of 22 individual cubes printed with $\boldsymbol{c_b}$ = 0.430 mg/mL. Prints that retain mechanical integrity are plotted as green circles and prints that do not retain integrity are plotted as red squares. Dashed line represents the expected success-failure boundary, $\boldsymbol{C_d} = \ell_z$.

For print conditions where $\ell_z > C_d$, a newly-cured layer should have insufficient thickness to bridge the gap between the bottom of the tray and the bottom surface of the previous printed layer. Thus, one would expect print failure due to non-adherence between layers. We find that near the $\ell_z = C_d$, boundary, layers still adhere to one another, but the object collapses and deforms as it is printed (**Fig. 5.3a**, right: failure). As ℓ_z is increased, we eventually observe total failure; layers do not adhere to one another and remain dispersed in the resin bath (not shown). Surface irregularities are not used as a criterion for success-failure as successfully printed objects well within the $\ell_z < C_d$ region have rough surfaces (**Fig. 5.3a**, left: success). This issue, which is common with light-based 3D printers, is easily resolved by including a high-exposure raster step around the boundary of each layer, creating a smooth outer surface. For layer-layer adhesion tests, this step was excluded.

Results for all printed objects are compiled as a plot of C_d versus ℓ_z in **Fig. 5.3b**. Here, each data point represents an individually-printed cube, with green circles corresponding to successful prints and red squares corresponding to failed prints. The data falls into two regions, with successful prints at low ℓ_z, failed prints at high ℓ_z, and a distinct transition between success and failure. Successfully-printed objects subjected to tensile and shear stresses do not fail along layer-layer interfaces. This indicates that the adhesive yield stress is equal to or greater than the cohesive yield stress and that layer-layer adhesion is chemical in nature, rather than mechanical. This is not surprising, given that residual free radicals and unreacted monomers and oligomers remain in previously-printed layers[26] which could lead to reaction and interpenetration between gel layers.

To understand the success-failure transition, we superimpose the defining line at which we would expect layer-layer adhesion to fail: $C_d = \ell_z$. This line represents a boundary to the right of which one would expect objects to lose mechanical integrity. When we overlay this line onto our data, the agreement in the center of our data range ($C_d = \ell_z = 150$ μm) is good; however, at low C_d, the ℓ_z value associated with the transition from success to failure occurs at a lower value than predicted, while at high C_d, the ℓ_z value associated with the transition from success to failure occurs at a greater value than predicted. The discrepancy between our data and the prediction can potentially be explained by several scenarios. First, the resin tray used to determine the working curves in **Fig. 5.2c** differs, by necessity, from the resin tray used to print 3D objects, and differences in tray thickness and material refractive index (see Methods) could result in differences in light attenuation. Second, the gel-liquid boundary is likely not a sharp interface but rather a diffuse boundary, and it is not clear how thick this boundary is or how boundary thickness changes with C_d. Despite the lack of agreement, mapping print parameters in this manner provides a valuable and practical guide for choosing print coordinates.

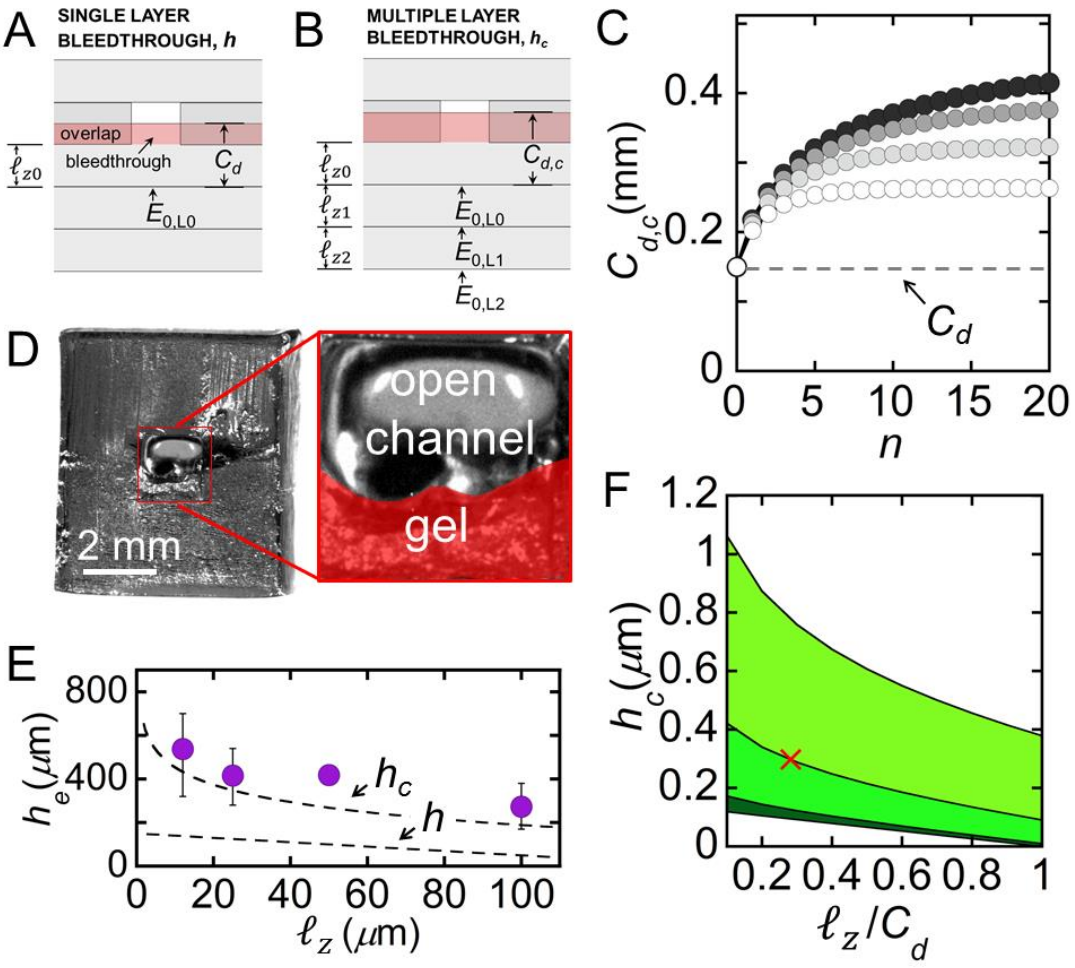


Figure 5.4. *Modeling and measuring channel bleedthrough*. (**A**) *Single-layer model:* The simplest scenario; bleedthrough into a void is just $h = C_d - \ell_z$. In this illustration (A), as well as (B) and (D), the laser is directed upwards along the *z*-axis (from bottom to top). (**B**) *Multiple-layer model*: The effect of repeated exposure results in a cumulative cure depth $C_{d,c}$ larger than C_d. (**C**) Calculated C_d, c as a function of *n* for C_d = 0.15 mm and (from bottom to top) ℓ_z = 12 μm, 25 μm, 50 μm, and 100 μm. (**D**) Image of a hydrogel cube containing an enclosed void space after being cut in half and an exposed face imaged with stereomicroscopy. Channel bleedthrough, h_e is quantified by measuring the extent of channel occlusion (see inset). (**E**) Plot of channel bleedthrough, h_e as a function of layer thickness ℓ_z, for C_d = 0.15 mm and c_b = 0.430 mg/ml. Measured bleedthrough is greater than predicted by the single-layer model (lower dashed line), but consistent with the multiple-layer model (upper dashed line). (**F**) Numerical calculations of h_c as a function of ℓ_z for C_d = 132 μm over the range: 13.2 μm ≤ ℓ_z ≤ 132 μm for differing c_b plotted as a function of ℓ_z/C_d. From top to bottom, the bounding lines represent h_c values for c_b = 0.215 mg/mL, 0.430 mg/mL, and 0.860 mg/mL. The lowest bounding line represents $h = C_d - \ell_z$. The red mark represents print conditions for Fig. 2. 5b, c.

For solid objects with no internal voids or overhangs, choice of print parameters should not significantly affect print quality as long as the parameters fall to the left of the success-fail transition. However, for objects containing internal voids, choice of print parameters will determine the amount of bleedthrough into the void space. To define the expected upper and lower limits of bleedthrough, we construct two models. In the lower limit, bleedthrough is described by considering only the contribution of the layer directly beneath a void. This is simply the difference between the cure depth and layer thickness: $h = C_d - \ell_z$ (**Fig. 5.4a**). In the upper limit, the contribution of multiple subsequent exposures must be considered. That is, when multiple layers are printed beneath a void, even if light is attenuated such that it is below the gelation threshold when it reaches the void, repeated exposure will have a cumulative effect (**Fig. 5.4b**). To model this effect, we define the cumulative incident exposure for a particular layer as $E_{0,c} = (\sum_{i=0}^{n} E_0 10^{-[\varepsilon c_b] i \ell_z})$, where n is the number of layers printed below a void. This summation of exposures is based on the assumption that the same resin volume is being repeatedly exposed and is not mixed in the channel or freely exchanged with the resin bath. The cumulative cure depth is then described as $C_{d,c} = D_p \ln (E_{0,c}/E_c)$ and the overlap is $h_c = C_{d,c} - \ell_z$. It is important to note that the cumulative cure depth, $C_{d,c}$ can be much larger than C_d. To demonstrate this, theoretical predictions for $C_{d,c}$ for C_d = 150 μm and ℓ_z = 12 μm, 25 μm, 50 μm, and 100 μm are plotted as a function of n in **Fig. 5.4c**. For the curves plotted here, $C_{d,c}$ approaches an asymptote, the value of which increases as ℓ_z decreases, and this asymptote in $C_{d,c}$ can be significantly larger than C_d. For example, for C_d = 150 μm and ℓ_z = 100 μm, $C_{d,c} \approx$ 450 μm, three times larger than C_d.

To experimentally determine the extent to which cumulative exposure impacts bleedthrough, we select printed hydrogel cubes, each containing an internal, fully-enclosed

rectangular channel with square cross-section, cut each cube in half, and image the channel cross-section using stereomicroscopy (**Fig. 5.4d**). We do this for four cubes, all printed using C_d = 150 μm (c_b= 0.430 mg/mL), but with varying ℓ_z = 12.5 μm, 25 μm, 50 μm, and 100 μm. After measuring the average bleedthrough in the enclosed channel, h_e, find that h_e decreases with increasing ℓ_z, as expected (**Fig. 5.4e**). To compare our data with the minimum and maximum theoretical estimates for bleedthrough, we include these predictions as dashed lines and find that our measurements agree well with the cumulative model prediction (**Fig. 5.4e**, upper line). This supports our hypothesis that the cumulative effect of repeated exposure must be considered and provides a theoretical framework for minimizing channel occlusion during printing.

To better understand the dependence of h_c on experimental parameters, we rearrange the expression for the cumulative model (see SI Text) to obtain: $h_c = h + D_p \ln(\sum_{i=0}^{n} 10^{-[\varepsilon c_b] i \ell_z})$. This form reveals that for fixed C_d and ℓ_z, h_c should decrease with increasing photoblocker concentration, and, in the limit where $c_b \to \infty$, $h_c \to h$. This can be understood by considering two formulations with different c_b. The solution with greater c_b will have a smaller D_p. Thus, to achieve the same C_d, E_0 for the more concentrated solution must be increased until the exposure curves cross over at the same z value ($z = C_d$). Importantly, beyond this crossover, $E(z)$ will decrease more precipitously for the more concentrated solution than the less concentrated solution. This means that cumulative exposure will decrease with increasing c_b for fixed C_d. To show this, we solve the expression above numerically for our chlorophyllin formulation. We choose C_d = 132 μm, calculate h_c as a function of ℓ_z over the range: 13.2 μm ≤ ℓ_z ≤ 132 μm for c_b= 0.215 mg/mL, 0.430 mg/mL, and 0.860 mg/mL, and plot h_c as a function of ℓ_z/C_d. Our numerical calculations

confirm that h_c decreases with increasing c_b, as shown in **Fig. 5.4f.** This provides a guide for choosing the c_b necessary to print channels of a given size with an acceptable degree of occlusion. To show the value of this approach, we use our results to print hydrogels containing well-defined channels with centimeter-scale length, submillimeter-scale cross-section and varying orientation. We do this by choosing print conditions (C_d = 132 μm and ℓ_z = 37.5 μm) that lie within the success region in **Fig. 5.3b**. Under these conditions, for c_b= 0.430 mg/mL and $\ell_z/C_d = 0.28$, the estimated value of cumulative bleedthrough is $h_e \approx 200$ μm (**Fig. 5.4f**, red mark). A spiral channel geometry is chosen as a printing benchmark because the channel orientation varies continuously between vectors parallel and perpendicular to the light-path throughout the length of the channel, and print success is easily determined by observation of flow through the channel. An illustration of the print design is shown in **Fig. 5.5a**, and liquid flow through the printed object is shown by the series of microscopy images in **Fig. 5.5b**. In these images, air bubbles entrained in the liquid provide an indication of flow. The inscribed sectional diameter of the channel in the print file is 800 μm, and the inscribed sectional diameter of the channel in the printed object is approximately 600 μm. This is consistent with our bleedthrough prediction. To illustrate a slightly more complex channel design, we use the same conditions to print an object containing two separate, co-rotating spiral channels as shown in **Fig. 5.5c**. While the channels presented here are simple we fully expect to achieve channels approaching *in vivo* complexity. To print even smaller channels, with minimal bleedthrough, parameters must be chosen such that $\ell_z/C_d \rightarrow 1$ and c_b is sufficiently high such that $h_c \rightarrow h$ (**Fig. 5.4f**).

Lower limits for photoblocker concentration and exposure are set by c_b = 0 mg/mL and E_c, respectively. Upper limits for photoblocker concentration and exposure are set by the saturation

solubility of photoblocker and exposure at which printing parameters begin to deviate from the theoretical prediction. In practice, parameter selection will likely depend on experimental constraints such as chemical and biological compatibility with photoblocker and sensitivity to light exposure. This optimization approach can presumably be used to characterize any light-based 3D printing formulation. To illustrate this point, we replace chlorophyllin with tartrazine and measure C_d as a function of E_0 for c_b = 0.15, 0.30, and 0.45 mg/mL. We find the working curves to be well fit by the theoretical prediction $C_d = D_p \ln(E_0/E_c)$, the characteristic penetration depth to follow $D_p \sim 1/\varepsilon c_b$, and E_c to increase proportionally with c_b from a constant value at c_b = 0 (see SI Fig. 2.4). We then choose print conditions such that $C_d = \ell_z$ = 55 μm, c_b= 0.75 mg/mL and print a single spiral geometry with equivalent dimensions to the chlorophyllin single spiral geometry as pictured in **Fig. 5.5d**. By contrast to chlorophyllin, tartrazine does not bind to the gel; instead, when the hydrogel is placed in water, tartrazine diffuses out of the gel into the water. Thus, tartrazine provides an alternative photoblocker for creating transparent, nearly-colorless hydrogels with complex internal structures. This result supports the validity of our approach and introduces a second photoblocker for use printing hydrogels with violet light.

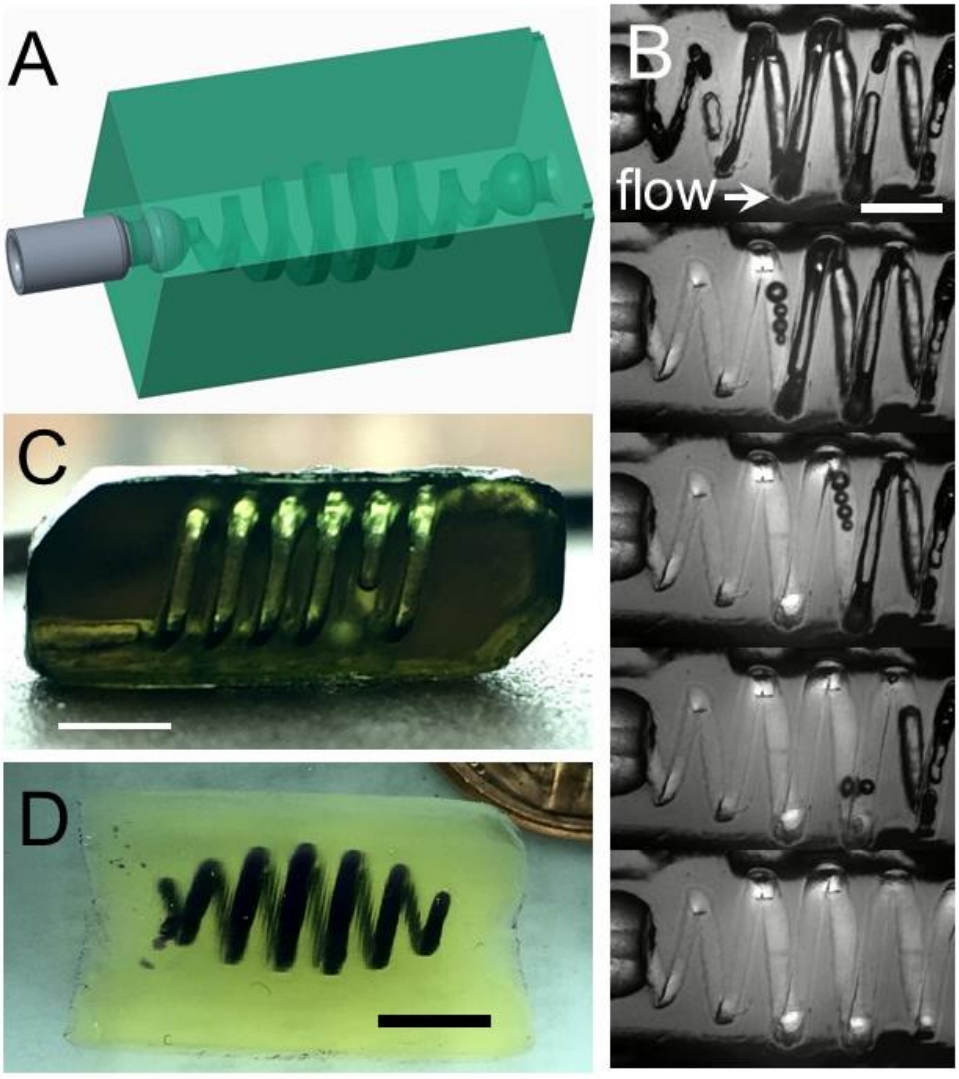


Figure 5.5. *Printed hydrogels with submillimeter channels.* (**A**) Illustration of a rectangular hydrogel containing a single spiral channel. (**B**) Microscopy image series depict flow of aerated liquid through a printed chlorophyllin hydrogel (design from (A)). Images are separated by Δt = 10 s. Scale bar corresponds to 2 mm. (**C**) Photograph of rectangular chlorophyllin-containing hydrogel containing two independent spiral channels. Two input/output channels are apparent on the ends of the rectangular cube; the remaining two are on the back of the cube. Water within the channels was expelled using compressed air for improved channel contrast, though some residual water remains, as apparent from the air-water meniscus in the second channel from the right. (**D**) Hydrogel cube containing a single spiral channel printed using tartrazine as photoblocker. Oil-based paint was injected into the channel for visualization purposes. Scale bars in (C) and (D) correspond to 5 mm.

For the commercial printer used here, the *xy*-resolution of our printed objects is ultimately limited by the beam waist of the focused laser spot (140 μm, FWHM), and the resolution in ℓ_z is limited by the minimum step size of the motor (2.5 μm). These instrument specifications were presumably chosen by the equipment manufacturer to optimize resolution while creating objects with large build volumes; however, improved resolution could be achieved by the incorporation of focusing optics. Custom-built printing setups with highly-focused, diffraction-limited laser light can achieve much finer resolution than this commercial printer; however, it is our expectation that our resin development approach could be used in these printers as well to optimize print parameters.

Conclusion

Here, we present a systematic approach for structuring hydrogels containing well-defined microchannels using light-based 3D printing methods. The components used in the formulation are nontoxic, so the printed gels could potentially be used for applications involving living cells. In addition, the formulation composition could easily be modified to alter the physical and chemical properties of the gel, for example, through the addition of multifunctional crosslinkers or by chemical modification of the monomer. High print resolution is enabled by the incorporation of water-soluble photoblockers, which strongly absorb violet light; chlorophyllin and tartrazine are used here, but other water-soluble compounds that absorb violet light could be used. Our measurements of channel bleedthrough reveal that cumulative exposure contributes to undesired channel occlusion and must be incorporated into future models of channel bleedthrough. Finally, our experimental quantification of cure depth reveals a relationship between characteristic

penetration depth, photoblocker concentration, and photoblocker absorptivity coefficient, which, to our knowledge, has not been reported and could provide an approach for rapidly quantifying new formulations.

Methods

Chemicals

Compounds were purchased from the following manufacturers and used directly without additional purification: polyethylene glycol diacrylate (PEG-DA, MW 700; Sigma Aldrich), lithium phenyl-2,4,6-trimethylbenzoylphosphinate (LAP, TCI Chemicals); sodium copper chlorophyllin (TCI Chemicals), 3-methacryloxypropyltrimethoxysilane (Amersham Biosciences), tartrazine (Fisher Scientific).

Resin formulation

Stock solutions containing 10 wt% PEG-DA and 0.1 wt% LAP dissolved in water were made in 200 mL batches. This concentration of PEG-DA was chosen to create gels with elastic moduli on the order of 10^3 Pa[46]. Each batch was prepared by combining 18 mL PEG-DA, 0.2 g LAP, and 182 mL water. Concentrated photoblocker solution was made by mixing 1 g chlorophyllin in 20 mL deionized water. Chlorophyllin concentrations were then set by adding microliter quantities of the concentrated chlorophyllin solution to milliliter quantities of the stock PEG-DA solution. The resulting dilution of PEG-DA and LAP was considered negligible. Chlorophyllin containing formulations were found to age (see SI Fig. 2.5); thus, for all experiments, solutions were used within 8 h of mixing.

SLA printer

The Form 1+ is a consumer SLA-based 3D printer manufactured by Formlabs (Somerville, MA) with the following specifications: laser wavelength λ = 405 nm (violet); maximum laser power, P_{max} = 62 mW, beam diameter d = 0.16 mm; z-axis minimum step increment, z_d = 2.5 μm;

maximum build volume (OEM) V_{max} = 12.5 cm × 12.5 cm × 16.5 cm (4.9 × 4.9 × 6.5 in).

Modifications

A print head was modeled to match the OEM head thickness reduced by 1 mm and printed in methacrylate on a Form 2 printer. A silanized, 1 mm glass microscopy slide was bonded to the bottom of the head with silicone caulk. A bottomless tray was bonded to the PDMS surface of the OEM resin tray, centered about the modified head, to reduce the volume necessary to fill the tank to a workable printing depth (see SI Fig. 2.6).

Print head silanation

To ensure adhesion of printed hydrogel to the print head, microscopy slides (Fisherbrand Colorfrost, 25 mm x 75 mm x 1 mm) were submerged in a 2.0 vol% solution of 3-trimethoxysilyl) propyl methacrylate in ethanol (Bind-Silane, GE Healthcare, 17-1330-01) for at least five minutes then held at 100°C for five minutes. This is a well-established protocol for coupling polymerizing hydrogel to a glass surface[16].

Print control

OpenFL, a version of Formlabs' proprietary slicing software with user adjustable curing profiles was used to control the 3D printer. All parameters relevant to exposure such as laser power P, laser velocity v, scanline spacing S, number of exposures per layer N, and layer thickness ℓ_z, were adjustable. The average incident exposure per layer per unit area was calculated as: $E_0 = \frac{PN}{Sv}$. This definition is made with the assumption that the sum of multiple repeated low power exposures is equivalent to a single higher power exposure, which has been shown to be valid for current SLA printers. For all prints, the scanline spacing was fixed at S = 0.09 mm for appropriate overlap of

scanlines. Exposure was controlled by (1) increasing *N*, which effectively lengthened the duration of the exposure, (2) reducing *v*, which effectively lengthened the duration of the exposure, or (3) increasing *P*, which kept exposure duration constant.

Cure depth measurements

Single hydrogel layers did not adhere to the bottom of the PDMS-coated, OEM resin tray. Thus, to test single layer cure depth, curing trays were made by gluing large (50 mm x 75 mm x 1 mm) silanized glass slides to the bottom of small bottomless Petri dishes (35 mm inner diameter) using silicone caulk. A clear cast acrylic plate (McMaster Carr, thickness, h = 4.5 mm) was laser cut to replace the OEM resin tray and fit into the resin tray slot (17.3 cm x 19.3 cm) of the printer. In the center of the acrylic, a hole was made to hold a curing tray. A basic working profile, which produced gels of acceptable quality was developed as a baseline for subsequent testing of cure depth. Beginning with the baseline profile, alternate profiles of varying exposures were added by increasing the number of exposures per layer N while keeping all other variables constant. For each measurement, the print head was removed and a single layer printed. The uncured liquid resin remaining in the cup was then discarded, the cup gently rinsed with water, and the gel thickness was measured with optical coherence tomography. Strong adherence of hydrogel layers to the glass-bottom resin tray precluded its use for printing multilayered objects. Differences between the OEM tray and custom, single-layer curing trays may lead to discrepancies between theory and experiment (**Fig. 5.3b**). For example, the OEM tray is composed of two layers: a 6.5 mm thick layer of PMMA (refractive index, n = 1.49) covered with a 1.5 mm thick layer of PDMS (n = 1.40), and the custom tray is composed of one layer of 1.0 mm thick layer of glass (n = 1.52).

OCT measurements

Gel layer thickness measurements were made using an optical coherence tomography machine (Leica Microsystems, Envisu 4310). A rectangular volume capture with two A-scans per pixel, were scanned over a 1 mm x 4 mm area. For samples thicker than 1 mm, a 3 mm x 3 mm area was scanned. The average gel thickness, as well as the upper and lower limits in thickness, were determined by analyzing individual B-scans.

Absorbance measurements

Measurements were performed using a plate reader (Biotek Synergy H1 Hybrid Reader). To hold the samples, a custom-built well plate was printed on the Form 2 printer. Six 25 mm diameter wells were positioned concentric to the equivalent positions of the B2, B6, B10, F2, F6, and F10 wells of a standard 96 well plate. Thin concentric lips were modeled at the bottom of the six holes to retain a 25 mm coverslip. For each sample, a small volume of liquid resin ($V = 130\ \mu l$) was sandwiched between two round coverslips (Thomas Scientific, 25 Cir-No. 1) separated by an annular-shaped spacer (McMaster Carr, 90214A438; thickness, $h = 0.5 \pm 0.05$ mm, outer diameter, $d_o = 22$ mm; inner diameter, $d_i = 16$ mm) and loaded into each of the 6 wells. One well was reserved for water as a blank. To determine if the molar extinction coefficient of the resin changed with exposure time, a custom-built UV lamp was constructed to expose samples to spatially-uniform light, similar in wavelength to the Form1+ laser. The UV lamp was constructed using 13 individual LEDS (Mouser.com, EAUVA35352IJ8, 400 nm $\leq \lambda \leq$ 410 nm), mounted in parallel to each other, distributed evenly across a six inch square, copper clad, photo-etched circuit board. A 2.7 Ω resistor (Mouser.com, 279-SMW32R7JT) was mounted in series with each LED. A 5 V, 10 amp peak power supply was used to power the LEDs. The emitter array was mounted into a 20 cm^3

cardboard box with the bottom removed and a portion of the top cut out to receive the emitter. The current demand was then measured with all LEDs installed. Average current through each LED was taken as total current divided by the number of LEDs. With LED power emission plotted against current on the EAUVA35352IJ8 datasheet, power of each LED could be determined, summed amongst all LED's and divided by the box cross sectional area to determine power per unit area. Thus, exposure of any sample placed under the box could be controlled by duration of exposure. A series of varying exposure times for various photoblocker concentrations were then conducted to determine molar extinction coefficient of the photoblocker at various exposures.

Supplementary Information

Cumulative Bleedthrough

Since attenuation of light through each cured and curing hydrogel layer follows the Beer-Lambert Law, it follows that the combined exposure acting on any single layer, i, can be expressed as a sum of the first exposure incident to layer i with the attenuated exposures that reach layer i during irradiation of all subsequent layers. This cumulative exposure for layer $i = 0$, is expressed as $E_{0,c} = (\sum_{i=0}^{n} E_0 10^{-[\varepsilon C_b] i \ell_z})$. It then follows that the cure depth resulting from this cumulative exposure, the cumulative cure depth, can be defined as $C_{d,c} = D_p \ln (E_{0,c}/E_c)$. By expanding and simplifying this expression, a meaningful physical relationship is explained. The expression for cumulative cure depth can be expanded into the form,

$$C_{d,c} = D_p \ln\left(E_0 \sum_{i=0}^{n} 10^{-[\varepsilon C_b] i \ell_z})/E_c\right).$$

Expanding further by separating terms within the natural log, the expression then becomes $C_{d,c} = D_p \left[\ln(E_0/E_c) + \ln\left(\sum_{i=0}^{n} 10^{-[\varepsilon C_b] i \ell_z}\right)\right]$. Because the single layer cure depth is defined as $C_d = D_p \ln(E_0/E_c)$, cumulative cure depth can then be expressed as a sum of the single layer cure depth with some addendum depth dependent on D_p, ε, C_b, and ℓ_z.

$$C_{d,c} = C_d + D_p \ln\left(\sum_{i=0}^{n} 10^{-[\varepsilon C_b] i \ell_z}\right) \quad \textbf{(Equation 1)}$$

Bleedthrough according to the cumulative model is defined as the difference between cumulative cure depth and layer thickness, or $h_c = C_{d,c} - \ell_z$. Combining h_c with **Equation** 1, cumulative cure depth can then be expressed as, $h_c = C_d + D_p \ln\left(\sum_{i=0}^{n} 10^{-[\varepsilon C_b] i \ell_z}\right) - \ell_z$. Since bleedthrough, according to the simple model, is defined as the difference between cure depth and layer thickness, substituting the expression, $h = C_d - \ell_z$, into the expanded form of h_c,

cumulative bleedthrough simplifies to a sum of the single layer bleedthrough with an addendum depth.

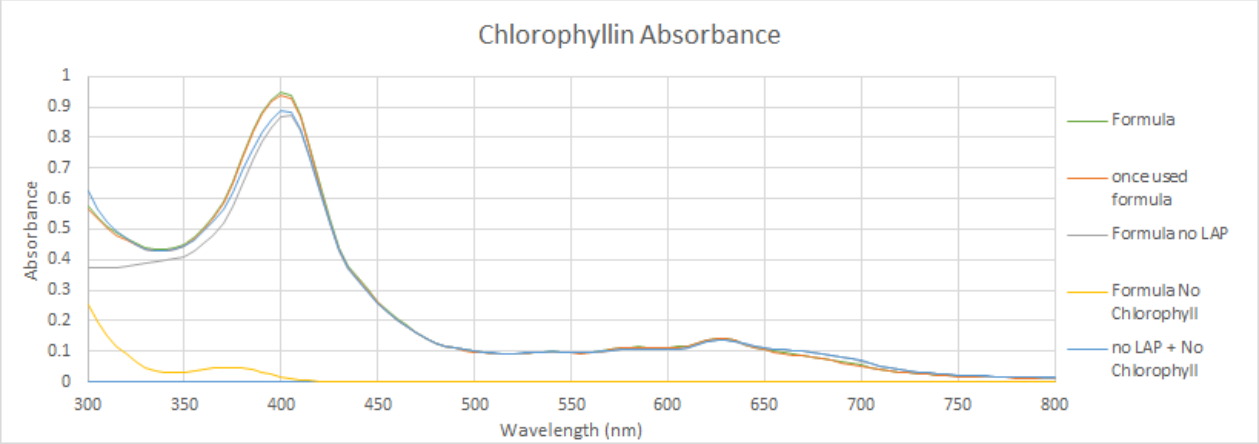
$h_c = h + D_p \ln\left(\sum_{i=0}^{n} 10^{-[\varepsilon C_b] i \ell_z}\right)$ **(Equation 2)**

From **Equation 2**, it follows that the cumulative bleedthrough depth approaches the single layer bleedthrough depth as the blocker concentration increases significantly.

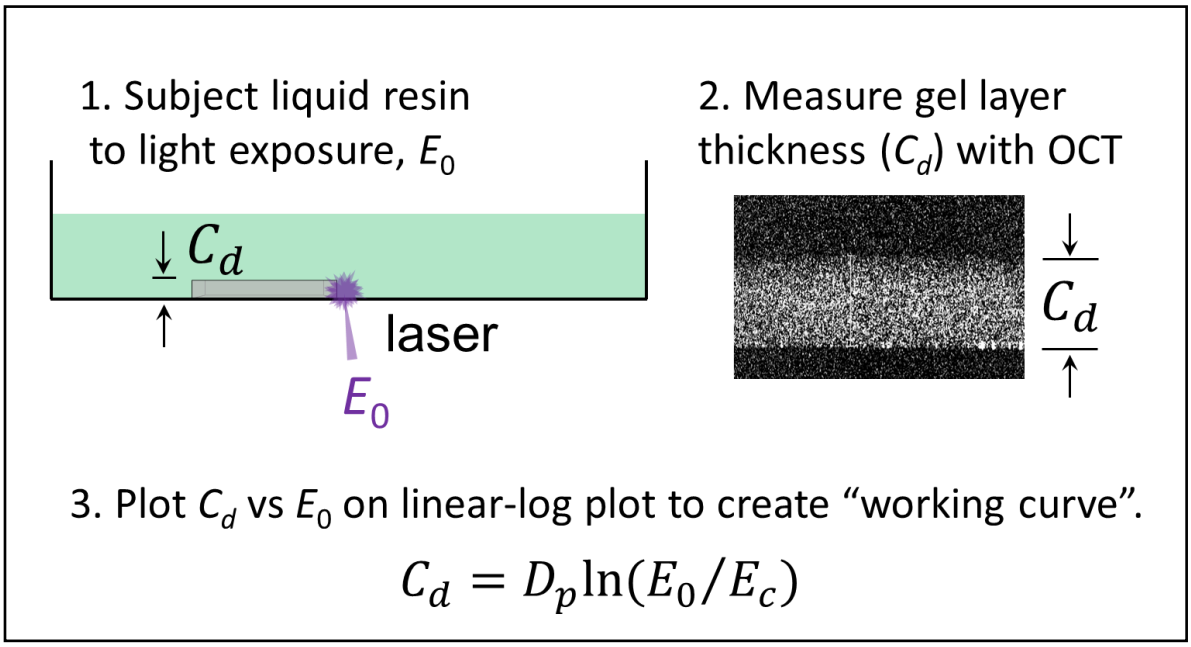
$\lim_{C_b \to \infty} (h_c) = h$ **(Equation 3)**

Funding

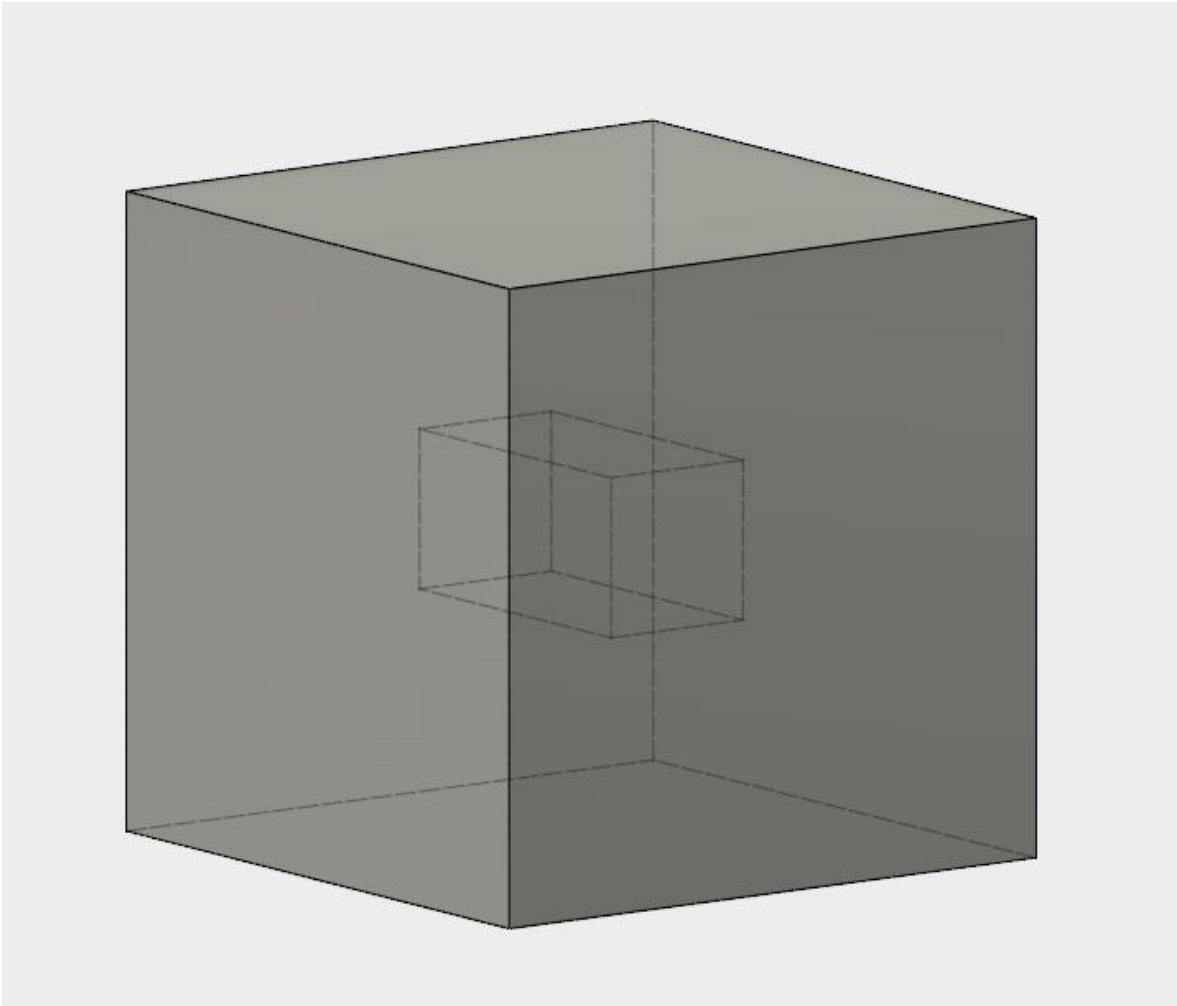
This work was supported by the National Science Foundation (DMR-1455247, CBET-1626604, and OIA-1736255).



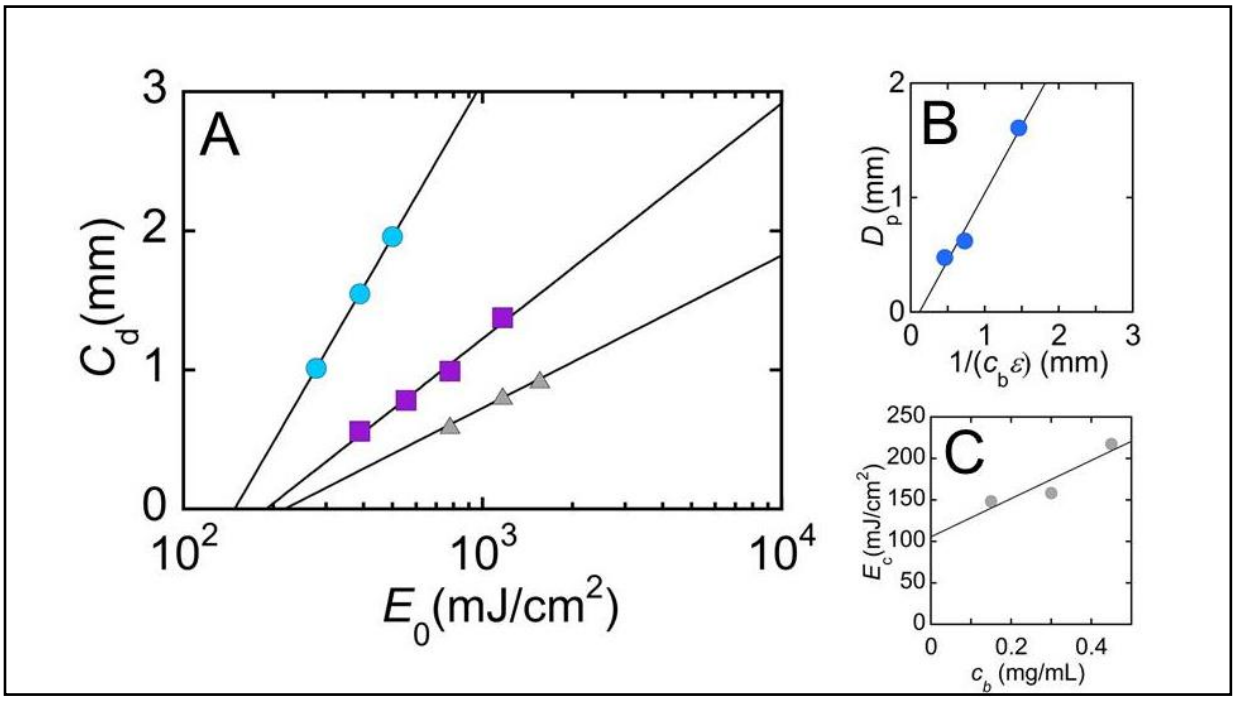
Supplementary Figure 5.1. Absorbance measurements as function of wavelength for different resin formulations taken using a plate reader (Biotek Synergy H1 Hybrid Reader). See Methods section for more details. Chlorophyllin exhibits strong absorbance around 400 nm. The photoblocker LAP exhibits some absorption in this region as well, but the absorbance is dominated by chlorophyllin. There is no measureable change in the intensity and shape of the absorbance spectrum, even after exposure to violet light (400 nm $\leq \lambda \leq$ 410 nm) and subsequent crosslinking.



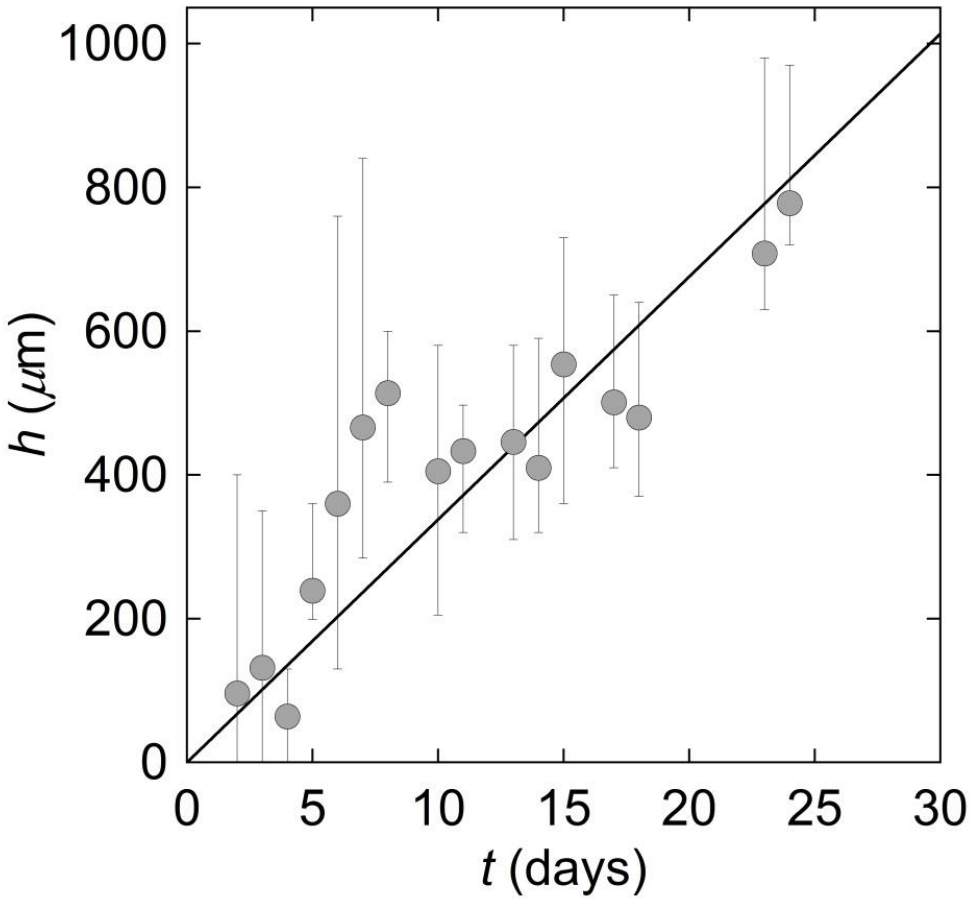
Supplementary Figure 5.2. Experimental approach for measuring single-layer cure depth.



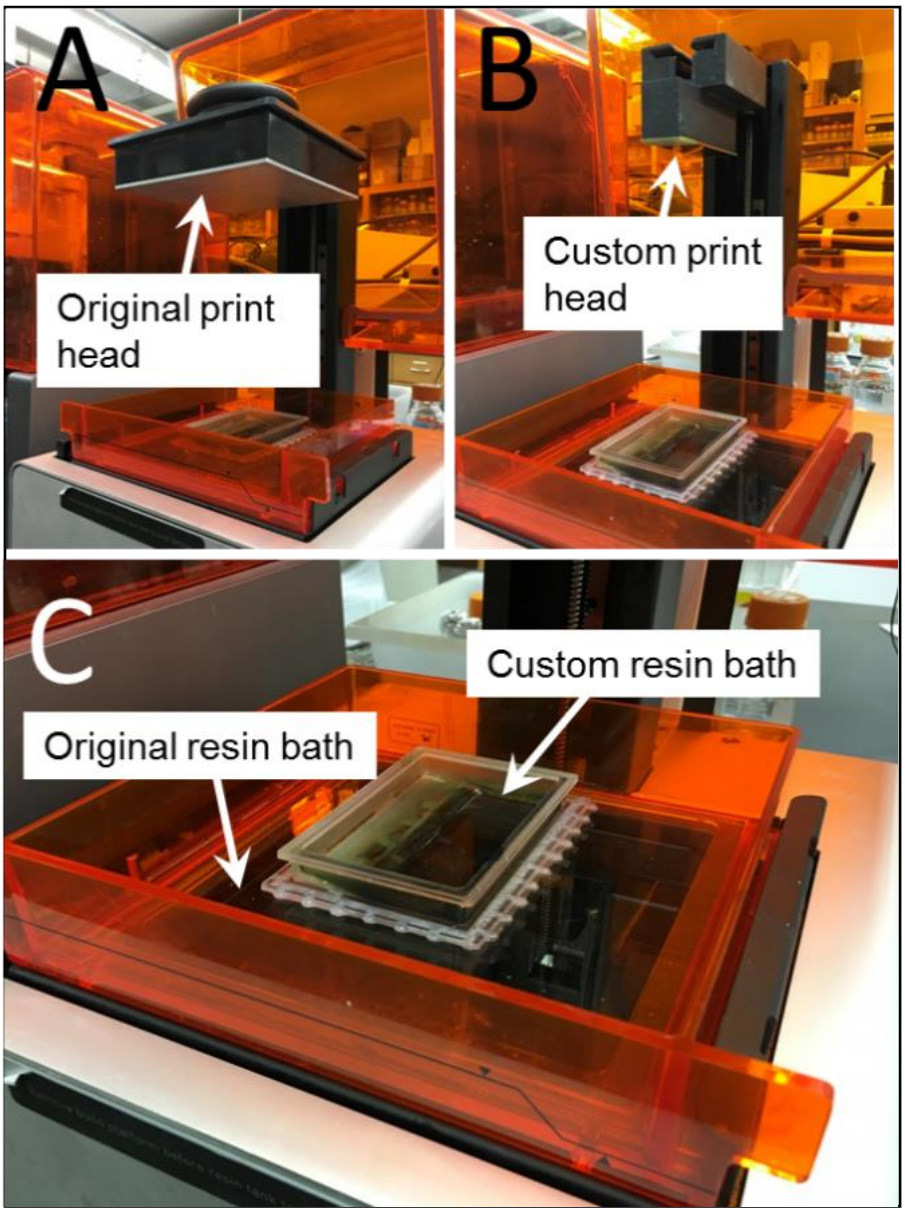
Supplementary Figure 5.3. Rendering of hydrogel cube containing enclosed rectangular void used for bleedthrough measurements. Cube dimensions: 6 mm × 6 mm × 6 mm. Internal rectangular channel with a square cross-section dimensions: 1.5 mm × 1.5 mm × 3 mm.



Supplementary Figure 5.4. *Tartrazine as a photoblocker*. (A) Single layer cure depth, $\boldsymbol{C_d}$ as a function of light exposure, E_0 for PEG-DA/LAP aqueous formulations with different tartrazine concentrations ($\boldsymbol{c_b}$ = 0.15 (•), 0.30 (■), 0.45 (▲). Lines are fits of solid symbols to $\boldsymbol{C_d = D_p \ln(E_0/E_c)}$. (B) Characteristic length scale associated with light attenuation, D_p as extracted from the slope of the fits in (C), and plotted as a function of $(\boldsymbol{c_b \varepsilon})^{-1}$. (C) Critical exposure, E_c determined from the *x*-intercept of the fits in (C) and plotted as a function of $\boldsymbol{c_b}$.



Supplementary Figure 5.5. Channel bleedthrough as a function of time (over 24 days) for our PEG-DA/LAP/chlorophyllin hydrogel formulation. Each point represents an individually printed rectangular hydrogel (dimensions: 3 mm x 3 mm x 10 mm) containing an open ended channel with square cross-section (dimensions: 1.5 mm x 1.5 mm x 10 mm) that was printed, and then imaged on a stereomicroscope to determine channel bleedthrough. Our results show significant aging of the resin. For this reason, for all experiments, resin was used within 8 h of mixing.



Supplementary Figure 5.6. Modified (**A**) print head and (**B**) resin bath for printing hydrogels on the Formlabs Form 2 or Form1+ using small volumes of liquid resin.

References Cited

1. Drury, J. L.; Mooney, D. J., Hydrogels for tissue engineering: scaffold design variables and applications. *Biomaterials* **2003,** *24* (24), 4337-4351.

2. Peppas, N. A.; Bures, P.; Leobandung, W.; Ichikawa, H., Hydrogels in pharmaceutical formulations. *European Journal of Pharmaceutics and Biopharmaceutics* **2000,** *50* (1), 27-46.

3. Qiu, Y.; Park, K., Environment-sensitive hydrogels for drug delivery. *Adv Drug Deliver Rev* **2001,** *53* (3), 321-339.

4. Zhu, J. M., Bioactive modification of poly(ethylene glycol) hydrogels for tissue engineering. *Biomaterials* **2010,** *31* (17), 4639-4656.

5. Bowman, C. N.; Kloxin, C. J., Toward an enhanced understanding and implementation of photopolymerization reactions. *AIChE Journal* **2008,** *54* (11), 2775-2795.

6. Zhu, W.; Li, J.; Leong, Y. J.; Rozen, I.; Qu, X.; Dong, R.; Wu, Z.; Gao, W.; Chung, P. H.; Wang, J.; Chen, S., 3D-Printed Artificial Microfish. *Adv Mater* **2015**.

7. Slaughter, B. V.; Khurshid, S. S.; Fisher, O. Z.; Khademhosseini, A.; Peppas, N. A., Hydrogels in regenerative medicine. *Adv Mater* **2009,** *21* (32-33), 3307-29.

8. Bae, M.; Divan, R.; Suthar, K. J.; Mancini, D. C.; Gemeinhart, R. A., Fabrication of Poly(ethylene glycol) Hydrogel Structures for Pharmaceutical Applications using Electron beam and Optical Lithography. *J Vac Sci Technol B Microelectron Nanometer Struct Process Meas Phenom* **2010,** *28* (6), C6P24-C6P29.

9. Qu, X.; Gou, M.; Zaidan, J.; Zhang, K.; Chen, S., Challenges and opportunities in developing nanoparticles for detoxification. *Nanomedicine (Lond)* **2014,** *9* (16), 2437-2439.

10. Waheed, S.; Cabot, J. M.; Macdonald, N. P.; Lewis, T.; Guijt, R. M.; Paull, B.; Breadmore, M. C., 3D printed microfluidic devices: enablers and barriers. *Lab Chip* **2016,** *16* (11), 1993-2013.

11. Floren, M.; Migliaresi, C.; Motta, A., Processing Techniques and Applications of Silk Hydrogels in Bioengineering. *J Funct Biomater* **2016,** *7* (3).

12. Billiet, T.; Vandenhaute, M.; Schelfhout, J.; Van Vlierberghe, S.; Dubruel, P., A review of trends and limitations in hydrogel-rapid prototyping for tissue engineering. *Biomaterials* **2012,** *33* (26), 6020-41.

13. Ma, X.; Qu, X.; Zhu, W.; Li, Y. S.; Yuan, S.; Zhang, H.; Liu, J.; Wang, P.; Lai, C. S.; Zanella, F.; Feng, G. S.; Sheikh, F.; Chien, S.; Chen, S., Deterministically patterned biomimetic

human iPSC-derived hepatic model via rapid 3D bioprinting. *Proc Natl Acad Sci U S A* **2016,** *113* (8), 2206-11.

14. A.Liu, V.; Bhatia, S. N., Three-Dimensional Photopatterning of Hydrogels Containing Living Cells. *Biomedical Microdevices* **2002,** *4* (4), 257-266.

15. El-Sherbiny, I. M.; Yacoub, M. H., Hydrogel scaffolds for tissue engineering: Progress and challenges. *Glob Cardiol Sci Pract* **2013,** *2013* (3), 316-42.

16. Raman, R.; Bhaduri, B.; Mir, M.; Shkumatov, A.; Lee, M. K.; Popescu, G.; Kong, H.; Bashir, R., High-Resolution Projection Microstereolithography for Patterning of Neovasculature. *Adv Healthc Mater* **2016,** *5* (5), 610-9.

17. Ling, Y.; Rubin, J.; Deng, Y.; Huang, C.; Demirci, U.; Karp, J. M.; Khademhosseini, A., A cell-laden microfluidic hydrogel. *Lab on a Chip* **2007,** *7* (6), 756-762.

18. Ziaie, B.; Baldi, A.; Lei, M.; Gu, Y.; Siegel, R. A., Hard and soft micromachining for BioMEMS: review of techniques and examples of applications in microfluidics and drug delivery. *Adv Drug Deliver Rev* **2004,** *56* (2), 145-172.

19. Warner, J.; Soman, P.; Zhu, W.; Tom, M.; Chen, S., Design and 3D Printing of Hydrogel Scaffolds with Fractal Geometries. *ACS Biomaterials Science & Engineering* **2016,** *2* (10), 1763-1770.

20. Do, A. V.; Khorsand, B.; Geary, S. M.; Salem, A. K., 3D Printing of Scaffolds for Tissue Regeneration Applications. *Adv Healthc Mater* **2015,** *4* (12), 1742-62.

21. Shi, W.; He, R.; Liu, Y., 3D printing scaffolds with hydrogel materials for biomedical applications. *European Journal of BioMedical Research* **2015,** *1* (3).

22. Melchels, F. P.; Feijen, J.; Grijpma, D. W., A review on stereolithography and its applications in biomedical engineering. *Biomaterials* **2010,** *31* (24), 6121-30.

23. Tumbleston, J. R.; Shirvanyants, D.; Ermoshkin, N.; Janusziewicz, R.; Johnson, A. R.; Kelly, D.; Chen, K.; Pinschmidt, R.; Rolland, J. P.; Ermoshkin, A.; Samulski, E. T.; DeSimone, J. M., Continuous liquid interface production of 3D objects. *Science* **2015,** *347* (6228), 1349.

24. Zhang, A. P.; Qu, X.; Soman, P.; Hribar, K. C.; Lee, J. W.; Chen, S.; He, S., Rapid fabrication of complex 3D extracellular microenvironments by dynamic optical projection stereolithography. *Adv Mater* **2012,** *24* (31), 4266-70.

25. Gauvin, R.; Chen, Y. C.; Lee, J. W.; Soman, P.; Zorlutuna, P.; Nichol, J. W.; Bae, H.; Chen, S.; Khademhosseini, A., Microfabrication of complex porous tissue engineering scaffolds using 3D projection stereolithography. *Biomaterials* **2012,** *33* (15), 3824-34.

26. Jacobs, P. F., *Rapid Prototyping & Manufacturing: Fundamentals of StereoLithography*. 1992.

27. Zhang, R.; Larsen, N. B., Stereolithographic hydrogel printing of 3D culture chips with biofunctionalized complex 3D perfusion networks. *Lab on a Chip* **2017,** *17* (24), 4273-4282.

28. Arcaute, K.; Mann, B. K.; Wicker, R. B., Stereolithography of Three-Dimensional Bioactive Poly(Ethylene Glycol) Constructs with Encapsulated Cells. *Annals of Biomedical Engineering* **2006,** *34* (9), 1429-1441.

29. Lu, Y.; Mapili, G.; Suhali, G.; Chen, S.; Roy, K., A digital micro-mirror device-based system for the microfabrication of complex, spatially patterned tissue engineering scaffolds. *Journal of biomedical materials research. Part A* **2006,** *77* (2), 396-405.

30. Chan, V.; Zorlutuna, P.; Jeong, J. H.; Kong, H.; Bashir, R., Three-dimensional photopatterning of hydrogels using stereolithography for long-term cell encapsulation. *Lab Chip* **2010,** *10* (16), 2062-70.

31. R., S. K.; S., M. J.; L., B. B.; S., C. C.; N., B. S., Degradable hydrogels derived from PEG-diacrylamide for hepatic tissue engineering. *Journal of Biomedical Materials Research Part A* **2015,** *103* (10), 3331-3338.

32. Suntornnond, R.; Tan, E. Y. S.; An, J.; Chua, C. K., A highly printable and biocompatible hydrogel composite for direct printing of soft and perfusable vasculature-like structures. *Sci Rep-Uk* **2017,** *7* (1), 16902.

33. Seo, H.; Heo, S. G.; Lee, H.; Yoon, H., Preparation of PEG materials for constructing complex structures by stereolithographic 3D printing. *RSC Adv.* **2017,** *7* (46), 28684-28688.

34. Sambrook, J., *Molecular cloning : a laboratory manual*. Third edition. Cold Spring Harbor, N.Y. : Cold Spring Harbor Laboratory Press, [2001] ©2001: 2001.

35. Jones, C. A.; Huberman, E.; Cunningham, M. L.; Peak, M. J., Mutagenesis and Cytotoxicity in Human Epithelial Cells by Far- and Near-Ultraviolet Radiations: Action Spectra. *Radiation Research* **1987,** *110* (2), 244-254.

36. Wells, R. L.; Han, A., Action spectra for killing and mutation of Chinese hamster cells exposed to mid- and near-ultraviolet monochromatic light. *Mutation Research/Fundamental and Molecular Mechanisms of Mutagenesis* **1984,** *129* (2), 251-258.

37. M., T. R.; P., W.; C., M. E., LETHAL ACTION OF ULTRAVIOLET AND VISIBLE (BLUE-VIOLET) RADIATIONS AT DEFINED WAVELENGTHS ON HUMAN LYMPHOBLASTOID CELLS: ACTION SPECTRA AND INTERACTION SITES. *Photochemistry and Photobiology* **1984,** *39* (2), 183-189.

38. Andley, U. P.; Lewis, R. M.; Reddan, J. R.; Kochevar, I. E., Action spectrum for cytotoxicity in the UVA- and UVB-wavelength region in cultured lens epithelial cells. *Investigative ophthalmology & visual science* **1994,** *35* (2), 367-73.

39. Browning, M. B.; Cereceres, S. N.; Luong, P. T.; Cosgriff-Hernandez, E. M., Determination of the in vivo degradation mechanism of PEGDA hydrogels. *Journal of biomedical materials research. Part A* **2014,** *102* (12), 4244-51.

40. Fairbanks, B. D.; Schwartz, M. P.; Bowman, C. N.; Anseth, K. S., Photoinitiated polymerization of PEG-diacrylate with lithium phenyl-2,4,6-trimethylbenzoylphosphinate: polymerization rate and cytocompatibility. *Biomaterials* **2009,** *30* (35), 6702-6707.

41. Majiama, T.; Schnabel, W., Phenyl-2,4,6-trimethylbenzoylphosphinates as water-soluble photoinitiators. Generation and reactivity of $O=P(C_6H_5)(O^-)$ radical anions. *Makromol. Chem.* **1991,** *192* (10), 2307-2315.

42. Han, D.; Lu, Z.; Chester, S. A.; Lee, H., Micro 3D Printing of a Temperature-Responsive Hydrogel Using Projection Micro-Stereolithography. *Sci Rep-Uk* **2018,** *8* (1), 1963.

43. Oster, G.; Broyde, S. B.; Bellin, J. S., Spectral Properties of Chlorophyllin a. *Journal of the American Chemical Society* **1964,** *86* (7), 1309-1313.

44. Sikorski, Z., Caris-Veyrat, C., Pintea, A., Wurtzel, E., Otles, S., Giusti, M., Marquez, U., During, A., Mercandante, A., Luning, P., Dufosse, L., Stintzing, F., Amiot, M., Brat, P., Matthews, P., Diehl, H., Carle, R., Sinnecker, P., Bobbio, F., Jing, P., Laurent, C., Tourniaire, F. , *Food Colorants*. CRC Press: Boca Raton, 2008.

45. Miller, G. A.; Gou, L.; Narayanan, V.; Scranton, A. B., Modeling of Photobleaching for the Photoinitiation of Thick Polymerization Systems. *Journal of Polymer Science Part A: Polymer Chemistry* **2001,** *40* (6), 793-808.

46. Rubinstein, M. C., Ralph *Polymer Physics*. Oxford University Press: 2003.

CHAPTER SIX

AN INEXPENSIVE, VERSATILE, COMPACT PROGRAMMABLE TEMPERATURE CONTROLLER AND THERMOCYCLER FOR SIMULTANEOUS ANALYSIS AND VISUALIZATION WITHIN A MICROSCOPE

Contribution of Authors and Co-Authors

Manuscript in Chapter 6

Author: Pablo Martínez Cruz

Contributions: Planned and performed the experiments, analyzed the data, and wrote the manuscript.

Co-Author: Mikayla Wood

Contributions: Performed the experiments, analyzed the data, and wrote the manuscript.

Co-Author: Reha Abbasi

Contributions: Analyzed the data and wrote the manuscript.

Co-Author: Thomas B. LeFevre

Contributions: Planned and oversaw the experiments, analyzed the data, and wrote the manuscript.

Co-Author: Stephanie E. McCalla

Contributions: Planned and oversaw the experiments, analyzed the data, and wrote the manuscript.

Manuscript Information

Pablo Martínez Cruz, Mikayla Wood, Reha Abbasi, Thomas B. LeFevre, Stephanie E. McCalla

Microfluidics Nanofluidics

Status of Manuscript:
___ Prepared for submission to a peer-reviewed journal
___ Officially submitted to a peer-reviewed journal
___ Accepted by a peer-reviewed journal
_X_ Published in a peer-reviewed journal

DOI: 10.1007/s10404-021-02440-z

Springer

Abstract

Microfluidic Lab on a Chip (LOC) devices are key enabling technologies for research and industry due to their compact size, which increases the number of integrated operations while decreasing reagent use. Common operations within these devices such as chemical and biological reactions, cell growth, or kinetic measurements often require temperature control. Commercial temperature controllers are constrained by cost, complexity, size, and especially versatility for use in a broad range of applications. Small companies and research groups need temperature control systems that are more accessible, which have a wide applicability. This work describes the fabrication and validation of an inexpensive, modular, compact, and user-friendly temperature control system that functions within a microscope. This system provides precise temperature acquisition and control during imaging of any arbitrary sample which complies with the size of a microscope slide. The system includes two parts. The first part is a compact and washable Device Holder that is fabricated from high temperature resistant material and can fit securely inside a microscope stage. The second part is a robust Control Device that incorporates all the necessary components to program the temperature settings on the device and to output temperature data. The system can achieve heating and cooling times between 50°C and 100°C of 32 seconds and 101 seconds, respectively. A Bluetooth enabled smartphone application has been developed for real-time data acquisition and visualization. The utility of the temperature control system was shown by monitoring rhodamine B fluorescence in a microfluidic device over a range of temperatures, and by performing a polymerase chain reaction (PCR) within a microscope. This temperature control system could potentially impact a broad scope of applications that require simultaneous imaging and temperature control.

Introduction

The development of Lab on a chip (LOC) technology has impacted and advanced fields from engineering to biology[1]. These technologies have contributed to the understanding of fluid motion and associated transport processes[2] and offer promising solutions to drug discovery and development by significantly reducing sample consumption among other factors[3]. LOC technology revolutionized chemical and biological analysis by miniaturizing experimental techniques such as cell growth and manipulation[4], single cell analysis[5], molecular diagnostics[6-8], and complex chemical reactions[9], including the polymerase chain reaction (PCR) used for nucleic acid amplification. PCR is a powerful and sensitive technique used to quantify DNA and mRNA expression which has applications ranging from forensics to medical diagnostics[6, 10]. These processes can now be performed on a device that fits on a standard microscope slide, which manipulates picoliter to microliter volumes of liquid[11, 12] using microchannel dimensions ranging from tens to hundreds of microns. Small volumes enable massively parallel experiments[13, 14] and allow multiple operations to be integrated onto one device[15]. The microfluidics industry is currently in the spotlight, as new LOC technologies could help curb pandemics through enhanced diagnostics and drug discovery[16]. For this reason, a significant growth is expected for the microfluidic diagnostic industry due to the immediate demand for global healthcare.

While the miniaturized format of LOC technology is highly advantageous, these dimensions frequently require a microscope or specialized imaging equipment to monitor experiments. Many of these operations, such as cell growth[17], chemical reactions and kinetic measurements[18, 19], microfluidic mixing experiments, or biochemical reactions such as polymerase

chain reaction (PCR)[20], additionally require precise temperature control, leading to the challenge of integrating temperature control into microfluidic systems.

Both external and internal heating techniques such as pre-heated liquids, microwaves, lasers, chemical reactions and Joule heating have been used on microfluidic devices for temperature control[7]. Many microfluidic temperature control systems are designed and fabricated with at least one component that is limited to a particular device design[15, 21-25]. Thus, this prevents these temperature control systems to be used for more than one microfluidic design. While these systems provide rapid thermal cycling or localized heating of a reaction chamber, these experiments require extra fabrication steps to integrate thermal control for every device or are not suitable for arbitrary device designs.

A thermal cycler with a large attached optical system has also been reported, which provides fluorescent images of microfluidic devices, but it includes a full sized commercial thermocycler and it cannot be used within a standard microscope[26]. Conversely, an inexpensive and portable thermal cycler with imaging capabilities was reported, but it does not integrate with a microscope and is therefore not intended to image small feature sizes[27]. Current commercial temperature control instrumentation for microscope stages can produce a steady temperature for the entire microscope stage; for example, the Microscope Temperature Control Heating Stage, Slide Warmer by BoliOptics provides whole-stage temperature control. However, they have a slow temperature acquisition rate and a narrow temperature range, as they were mainly designed for the purpose of cell culture. Another recent commercial device developed for fast temperature acquisition and control is the VAHEAT by Linnowave, but it is limited to a small temperature control region and is expensive. While these advances have been an exciting addition to the field

of microfluidic temperature control, there are currently no available inexpensive, modular, versatile instruments that can fit securely within most microscopes, operate during imaging steps, and uniformly control over a wide range of temperatures on any sample secured to a standard microscope slide.

To address these issues, we present an inexpensive system for simultaneous temperature control and imaging. The system can uniformly heat or cool any sample that can fit on a standard microscope slide, allowing simultaneous temperature acquisition and control as well as visualization of the sample. The system is divided into two main components: 1) The Device Holder, which is a stereolithography (SLA) 3D printed component that serves as a housing for the microfluidic device, the cooling fan, and the heating element and 2) The Control Device, which encloses the power supplies, the electronics, and the microcontroller. Powering the system requires only a single connection to the standard 120V wall power and can be programmed using a simple interface on the Control Device. The Device Holder is temperature resistant and can be removed from the electronic components, so it can be sterilized by autoclaving at the end of every experiment. The accuracy and uniformity of the temperature control was validated using an external thermometer and an IR camera. The functionality of the temperature control system was validated by monitoring temperature sensitive rhodamine B fluorescence in a microfluidic channel, as well as amplification of cDNA on a microscope slide within a microscope stage. Finally, a mobile application has been developed to plot temperature data in real-time, which is sent via Bluetooth connection from the Control Device to a smartphone. This temperature control system can be used on any device or sample that fits on a standard microscope slide. Therefore, it has the potential to enable the experiments involving live cell imaging, nucleic acid and protein analysis,

in vitro drug studies, diffusion studies, crystallization, material characterization, microfluidic fluid mechanics; or any other application in which temperature control and simultaneous microscopic observation are required. Therefore, this temperature control system has implications for a broad scope of applications that require concurrent imaging and temperature control.

Materials and Methods

3D design of the Device Holder and Control Device

The Device Holder incorporates the microscope slide or microfluidic LOC device with all heating and cooling components and fits securely on a microscope stage. In the presented design, all components that surround the microfluidic sample (**Fig. 6.1a ii**) are symmetric to avoid temperature gradients. The presented system is designed for inverted microscopy, but upright microscopy could also be used without cooling if the sample and the aluminum plate (**Fig. 6.1a iii**) are flipped and the fan (**Fig. 6.1a v**) is removed.

The Control Device case was designed to enclose all the electronic components, such as the microcontroller and power supplies, to provide an accurate temperature control and to interface with the user (**Fig. 6.1b and d**). Both designs were drawn using SolidWorks (Waltham, MA).

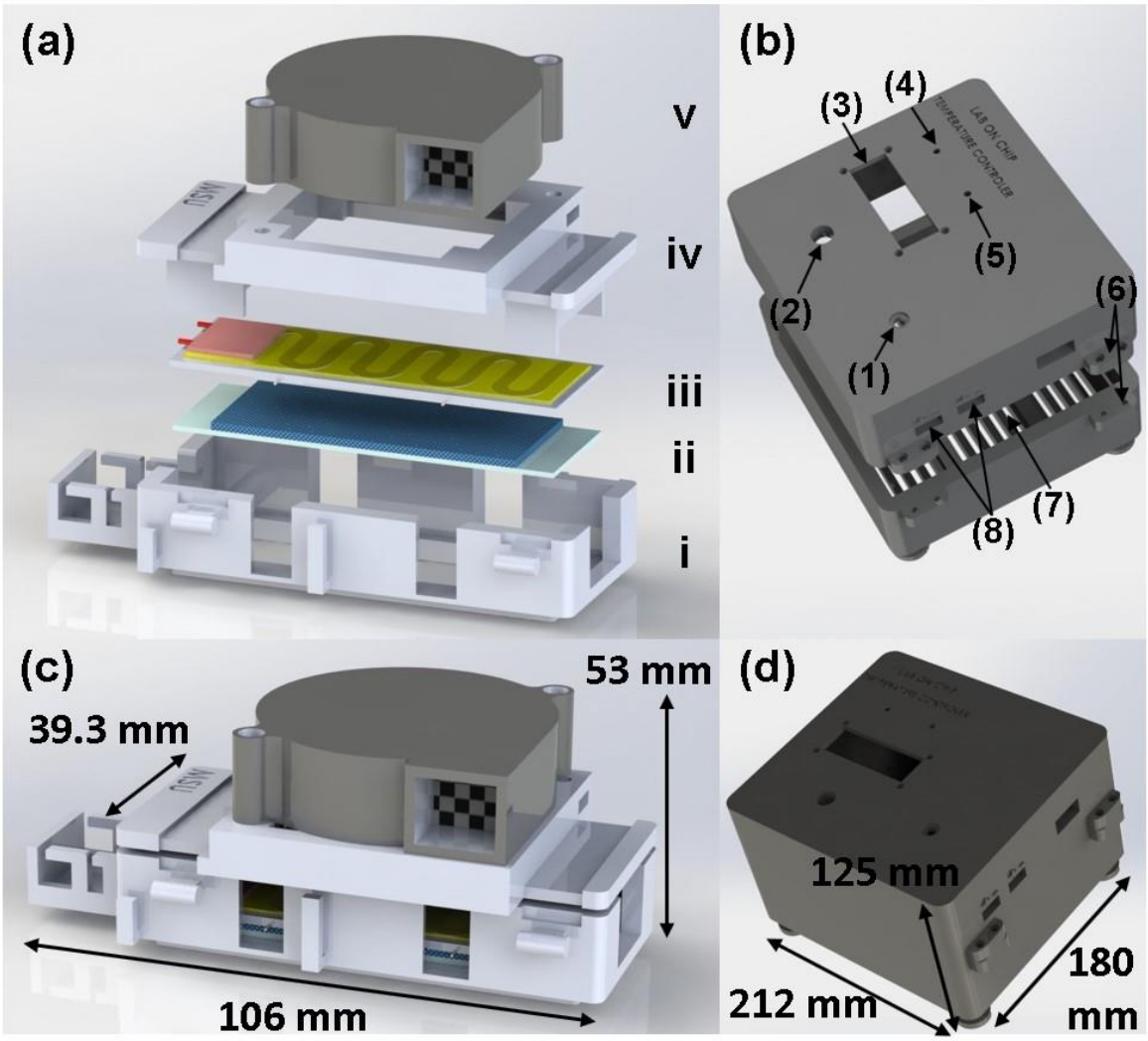


Figure 6.1. *Schematics of the temperature control system*: (a) CAD design of the experimental Device Holder, LOC device, and the heating and cooling components which fit into the microscope tray. (i) Lower part of the Device Holder. (ii) LOC device, which here is shown as a 1.5 mm thick microfluidic device layer bonded to a standard microscope slide. (iii) Heating Unit bonded to an aluminum sheet. (iv) Upper cap of the Device Holder. (v) Fan. (b) CAD design of the of the Control Device case for the microcontroller and all the electronical components used to create the interface of the Control Device. Shown here are the positions of the (1) Rotary encoder. (2) 6 pin connector for Device Holder linkage. (3) LCD display screen. (4) Green LED. (5) Yellow LED. (6) Couplings for the screws. (7) Ventilation slots. (8) Two type K thermocouple connections. (c) CAD design of the assembled experimental Device Holder with dimensions. (d) CAD design of the assembled Control Device case with dimensions.

Fabrication of the Device Holder

The Device Holder incorporates a device or microscope slide with the cooling and heating unit. The breakdown of the components is shown in Figure 1a, the assembled Holder is shown in Figure 1c, and the final Device Holder prototype is shown in **Figure 6.2**. A Formlabs (Somerville, MA) Form 2 SLA 3D printer and High Temp Resin (RS-F2-HTAM-02) was used to fabricate the Device Holder (**Fig. 6.1a, i and iv**). The final design, including all the components, was 106x53x39.3mm. The Device Holder fits into the stage of the microscope and is secured by notches on the bottom of the holder. An Adhesive Polyimide Insulated Flexible Resistance Heater (OMEGA^{TM}, Norwalk, CT) was adhered to an aluminum sheet to create the heating module (figure 1a, component iii) and a 12Volt fan (WINSINN, Shenzhe, Guangdong) constitutes the cooling module. The pressure sensitive adhesive on the heater is rated for temperatures between -40ºC to 149ºC. Two special limits of error type K thermocouples (OMEGA^{TM}, Norwalk, CT) are adhered to the underside of the aluminum sheet in contact with the sample (figure 1a, between components ii and iii), which are 33.5mm apart and provide the feedback for temperature control. Flexible rubber clamps (Ceeyali, Shenzhe, Guangdong) create full contact between the aluminum sheet and the LOC device by clamping the top and bottom 3D printed Device Holder elements together (Fig. 1a, i - iv). The estimated expenses for the Device Holder fabrication is $122.94 for the components and $12.42 for the High Temperature Resin.

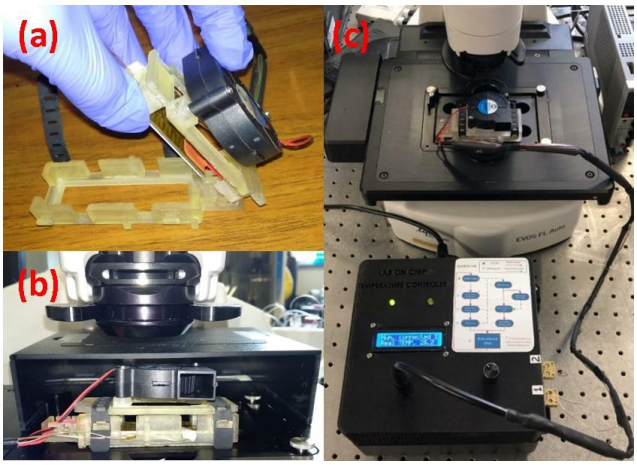


Figure 6.2. *The Device Holder prototype*. (a) Open Device Holder. (b) Clamped Device Holder within an epifluorescence microscope, which fits underneath a compact light shield. (c) Device Holder in a microscope with a connected Control Device.

Fabrication of the Control Device

The Control Device encloses all of the electronic components to control the device temperature and to interface with the user inside a case. The case design is shown in Figure 1b and d, and the entire Control Device prototype is shown in Figure 3. The case was 3D-printed using a Stanley Model 1 extrusion printer (Stanley Tools, New Britain, CT) and Prusa i3 MK3S (Prusa Research, Prague, Czech Re-public) with Sindoh 3DWOX Refill Black polylactic acid (PLA) filament. Figure 1d shows a schematic of the assembled Control Device casing, which is 212x180x125mm. The total estimated cost of the Control Device fabrication is $131.1 for the components and $52.4 for the PLA material.

The Control Device is connected into the electrical grid **(**wall power) and turned on using the green switch shown in **Figure 6.3 component 5**. The heating unit is controlled using a Pulse Wave Modulation (PWM) coming from one of the power supplies incorporated in the Control Device for voltage regulation. The power supplies are currently configured for a 120 Volts AC

conversion, but they could be adjusted for 220-240 Volts conversion. A fuse is incorporated into the system to open the circuit and stop the device operation in the case of electrical failure. An LCD screen is integrated into the Control Device to visualize the different menu options and real time temperature readings (**Fig. 6.3,** component 3). A rotary encoder is used to navigate through the eleven menu options (**Fig. 6.3,** component 2). In addition, one green LED and one yellow LED are used to help identify the menu option in which the user is positioned (figure 3, component 6). Two MAX6675 thermocouple temperature sensor modules from HiLetgo (Shenzhen, Guangdong) are used for cold-junction compensation and digitization of the type K thermocouple signal; details on the temperature calibration of the instrument are given in the Supporting Information (figure SI6). A user guide schematic is printed on the Control Device to help the user navigate through the menu and produce customized experiments (**Fig. 6.3**, component 4, and shown in more detail in **SI Figure 6.1**).

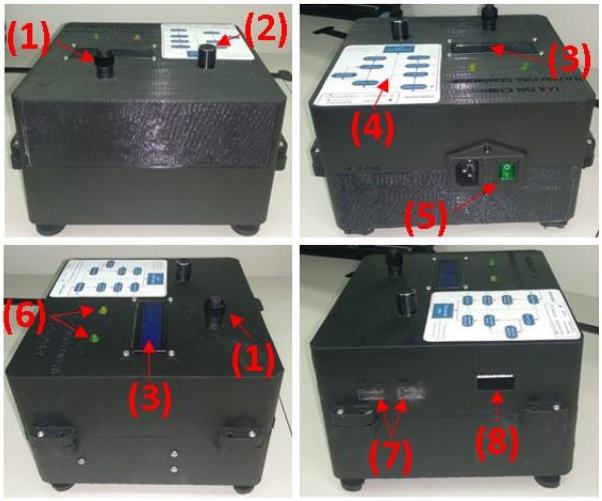


Figure 6.3. *The Control Device*: PLA black filament printed case with all hardware components needed for power conversion, parameter selection, visualization, and temperature control enclosed inside. (1) Device Holder to Control Device connection. (2) Rotary encoder. (3) LCD display screen. (4) User guide for menu navigation and device operation. (5) On switch. (6) LEDs

indicating device operation. (7) Thermocouple connection slots. (8) USB 2.0 cable connection slot used to upload new experimental code.

Temperature Control System software

The menus programmed into the microcontroller allow the user to customize an experiment by selecting the specific temperatures of the different steps, times, and number of desired cycles. The user can input the temperature control parameters either by modifying the Arduino-based code and uploading this into the Arduino microcontroller via the USB port (**Fig. 6.3**, component 8) or by using the rotary encoder on the top of the control device (**Fig. 6.3**, component 2). An example of the rotary encoder use is given in a supporting video. An additional input option to consider the microfluidic device thickness for internal device temperature inference was included for future applications but was not used in this work. The real time temperature is shown on the display of the Control Device (**Fig. 6.3**, component 3) and sent via Bluetooth to the LOC mobile application (**SI Fig. 6.2**). Temperature data can also be monitored in the Arduino software when a computer is connected to the Control Device via USB. When both thermocouples are connected, the control temperature will be the average of both measurements. A gain scheduling closed loop feedback PID control has been programmed based on the general equation of PID controller to regulate the duty cycle of the PWM. Thus, the optimal proportional, integral, and derivative were found using a trial and error procedure[28].

Smartphone application development

A smartphone application (app) was developed to acquire the real time temperature data of experiments performed with no need for the Arduino IDE. When the control has been activated through the rotary encoder in the Control Device and after the Bluetooth has been paired, the

Control Device will send the temperature data via Bluetooth to the smartphone app. The temperature and time will be displayed as an integer value in a two-dimensional plot on the screen of the smartphone (**SI Fig. 6.2**).

Rhodamine B temperature validation

Rhodamine B ≥95%, a temperature sensitive dye, was purchased in powdered form from Sigma Aldrich (St. Louis, MO), and a 10mM rhodamine solution was made in ultrapure MilliQ water. The PDMS microfluidic device was produced using standard soft lithography techniques and bonded to a glass microscope slide[29]. The rhodamine solution was pumped into the channels and wells of the PDMS microfluidic device using a syringe, and was covered by glass cover slip and mineral oil to prevent evaporation. The microfluidic device was inserted into the device holder and placed in the epifluorescent microscope oriented as shown in figure 1a. The temperature was varied by 5ºC increments during both heating and cooling, which was maintained for 5 minutes before measurement. Measurements were taken using the Evos Texas Red light cube and a 10x PlanFluor objective with a 0.3 NA (Thermofisher Scientific, Waltham, MA). Illumination was constant throughout the course of the experiments. Average red fluorescent pixel values were evaluated using ImageJ[30].

PCR validation experiments

Reagents: Nuclease-free water was purchased from IDT (Coralville, IA). Cel-miR-39 mimic was purchased from Qiagen (Hilden, Germany). Luna® universal probe qPCR master mix and molecular grade bovine serum albumin (BSA) were purchased from New England Biolabs (Ipswich, MA). The cel-miR-39 TaqMan Assay and TaqMan microRNA Reverse Transcription Kit was purchased from Thermofisher (Waltham, MA). Molecular biology grade mineral oil and

Sigmacote® were purchased from Sigma Aldrich (St. Louis, MO). Eliminase was purchased from Fisher Scientific (Hampton, NH).

PCR setup: The working stock was diluted to 9.6e7 copies/µL in nuclease free water and cDNA was created using the TaqMan microRNA Reverse Transcription Kit according to manufacturer's instructions. PCR reactions contained 1µL 20x TaqMan small RNA assay reagents for cel-miR-39, 10µL Luna® universal probe qPCR master mix, 1 µL of 20mg/mL BSA, 1.2µL of cDNA, and 6.8 µL of nuclease-free water for a total of 20 µL. The negative control reaction contained a reverse transcription reaction performed with nuclease-free water instead of target miRNA. The final concentration of cDNA in the PCR reaction was theoretically $1.9x10^6$ copies/µL.

qPCR within the microscope: A LOC device mimic was made by cutting two rectangular 10x6.5mm wells in a 0.2mm thick PDMS layer. The PDMS layer was bonded to a standard 1mm thick glass microscope slide (Globe Scientific, Mahwah, NJ) after exposure to oxygen plasma using standard PDMS bonding techniques. The exposed glass of the wells and a glass cover slide (22x50mm #1 thickness) (Thermo Scientific, Portsmouth, NH) were treated with Sigmacote® according to manufacturer's instructions. The device and the glass cover slide were rinsed thoroughly with milliQ water, then Eliminase, and finally nuclease free water.

A 1µL droplet of the positive sample was placed in one rectangular well and a 1 uL droplet of the negative sample was placed in the other rectangular well. The droplets were placed in the middle of the wells and immersed in mineral oil, and therefore did not contact the PDMS. Both wells were covered with approximately 8 µL of mineral oil. The glass cover slide was placed on top of the PDMS layer. Next, the LOC device mimic was placed in the Device Holder,

approximately 50 uL of mineral oil was placed on top of the device to ensure full contact between the aluminum plate and the glass, and then the Device Holder was closed and placed in the epifluorescence microscope. Thermal cycling was as follows: initial denaturation (91ºC for 4 minutes), followed by 40 cycles with two steps (91ºC for 15 seconds and 60ºC for 45 seconds). The total amount of time spent for the qPCR was 95.2 minutes (figure 7a). The LOC device mimic was imaged using an Evos FL Auto (Fisher Scientific, Waltham, MA) and a 2x objective with a GFP Evos light cube. Two positive and two negative samples (1 uL each and 9 uL of mineral oil) were loaded into a standard commercial thermal cycler CFX Connect (BioRad, Hercules, California) and subjected to the same thermal cycling steps as described above. ImageJ[30] was used to find the pixel intensity of green fluorescent light within a 75-pixel diameter circle in the center of the droplet in the fluorescent microscope images. The mean pixel intensity of the droplet during the 60˚C stage was baseline corrected using cycle 1 and normalized to the fluorescence of the positive sample during cycle 40. To compare the droplets in the device to those in the CFX Connect, baseline corrected data from the CFX Maestro software was also normalized to the fluorescence of the positive sample during cycle 40.

Results and Discussion

Analysis of temperature control performance

Analysis of the temperature control was performed in a temperature range that is standard during chemical and biochemical experimentation. One example is the ubiquitous PCR; temperature and time of PCR cycles and steps depend on the chosen chemistry and target length, but most PCR cycles require temperatures between 50ºC and 100ºC[31]. The performance of the temperature control system was therefore analyzed in this temperature range (**Fig. 6.4**). In this

range, the temperature follows a linear trend during heating ($R^2 = 0.99$) and the cooling behavior could be approximated in the working range to a linear trend to show the approximate average cooling rate ($R^2 = 0.95$). The maximum temperature difference between the two thermocouples was 1.8ºC and 2.3ºC during the heating and the cooling, respectively. The average temperature difference between the thermocouples was 1.4ºC during heating and 0.9ºC during cooling, which does not exceed the type K thermocouple standard limit of error of ±1.1 ºC (2.2ºC maximum difference) given by the manufacturer; the maximum deviation between the thermocouples during cooling only exceeds this expected error range by 0.1 ºC. The average numerically calculated heating rate within the PCR working range was 1.5 ºC/seconds, and the temperature of the aluminum sheet increased 50ºC in 32 seconds (**Fig. 6.4a**). The average numerically calculated cooling rate within the PCR working range was 0.5ºC/second, and the temperature of the aluminum sheet decreased by 50ºC in 101 seconds (**Fig. 6.4b**).

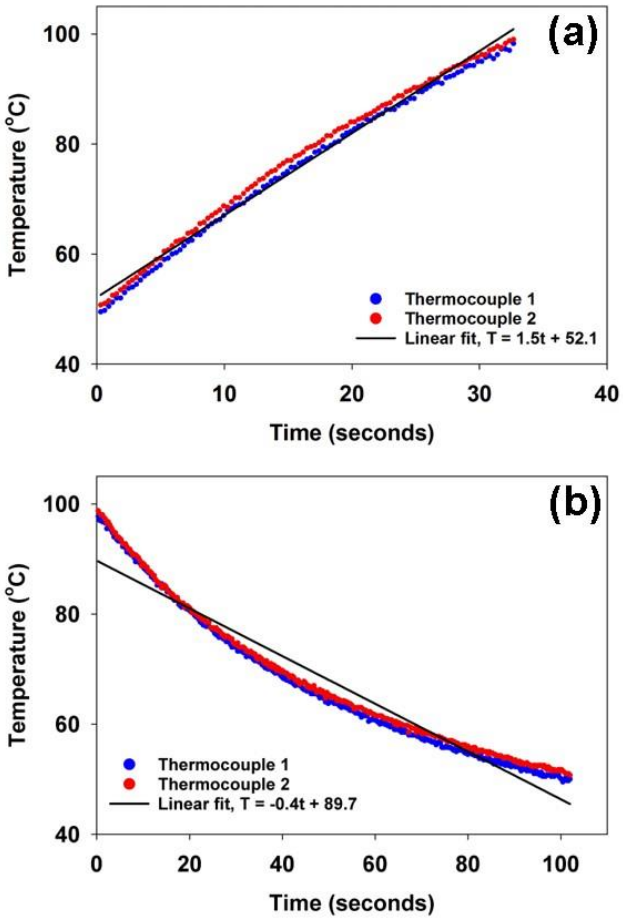


Figure 6.4. *Heating and cooling rates*. (a) Monitoring of the heating behavior. (b) Monitoring of the cooling behavior. The average difference between the thermocouples is 1.4°C during heating and 0.9°C during cooling, which is within the standard special limits of error for the incorporated type K thermocouples.

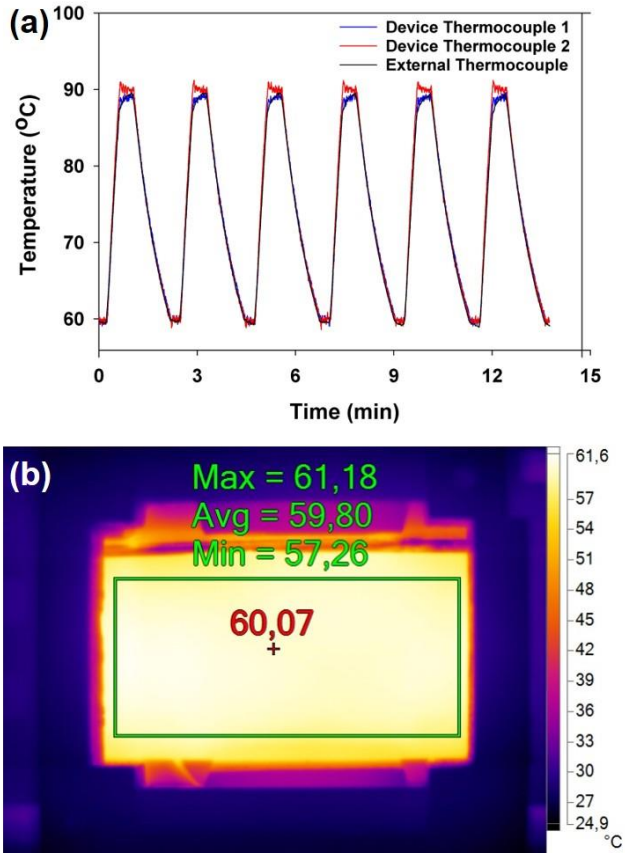


Figure 6.5. *External validation of temperature accuracy*. a) Temperature measurement at the base of the microscope slide bonded to PDMS for an arbitrary set of PCR cycles. The temperature is read from both type K thermocouples incorporated in the device and an external type K thermocouple. B) Thermal image taken with FLUKE TiX560 (Everett, Washington) of a glass microscope slide inside the device holder programmed to maintain a temperature of 60ºC. The cross indicates a temperature of 60.07ºC.

External validation of temperature control

The temperature controller system output was validated by tracking the temperatures over time both within the system and on an external analog thermometer. An external type K thermocouple connected to a SensorDAQ (Vernier, Beaverton, OR) was placed at the center of the device. The SensorDAQ readout was acquired using LabVIEW (National Instruments, Austin, TX). The Device Holder was assembled with a LOC device mimic and placed within the

microscope as shown in Figure 6.2a. The temperature from each thermocouple during a set of arbitrary temperature cycles (90 ˚C for 25 seconds, 60 ˚C for 15 seconds) is shown in figure 5a, with the externally measured temperature comparable to the temperature measured by the device. The temperature remained stable during each cycle at every measurement point. Additionally, the temperature at the surface of a glass slide was validated using a TiX501 thermal camera (Fluke, Everett, WA) to show uniformity of temperature across the top of a glass substrate (**Fig. 6.5b**) using an emissivity of 0.95[32].

Rhodamine B temperature dependence measured inside a PDMS/glass microfluidic device

Rhodamine B is frequently used to evaluate temperature in microfluidic devices based on fluorescent signal intensity ratios for temperature distributions[33]. To demonstrate the functionality of the temperature control system, the fluorescence of rhodamine B was monitored over temperatures ranging from 30 ˚C to 70 ˚C. A characteristic drop in Rhodamine B fluorescence relative to the fluorescence at 30 ˚C is seen with increasing temperature during both heating (n=1) and cooling (n=2) using two separate devices (figure 6). While a broader temperature range typically requires a nonlinear polynomial fit, in our temperature range a linear fit was suitable (R^2 = 0.99). This confirms the system can control temperature in a microfluidic device during fluorescent microscopy measurements.

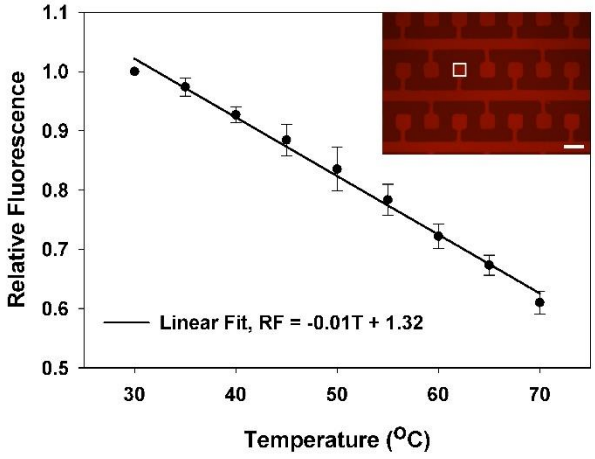


Figure 6.6. *Average relative fluorescence change of rhodamine B in a microfluidic device during heating and cooling*. The white square in the inset of the representative image of Rhodamine B is a dead-end filled microfluidic well (70 ˚C) which shows the area where the average fluorescence was taken. Error bars show ± one standard deviation for n=3 measurements. Scalebar = 100 µm.

qPCR amplification within the temperature control system

PCR amplification on droplets containing target cDNA and droplets without target cDNA was performed in a standard epifluorescent microscope in approximately 95.2 minutes (**Fig. 6.7a**). The LOC device mimic was imaged during cycles 1, 5, 10, 15, 20, 24, 28, 32, 36, and 40. A histogram of the droplet pixel intensities for cycles 1 and 40 is also is shown in **SI Figure 6.5**. An increase in the positive droplet fluorescence was observed between cycles 20 and 24, which matches the approximate time to positive seen in the BioRad commercial qPCR instrument (**Fig. 6.7b**). It is worth noting that the shape of the curve acquired from the microscope is not identical to the shape seen in the commercial qPCR instrument. This could be due to a variety of factors, such as interactions between the TaqMan chemistry and the hydrophobic Sigmacote; kinetic differences between PCR within custom devices and in optimized PCR tubes have been previously reported[27]. Figure 7 demonstrates that successful PCR amplification of reagents within a

microscope can be achieved with the same approximate time to positive as a commercially available qPCR instrument.

Before running the real-time amplification, an additional endpoint PCR experiment was successfully performed within the microscope stage. The figures and results are described in the SI (**SI Fig. 6.3** and **SI Fig. 6.4**).

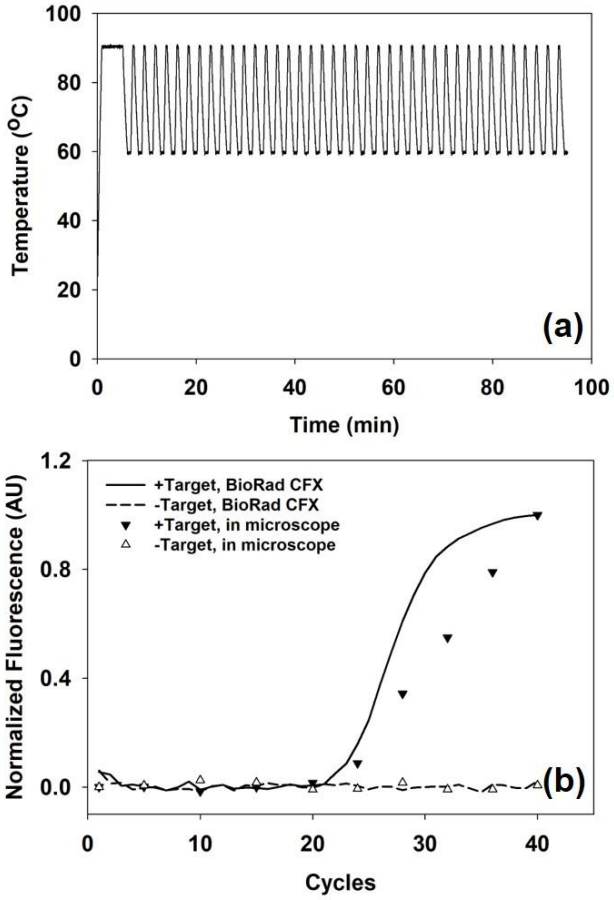


Figure 6.7. *Real time PCR amplification using the temperature control system*. (a) The temperature over the course of the real time PCR amplification, which was completed in 95.2 minutes. (b) Normalized fluorescence from 1µL droplets of PCR solution in a standard commercial qPCR instrument (lines) and using the temperature control system in a microscope (triangles). Open triangles indicate a sample with no target cDNA, closed triangles indicate a sample with target cDNA.

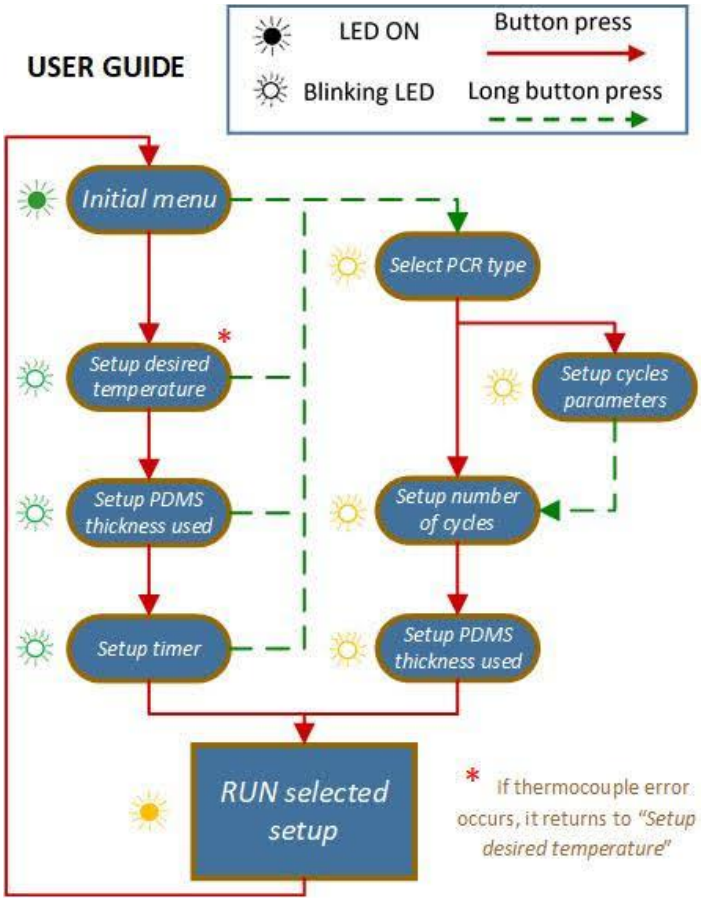
Conclusion

We have demonstrated and validated a compact, portable, modular, and user-friendly temperature control system that was created using an estimated budget of $318.86 without the benefit of production scale-up. It enables simple programming and control of temperatures on LOC devices or for any sample that fits on a standard microscope slide. The system precisely controls the temperature at the surface of a sample during imaging steps in an epifluorescent microscope. Temperature data can be displayed through a smartphone app and on the Control Device. While the system does not require an attached computer to function, temperature data can also be collected on a computer through a USB connection to the Control Device if desired. The system was validated by an external thermometer as well as an IR thermal camera. In addition, the system temperature was monitored by measuring the fluorescence of the temperature sensitive dye Rhodamine B inside a microfluidic device. Finally, the system was tested by a successful initial-endpoint PCR and a real-time PCR amplification of a cel-miR-39 miRNA cDNA. The entire 40 cycle PCR, including the 4 minutes initial denaturation, occurred in 95.2 minutes.

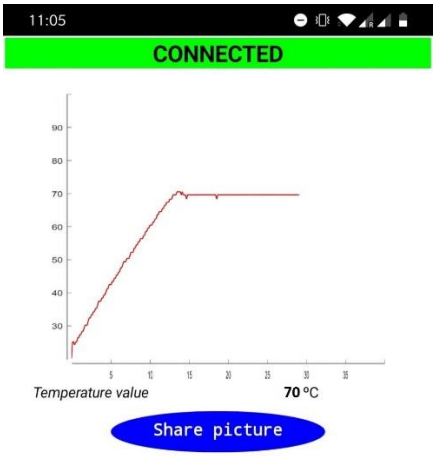
While the temperature control system shown here is sufficient for many applications, including PCR amplification, users can easily modify the system according to their needs. The customizable nature of the system allows it to be manipulated by the user and add additional components based on the experiment requirements. This provides even greater flexibility to end users and expands the potential applications of the temperature control system. The modular nature of the system also allows the user to easily replace the components if they become damaged.

The temperature control system described here is an inexpensive, portable, reusable, enabling technology with potential applications in chemistry, biology, physics, medicine, material science, and other industries that require concurrent imaging and temperature control.

Supplemental Information



SI Figure 6.1: The user guide demonstrating how to navigate through the menus programmed into the microcontroller.



SI Figure 6.2: The Bluetooth-enabled application, which will output a graph of the real-time temperature.

Initial Endpoint PCR amplification setup

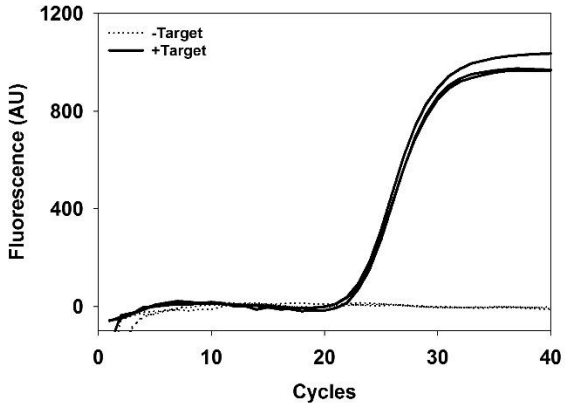
Before real-time amplification was run, a simple endpoint PCR experiment was performed. An initial LOC device mimic was made by cutting two rectangular 8x8mm square wells in a 0.2mm thick PDMS layer. A standard 1 mm thick glass microscope slide (Globe Scientific, Mahwah, NJ) and a 22 x 50 mm thickness #1 glass cover slide (Thermo Scientific, Portsmouth, NH) were treated with Sigmacote® (Sigma-Aldrich, St. Louis, MO) according to manufacturer's instructions. The PDMS layer was bonded to the standard 1mm thick glass microscope slide after exposure to oxygen plasma using standard PDMS bonding techniques[34]. A 1µL droplet of the positive sample and a 1µL droplet of the negative sample were placed in the center of separate square wells and covered with approximately 6 µL of mineral oil each; the droplets were completely surrounded by mineral oil on all sides. The glass cover slide was placed on top of the PDMS layer. Next, the LOC device mimic was placed in the Device Holder, the Device Holder

was closed and placed in the epifluorescence microscope. The following thermal cycling steps were setup in the Control Device using the user guide (showed in Figure SI1 as guidance for the internal menu navigation: initial denaturation (95˚C for 10 minutes), followed by 40 cycles with two steps (95˚C for 15 seconds and 60˚C for 60 seconds). Finally, it was followed by a final extension (68˚C for 5 minutes). The total amount of time spent for the qPCR was 130 minutes. The temperature on the device was confirmed using a type K thermocouple connected to an external handheld digital thermometer (Omega, Norwalk, CT). Three positive and three negative samples (10 µL each) were loaded into a standard commercial thermal cycler CFX Connect (BioRad, Hercules, California) and subjected to the same thermal cycling steps as described above.

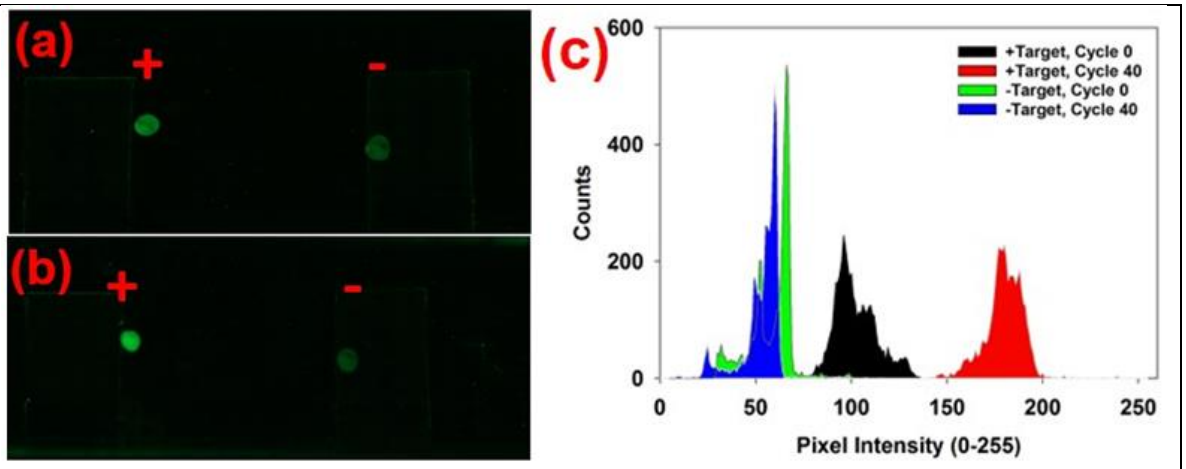
Endpoint PCR amplification within the temperature control system

The LOC device mimic was imaged using an Evos FL Auto (Fisher Scientific, Waltham, MA) with 4x objective and the EVOS GFP light cube. The device was imaged before and after thermal cycling, but not in real time. An increase in the fluorescence before the PCR cycles (cycle 0) and after the PCR cycles (cycle 40) is visible to the naked eye in the droplet containing target and not in the negative control droplet (Figure SI4a,b). The quantitative increase is also shown in the histograms of the pixel intensity which was measured using ImageJ for green light only and with a 75 pixel diameter circle (Figure SI4c). The average pixel intensity in the positive droplet is 102 +/- 11 before amplification and 180 +/- 11 after amplification. In contrast, the average pixel intensity in the negative droplet is 59 +/- 11 before amplification and 54 +/- 10 after amplification. More information on the histogram statistics can be found in Figure SI4. As expected, the positive samples in the standard commercial thermal cycler amplified and the negative samples did not (**SI**

Fig. 6.3). After the endpoint PCR amplification was successful, amplification in real time was studied (Figure SI5 and Figure 6).



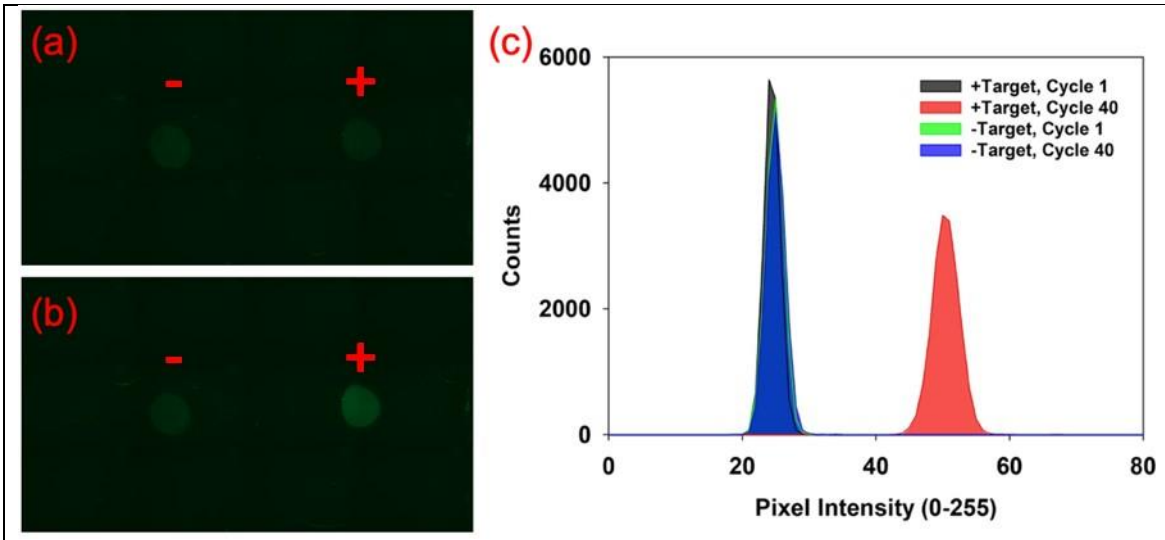
SI Figure 6.3: 10 µL PCR reactions run in a standard thermal cycler. Data show expected amplification in the presence of target (solid lines) and no amplification in the absence of target (dotted lines). Repeats represent n = 3 technical replicates.



+ Target, Cycle 0		+ Target, Cycle 40		- Target, Cycle 0		- Target, Cycle 40	
Count	4421	**Count**	4421	**Count**	4421	**Count**	4421
Mean	102.479	**Mean**	179.867	**Mean**	58.825	**Mean**	53.594
StdDev	10.771	**StdDev**	10.499	**StdDev**	11.354	**StdDev**	10.237
Min	79	**Min**	20	**Min**	29	**Min**	5

Max	136	**Max**	248	**Max**	117	**Max**	115
Mode	96 (244)	**Mode**	180 (228)	**Mode**	66 (536)	**Mode**	60 (502)

SI Figure 6.4: Fluorescent images and table with statistical data of the fluorescence at cycle 1 and cycle 40 of an endpoint PCR reaction. a) Droplet images at cycle 0. b) Droplet images at cycle 40. c) Histogram of pixel intensity for positive and negative samples at cycle 0 and cycle 40. The table shown above includes detailed statistical data given by ImageJ of an endpoint PCR before thermal cycling (cycle 0) and after 40 cycles of PCR on the microscope stage.



.

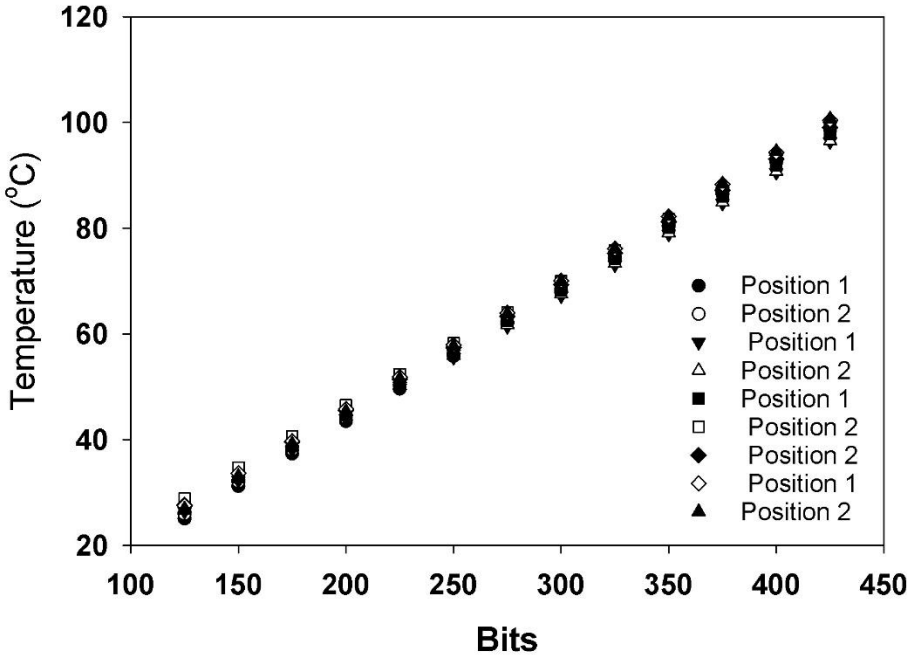
+ Target, Cycle 1		**+ Target, Cycle 40**		**- Target, Cycle 1**		**- Target, Cycle 40**	
Count	17692	**Count**	17692	**Count**	17692	**Count**	17692
Mean	24.455	**Mean**	50.439	**Mean**	24.829	**Mean**	24.997
StdDev	1.181	**StdDev**	2.007	**StdDev**	1.317	**StdDev**	1.365
Min	20	**Min**	43	**Min**	20	**Min**	19
Max	34	**Max**	67	**Max**	31	**Max**	32
Mode	24 (5636)	**Mode**	50 (3485)	**Mode**	25 (5331)	**Mode**	25 (5123)

SI Figure 6.5: Fluorescent images and table with statistical data of the fluorescence at cycle 1 and cycle 40 of a real-time PCR, presented in the manuscript. a) droplet images at cycle 0. b) Droplet

images at cycle 40. c) Histogram of pixel intensity for positive and negative samples at cycle 1 and cycle 40. The table shown above includes detailed statistical data given by ImageJ of the real time PCR before thermal cycling (cycle 0) and after 40 cycles of PCR on the microscope stage.

Calibration of the MAX6675 thermocouple temperature sensor

For optimal real-time PCR, MAX6675 digitization of the type K thermocouple signals were calibrated by running the temperature control system for two minutes at 40˚C, 50˚C, 60˚C, 70˚C, 80˚C, and 90˚C and measuring the output of a type K or type T thermocouple plugged in to an external handheld digital thermometer (Omega, Norwalk CT). The number of bits read by the temperature control system was compared to the actual temperature read from the external thermometer and the temperature was fit linearly to the MAX6675 bit output to find the bits per ˚C and y intercept (**SI Fig. 6.6**).



SI Figure 6.6: Calibration of the temperature control system thermocouples. Thermocouples attached to an external thermometer (both type T and K) were placed next to the thermocouples attached to the device. The number of bits read by the MAX6675 was correlated to the temperature measured by the external thermocouple/thermometers to determine the number of bits per ˚C given by the MAX6675. Data shown for 9 different measurements at the two thermocouple positions.

Acknowledgements

This material is based upon work supported by the National Science Foundation under Grant No. 1847245. We thank the Wilking lab at Montana State University for use of their 3D printers and printing materials.

References cited

1. Reyes, D. R.; Iossifidis, D.; Auroux, P.-A.; Manz, A., Micro total analysis systems. 1. Introduction, theory, and technology. *Analytical chemistry* **2002,** *74* (12), 2623-2636.

2. Stone, H. A.; Stroock, A. D.; Ajdari, A., Engineering flows in small devices: microfluidics toward a lab-on-a-chip. *Annu. Rev. Fluid Mech.* **2004,** *36*, 381-411.

3. Dittrich, P. S.; Manz, A., Lab-on-a-chip: microfluidics in drug discovery. *Nature reviews Drug discovery* **2006,** *5* (3), 210-218.

4. Andersson, H.; Van den Berg, A., Microfluidic devices for cellomics: a review. *Sensors and actuators B: Chemical* **2003,** *92* (3), 315-325.

5. Dusny, C.; Grünberger, A., Microfluidic single-cell analysis in biotechnology: from monitoring towards understanding. *Current opinion in biotechnology* **2020,** *63*, 26-33.

6. McCalla, S. E.; Tripathi, A., Microfluidic reactors for diagnostics applications. *Annual review of biomedical engineering* **2011,** *13*, 321-343.

7. Miralles, V.; Huerre, A.; Malloggi, F.; Jullien, M.-C., A review of heating and temperature control in microfluidic systems: techniques and applications. *Diagnostics* **2013,** *3* (1), 33-67.

8. Jung, W.; Han, J.; Choi, J.-W.; Ahn, C. H., Point-of-care testing (POCT) diagnostic systems using microfluidic lab-on-a-chip technologies. *Microelectron Eng* **2015,** *132*, 46-57.

9. Kaminski, T.; Garstecki, P., Controlled droplet microfluidic systems for multistep chemical and biological assays. *Chemical Society Reviews* **2017,** *46* (20), 6210-6226.

10. Bruijns, B.; Van Asten, A.; Tiggelaar, R.; Gardeniers, H., Microfluidic devices for forensic DNA analysis: A review. *Biosensors* **2016,** *6* (3), 41.

11. Zheng, B.; Roach, L. S.; Ismagilov, R. F., Screening of protein crystallization conditions on a microfluidic chip using nanoliter-size droplets. *Journal of the American chemical society* **2003,** *125* (37), 11170-11171.

12. Beer, N. R.; Hindson, B. J.; Wheeler, E. K.; Hall, S. B.; Rose, K. A.; Kennedy, I. M.; Colston, B. W., On-chip, real-time, single-copy polymerase chain reaction in picoliter droplets. *Analytical chemistry* **2007,** *79* (22), 8471-8475.

13. Srivannavit, O.; Gulari, M.; Hua, Z.; Gao, X.; Zhou, X.; Hong, A.; Zhou, T.; Gulari, E., Microfluidic reactor array device for massively parallel in situ synthesis of oligonucleotides. *Sensors and Actuators B: Chemical* **2009,** *140* (2), 473-481.

14. Geertz, M.; Shore, D.; Maerkl, S. J., Massively parallel measurements of molecular interaction kinetics on a microfluidic platform. *Proceedings of the National Academy of Sciences* **2012,** *109* (41), 16540-16545.

15. Burns, M. A.; Johnson, B. N.; Brahmasandra, S. N.; Handique, K.; Webster, J. R.; Krishnan, M.; Sammarco, T. S.; Man, P. M.; Jones, D.; Heldsinger, D., An integrated nanoliter DNA analysis device. *Science* **1998,** *282* (5388), 484-487.

16. Lamprou, D. A., Emerging technologies for diagnostics and drug delivery in the fight against COVID-19 and other pandemics. *Expert review of medical devices* **2020**, 1-6.

17. Chen, T.; Gomez-Escoda, B.; Munoz-Garcia, J.; Babic, J.; Griscom, L.; Wu, P.-Y. J.; Coudreuse, D., A drug-compatible and temperature-controlled microfluidic device for live-cell imaging. *Open biology* **2016,** *6* (8), 160156.

18. Jähnisch, K.; Hessel, V.; Löwe, H.; Baerns, M., Chemistry in microstructured reactors. *Angewandte Chemie International Edition* **2004,** *43* (4), 406-446.

19. Demello, A. J., Control and detection of chemical reactions in microfluidic systems. *Nature* **2006,** *442* (7101), 394-402.

20. Woolley, A. T.; Hadley, D.; Landre, P.; deMello, A. J.; Mathies, R. A.; Northrup, M. A., Functional integration of PCR amplification and capillary electrophoresis in a microfabricated DNA analysis device. *Analytical Chemistry* **1996,** *68* (23), 4081-4086.

21. Casquillas, G. V.; Fu, C.; Le Berre, M.; Cramer, J.; Meance, S.; Plecis, A.; Baigl, D.; Greffet, J.-J.; Chen, Y.; Piel, M., Fast microfluidic temperature control for high resolution live cell imaging. *Lab on a Chip* **2011,** *11* (3), 484-489.

22. Angione, S. L.; Chauhan, A.; Tripathi, A., Real-time droplet DNA amplification with a new tablet platform. *Analytical chemistry* **2012,** *84* (6), 2654-2661.

23. Amasia, M.; Cozzens, M.; Madou, M. J., Centrifugal microfluidic platform for rapid PCR amplification using integrated thermoelectric heating and ice-valving. *Sensors and Actuators B: Chemical* **2012,** *161* (1), 1191-1197.

24. Bu, M.; Perch-Nielsen, I. R.; Sørensen, K. S.; Skov, J.; Sun, Y.; Bang, D. D.; Pedersen, M. E.; Hansen, M. F.; Wolff, A., A temperature control method for shortening thermal cycling time to achieve rapid polymerase chain reaction (PCR) in a disposable polymer microfluidic device. *J Micromech Microeng* **2013,** *23* (7), 074002.

25. Kimura, Y.; Ikeuchi, M.; Inoue, Y.; Ikuta, K., 3D microdevices that perform sample purification and multiplex qRT-PCR for early cancer detection with confirmation of specific RNAs. *Sci Rep-Uk* **2018,** *8* (1), 1-10.

26. Selck, D. A.; Ismagilov, R. F., Instrument for real-time digital nucleic acid amplification on custom microfluidic devices. *PLoS One* **2016,** *11* (10).

27. Mendoza-Gallegos, R. A.; Rios, A.; Garcia-Cordero, J. L., An affordable and portable thermocycler for real-time PCR made of 3D-printed parts and off-the-shelf electronics. *Analytical chemistry* **2018,** *90* (9), 5563-5568.

28. Wade, H., Trial and error: An organized procedure. *InTech* **2005,** *52* (5), 38-42.

29. Duffy, D. C.; McDonald, J. C.; Schueller, O. J.; Whitesides, G. M., Rapid prototyping of microfluidic systems in poly (dimethylsiloxane). *Analytical chemistry* **1998,** *70* (23), 4974-4984.

30. Schneider, C. A.; Rasband, W. S.; Eliceiri, K. W., NIH Image to ImageJ: 25 years of image analysis. *Nat. Methods* **2012,** *9* (7), 671.

31. Klein, D., Quantification using real-time PCR technology: applications and limitations. *Trends in molecular medicine* **2002,** *8* (6), 257-260.

32. Schweiz, M. V., Table of Emissivity of various surfaces. *Schaffhausen: Mikron Instrument, nd Print* **2012**.

33. Shah, J. J.; Gaitan, M.; Geist, J., Generalized temperature measurement equations for rhodamine B dye solution and its application to microfluidics. *Analytical chemistry* **2009,** *81* (19), 8260-8263.

34. Temiz, Y.; Lovchik, R. D.; Kaigala, G. V.; Delamarche, E., Lab-on-a-chip devices: How to close and plug the lab? *Microelectron Eng* **2015,** *132*, 156-175.

CHAPTER SEVEN

SARS-COV-2 DETECTION IN THE NASOPHARYNGEAL SWABS AND SALIVA OF COLLEGE STUDENTS USING RT-QPCR AND RT-LAMP

Contribution of Authors and Co-Authors

Manuscript in Chapter 7

Author: Dimitri A. Bikos

Contributions: Planned and performed the experiments, analyzed the data, and wrote the manuscript.

Co-Author: Chiachi Hwang

Contributions: Planned and performed the experiments, analyzed the data, and wrote the manuscript.

Co-Author: Kristen A. Brileya

Contributions: Planned and performed the experiments, analyzed the data, and wrote the manuscript.

Co-Author: Al Parker

Contributions: Planned the experiments, analyzed the data, and wrote the manuscript.

Co-Author: Emma K. Loveday

Contributions: Planned the experiments, analyzed the data, and wrote the manuscript.

Co-Author: Maya Rodriguez

Contributions: Planned the experiments, analyzed the data, and wrote the manuscript.

Co-Author: Isaak J. Thornton

Contributions: Design and fabrication.

Co-Author: Thomas B. LeFevre

Contributions: Design and fabrication.

Co-Author: James N. Wilking

Contributions: Planned and oversaw the experiments, analyzed the data, and wrote the manuscript.

Co-Author: Michael Dills

Contributions: Planned the experiments, analyzed the data, and wrote the manuscript

Co-Author: Seth T. Walk

Contributions: Planned and oversaw the experiments, analyzed the data, and wrote the manuscript.

Co-Author: Alexandra K. Adams

Contributions: Planned and oversaw the experiments, analyzed the data, and wrote the manuscript.

Co-Author: Raina K. Plowright

Contributions: Planned and oversaw the experiments, analyzed the data, and wrote the manuscript.

Co-Author: Andrew B. Hoegh

Contributions: Planned and oversaw the experiments, analyzed the data, and wrote the manuscript.

Co-Author: Jason R. Carter

Contributions: Secured funding.

Co-Author: Jayne Morrow

Contributions: Planned and oversaw the experiments, analyzed the data, and wrote the manuscript.

Co-Author: Matthew P. Taylor

Contributions: Planned and oversaw the experiments, analyzed the data, and wrote the manuscript.

Co-Author: Deborah E. Keil

Contributions: Planned and oversaw the experiments, analyzed the data, and wrote the manuscript.

Co-Author: Matthew W. Fields

Contributions: Planned and oversaw the experiments, analyzed the data, and wrote the manuscript.

Co-Author: Connie B. Chang

Contributions: Planned and oversaw the experiments, analyzed the data, and wrote the manuscript.

Manuscript Information

Dimitri A. Bikos, Chiachi Hwang, Kristen A. Brileya, Al Parker, Emma K. Loveday, Maya Rodriguez, Isaak J. Thornton, Thomas B. LeFevre, James N. Wilking, Michael Dills, Seth T. Walk, Alexandra Adams, Raina K. Plowright, Andrew B. Hoegh, Jason R. Carter, Jayne Morrow, Matthew P. Taylor, Deborah E. Keil, Matthew W. Fields, and Connie B. Chang

New England Journal of Medicine

Status of Manuscript:
_X_ Prepared for submission to a peer-reviewed journal
___ Officially submitted to a peer-reviewed journal
___ Accepted by a peer-reviewed journal
___ Published in a peer-reviewed journal

DOI:

NEJM Group

Abstract

Background

Diagnostic testing can identify outbreaks and inform preventive strategies for slowing the spread of SARS-CoV-2, the virus that causes Covid-19. The “gold standard” method for detection of SARS-CoV-2 is reverse transcription quantitative polymerase chain reaction (RT-qPCR) performed on samples collected using nasopharyngeal (NP) swabs. While NP RT-qPCR achieves high sensitivity, it requires trained personnel to administer and suffers from lengthy time-to-result. Instead, rapid saliva-based reverse transcription loop-mediated amplification (RT-LAMP) screening methods may offer advantages in sample collection and speed.

Methods

Regardless of symptomatic presentation, a total of 233 individuals were tested for SARS-CoV-2 using NP RT-qPCR, alongside saliva-based RT-qPCR (SalivirDetect) and RT-LAMP (SLAMP), a simple and rapid fluorometric RT-LAMP assay performed directly on heat-inactivated saliva without any additional treatments or RNA extraction. SLAMP is conducted in triplicate and takes 45 min. Samples found negative using both saliva-based methods but positive under CDC NP RT-qPCR above the saliva method LoD were excluded from evaluation, suggesting significant differences in viral titer between sampling sites. Individuals who consumed potential inhibitors in the form of food, drink, and oral health products within 30 min of sampling were identified using a self-reported questionnaire.

Results

Of the 233 NP RT-qPCR tests, 58 were positive and 175 were negative. Comparatively, SLAMP resulted in 95% sensitivity and 98% specificity and SalivirDetect 97% sensitivity and 98% specificity. Prior consumption had no measurable effect on test outcomes, except for drinking, which lowered Ct values in saliva.

Conclusions

SLAMP requires less technician and instrument time than CDC-approved NP RT-qPCR and demonstrates that saliva-based RT-LAMP can enable frequent and rapid identification of pre-symptomatic and asymptomatic SARS-CoV-2 infections with high sensitivity and specificity.

Introduction

The SARS-CoV-2 virus[1] emerged in late 2019, rapidly developing into a worldwide pandemic still posing a persistent threat to public health, economics, and quality of life. While real-world vaccine efficacy continues to be evaluated[2], uncertainties over variant escape[3], vaccine availability[4], and duration of immunity[5] suggest that testing will continue to play an indispensable role in managing the disease into the future. Viral spread can be controlled by deploying diagnostic tests that rapidly identify infected individuals for quarantine and contact tracing. Rapid and frequent SARS-CoV-2 testing is needed to identify new outbreaks as the world struggles to lift lockdowns[6] and reopen schools for in-person instruction in Fall 2021[7].

The “gold standard" method for detecting SARS-CoV-2 has been reverse transcription quantitative polymerase chain reaction (RT-qPCR) performed on samples collected using nasopharyngeal (NP) swabs[8, 9]. However, RT-qPCR testing requires significant reagent

consumption, specialized equipment, trained operators, and several hours to perform. Collection of NP swab samples is invasive and must be performed by trained medical personnel. Performing surveillance at scale calls for innovative testing strategies that are inexpensive, minimize reagent consumption, decrease assay time-to-result, and avoid restrictions in available personnel[10, 11].

One such alternative to RT-qPCR is reverse transcriptase loop-mediated isothermal amplification (RT-LAMP), an isothermal technique for the amplification of RNA[12-14]. RT-LAMP simplifies SARS-CoV-2 testing by eliminating the long assay times and technical barriers such as the electronically controlled thermal cycling at high temperatures required by PCR-based methods[15-20]. RT-LAMP is substantially faster than RT-qPCR, and when performed on saliva samples[21], eliminates the need for specialized swabs and operators while assuaging the public reluctance to testing, largely brought on by invasive NP swabs[22, 23]. The RT-LAMP assay is usually[24, 25] completed within 45 min to confirm a negative, while some exceptionally high viral loads are detectable within 5-10 min.

Here, we report the findings of a multi-day pilot study to evaluate saliva-based SARS-CoV-2 detection using RT-qPCR and RT-LAMP methods compared alongside to Centers for Disease Control and Prevention (CDC)-approved NP RT-qPCR testing at Montana State University (MSU) during mid-November 2020, a time when Covid-19 cases reached county-wide highs (**SI Fig. 7.1**). We present the results of SLAMP, a rapid fluorometric RT-LAMP assay performed directly on saliva without chemical extraction steps. Additionally, we compare SLAMP to SalivirDetect, a direct saliva-to-RT-qPCR assay and both saliva tests are compared to CDC-approved RT-qPCR performed on samples swabbed from the nasopharynx. Each participant was provided a self-reported survey identifying samples collected within 30 min of consuming food,

drink, or oral hygiene products to determine the extent to which saliva test results might be affected.

Methods

Participants

Samples were collected from 233 participants who visited the on-campus CDC-approved RT-qPCR testing site provided for persons exhibiting Covid-19 symptoms or who suspected recent contact with SARS-CoV-2-positive individuals. We directly compared samples from two sources on the body of each participant, NP swabs, tested using CDC-approved RT-qPCR, and saliva, tested using SLAMP and SalivirDetect. All individuals tested signed a consent form before participating in this study (Supplementary Information – Consent Form).

Self-Reported Questionnaire

Participants were provided with a self-reported questionnaire (Supplementary Information - Questionnaire) that collected demographic information including age, gender, race, and ethnicity. Additionally, subjects were asked to confirm whether they were currently symptomatic or asymptomatic and whether they had recent contact with infected individuals. Finally, subjects were asked to disclose if they had, in the last 30 min, consumed food or liquid, used mouthwash, gum or lozenges, smoked, vaporized or chewed tobacco, or brushed their teeth.

Sample Collection

All sampling occurred at an outdoor parking lot in drive-thru format while participants remained inside automobiles as an additional precaution against viral transmission. Individuals who expressed interest in participating in our pilot study were administered NP swabs by trained

staff before donating an additional saliva sample as outlined by the university IRB (Supplementary Information – IRB).

Viral Inactivation - NP Swab

NP swabs were heat-inactivated by diluting collection buffer 1:2 with molecular biology grade H_2O (50 μL buffer: 50 μL H_2O) and assigned a location on a 96-well PCR plate. Plates were covered with sealing foil and heated to 95 °C for 5 min in a standard thermocycler before being cooled to 4 °C until ready to test.

Viral Inactivation - Saliva

In the case of saliva collection, participants were given a 3D-printed accessory caddy (**SI Fig. 7.2**) containing a 30-mL polypropylene medicine cup (MedPride 97205), a generic 1-mL transfer pipet, and a screw cap tube (VWR 16466-040). Saliva was expressed into the medicine cup (Fig. S3i) before using the pipet to transfer ≈1.0 mL into the screw-cap tube (Fig. S3ii). Tubes were indexed with heat- and water-resistant adhesive labels (Electronic Imaging Materials, Inc. 667) prepared via barcode printer (TSC MB340T). Samples were inactivated using a heat block (Labnet AccuBlock) set to 95 °C for 15 min (Fig. S3iii) simultaneously during which time ribonucleases were denatured and virions lysed. While not strictly necessary, samples were removed from heat treatment and left at room temperature for 20 min to allow debris in the saliva to settle for easier pipetting. Barcodes were entered into records using a handheld scanner (Motorola Symbol LS2208-SR20007R-NA).

CDC-approved RT-qPCR from NP Swab

Next, 10 uL of diluted, previously heat-inactivated[26] sample material was mixed with 15 µL of each 1-step PCR master mix consisting of: 1.) 1.5 µL each N1 and N2 primer probe set, 5 µL Quantabio Ultraplex 1-Step Toughmix (4×), and 7 µL H_2O per reaction; 2.) 1.5 µL human RNase P reaction primer probe mix, 5 µL Quantabio Ultraplex 1-Step Toughmix (4×), and 8.5 µL H_2O per reaction. Real-time PCR thermocycling was performed per CDC guidelines[27]. Each sample was screened in a combined N1, N2 reaction with an internal control human RNase P reaction (Supplementary Methods). Samples with no detectable fluorescence for either assay and those with SARS-CoV-2 target fluorescence between 39.5 and 45 cycle thresholds (Ct) were re-tested using a validated RNA purification kit (Promega Maxwell RSC Viral Total Nucleic Acid Multi-Pack Kit, ASB1330). RNA-purified samples were assayed under the same conditions, but with 5 µL of purified sample added to each reaction for 20 µL total reaction volume. No replicates were performed.

SalivirDetect - RT-qPCR in saliva

SLAMP was compared to a saliva-based RT-qPCR assay called SalivirDetect with FDA Emergency Use Authorization (EUA) application number EUA202615, submitted August 25, 2020 and developed by Drs. Phillip Buckhaults and Carolyn Banister (University of South Carolina). SalivirDetect, like SLAMP, uses heating at 95 °C to process saliva without inactivation buffers or additives. SalivirDetect was conducted in the InHealth Life Sciences CLIA/CAP laboratory led by Dr. Deborah Keil (MSU). Briefly, ≈5 mL of saliva was collected in a 50-mL centrifuge tube. The tube was placed in a 95 °C oven (Fisherbrand Isotemp General Purpose Heating and Drying Oven) for 45 min, then allowed to sit at room temperature to cool. Two 5-µL

aliquots of the saliva were transferred to two wells in a 96-well plate containing Luna Kit RT-qPCR reagents (E3600, New England Biolabs), one well containing N1 primers and the second well containing human RNase P primers from the United States CDC Real-Time Reverse Transcription PCR Panel [cite] for SARS-CoV-2 detection (Supplementary Methods). Samples were run on a CFX Opus 96 Real-Time qPCR instrument (Bio-Rad, cat no. 12011319). Only a single test per sample was performed with no replicates.

SLAMP - RT-LAMP in saliva

RT-LAMP reactions were set up as described by protocol E1700 (New England Biolabs) at 25 μL final reaction volume with the following modified formulation: 12.5 μL WarmStart 2X Master Mix (E1700L, New England Biolabs) 0.175 μL of dUTP (N0459S, New England Biolabs), 0.5 μL of UDG (M0372L, New England Biolabs), 2.5 μL of duplex NE primer mix (Supplementary Methods), 0.5 μL of 25-μM SYTO-9 (S34854, Invitrogen), 0.25 μL of 25-μL ROX reference dye (61110, Lumiprobe), 2.5 μL of 400-mM molecular biology grade guanidine HCl (GuHCl) (J65661, Alfa Aesar), 1.075 μL of nuclease-free water (B1500L, New England Biolabs), and 5 μL of heat-inactivated saliva sample. Controls were run on each 96-well plate, including SARS-CoV-2-negative heat-inactivated saliva as a no-template control (NTC), human beta-actin (ACTB) as a positive internal control, and three positive test controls of 5×10^4, 5×10^2, and 5×10^0 copies/μL synthetic SARS-CoV-2 RNA (NIST, RGTM 10169 Fragment 1) (Supplementary Methods). Positive test control dilutions were made using heat-inactivated SARS-CoV-2-negative saliva. All SLAMP reactions were prepared in 96-well qPCR plates (Applied Biosystems, 4483485) sealed using an ALPS 50V manual heat sealer (Thermo Scientific) with Clear Seal Diamond films (AB-0812, Thermo Scientific). Reactions were performed at 65 °C (1.6

°C/s ramp) on a QuantStudio 3 Real-Time PCR System (Applied Biosystems) (**SI Fig. 7.3 iv**) for 45 min. Fluorescence measurements for SYTO-9 and ROX channels were recorded every 1 min. SARS-CoV-2 may be present in the nasopharynx while not in the saliva [cite]. To avoid invalid test samples, only NP RT-qPCR-positive samples that also tested positive under at least one of the two saliva methods were included in this study. Any time-to-positive Tp > 40 min was considered negative. See Supplementary Methods for reaction curve-fitting procedure and SLAMP formulation optimization. Each saliva sample was run in triplicate.

Statistical Analysis

Statistical bootstrapping[28] methods can predict how the normally triplicate SLAMP sensitivity and specificity may change when performed only in duplicates or single tests. Using our (triplicate, 45 min) SLAMP test results, 1,000 random bootstrap samples were used to predict sensitivity with respect to CDC-approved NP RT-qPCR at 95% confidence intervals when only 1 or 2 SLAMP reactions are performed per sample. In addition, we model the outcomes of SLAMP testing under hypothetical disease prevalence scenarios. Based upon the experimental sensitivity of SLAMP in triplicate and the bootstrap-predicted sensitivities of duplicate and single SLAMP tests, we determine the total number of detectable positive individuals based on a daily testing capacity of six 384-well plates, reserving 10 wells for controls when performed in triplicate, duplicate, or single tests. Specificity is assumed to remain constant.

All t-tests are reported as p values. Pearson correlation coefficients are reported as r values.

Results

Comparing testing methods: SLAMP, SalivirDetect, and NP RT-qPCR.

We compare samples from two matrices, NP swab and saliva, across three different testing methods, SLAMP, SalivirDetect, and the "gold standard" CDC-approved NP RT-qPCR, the latter performed using NP swab while saliva, shown to provide sufficient viral RNA for detection[29, 30], was used for both SLAMP and SalivirDetect. Both SalivirDetect and CDC-approved NP RT-qPCR are PCR-based while SLAMP uses isothermal LAMP amplification. SLAMP was performed in triplicate while SalivirDetect and NP RT-qPCR tests were performed only once (**Fig. 7.1**).

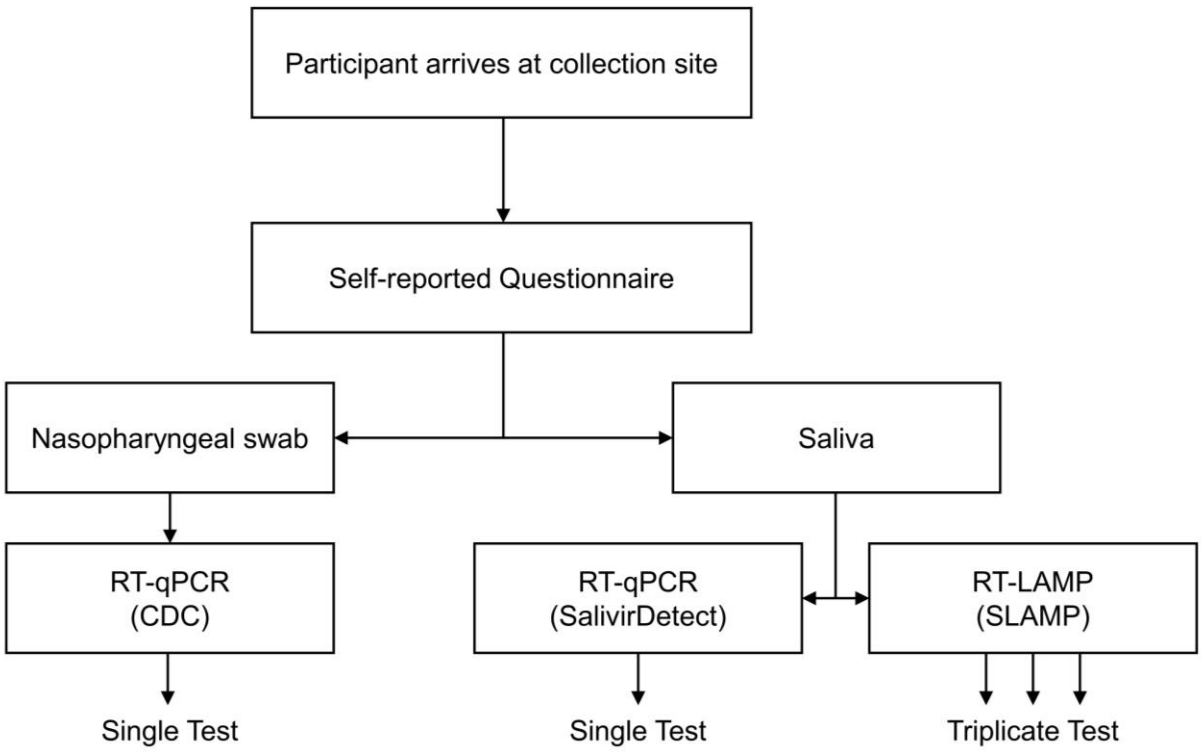


Figure 7.1. *Sample collection and testing process flow.*

Demographics

Participant ages ranged from 17 to 63 with a median age of 20. Males made up 47% and females 53%. Participants were comprised of 94% white and 6% other races including Asian and mixed-race individuals of American Indian, Alaskan Native, Native Hawaiian or Pacific Islander, and African American descent. Ethnically, 9 individuals self-reported as Hispanic or Latino, 207 as not Hispanic or Latino, and 17 chose not to respond (**Table 7.1**).

Clinical presentation

Participants self-reported their illness presentation as either symptomatic or asymptomatic and indicated whether they had knowledge of recent exposure to a confirmed Covid-19-positive individual [cite]. A majority 74% of study participants self-reported as symptomatic among whom 46% indicated knowledge of recent exposure. Among the 29% asymptomatic, 6% were unaware of exposure, the remaining 94% sought testing after learning of SARS-CoV-2 exposure (**Table 7.1**).

Potential saliva contamination

Testing was conducted on a first come, first served basis without appointments. Therefore, instructions to abstain from food, drink, or oral hygiene products before donating saliva could not be provided to participants ahead of time. To determine the extent to which saliva may have been affected, the questionnaire asked participants whether they had eaten food or consumed drinks within 30 min of sampling. In addition, other consumables or hygiene products that may have persisted in saliva were also included, namely mouthwash, gum/lozenge, tobacco (whether smoked, vaporized, or chewed), and toothpaste from brushing teeth. Many participants had consumed multiple items. In order to make quantitative comparisons between saliva sample Ct

values, we report the consumption survey results for individuals who testing positive using SalivirDetect (**Table 7.1**).

Table 7.1. Self-reported Demographic Information and Clinical Presentation.	
Characteristic	**Participants (N = 233)**
Sex - no.	
Male	109
Female	124
Median Age (IQR)* – yr	20 (19-22)[†]
Race – no.	
White	220
Asian	1
Mixed race	11
Not provided	1
Ethnicity – no.	
Hispanic or Latino	9
Not Hispanic or Latino	207
Not provided	17
Clinical Presentation – no.	
Symptomatic (known exposure)	76
Symptomatic (no known exposure)	88
Asymptomatic (known exposure)	64
Asymptomatic (no known exposure)	4
Not provided	1
Consumption within 30 min of Saliva Sampling[††] – no.	

Only Food	4
Only Drink	23
Both Food and Drink	10
Neither Food nor Drink	21
Mouthwash†††	
Yes	5
No	52
Gum or Lozenge†††	
Yes	6
No	52
Tobacco††† **(Smoke, Vape, or Chew)**	
Yes	7
No	51
Brushed Teeth†††	
Yes	31
No	27

* Interquartile range.

† N = 223 (10 non-respondent).

††Tested positive using SalivirDetect.

†††Multiple selections possible.

Testing outcomes - performance of the three methods

Performance metrics of saliva methods SalivirDetect and SLAMP were evaluated by comparing results to the "gold-standard" CDC-approved NP RT-qPCR method between 233 individuals tested using all three methods. We report the true positive (TP), true negative (TN), false positive (FP), and false negative (FN) counts along with the true positive rate (TPR) and true negative rate (TNR), also called sensitivity and specificity, respectively (**Table 7.2**). The

sensitivity/specificity (in %) of SalivirDetect and SLAMP methods were 97/98 and 95/98, respectively. Based on NP RT-qPCR, 58 positive and 175 negative individuals were identified resulting in a disease prevalence of 25%.

Table 7.2. Test Outcomes and Performance Metrics.	
Method and Category	
NP RT-qPCR (CDC-approved "gold standard")	
Diseased	58
Non-diseased	175
Saliva RT-qPCR (SalivirDetect)	
True Positives (TP)	56
True Negatives (TN)	220
False Positives (FP)	3
False Negatives (FN)	2
Sensitivity (%)	97
Specificity (%)	98
Saliva RT-LAMP (SLAMP)	
True Positives (TP)	55
True Negatives (TN)	172
False Positives (FP)	3
False Negatives (FN)	3
Sensitivity (%)	95
Specificity (%)	98

Comparing positive samples - two sample matrices and three testing methods

The 58 samples found positive under CDC-approved NP RT-qPCR are placed in order of increasing Ct value (decreasing effective SARS-CoV-2 genome concentration or viral titer) and compared to Ct values under SalivirDetect (**Fig. 2A**) and Tp values using SLAMP (**Fig. 7.2B**). Samples positive under saliva-based tests are compared in order of increasing SalivirDetect Ct value (**Fig. 7.2C**) and increasing SLAMP Tp value (**Fig. 7.2D**). False negatives are shown as missing bars and indicated by black arrows.

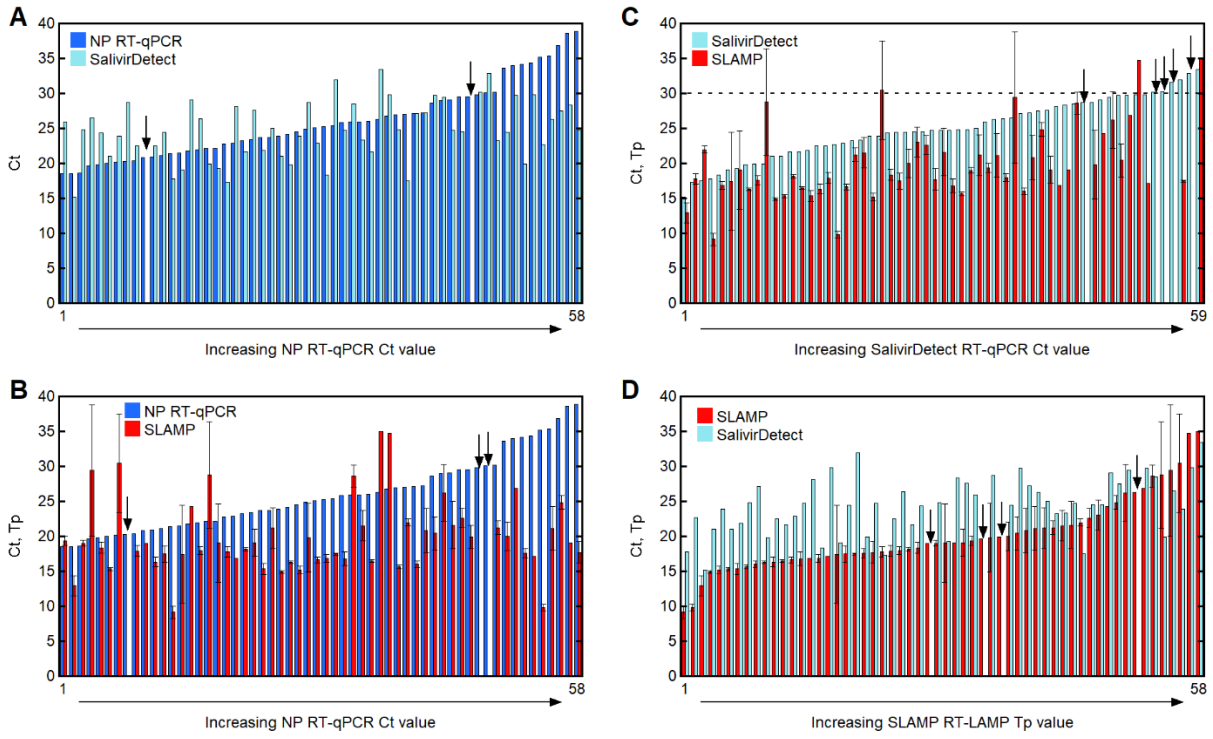


Figure 7.2. *Positive sample results compared between three tests.* Ct values of N=58 positive NP RT-qPCR and SalivirDetect samples in order of increasing CDC-approved NP RT-qPCR Ct value (Panel A). Ct values of N=58 positive CDC-approved NP RT-qPCR and Tp values of SLAMP samples in order of increasing CDC-approved NP RT-qPCR Ct value (Panel B). Ct values of N=59 positive SalivirDetect and Tp values of SLAMP samples presented in order of increasing

SalivirDetect Ct value. Dashed line indicates 95% confidence interval SLAMP limit of detection (Panel C). Tp and Ct values of N=58 positive SLAMP and SalivirDetect tests, respectively, in order of increasing SLAMP Tp value (Panel D). Black arrows indicate undetected samples. Error bars represent one standard deviation.

Test outcomes and viral titers by age

A total of 223 participants provided age information and among these 56 were confirmed positive for SARS-CoV-2 using CDC-approved NP RT-qPCR. A histogram of these ages shows the positive results (gray) superimposed over the negative results (white), including one outlier age of 63 (**Fig 7.3A**). The most common age to be positive and negative is equal to the mode of 19 years old. Not surprisingly, the positive and negative distributions are similar ($p = 0.407$). Average Ct values as a function of age also indicate no trend in positivity as a function of this narrow age window (**Fig 7.3A**, inset).

Self-reported clinical presentations and test results

Participants were classified into four categories defined by their questionnaire responses: symptomatic exposed, symptomatic unexposed, asymptomatic exposed, and asymptomatic unexposed. Samples in each self-reported category were confirmed negative or positive based on CDC-approved NP RT-qPCR and positive individuals were assigned a Ct value. The 2nd largest category was symptomatic exposed numbering 76 individuals. Among these, only 20 participants were confirmed SARS-CoV-2-positive, around 26%. Symptomatic unexposed, the largest of all four categories, was comprised of 88 individuals from which 27 were confirmed positive, around 31%. The asymptomatic and exposed respondents numbered 64, of which only 9 tested positive, a total of only 14%. The smallest category was comprised of four participants who were asymptomatic and unexposed. Of these, half tested positive. Histograms of Ct values among the

positive results with inset pie charts representing the fraction of confirmed SARS-CoV-2 positives (blue) among the negatives (white) for each category are shown in Figure 7.3B.

Consumption of potential inhibitors – effect on SalivirDetect Ct values

Distributions of SalivirDetect Ct values among individuals who had or had not consumed each potential inhibitor are shown in Figure 7.3C. Among those engaging in eating and drinking, only the Ct values of those who drank were statistically distinct compared to those who did not ($p = 0.041$). No other items consumed resulted in statistically significant differences in the Ct distributions of those populations. The p-values for comparisons of all other sets were >0.05.

Site comparison: Nasopharynx versus saliva

CDC-approved NP RT-qPCR and SalivirDetect provide Ct results that can be quantitatively compared between NP swabs and saliva (Figure 3D). We compare the viral titers of 56 individuals who tested positive under both methods. Viral titer has been shown to vary between these sites [31]. Among samples with lower NP swab Ct values, assumed to correspond to a higher viral titer, saliva samples Ct values were higher, implying a lower viral titer than in the nasopharynx. However, when NP swab Ct values imply lower viral titers, Ct values in saliva were significantly lower, implying a difference in viral concentration between nasopharynx and oral mucosa (saliva) of possibly four orders of magnitude. Furthermore, there is a definite jump in values for the NP swab results from Ct=30-34, after which saliva Ct values are all lower than NP swab (**Fig. 7.3D**, left). A correlation plot of NP vs. saliva Ct values reveals that the results have only a weak positive correlation ($r = 0.310$).

Statistical predictions for SLAMP tests at triplicate, duplicate, or as a single replicate

For each number of test replicates, sensitivity increases as a function of SLAMP assay duration (**Fig. 7.3E**). As reported here, 45-min SLAMP with 3 replicates produced a sensitivity of 95% (95% CI: [87.9%, 100%]) as compared to the CDC-approved NP RT-qPCR standard results. Bootstrapping predicted a 90% sensitivity (95% CI: [82.8%, 96.6%]) for SLAMP with two replicates, and a 82% sensitivity (95% CI: [70.7%, 89.7%]) for SLAMP with a single replicate after the full assay time of 45 min had passed. For example, half of all positives in a test population would be detected by a single SLAMP test after 19.0 min (95% CI: [17.7 min, 21.5 min]), duplicate tests after 18.4 min (95% CI: [17.4 min, 19.3 min]), and triplicate tests after 17.7 min (95% CI: [16.9 min, 18.8 min]).

Based upon an estimated testing capacity of six 384-well plates per day (see Methods), we compare three scenarios of running samples with a single replicate, duplicate, and triplicate (Figure 3F). For these scenarios, we use the sensitivity values from Figure 7.3E. The specificity is assumed to be a constant 98% for all scenarios and there are 10 wells in each plate reserved for controls. Given the fixed constraint on the number of tests ($\approx 384 \times 6$), screening a larger number of individuals can identify more positive cases. For example, at a disease prevalence of 10%, triplicate SLAMP would identify approximately 10.0 true positives (TP) at the cost of 2.4 false positives (FP) per 384-well plate with FPs equaling the number of TPs at a disease prevalence of 2.5%. For duplicate SLAMP, TP = 16.8, FP = 3.3, and TP = FP at a disease prevalence of 2.2%. Finally, for single test SLAMP, TP = 35.4, FP = 6.9, and TP = FP at a disease prevalence of and 2.0%.

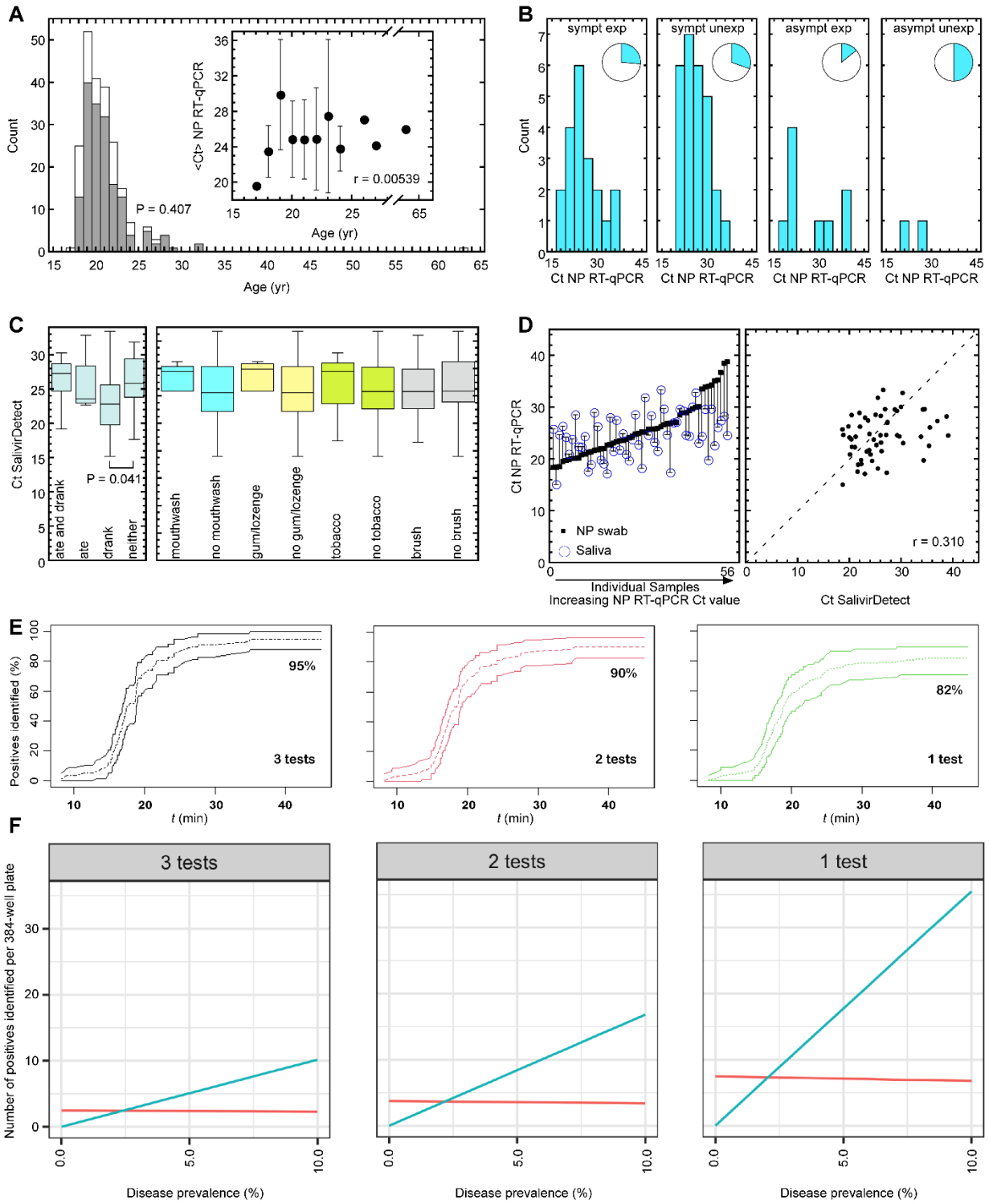

A
Count
Age (yr)
P = 0.407
<Ct> NP RT-qPCR
r = 0.00539
Age (yr)
B
sympt exp
sympt unexp
asympt exp
asympt unexp
Count
Ct NP RT-qPCR
C
Ct SalivirDetect
P = 0.041
ate and drank
ate
drank
neither
mouthwash
no mouthwash
gum/lozenge
no gum/lozenge
tobacco
no tobacco
brush
no brush
D
Ct NP RT-qPCR
NP swab
Saliva
Individual Samples
Increasing NP RT-qPCR Ct value
r = 0.310
Ct SalivirDetect
E
Positives identified (%)
95%
3 tests
90%
2 tests
82%
1 test
t (min)
F
3 tests
2 tests
1 test
Number of positives identified per 384-well plate
Disease prevalence (%)

Figure 7.3. *Study results and statistical predictions*. Histogram of participant age distributions, N=223. Gray and white bars represent positive and negative participants, respectively, tested using CDC-approved NP RT-qPCR (p = 0.407). Inset: average Ct values of SARS-CoV-2-positive CDC-approved NP RT-qPCR tests as a function of participant age (r = 0.00539). Error bars represent one standard deviation (Panel A). Histograms of CDC-approved NP RT-qPCR Ct values of SARS-CoV-2-positive participants self-reported as (from left-to-right) symptomatic exposed (N=76), symptomatic unexposed (N=88), asymptomatic exposed (N=64), and asymptomatic unexposed (N=4). Insets: fraction of positive tests (blue) and negative tests (white) within each category (Panel B). Box-and-whisker plots of SalivirDetect Ct values for individuals who both ate and drank (N=10), ate only (N=4), drank only (N=23), and did neither (N=21) (left panel) in addition to having used mouthwash (N=5), no mouthwash (N=52), gum/lozenge (N=6), no gum/lozenge (N=52), tobacco (N=7), no tobacco (N=51), brushing (N=31), and no brushing (N=27) (right panel) within 30 min of saliva sampling. Box-and-whisker plots define minimum, first quartile, median, third quartile, and maximum values (Panel C). Comparison between collection sites on the body. The Ct values of 56 positive CDC-approved NP RT-qPCR samples are plotted in increasing order (closed black squares). Open blue circles represent the SalivirDetect Ct values of the 56 corresponding saliva samples. Vertical lines connect NP and saliva values to guide the eye (left subplot). Cluster plot of Ct values of CDC-approved NP RT-qPCR vs. SalivirDetect. Dashed line indicates perfect correlation (r = 0.310) (right subplot) (Panel D). Bootstrap-predicted percentage of total positive individuals detected within a testing population as a function of SLAMP assay time for triplicate, duplicate or single replicate test conditions. Dashed lines indicate the mean. Solid lines indicate 95% bootstrap confidence intervals (Panel E). Total number of positive cases identified using SLAMP per 384-well plate as a function of disease prevalence of testing population for each replicate strategy. True positives (blue) and false positives (red) are generated for disease prevalence rates between 0 and 10% for single replicates, duplicates, and triplicates based on a daily capacity of six 384-well plates, reserving 10 wells for controls (Panel F).

Safety

Testing site volunteers were equipped with powered air-purifying respirators (PAPRs) during sample collection. Samples were transported in hard-sided coolers with biohazard labels. Contact surfaces were frequently disinfected using 70% ethanol solutions. All samples should be assumed to contain infectious SARS-CoV-2 virus and must be rendered safe through viral inactivation[32] before testing. HEPA air purifiers (Medify Air MA-25) were used in the testing

laboratory. All samples were heat inactivated before storage. See Supplementary Methods and **SI Fig. 7.4** for validation of viral heat-inactivation procedure.

Discussion

We have evaluated RT-LAMP (SLAMP) and RT-qPCR (SalivirDetect) Covid-19 tests on the saliva of 233 adults[33] collected on the MSU campus in mid-November 2020. Performance was determined by comparison to CDC-approved NP swab RT-qPCR results of the same individuals, resulting in 95% and 97% sensitivity, respectively, and 98% specificity for the two saliva methods. We found that among all potentially interfering items consumed within 30 min of testing, only drinking produced an effect and it was to increase the apparent saliva sample viral titer. We have demonstrated our SLAMP method offers a faster and simpler, while still comparatively sensitive, alternative to NP swabs and RT-qPCR methods for routine sampling, particularly of a college population.

The demographics of our study reflect those of many universities throughout the US, and similar SLAMP performance is expected. Unlike most universities in the US during Fall semester 2020, MSU was open and offering limited in-person classes [cite], providing a similar scenario that will be faced by universities in Fall 2021, when in-person learning is expected to resume throughout the country [cite]. The City of Bozeman 2010 census[34] reports 92.1% white and 3.3% other race, similar to the 94.4% white participants of our study. However, the MSU student body is 84% white (https://www.montana.edu/opa/facts/quick.html#Demo). This difference of 10% may be related to whites exhibiting the highest rates of likelihood to seek Covid-19 testing [cite]. Furthermore, our study was comprised of 53% females and 47% males despite both Bozeman and MSU populations being majority male. However, it is known that compared to females, Covid-19

treatment, including testing, is less sought by males (www.cdc.gov/pcd/issues/2020/20_0247.htm). While testing was not formally restricted to university students, the test survey median age of 20 years suggests this is the case when compared to 2010 Census data of 27.8 years median age of the city of Bozeman. According to MSU itself, an average of 21. While 84% of American universities are more racially diverse than represented within this study (https://www.collegefactual.com/colleges/montana-state-university/student-life/diversity/#ethnic_diversity), our study otherwise represents a typical campus student body of majority 18-24 year olds, which comprised 94% of our participants. We suggest that SLAMP testing would be successfully employed among the student populations of other universities.

Surveying revealed that while 70% of pilot study participants identified as symptomatic, only 29% of these tested positive for SARS-CoV-2, consistent with the prevalence of cases of flu, seasonal coronaviruses, and other respiratory virus infections that have persisted[35]. Overall, our study Covid-19 disease prevalence was 25%, a number that coincides with incidence levels estimated in the months prior between 9-31% throughout the United States[36]. Only 5% were asymptomatic positives compared to the estimates of 40-50% asymptomatic among the general population [cite] which is likely due to testing being reserved only for those with symptoms or recent exposures. A random screening of the population would likely have produced a higher asymptomatic positive rate. [cite rates among different campuses at the time].

The positivity rate among the symptomatic according to CDC-approved NP RT-qPCR is 29% while among the asymptomatic was 17%.

Contaminants from food, drink, or products remain a concern for saliva diagnostics[37]. However, SalivirDetect Ct values were statistically distinct from the rest of the positive samples only for those who had consumed drink. Most interestingly, those who had consumed drink within 30 min of saliva sampling produced significantly lower Ct values ($p = 0.407$) than those who had not (Figure 3C). We observed no significant differences in Ct distributions of SalivirDetect positive results who had or had not consumed food or oral care products (**Fig. 7.3C**). This suggests that hydrating the mouth [cite] before expressing saliva may have contributed to the supply of greater viral genome from the oral mucosa[38]. Regardless, among all potential inhibitors surveyed, none appeared to significantly raise Ct values in the saliva samples, potentially allaying the concerns over performing saliva-based testing, especially without being able to ensure compliance with sampling instructions.

Another interesting comparison between RT-qPCR tests of NP swabs and saliva for the same individuals. Clearly, among positive samples with the lowest CDC NP RT-qPCR Ct values, the Ct values obtained for saliva are significantly lower, representing a higher concentration of virus in the saliva of the oral mucosa under conditions of low titer in the nasopharynx (Figure 3D). No saliva samples had Ct values of 35 or greater. All NP swabs with Ct > 35 were much lower in Ct for the corresponding saliva sample, true for the lowest 9 NP swab virus concentrations.

While the test has higher precision when run in triplicate, running a single test can be advantageous. Given finite resources, driven by cost or supply availability, a single test on an individual can identify a substantially larger amount of infected, and infectious, individuals. Figure 3F demonstrates that total number of positive individuals that can be identified by running a single plate in either triplicate, duplicate, or with a single test. Triplicate and duplicate have higher

sensitivity, with 95% and 90% respectively, than a single test, 82% but running a single test allows more individuals to be tested. More individuals tested, even with relatively lower sensitivity, can identify substantially more positive cases and can be an advantageous strategy when testing capacity is limited.

It should be noted that specificity is assumed constant across the three replicate SLAMP tests, but will be higher as the number of SLAMP tests decreases and sensitivity decreases . as with single replicates or duplicates than for triplicates. Therefore, running more tests, with a lower specificity can also lead to more false positives that may require confirmatory testing. Our analyses regarding sensitivity predict that running more samples with single replicates will lead to more false negatives, but ideally a high frequency testing strategy would catch those other cases. Based on validation results, there appears to be a relationship between Ct value from the PCR and sensitivity, so perhaps these cases have lower viral load and are less infectious). Nonetheless, the data suggest that the SLAMP assay run in triplicate per individual could perform at the level of a clinical diagnostic, while when run as a single replicate could be used as a broad screening tool to identify unknown positives. Recent work [11] has demonstrated that more frequent testing with LAMP was more effective at reducing epidemic size than deploying more sensitive tests.

Our study has several strengths. Our results represent the intersection of three methods and two sample matrices along with self-reported demographics, disease presentation, and potential interferences. Additionally, our sample population came largely from a college student population, a segment of great importance as in-person learning is anticipated to resume in Fall 2021 [cite?]. Our study size of N=233 with 58 diseased meets the standard for an FDA EUA clinical trial and results can be statistically interpreted with acceptable accuracy [cite].

Our study has some weaknesses. Number in the case of some potential interferences is low and limits the extent of statistical arguments.

SARS-CoV-2 testing that is rapid, simple, and requires no specially trained medical personnel is indispensable when large numbers of individuals must be frequently screened while remaining economical, a practical concern for anticipated return to in-person instruction at schools and universities in Fall 2021. In this study, we have compared three testing methods, NP RT-qPCR, SalivirDirect, and SLAMP. All three methods use simple heat inactivation and extraction, which avoids costly reagents and potential supply bottlenecks. We conducted a comparison of these tests between 233 individuals from the MSU symptomatic testing site in mid-November of 2020, at the height of the largest county-wide wave of Covid-19 cases, where we detected a disease prevalence of 25%. Compared to the "gold standard" NP RT-qPCR results, SalivirDetect and SLAMP achieved 97% and 95% sensitivity and 98% and 98% specificity, respectively.

Supported by the State of Montana through the Coronavirus Aid, Relief and Economic Security Act (CARES) Act.

Connie B. Chang and James N. Wilking are co-founders of ULTSafety, Inc. which has licensed technology from Montana State University and Harvard University relating to this publication.

We thank Nathan Tanner at New England Biolabs, Kathryn Kundrod in the Richards-Kortum group (Rice University), Paul Hergenrother (UIUC), and the Global LAMP R&D Consortium led by Christopher Mason (Weill Cornell Medicine) for helpful discussions. We thank MSU students Kyle Hain, Shawna Pratt, Emily Walter, Matthew Fisher, and Jerrica Bursik for

sample collection and Donna Gollehon (MSU University Health Partners), Ryan Brickman (MSU Safety and Risk Management), and Ryan Bartlett (MSU Office of Research Compliance) for their assistance throughout the approval process and especially with sample site logistics. We thank the MSU Center for American Indian and Rural Health Equity for the use of the Health Education and Research Bus (HERB) at the sample collection site. HERB is a mobile laboratory and outreach facility supported by an Institutional Development Award (IDeA) from the National Institute of General Medical Sciences of the National Institutes of Health under grant numbers P20GM104417 and P20GM103474.

Supplementary Information

Methods

3D-printed caddy accessory for efficient saliva collection Each subject was provided a 3D-printed caddy accessory containing a medicine cup, transfer pipet, and sample tube (**SI Fig. 7.1A**) to facilitate saliva collection. Accessory designs were optimized for low cost and high throughput, enabling the printing of five caddies at a time (Fig. S1B) using an SLA 3D-printer (Formlabs, Form 2 and 3) loaded with clear UV cross-linkable resin (Formlabs, RS-F2-GPCL-04), before soaking in isopropanol for 20 min, and post-curing under UV light (Formlabs, Form Cure FH-CU-01) at 60 °C for 15 min. Drainage holes were included at the bottom of each caddy to drain excess resin during printing and post-processing and drain 70% ethanol during decontamination sprays. 3D models and print files are available as supplementary material.

Duplex RT-LAMP primers for SARS-CoV-2 detection and internal control All primers were based on New England Biolabs designs (CITE Zhang, Y.; Ren, G.; Buss, J.; Barry, A. J.;

Patton, G. C.; Tanner, N. A., Enhancing colorimetric loop-mediated isothermal amplification speed and sensitivity with guanidine chloride. *BioTechniques* **2020,** *69* (3), 178-185.), ordered from Integrated DNA Technologies (Coralville, IA, USA), and resuspended to 100 μM in nuclease-free water (NEB B1500L). All primers were desalted except FIP and BIP sequences, which were HPLC purified. For 100 reactions, the SARS-CoV-2 primer sets (N2, E1) were prepared as a duplex primer mix in the following manner: 40 μL of FIP, 40 μL of BIP, 10 μL of LF, 10 μL of LB, 5 μL of F3, 5 μL of B3, and 30 μL nuclease-free water (250 μL total volume). A third internal control primer set targeting human beta-actin (ACTB) was also similarly prepared, except with the addition of 140 μL of nuclease-free water (250 μL total volume). The prepared working primer solutions thus consisted of 16 μM of each FIP and BIP, 4 μM of each LF and LB, and 2 μM of each F3 and B3. The primer stocks and prepared working primer solutions were stored at -20 °C until use.

A 25X Primer Mix should contain: 40 μM FIP, 40 μM BIP, 5 μM F3, 5 μM B3, 10 μM LoopF, 10 μM LoopB in TE or water.

FIP/BIP Primers (25X) 1.6 μM

F3/B3 Primers (25X) 0.2 μM

LoopF/B Primers (25X) 0.4 μM

SLAMP primers

SI Table 7.1: SLAMP primer sequences

Primers	Sequence 5’-3’

N2_FIP	TTCCGAAGAACGCTGAAGCGGAACTGATTACAAACATTGGCC
N2_BIP	CGCATTGGCATGGAAGTCACAATTTGATGGCACCTGTGTA
N2_F3	ACCAGGAACTAATCAGACAAG
N2_B3	GACTTGATCTTTGAAATTTGGATCT
N2_LF	GGGGGCAAATTGTGCAATTTG
N2_LB	CTTCGGGAACGTGGTTGACC
E1_FIP	ACCACGAAAGCAAGAAAAAGAAGTTCGTTTCGGAAGAGACAG
E1_BIP	TTGCTAGTTACACTAGCCATCCTTAGGTTTTACAAGACTCACGT
E1_F3	TGAGTACGAACTTATGTACTCAT
E1_B3	TTCAGATTTTTAACACGAGAGT
E1_LF	CGCTATTAACTATTAACG
E1_LB	GCGCTTCGATTGTGTGCGT
ACTB_FIP	GAGCCACACGCAGCTCATTGTATCACCAACTGGGACGACA
ACTB_BIP	CTGAACCCCAAGGCCAACCGGCTGGGGTGTTGAAGGTC
ACTB_F3	AGTACCCCATCGAGCACG
ACTB_B3	AGCCTGGATAGCAACGTACA
ACTB_LF	TGTGGTGCCAGATTTTCTCCA
ACTB_LB	CGAGAAGATGACCCAGATCATGT

NEB Luna Kit RT-qPCR Reactions All RT-qPCR reactions used for SLAMP standard curve comparisons were prepared according to manufacturer protocol (NEB E3006L): 10 μL of Luna Universal Probe One-Step Reaction Mix (2×), 1 μL of Luna Warm Start RT Enzyme Mix (200×), 4 μL of primer mix, and 5 μL of template for a final reaction volume of 20 μL. The CDC N1 forward primer was

GACCCCAAAATCAGCGAAAT, CDC N1 reverse primer

TCTGGTTACTGCCAGTTGAATCTG, and probe FAM-

ACCCCGCATTACGTTTGGTGGACC-BHQ1

The primer mix was prepared from a 20 μM stock of each primer and constituted the following: 0.4 μL of both forward and reverse primers (0.4 μM final concentration), 0.2 μL of probe (0.2 μM final concentration), 0.5 μL of UDG, and 2.5 μL of nuclease-free water. The reactions were performed in a QuantStudio 7 Real-Time PCR system with the following thermocycler conditions: reverse transcription at 55 °C for 10 min, initial denaturation at 95 °C for 1 min, followed by 44 cycles of denaturation at 95 °C for 10 s, extension at 55 °C for 30 s, and plate read. The data was analyzed using Design & Analysis Software, Release Version: 2.5.0, Copyright 2020 Thermo Fisher Scientific.

SalivirDetect Primers

SI Table 7.2: SalivirDetect Primer Sequences

Primers	Sequence 5’-3’
2019-nCoV_N1-F	GACCCCAAAATCAGCGAAAT

2019-nCoV_N1-R	TCTGGTTACTGCCAGTTGAATCTG
2019-nCoV_N1-P	**FAM**-ACCCCGCATTACGTTTGGTGGACC-**IBFQ**
RP-F	AGATTTGGACCTGCGAGCG
RP-R	GAGCGGCTGTCTCCACAAGT
RP-P	**Cy5**-TTCTGACCTGAAGGCTCTGCGCG-**IBRQ**

RT-LAMP Curve Fitting RT-LAMP amplification curves were described by equation $Rn(t) = a + (k - a)(1 + \exp[-b(t - m)])$ where $\Delta Rn(t)$ represents a scaled and baselined fluorescence intensity as a function of reaction time t.[39] Fit parameters a and k define the lower and upper saturation limits, respectively, while m and b describe the x-coordinate and slope at the inflection point, respectively. The time-to-positive $Tp = m - 2/b$ is derived from m and b fitting parameters and serves as an analog to the familiar cycle threshold Ct used in qPCR results interpretation. Fitting was performed using KaleidaGraph v4.1 non-linear least squares routine.

Synthetic vRNA standards for determining LoD Standards were prepared from heat- and TCEP-inactivated saliva to protect RNA from endonucleases and represent ideal backgrounds. Final TCEP concentrations in reactions were 2.5 mM. Full-length synthetic genomic vRNA was purchased from Twist Biosciences (Control 9 Genbank ID: MT152824, GISAID ID: USA/WA2/2020).

Synthetic SARS-CoV-2 RNA (NIST, RGTM 10169 Fragment 1) NIST fragment which has a total length of 3985 nt and spans the sequence between bases 25949-29698 of isolate USA-WA1/2020 used in pilot study standards.

BSL-3 SARS-CoV-2 growth and heat inactivation of infectivity Plaque assays (sensitivity limit 5 plaque-forming units (PFU)/mL) were performed on infectious solutions of USA/WA1/2020 strain (BEI Resources) SARS-CoV-2 serially diluted 10-fold in viral media which consists of 1× Dulbecco's Modified Eagle's Medium (DMEM), 2% fetal bovine serum (FBS), and 1× Pen Strep. Dilutions are inoculated onto susceptible E6-Vero cells (ATCC) and incubated for 1 h to facilitate infection. Subsequently, cells are overlaid with a diffusion-limiting agent composed of 0.75% methylcellulose and incubated at 37 °C for 3-4 days. Viral replication causes "plaques" to form on the cell monolayer, the number of which correlate with infectivity present in the original sample. Heat treatment was conducted in 1.5 mL screw cap tubes from 1.5 mL of viral supernatant at 1.2×10^7 PFU/mL and temperatures were confirmed with thermometers and digital probes[40].

Results

Optimizing saliva sample heat inactivation Collected saliva samples may contain infectious SARS-CoV-2 virus and must be rendered safe through viral inactivation[32]. Frequently, a chemical inactivation agent is added to the sample or is present in vials prior to sample collection[41]. However, components of such inactivation buffers are often costly (such as tris(2-carboxyethyl)phosphine (TCEP) or thermolabile proteinase K) and have seen limited available during the COVID-19 pandemic. Chemical inactivation methods often function in a dual capacity to decrease viral infectivity[42] and to inactivate the abundant endonucleases that could rapidly degrade SARS-CoV-2 viral RNA (vRNA) and potentially inhibit downstream amplification during the RT-LAMP reaction[43]. The SLAMP method does not require the addition of any chemical agents, using instead a simple heat inactivation procedure that accomplishes viral inactivation. A

range of effective temperatures and heating times have been reported[29] for sputum and other viruses[44] sometimes with chemical additives prior or post heating[45, 46]. In addition, previous work has suggested that SARS-CoV-2 vRNA is stable in human saliva and detectable with molecular-based approaches[47]. However, most previous LAMP studies have used colorimetric detection with or without RNA extraction[45, 48, 49].

We explored heating times at a temperature of 95 °C, reported[50] to most completely inactivate SARS-CoV-2 in viral transport media. A high titer stock of SARS-CoV-2 was diluted in viral growth media in triplicate to a final volume of 200 µL. The diluted viral supernatant was then heated to 95 °C for variable lengths of time, ranging from 0 - 10 min. Infectivity was then measured via plaque assay in which a limiting dilution of virus was inoculated onto susceptible cells to determine the quantity of infectious virus present in each sample (**SI Fig. 7.4A**). Non-inactivated virus (Fig. S4A, solid black circles) contained 1.21×10^7 PFU/mL. The same diluted viral supernatant heated at 95 °C for 3 min (SI Fig. 7.4A, solid black squares) resulted in 3.41×10^2 PFU/mL representing a decrease of $\approx 10^5$ PFU/mL. Heating for a total of 5 min resulted in a further decrease to 5.0×10^1 PFU/mL (SI Fig. 7.4A, solid black upright triangles). The final times of 7 and 10 min resulted in complete inactivation of viral infectivity with no detectable plaques at any dilution.

Similar time points were performed for infectious SARS-CoV-2 spiked into saliva that had tested negative for SARS-CoV-2 (**SI Fig. 7.4B**). Spiked dilutions reduced the initial infectious viral titer from 1.09×10^7 PFU/mL to 8.40×10^5 PFU/mL (Fig. S4B, solid black circles). Due to the high number of infectious virus particles present after 3 min of heating at 95 °C from the previous inactivation studies in viral supernatant, we only evaluated time points ≥5 min for saliva

spiked samples. Infectious virus was undetected following exposure to 95 °C heat for 5, 7, and 10 min, indicating high titers of SARS-CoV-2 can be completely heat-inactivated in saliva in <5 min (SI Fig. 7.4B). Comparable heat inactivation of SARS-CoV-2 is only achieved at 65 °C after 20 min[51]. With the loss of some viral infectivity following the spike into saliva, we suggest a minimum heating time of 10 min at 95 °C to ensure samples are fully inactivated before use. In addition, heating at 95 °C represents a potential 2× faster option for viral inactivation compared to inactivation times reported for 65 °C.

While infectivity experiments suggest that 5 min at 95 °C of heat inactivation is sufficient to eliminate risk of infection, the viral envelope must also be lysed to access vRNA if the most sensitive detection limits are to be achieved. Furthermore, nucleases and inhibitors present in human saliva must also be inactivated to protect free vRNA from degradation[52] while avoiding vRNA degradation due to prolonged heating. To optimize reaction conditions, we performed SLAMP reactions on raw positive saliva samples (**SI Fig. 7.5**). Three concentrations of SARS-CoV-2-positive saliva were prepared by dilution with negative saliva. The samples were left untreated or were heated at 95 °C for 5, 10, 15, 20, and 30 min, then amplified using SLAMP (**SI Fig. 7.5A-7.5C**). Undiluted positive saliva (**SI Fig. 7.5A**) amplified under all heating durations, but relative fluorescent detection was low, $\Delta Rn < 15$. Interestingly, undiluted positive saliva added to a SLAMP reaction, heat inactivated, and lysed for the 45 min duration at 65 °C exhibited a linear, instead of sigmoidal, increase in relative fluorescence intensity ΔRn (SI Fig. 5A, open blue circles). At 10-fold dilution, all incubation durations resulted in sigmoidal amplification curves (Fig. S5B). The unheated positive saliva amplified the slowest (**SI Fig. 7.5B**, open blue circles) suggesting that the heat inactivation step is resulting in viral lysis. At 100-fold dilution, a single

sample triplicate incubated at 95 °C for 5 min failed to amplify (**SI Fig. 7.5C**, open red squares). The mean time-to-positive Tp values <Tp> for each triplicate trial under each dilution and duration were plotted as a function of 95 °C heating time *t* (min) (**SI Fig. 7.5D**). As the positive saliva sample is diluted, greater scatter is observed between amplification curves as evidenced by greater standard deviations at all heating durations (SI Fig. 7.5D, solid green diamonds). Greater scatter between triplicates is observed as the SLAMP limit of detection (LOD) is approached. 10-fold diluted samples exhibited significant differences between <Tp> without heat inactivation and at heating times $t > 5$ min (SI Fig. 7.5D, solid red squares). The undiluted saliva samples exhibit diminishing <Tp> as a function of heating time, implying detectable vRNA increased consistently from 5 – 30 min (SI Fig. 7.5D, solid blue circles). Interestingly, across all dilutions, the 30 min heating time produced <Tp> values with low standard deviation and consistent separation of ≈2 min. Similar results are observed at 20 min heating. Therefore, we choose a 15-min heating time at 95 °C for SLAMP with an additional ≈5 min to allow temperature to ramp-up, closely approximating a 20 min total heating time.

Comparing testing methods: SLAMP, SalivirDetect, and NP RT-qPCR We compare samples across three different testing methods, SLAMP, SalivirDetect, and the "gold-standard" RT-qPCR. Sample collection was performed using nasopharyngeal (NP) swab for RT-qPCR while saliva, shown to provide sufficient viral RNA for detection[29], was used for both SLAMP and SalivirDetect. Both SalivirDetect and NP RT-qPCR are PCR-based while SLAMP uses isothermal LAMP amplification.

Standard curves and LOD for SLAMP reactions Effective tests for curbing the potential for asymptomatic or presymptomatic spread of SARS-CoV-2 must be able to detect the virus

reliably and early in the course of infection before the onset of symptoms[53]. In practice, this requires a test with high sensitivity and specificity at a low limit of detection (LOD). The LOD for the "gold-standard" NP qPCR method has been reported[54] as 10 copies/uL whereas publications have reported[43] the LOD and sensitivity levels for RT-LAMP assays at 2-700 copies/reaction. Furthermore, the sample matrix such as saliva, NP swab, or mid-turbinate swabs can influence the LOD due to the presence of different inhibitors, the variability in sampling methods, differences in infection between sites, or the time of sampling[55, 56].

We evaluated the LOD of SLAMP using spiked saliva samples. To accurately simulate a heat-inactivated SARS-CoV-2-positive sample, we harvested saliva from an individual confirmed negative for the presence of SARS-CoV-2 using RT-qPCR and heated it for 15 min at 95 °C to inactivate endonucleases before adding full-length synthetic SARS-CoV-2 RNA (Twist Biosciences). To completely eliminate heat-resistant endonucleases, we added TCEP to saliva for a final reaction concentration of 2.5 mM. If the saliva background is not completely inactivated, synthetic RNA quickly becomes degraded and undetectable in minutes by the action of RNases[57, 58] (data not shown).

Synthetic RNA-spiked samples were prepared at concentrations of 10^5, 10^4, 10^3, 10^2, 10, and 1 copies/μL and amplified using SLAMP (Fig. S6A). Amplification curves exhibit characteristic sigmoidal profiles seen in LAMP reactions, with fluorescence detection onsets ranging between 10-20 min. Each concentration is separated by ≈2 min (**SI Fig. 7.6A**, curves). Calculated time-to-positive Tp values are used to generate a SLAMP standard curve (SI Fig. 7.6A, inset). The apparent LOD = 1-10 copies/μL. In saliva without TCEP and only heat inactivated, the LOD is between 10-100x higher.

We provide further confirmation of contrived sample RNA concentrations by performing RT-qPCR amplification (**SI Fig. 7.6B**). The RT-qPCR LOD appears >1 copies/μL. The RT-qPCR standard curve (SI Fig. 7.6B, inset) spans a greater dynamic range of Ct values compared to the Tp values of RT-LAMP reactions with a significantly lower standard deviation.

RT-LAMP reaction optimized using GuHCl and duplex primer sets

RT-LAMP reactions involve a minimum of four primers per set to function. The addition of a loop primer pair for a total of six primers has been shown to increase the speed of the reaction. Furthermore, by including multiple 6-primer sets in a single reaction, the sensitivity and speed of the RT-LAMP reaction can be increased significantly.

Saliva is a challenging sample medium for nucleic acid testing, largely due to variability in pH[59], ionic strength , and the presence of nucleases that degrade vRNA before it can be detected[60]. RT-LAMP is more resistant to "dirty" samples, including saliva, than traditional RT-qPCR[47]. Here, we tested established methods to increase the sensitivity and speed of the RT-LAMP reaction on saliva using guanidine hydrochloride (GuHCl) and multiplexed primer sets.

Strategies to overcome sensitivity loss associated with saliva sampling include the addition of GuHCl to the RT-LAMP master mix, a strong chaotropic agent used frequently in molecular biology for varied applications including RNA isolation and protein extraction. Low GuHCl concentrations (40 mM) can be used as additives in the RT-LAMP reaction, facilitating enzyme/nucleic acid interactions and thereby increasing sensitivity without an accompanying reduction in specificity[61].

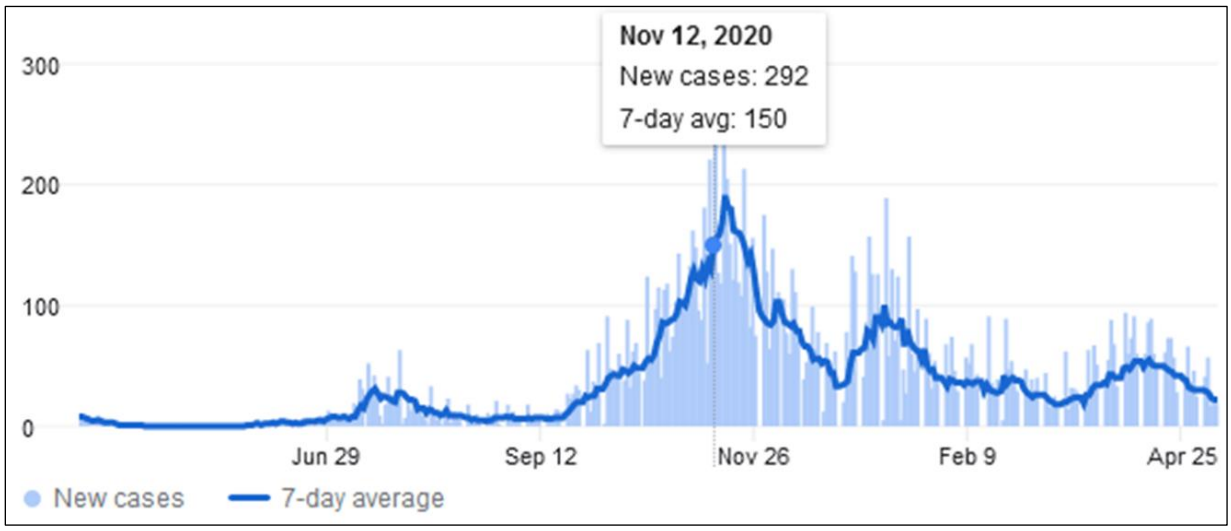
We compared triplicate SLAMP reactions of SARS-CoV-2-positive saliva using a single E1 or N2 primer set (Materials and Methods) and duplexed NE primer sets (**SI Fig. 7.7A – 7.7D**)

at 10^3 (**SI Fig. 7.7A**, open circles), 10^2 (Fig. S7B, open squares), and 10 (**SI Fig. 7.7C**, open diamonds) genome copies/μL concentrations *C*. At 10^3 c/μL, every primer set triplicate SLAMP reaction results in amplification and positive detection of SARS-CoV-2. At a ten-fold dilution, the E1 primer set alone begins to perform poorly, failing to amplify 2 triplicates (**SI Fig. 7.7B**, open blue squares). Additionally, the N2 primer set triplicates also begin to lose sensitivity at 100 c/μL. While no N2 primer set reactions failed to amplify, one reaction amplified much later (SI Fig. 7.7B, open red squares). All duplex NE primer reactions amplified (SI Fig. 7.7B, open orange squares). As the limit of detection is reached at 10 c/μL, each primer set condition drops at least a single replicate (SI Fig. 7.7C). However, the NE primer set most accurately amplifies at <Tp> appropriate for 10 c/μL (SI Fig. 7.7C, open orange diamonds). Comparison of <Tp> values for triplicates under different genome concentrations and primer sets reveal that the duplex NE primer set produces both an accurate prediction of the genome copies/uL and less variability between successful amplifications (**SI Fig. 7.7D**, solid green diamonds). The E1 and N2 single primer sets (SI Fig. 7.7D, solid blue circles and solid red squares, respectively) both exhibit significantly greater scatter and deviation from predicted concentrations based on the SLAMP standard curve.

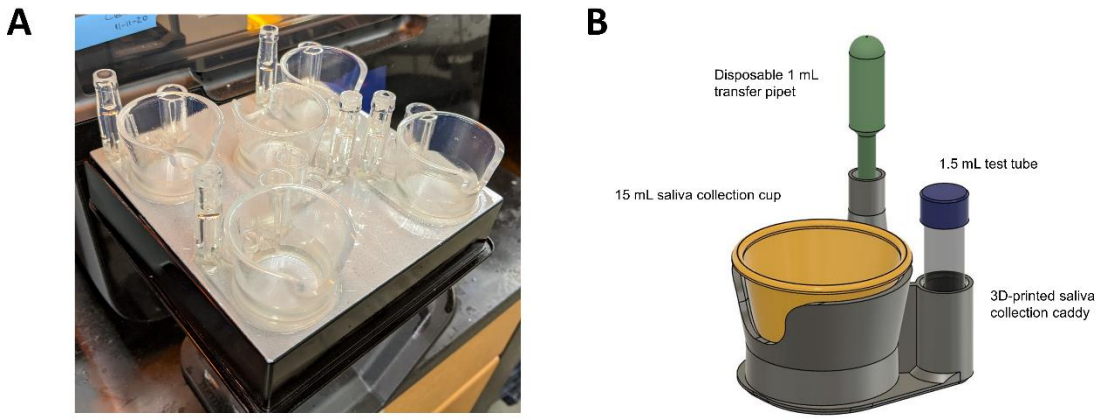
After establishing that duplex NE primer sets offer greater sensitivity and reproducibility than single E1 or N2 primer sets, we evaluated whether the addition of GuHCl improved amplification reliability. We performed triplicate SLAMP reactions at positive saliva concentrations of 1000, 100, and 10 copies/uL SARS-CoV-2 genomes using the duplex NE primer sets and 40 mM GuHCl (**SI Fig. 7.7E**, open orange circles, squares, and diamonds, respectively). While the addition of GuHCl has partially deviated <Tp> from the standard curve, every replicate amplified and standard deviations were low (**SI Fig. 7.7F**).

We demonstrate that the addition of GuHCl, along with the use of a duplex primer set composed of both N2 and E1 primers (see Materials and Methods) in the same reaction, optimizes the saliva RT-LAMP reaction, achieving greater sensitivity and more rapid time-to-result, thereby increasing the utility of SLAMP for more consistent detection of low viral titers in saliva.

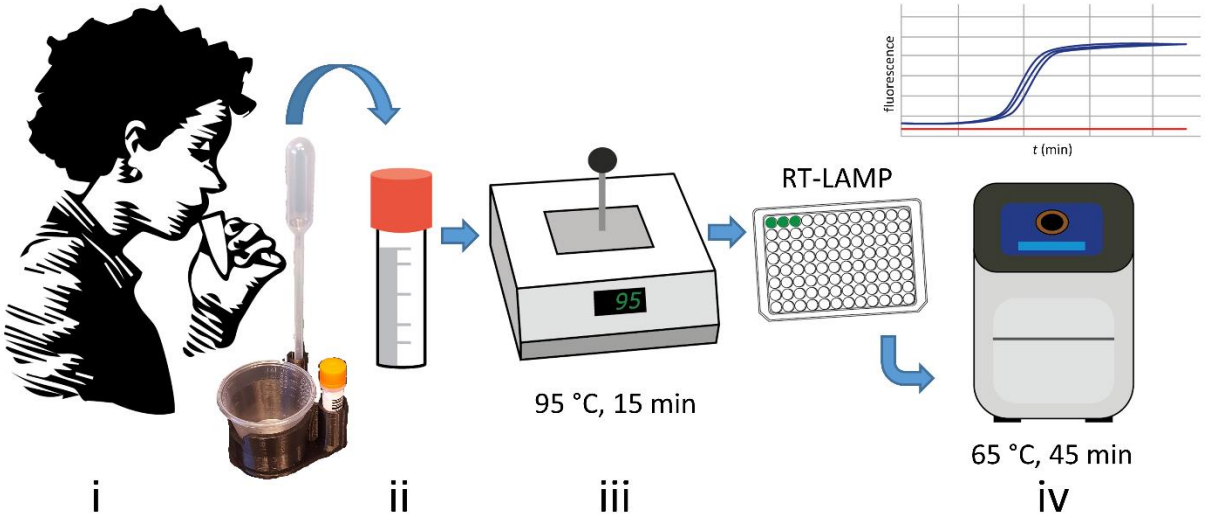
With an optimized assay (GuHCl, primers), knowledge of LOD and heating times, we performed our trial study. Volunteers operating at MSU's symptomatic testing site collected samples from 243 individuals who provided NP swabs for CDC RT-qPCR "gold standard" testing and saliva samples for SalivirDetect and SLAMP. A questionnaire (see Materials and Methods) was also provided to collect self-reported demographic and illness presentation data, in addition to determining whether any foods, drinks, or potential inhibitors were consumed 30 min prior to sample collection.



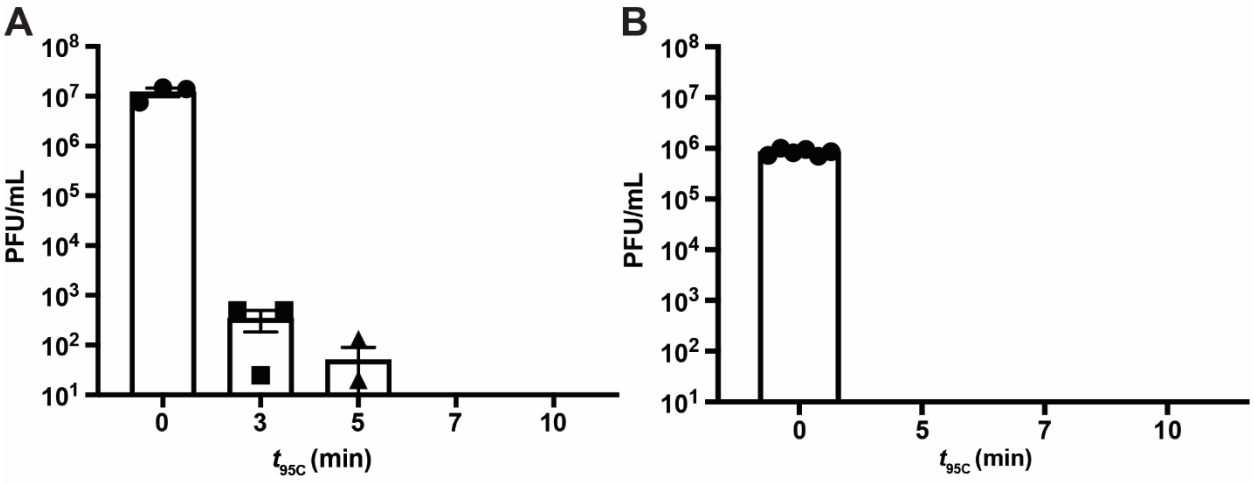
SI Figure 7.1. SARS-CoV-2 cases in Gallatin County, MT between Apr. 2020 – May 2021. This comparative study was conducted at a time of peak cases (cursor and dotted vertical line). Source: The New York Times.



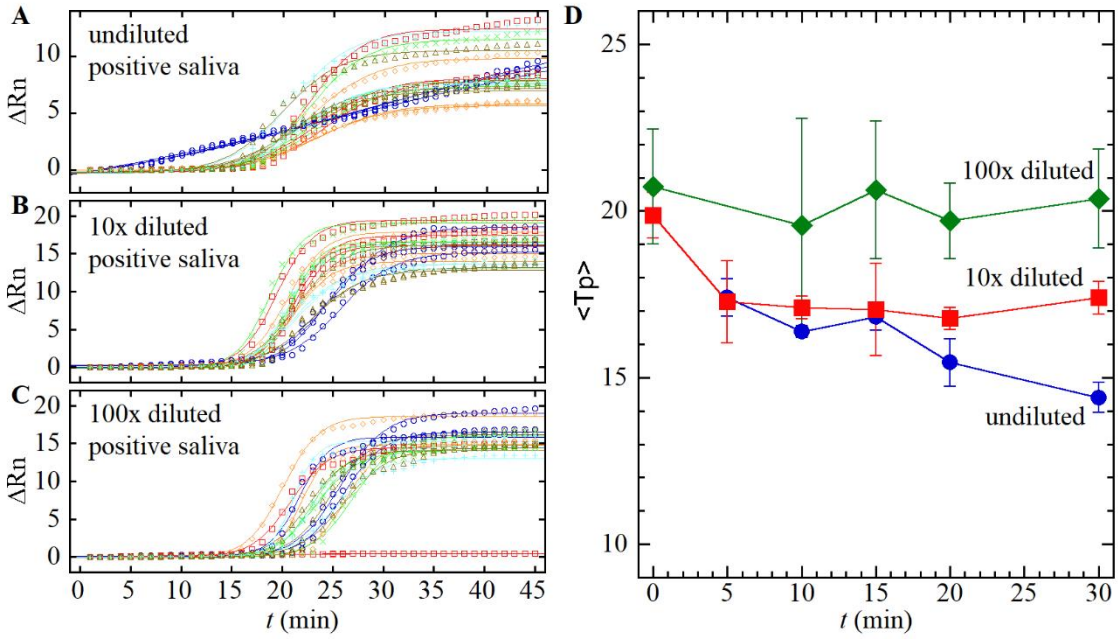
SI Figure 7.2. Saliva collection caddy. (A) photograph of 5 caddies printed simultaneously. (B) A caddy as presented to a study participant, ready to collect saliva.



SI Figure 7.3. Saliva RT-LAMP testing workflow. (i) 1 mL saliva is expressed directly into medicine cup before being pipetted (ii) into screw cap sample tube. (iii) Virus inactivation is performed directly on the saliva in the tube without any added buffers in a heat block at 95 °C for 15 min. Each sample is pipetted in triplicate RT-LAMP reactions in a qPCR machine (iv) at 65 °C for 45 min.

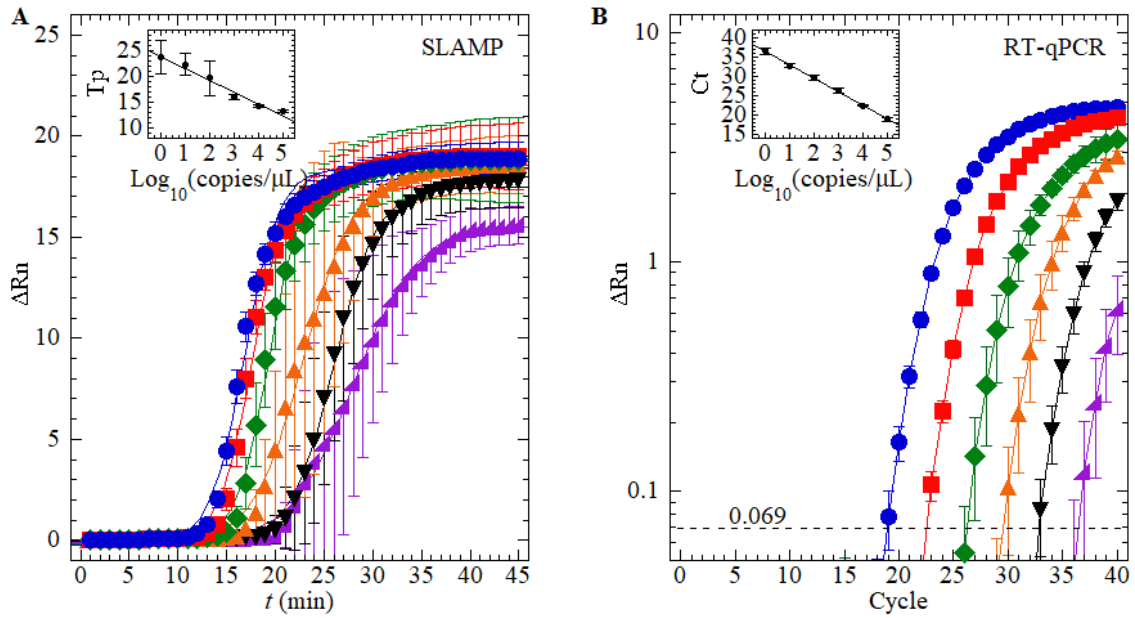


SI Figure 7.4. 95 °C heat-inactivation durations and subsequent SARS-CoV-2 virus infectivity. Plaque-forming units (PFU) per mL after 95 °C heat inactivation of infectious SARS-CoV-2 for no heating (solid black circles) and 3 (solid black squares), 5 (solid black upright triangles) min in (A) viral growth media and (B) human saliva. All data represent the mean of triplicate samples +/- Standard Error Mean (SEM).

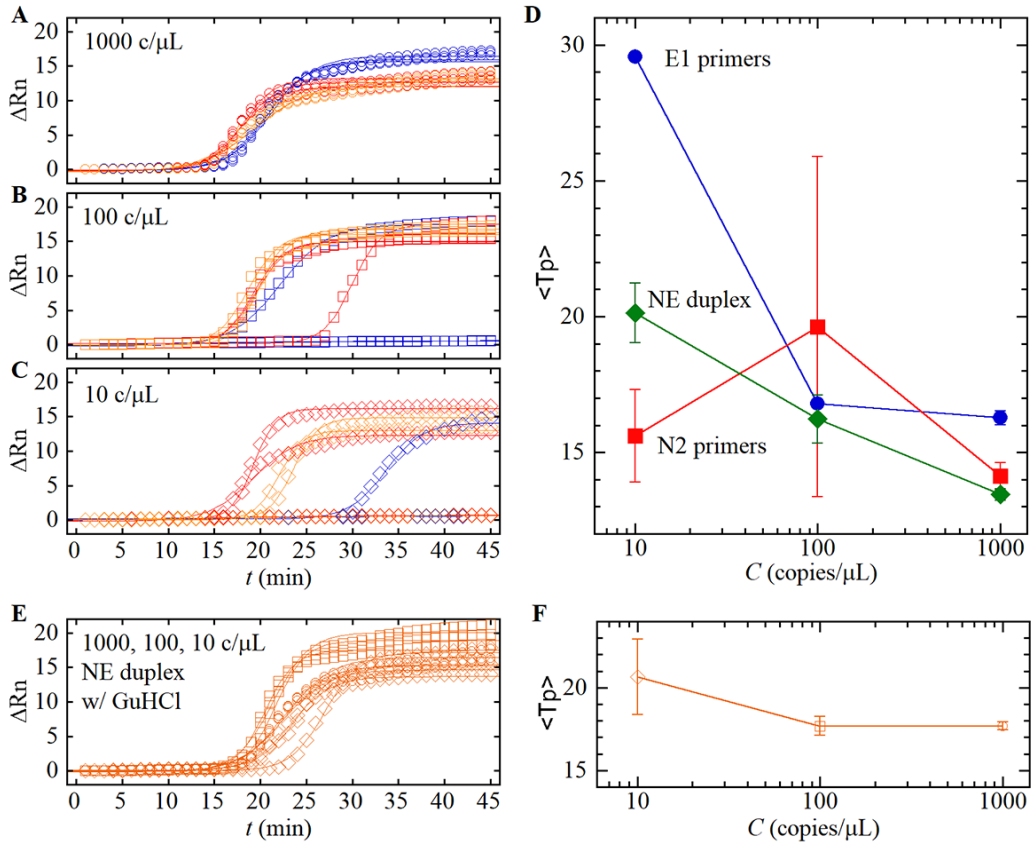


SI Figure 7.5. 95 °C heat inactivation duration optimization of positive saliva sample dilutions. Triplicate SLAMP reactions were performed on 95 °C heat inactivation for 5 (open red squares), 10 (open orange diamonds), 15 (green diagonal crosses), 20 (light blue upright crosses), and 30 (open brown upright triangles) min in addition to no heating (open blue circles) for **(A)**

undiluted, **(B)** 10× dilution, and **(C)** 100× dilution. Solid lines represent RT-LAMP curve fits (see Materials and Methods). **(D)** Mean time-to-positive <Tp> values as a function of 95 °C inactivation durations *t* (min) for undiluted (solid blue circles), 10× diluted (solid red squares), 100× diluted (solid green diamonds) from triplicate data in parts (A)-(C). Error bars represent a single standard deviation. Lines guide the eye.



SI Figure 7.6. Determining limit of detection (LOD) and standard curves for SLAMP. Contrived saliva samples prepared at 10^5 (solid blue circles), 10^4 (solid red squares), 10^3 (solid green diamonds), 10^2 (solid orange upright triangles), 10 (solid black inverted triangles), and 1 (solid purple right triangles) copies/uL. Synthetic full-length SARS-CoV-2 RNA diluted in inactivated negative human saliva and amplified using **(A)** SLAMP and **(B)** NEB Luna Kit RT-qPCR. (A) Relative fluorescence intensity ΔRn recorded as a function of time *t* (min). Limit of detection (LOD) lies between 1 and 10 c/μL. Inset: SLAMP standard curve $Tp = 23.99 - 2.30\log_{10}$ [copies/μL] ($R^2 > 0.97$) calculated using time-to-positive Tp values (see Materials and Methods) generated from data in part (A). (B) RT-qPCR standard curve. Ct values determined at ΔRn = 0.069 cutoff determined using Design & Analysis Software (see Materials and Methods). Inset: NEB Luna Kit RT-qPCR standard curve $Ct = 36.55 - 3.50\log_{10}$[copies/μL] ($R^2 > 0.999$) calculated using Ct values from part (B).



SI Figure 7.7. Duplex NE primer set and guanidine HCl (GuHCl) improves sensitivity and speed of SLAMP. Triplicate SLAMP reactions of **(A)** 1000 (open circles), **(B)** 100 (open squares), and **(C)** 10 (open diamonds) copies/µL positive saliva samples without GuHCl and only single E1 primer set (blue), single N2 primer set (red), or duplex NE primer sets (orange). Curve fits yield time-to-positive Tp values (see Materials and Methods). **(D)** <Tp> as a function of genome copies/µL *C* for single E1 primer set (solid blue circles), single N2 primer set (solid red squares), and duplex NE primer sets (solid green diamonds) from parts (A) – (C). Error bars represent one standard deviation. Lines guide the eye. **(E)** Triplicate SLAMP reactions of positive saliva samples at 1000 (open circles), 100 (open squares), and 10 (open diamonds) genome copies/µL using only duplex NE primer sets (orange) with 40 mM GuHCl. **(F)** <Tp> as a function of 1000 (open circle), 100 (open square), and 10 (open diamond) genome copies/µL *C* for duplex NE primer sets with 40 mM GuHCl from part (E). Error bars represent one standard deviation. Lines guide the eye.

References cited

1. Munster, V. J.; Koopmans, M.; van Doremalen, N.; van Riel, D.; de Wit, E., A novel coronavirus emerging in China — Key questions for impact assessment. *New England Journal of Medicine* **2020,** *382* (8), 692-694.

2. Olliaro, P.; Torreele, E.; Vaillant, M., COVID-19 vaccine efficacy and effectiveness-the elephant (not) in the room. *Lancet Microbe* **2021**.

3. Thompson, R. N.; Hill, E. M.; Gog, J. R., SARS-CoV-2 incidence and vaccine escape. *Lancet Infect Dis* **2021**.

4. Castillo, J. C.; Ahuja, A.; Athey, S.; Baker, A.; Budish, E.; Chipty, T.; Glennerster, R.; Kominers, S. D.; Kremer, M.; Larson, G.; Lee, J.; Prendergast, C.; Snyder, C. M.; Tabarrok, A.; Tan, B. J.; Wiecek, W., Market design to accelerate COVID-19 vaccine supply. *Science* **2021,** *371* (6534), 1107-1109.

5. Chia, W. N.; Zhu, F.; Ong, S. W. X.; Young, B. E.; Fong, S. W.; Le Bert, N.; Tan, C. W.; Tiu, C.; Zhang, J.; Tan, S. Y.; Pada, S.; Chan, Y. H.; Tham, C. Y. L.; Kunasegaran, K.; Chen, M. I.; Low, J. G. H.; Leo, Y. S.; Renia, L.; Bertoletti, A.; Ng, L. F. P.; Lye, D. C.; Wang, L. F., Dynamics of SARS-CoV-2 neutralising antibody responses and duration of immunity: a longitudinal study. *Lancet Microbe* **2021**.

6. Kirby, T., When should the UK lift its lockdown? *Lancet Respir Med* **2021,** *9* (4), e44-e45.

7. Head, J. R.; Andrejko, K. L.; Cheng, Q.; Collender, P. A.; Phillips, S.; Boser, A.; Heaney, A. K.; Hoover, C. M.; Wu, S. L.; Northrup, G. R.; Click, K.; Bardach, N. S.; Lewnard, J. A.; Remais, J. V., School closures reduced social mixing of children during COVID-19 with implications for transmission risk and school reopening policies. *J R Soc Interface* **2021,** *18* (177), 20200970.

8. Trotta, J. Why qPCR is the gold standard for COVID-19 testing. https://www.thermofisher.com/blog/ask-a-scientist/why-qpcr-is-the-gold-standard-for-covid-19-testing/.

9. COVID-19 and PCR Testing. https://my.clevelandclinic.org/health/diagnostics/21462-covid-19-and-pcr-testing.

10. Mina, M. J.; Andersen, K. G., COVID-19 testing: One size does not fit all. **2021,** *371* (6525), 126-127.

11. Rogers, W.; Ruiz-Aravena, M.; Hansen, D.; Madden, W.; Kessler, M.; Fields, M. W.; Ferrari, M. J.; Chang, C. B.; Morrow, J.; Hoegh, A.; Plowright, R. K., High-frequency screening combined with diagnostic testing for control of SARS-CoV-2 in high-density settings: an economic evaluation of resources allocation for public health benefit. **2021**, 2021.03.04.21252949.

12. Notomi, T.; Okayama, H.; Masubuchi, H.; Yonekawa, T.; Watanabe, K.; Amino, N.; Hase, T., Loop-mediated isothermal amplification of DNA. *Nucleic Acids Research* **2000,** *28* (12).

13. Curtis, K. A.; Rudolph, D. L.; Owen, S. M., Rapid detection of HIV-1 by reverse-transcription, loop-mediated isothermal amplification (RT-LAMP). *Journal of Virological Methods* **2008,** *151* (2), 264-270.

14. Parida, M.; Posadas, G.; Inoue, S.; Hasebe, F.; Morita, K., Real-time reverse transcription loop-mediated isothermal amplification for rapid detection of West Nile virus. *Journal of Clinical Microbiology* **2004,** *42* (1), 257-263.

15. Bhadra, S.; Maranhao, A. C.; Paik, I.; Ellington, A. D., A one-enzyme RT-qPCR assay for SARS-CoV-2, and procedures for reagent production. *Bio-protocol* **2021,** *11* (2), e3898.

16. Buck, M. D.; Poirier, E. Z.; Cardoso, A.; Frederico, B.; Canton, J.; Barrell, S.; Beale, R.; Byrne, R.; Caidan, S.; Crawford, M.; Cubitt, L.; Gamblin, S.; Gandhi, S.; Goldstone, R.; Grant, P. R.; Gulati, K.; Hindmarsh, S.; Howell, M.; Hubank, M.; Instrell, R.; Jiang, M.; Kassiotis, G.; Lu, W.-T.; MacRae, J. I.; Martini, I.; Miller, D.; Moore, D.; Nastouli, E.; Nicod, J.; Nightingale, L.; Olsen, J.; Oomatia, A.; O'Reilly, N.; Rideg, A.; Song, O.-R.; Strange, A.; Swanton, C.; Turajlic, S.; Walker, P. A.; Wu, M.; Sousa, C. R. e., Standard operating procedures for SARS-CoV-2 detection by a clinical diagnostic RT-LAMP assay. *medRxiv* **2020**, 2020.06.29.20142430.

17. Esbin, M. N.; Whitney, O. N.; Chong, S.; Maurer, A.; Darzacq, X.; Tjian, R., Overcoming the bottleneck to widespread testing: a rapid review of nucleic acid testing approaches for COVID-19 detection. *RNA (New York, N.Y.)* **2020,** *26* (7), 771-783.

18. Kashir, J.; Yaqinuddin, A., Loop mediated isothermal amplification (LAMP) assays as a rapid diagnostic for COVID-19. *Medical Hypotheses* **2020,** *141*, 109786.

19. Yan, C.; Cui, J.; Huang, L.; Du, B.; Chen, L.; Xue, G.; Li, S.; Zhang, W.; Zhao, L.; Sun, Y.; Yao, H.; Li, N.; Zhao, H.; Feng, Y.; Liu, S.; Zhang, Q.; Liu, D.; Yuan, J., Rapid and visual detection of 2019 novel coronavirus (SARS-CoV-2) by a reverse transcription loop-mediated isothermal amplification assay. *Clin Microbiol Infect* **2020,** *26* (6), 773-779.

20. Lamb, L. E.; Bartolone, S. N.; Ward, E.; Chancellor, M. B., Rapid detection of novel coronavirus/Severe Acute Respiratory Syndrome Coronavirus 2 (SARS-CoV-2) by reverse transcription-loop-mediated isothermal amplification. *PLoS One* **2020,** *15* (6), e0234682.

21. Tan, S. H.; Allicock, O.; Armstrong-Hough, M.; Wyllie, A. L., Saliva as a gold-standard sample for SARS-CoV-2 detection. *The Lancet Respiratory Medicine*.

22. Moisset, X.; Gautier, N.; Godet, T.; Parabere, S.; Pereira, B.; Meunier, E.; Gerbaud, L.; Lesens, O.; Henquell, C.; Beytout, J.; Clavelou, P., Nasopharyngeal swab-induced pain for SARS-CoV-2 screening: A randomised controlled trial of conventional and self-swabbing. *European Journal of Pain* **2021**.

23. Koenig, D. Brain Scraper: Why Do Some COVID Tests Hurt So Much?

24. Mahony, J.; Chong, S.; Bulir, D.; Ruyter, A.; Mwawasi, K.; Waltho, D., Multiplex loop-mediated isothermal amplification (M-LAMP) assay for the detection of influenza A/H1, A/H3 and influenza B can provide a specimen-to-result diagnosis in 40 min with single genome copy sensitivity. *Journal of Clinical Virology* **2013,** *58* (1), 127-131.

25. Aoki, M. N.; Coelho, B. d. O.; Bentim Goes, L. G.; Minoprio, P.; Durigon, E. L.; Morello, L. G.; Marchini, F. K.; Riediger, I. N.; Debur, M. d. C.; Nakaya, H. I.; Blanes, L., Colorimetric RT-LAMP SARS-CoV-2 diagnostic sensitivity relies on color interpretation and viral load. *Sci Rep-Uk* **2021,** *11* (1).

26. Scherf, U. A new process that can be used in place of the extraction method when materials for the current method are limited. https://www.fda.gov/media/138931/download.

27. Diseases, C. D. N. D. o. V., CDC 2019-Novel Coronavirus (2019-nCoV) Real-Time RT-PCR Diagnostic Panel. CDC-006-00019, Revision: 06 ed.; Prevention, C. f. D. C. a., Ed. 12/01/2020.

28. Efron, B.; Tibshirani, R., *An introduction to the bootstrap*. Chapman & Hall: New York, 1993; p xvi, 436 p.

29. Zhu, J.; Guo, J.; Xu, Y.; Chen, X., Viral dynamics of SARS-CoV-2 in saliva from infected patients. *J Infect* **2020,** *81* (3), e48-e50.

30. Corstjens, P. L. A. M.; Abrams, W. R.; Malamud, D., Saliva and viral infections. *Periodontol 2000* **2016,** *70* (1), 93-110.

31. Wyllie, A. L.; Fournier, J.; Casanovas-Massana, A.; Campbell, M.; Tokuyama, M.; Vijayakumar, P.; Warren, J. L.; Geng, B.; Muenker, M. C.; Moore, A. J.; Vogels, C. B. F.; Petrone, M. E.; Ott, I. M.; Lu, P.; Venkataraman, A.; Lu-Culligan, A.; Klein, J.; Earnest, R.; Simonov, M.; Datta, R.; Handoko, R.; Naushad, N.; Sewanan, L. R.; Valdez, J.; White, E. B.; Lapidus, S.; Kalinich, C. C.; Jiang, X.; Kim, D. J.; Kudo, E.; Linehan, M.; Mao, T.; Moriyama, M.; Oh, J. E.; Park, A.; Silva, J.; Song, E.; Takahashi, T.; Taura, M.; Weizman, O. E.; Wong, P.; Yang, Y.; Bermejo, S.; Odio, C. D.; Omer, S. B.; Dela Cruz, C. S.; Farhadian, S.; Martinello, R. A.; Iwasaki, A.; Grubaugh, N. D.; Ko, A. I., Saliva or nasopharyngeal swab specimens for detection of SARS-CoV-2. *N Engl J Med* **2020,** *383* (13), 1283-1286.

32. Adaway, J. E.; Hawley, J. M.; Lockhart, S. J.; Keevil, B. G., Heat inactivation of saliva samples for the analysis of cortisol and cortisone during the COVID-19 pandemic. *The Journal of Applied Laboratory Medicine* **2020,** *5* (6), 1413-1416.

33. Bujang, M. A.; Adnan, T. H., Requirements for Minimum Sample Size for Sensitivity and Specificity Analysis. *J Clin Diagn Res* **2016,** *10* (10), YE01-YE06.

34. 2019: American Community Survey 5-Year Estimates Data Profiles. 2019.

35. Nickbakhsh, S.; Ho, A.; Marques, D. F. P.; McMenamin, J.; Gunson, R. N.; Murcia, P. R., Epidemiology of Seasonal Coronaviruses: Establishing the Context for the Emergence of Coronavirus Disease 2019. *The Journal of Infectious Diseases* **2020,** *222* (1), 17-25.

36. Reese, H.; Iuliano, A. D.; Patel, N. N.; Garg, S.; Kim, L.; Silk, B. J.; Hall, A. J.; Fry, A.; Reed, C., Estimated Incidence of Coronavirus Disease 2019 (COVID-19) Illness and Hospitalization—United States, February–September 2020. *Clinical Infectious Diseases* **2020,** *72* (12), e1010-e1017.

37. Kapoor, P.; Chowdhry, A.; Kharbanda, O. P.; Popli, D. B.; Gautam, K.; Saini, V., Exploring salivary diagnostics in COVID-19: a scoping review and research suggestions. *Bdj Open* **2021,** *7* (1).

38. Benn, A. M.; Thomson, W. M., Saliva: an overview. *The New Zealand dental journal* **2014,** *110* (3), 92-6.

39. Subramanian, S.; Gomez, R. D., An Empirical Approach for Quantifying Loop-Mediated Isothermal Amplification (LAMP) Using Escherichia coli as a Model System. *Plos One* **2014,** *9* (6).

40. Loveday, E. K.; Hain, K. S.; Kochetkova, I.; Hedges, J. F.; Robison, A.; Snyder, D. T.; Brumfield, S. K.; Young, M. J.; Jutila, M. A.; Chang, C. B.; Taylor, M. P., Effect of Inactivation Methods on SARS-CoV-2 Virion Protein and Structure. *Viruses-Basel* **2020,** *13* (4).

41. Rogers, A. A.; Baumann, R. E.; Borillo, G. A.; Kagan, R. M.; Batterman, H. J.; Galdzicka, M. M.; Marlowe, E. M., Evaluation of Transport Media and Specimen Transport Conditions for the Detection of SARS-CoV-2 by Use of Real-Time Reverse Transcription-PCR. *Journal of Clinical Microbiology* **2020,** *58* (8).

42. Grishin, A. M.; Dolgova, N. V.; Harms, S.; Pickering, I. J.; George, G. N.; Falzarano, D.; Cygler, M., Spike protein disulfide disruption as a potential treatment for SARS-CoV-2. *bioRxiv* **2021**, 2021.01.02.425099.

43. Thompson, D.; Lei, Y., Mini review: Recent progress in RT-LAMP enabled COVID-19 detection. *Sensors and Actuators Reports* **2020,** *2* (1).

44. Sabiiti, W.; Azam, K.; Esmeraldo, E.; Bhatt, N.; Rachow, A.; Gillespie, S. H., Heat Inactivation Renders Sputum Safe and Preserves Mycobacterium tuberculosis RNA for Downstream Molecular Tests. *J Clin Microbiol* **2019,** *57* (4).

45. Rabe, B. A.; Cepko, C., SARS-CoV-2 detection using isothermal amplification and a rapid, inexpensive protocol for sample inactivation and purification. *Proceedings of the National Academy of Sciences* **2020,** *117* (39), 24450-24458.

46. Ranoa, D. R. E.; Holland, R. L.; Alnaji, F. G.; Green, K. J.; Wang, L.; Brooke, C. B.; Burke, M. D.; Fan, T. M.; Hergenrother, P. J., Saliva-Based Molecular Testing for SARS-CoV-2 that Bypasses RNA Extraction. *bioRxiv* **2020**, 2020.06.18.159434.

47. Ott, I. M.; Strine, M. S.; Watkins, A. E.; Boot, M.; Kalinich, C. C.; Harden, C. A.; Vogels, C. B. F.; Casanovas-Massana, A.; Moore, A. J.; Muenker, M. C.; Nakahata, M.; Tokuyama, M.; Nelson, A.; Fournier, J.; Bermejo, S.; Campbell, M.; Datta, R.; Dela Cruz, C. S.; Farhadian, S. F.; Ko, A. I.; Iwasaki, A.; Grubaugh, N. D.; Wilen, C. B.; Wyllie, A. L., Simply saliva: stability of SARS-CoV-2 detection negates the need for expensive collection devices. *medRxiv : the preprint server for health sciences* **2020**, 2020.08.03.20165233.

48. Chow, F. W.-N.; Chan, T. T.-Y.; Tam, A. R.; Zhao, S.; Yao, W.; Fung, J.; Cheng, F. K.-K.; Lo, G. C.-S.; Chu, S.; Aw-Yong, K. L.; Tang, J. Y.-M.; Tsang, C.-C.; Luk, H. K.-H.; Wong, A. C.-P.; Li, K. S.-M.; Zhu, L.; He, Z.; Tam, E. W. T.; Chung, T. W.-H.; Wong, S. C. Y.; Que, T.-L.; Fung, K. S.-C.; Lung, D. C.; Wu, A. K.-L.; Hung, I. F.-N.; Woo, P. C.-Y.; Lau, S. K.-P., A Rapid, Simple, Inexpensive, and Mobile Colorimetric Assay COVID-19-LAMP for Mass On-Site Screening of COVID-19. *Int. J. Mol. Sci.* **2020,** *21* (15).

49. Lalli, M. A.; Langmade, J. S.; Chen, X.; Fronick, C. C.; Sawyer, C. S.; Burcea, L. C.; Wilkinson, M. N.; Fulton, R. S.; Heinz, M.; Buchser, W. J.; Head, R. D.; Mitra, R. D.; Milbrandt, J., Rapid and Extraction-Free Detection of SARS-CoV-2 from Saliva by Colorimetric Reverse-Transcription Loop-Mediated Isothermal Amplification. *Clinical Chemistry* **2020,** *67* (2), 415-424.

50. Pastorino, B.; Touret, F.; Gilles, M.; de Lamballerie, X.; Charrel, R. N., Heat Inactivation of Different Types of SARS-CoV-2 Samples: What Protocols for Biosafety, Molecular Detection and Serological Diagnostics? *Viruses* **2020,** *12* (7), 735.

51. Loveday, E. K.; Hain, K. S.; Kochetkova, I.; Hedges, J. F.; Robison, A.; Snyder, D. T.; Brumfield, S. K.; Young, M. J.; Jutila, M. A.; Chang, C. B.; Taylor, M. P., Effects of inactivation method on SARS-CoV-2 virion protein and structure. *bioRxiv* **2020**, 2020.11.14.383026.

52. Park, N. J.; Li, Y.; Yu, T.; Brinkman, B. M. N.; Wong, D. T., Characterization of RNA in saliva. *Clinical chemistry* **2006,** *52* (6), 988-994.

53. Arons, M. M.; Hatfield, K. M.; Reddy, S. C.; Kimball, A.; James, A.; Jacobs, J. R.; Taylor, J.; Spicer, K.; Bardossy, A. C.; Oakley, L. P.; Tanwar, S.; Dyal, J. W.; Harney, J.; Chisty, Z.; Bell, J. M.; Methner, M.; Paul, P.; Carlson, C. M.; McLaughlin, H. P.; Thornburg, N.; Tong, S.; Tamin, A.; Tao, Y.; Uehara, A.; Harcourt, J.; Clark, S.; Brostrom-Smith, C.; Page, L. C.; Kay, M.; Lewis, J.; Montgomery, P.; Stone, N. D.; Clark, T. A.; Honein, M. A.; Duchin, J. S.; Jernigan, J. A., Presymptomatic SARS-CoV-2 Infections and Transmission in a Skilled Nursing Facility. *New England Journal of Medicine* **2020,** *382* (22), 2081-2090.

54. Ravi, N.; Cortade, D. L.; Ng, E.; Wang, S. X., Diagnostics for SARS-CoV-2 detection: A comprehensive review of the FDA-EUA COVID-19 testing landscape. *Biosens Bioelectron* **2020,** *165*, 112454-112454.

55. Wang, W.; Xu, Y.; Gao, R.; Lu, R.; Han, K.; Wu, G.; Tan, W., Detection of SARS-CoV-2 in Different Types of Clinical Specimens. *JAMA* **2020,** *323* (18), 1843-1844.

56. Mallett, S.; Allen, A. J.; Graziadio, S.; Taylor, S. A.; Sakai, N. S.; Green, K.; Suklan, J.; Hyde, C.; Shinkins, B.; Zhelev, Z.; Peters, J.; Turner, P. J.; Roberts, N. W.; di Ruffano, L. F.; Wolff, R.; Whiting, P.; Winter, A.; Bhatnagar, G.; Nicholson, B. D.; Halligan, S., At what times during infection is SARS-CoV-2 detectable and no longer detectable using RT-PCR-based tests? A systematic review of individual participant data. *BMC Medicine* **2020,** *18* (1), 346.

57. Roy, K. M.; Bagg, J.; McCarron, B., The effect of saliva specimen collection, handling and storage protocols on hepatitis C virus (HCV) RNA detection by PCR. *Oral Dis* **1999,** *5* (2), 123-7.

58. Gomes-Keller, M. A.; Gönczi, E.; Tandon, R.; Riondato, F.; Hofmann-Lehmann, R.; Meli, M. L.; Lutz, H., Detection of Feline Leukemia Virus RNA in Saliva from Naturally Infected Cats and Correlation of PCR Results with Those of Current Diagnostic Methods. *Journal of Clinical Microbiology* **2006,** *44* (3), 916-922.

59. Choi, J. E.; Lyons, K. M.; Kieser, J. A.; Waddell, N. J., Diurnal variation of intraoral pH and temperature. *Bdj Open* **2017,** *3* (1), 17015.

60. Nunes, L. A. S.; Macedo, D. V. d., Saliva as a diagnostic fluid in sports medicine: potential and limitations. *Jornal Brasileiro de Patologia e Medicina Laboratorial* **2013,** *49*, 247-255.

61. Zhang, J. M.; Hu, Q. P.; Wang, S.; Tao, J.; Gou, M. L., Digital Light Processing Based Three-dimensional Printing for Medical Applications. *Int J Bioprinting* **2020,** *6* (1), 12-27.

CHAPTER EIGHT

CONCLUSION

The experiments described in this dissertation have focused generally on soft materials and specifically on colloidal suspensions, saliva-based diagnostic devices, fluorescence microscopy, and 3D printing hydrogels.

In Chapter 2, we present a novel Fluorescence Centrifuge Force Microscope (F-CFM) that we use to characterize the interaction between colloidal particles and a glass surface dispersed in water. The F-CFM measurements were validated using a simple microsphere sedimentation experiment; the F-CFM rotational velocity was validated using acoustic analysis; the image quality was characterized by imaging a photomask and by tracking stationary 1-micron fluorescent particles; and the utility of the F-CFM was demonstrated by measuring the pull-off forces required to remove colloidal particles interacting with a glass cover slip under increasing salt conditions. The pull-off forces increased with increased salt concentration, as predicted by DLVO theory, although the increase was not as pronounced as predicted by DLVO theory, likely due to surface roughness effects and surface charge uncertainty and heterogeneity.

In Chapter 3, we presented a device for saliva point-of-care loop mediated isothermal amplification (SPOC-LAMP) for pathogen detection in human saliva. The device collects a predetermined small volume of saliva from a flocked swab and mixes the saliva with LAMP reagents and buffers in an attached standard 0.65 mL microcentrifuge tube vial. We show that the device accurately collects the small amount of saliva necessary to prevent dilution or inhibition of costly LAMP reagents. The device is carefully engineered to be simple to use, easy to actuate, and highly scalable. The device and all components are designed to facilitate the high-volume

manufacturing necessary to implement the ubiquitous levels of testing that would help contain the SARS-CoV-2 and future pandemics.

In Chapter 4 – 7, we presented several platforms investigating soft and biological materials. In chapter 4, we presented a parameter space for printing high resolution channels in hydrogels. In Chapter 5, we presented a leak-resistant, bulb-shaped connector design for porting modular vascularized hydrogels that relies on internal pressure and hydrogel elasticity to form a robust seal. In Chapter 6, we presented a temperature control microscopy system that enables temperature cycling of samples on a standard upright microscope stage, a very useful tool for investigating fluorescence amplification technologies and microfluid applications. In Chapter 7, we presented a LAMP formulation for detecting SARS-CoV-2 in human saliva and showed that the saliva LAMP (sLAMP) results are comparable with the saliva PCR, the current gold standard for pathogen detection.

REFERENCES CITED

1. Jones, R. A. L., Soft Condensed Matter. Oxford University Press Inc.: 2002.

2. Witten, T. A. a. P., Phillip A., Structured fluids: polymers, colloids, surfactants, . Oxford University Press Inc.: 2004.

3. Russel, W. B.; Russel, W. B.; Saville, D. A.; Schowalter, W. R., Colloidal Dispersions. Cambridge University Press: 1991.

4. Nishinari, K., Rheological and DSC study of sol-gel transition in aqueous dispersions of industrially important polymers and colloids. Colloid and Polymer Science 1997, 275 (12), 1093-1107.

5. Freundlich, H., Colloidal structures in biology. Journal of Physical Chemistry 1937, 41 (9), 1151-1161.

6. Krogh, A.; Landis, E. M.; Turner, A. H., The movement of fluid through the human capillary wall in relation to venous pressure and to the colloid osmotic pressure of the blood. Journal of Clinical Investigation 1932, 11 (1), 63-95.

7. Geoghegan, W. D.; Ackerman, G. A., ADSORPTION OF HORSERADISH-PEROXIDASE, OVOMUCOID AND ANTIIMMUNOGLOBULIN TO COLLOIDAL GOLD FOR INDIRECT DETECTION OF CONCANAVALIN-A, WHEAT-GERM AGGLUTININ AND GOAT ANTIHUMAN IMMUNOGLOBULIN-G ON CELL-SURFACES AT ELECTRON-MICROSCOPIC LEVEL - NEW METHOD, THEORY AND APPLICATION. Journal of Histochemistry & Cytochemistry 1977, 25 (11), 1187-1200.

8. Dobrovolskaia, M. A.; Patri, A. K.; Zheng, J.; Clogston, J. D.; Ayub, N.; Aggarwal, P.; Neun, B. W.; Hall, J. B.; McNeil, S. E., Interaction of colloidal gold nanoparticles with human blood: effects on particle size and analysis of plasma protein binding profiles. Nanomedicine-Nanotechnology Biology and Medicine 2009, 5 (2), 106-117.

9. Chi, E. Y.; Krishnan, S.; Kendrick, B. S.; Chang, B. S.; Carpenter, J. F.; Randolph, T. W., Roles of conformational stability and colloidal stability in the aggregation of recombinant human granulocyte colony-stimulating factor. Protein Science 2003, 12 (5), 903-913.

10. Shaldon, S.; Caesar, J.; Chiandussi, L.; Sherlock, S.; Guevara, L., ESTIMATION OF HEPATIC BLOOD FLOW AND INTRAHEPATIC SHUNTED BLOOD FLOW BY COLLOIDAL HEAT-DENATATURED HUMAN SERUM ALBUMIN LABELED WITH I131. Journal of Clinical Investigation 1961, 40 (7), 1346-&.

11. Pertoft, H.; Back, O.; Lindahlk.K, SEPARATION OF VARIOUS BLOOD CELLS IN COLLOIDAL SILICA-POLYVINYLPYRROLIDONE GRADIENTS. Exp Cell Res 1968, 50 (2), 355-&.

12. Matejtschuk, P.; Dash, C. H.; Gascoigne, E. W., Production of human albumin solution: a continually developing colloid. British Journal of Anaesthesia 2000, 85 (6), 887-895.

13. Hoeft, A.; Korb, H.; Mehlhorn, U.; Stephan, H.; Sonntag, H., PRIMING OF CARDIOPULMONARY BYPASS WITH HUMAN ALBUMIN OR RINGER LACTATE - EFFECT ON COLLOID OSMOTIC-PRESSURE AND EXTRAVASCULAR LUNG WATER. British Journal of Anaesthesia 1991, 66 (1), 73-80.

14. Toyofuku, M.; Tashiro, Y.; Hasegawa, Y.; Kurosawa, M.; Nomura, N., Bacterial membrane vesicles, an overlooked environmental colloid: Biology, environmental perspectives and applications. Advances in Colloid and Interface Science 2015, 226, 65-77.

15. Edwards, S. A.; Williams, D. R. M., Hofmeister effects in colloid science and biology explained by dispersion forces: analytic results for the double layer interaction. Current Opinion in Colloid & Interface Science 2004, 9 (1-2), 139-144.

16. Dholakia, K.; MacDonald, M. P.; Zemanek, P.; Cizmar, T., Cellular and colloidal separation using optical forces. In Laser Manipulation of Cells and Tissues, Berns, M. W.; Greulich, K. O., Eds. 2007; Vol. 82, pp 467-495.

17. Bostrom, M.; Williams, D. R. M.; Ninham, B. W., Specific ion effects: why colloid science has failed to contribute to biology. Trends in Colloid and Interface Science Xvi 2004, 123, 110-113.

18. Delabouret, A.; Thioune, O.; Fessi, H.; Devissaguet, J. P.; Puisieux, F., APPLICATION OF AN ORIGINAL PROCESS FOR OBTAINING COLLOIDAL DISPERSIONS OF SOME COATING POLYMERS - PREPARATION, CHARACTERIZATION, INDUSTRIAL SCALE-UP. Drug Development and Industrial Pharmacy 1995, 21 (2), 229-241.

19. Kang, S. K.; Choo, K. H., Use of MF and UF membranes for reclamation of glass industry wastewater containing colloidal clay and glass particles. Journal of Membrane Science 2003, 223 (1-2), 89-103.

20. Komesvarakul, N.; Scamehorn, J. F.; Gecol, H., Purification of phenolic-laden wastewater from the pulp and paper industry by using colloid-enhanced ultrafiltration. Separation Science and Technology 2003, 38 (11), 2465-2501.

21. Chuang, S. H.; Chang, T. C.; Ouyang, C. F.; Leu, J. M., Colloidal silica removal in coagulation processes for wastewater reuse in a high-tech industrial park. Water Science and Technology 2007, 55 (1-2), 187-195.

22. Quinson, J.; Neumann, S.; Wannmacher, T.; Kacenauskaite, L.; Inaba, M.; Bucher, J.; Bizzotto, F.; Simonsen, S. B.; Kuhn, L. T.; Bujak, D.; Zana, A.; Arenz, M.; Kunz, S., Colloids for Catalysts: A Concept for the Preparation of Superior Catalysts of Industrial Relevance. Angewandte Chemie-International Edition 2018, 57 (38), 12338-12341.

23. Pendse, H. P.; Sharma, A., PARTICLE-SIZE DISTRIBUTION ANALYSIS OF INDUSTRIAL COLLOIDAL SLURRIES USING ULTRASONIC SPECTROSCOPY. Particle & Particle Systems Characterization 1993, 10 (5), 229-233.

24. Huang, J. S.; Varadaraj, R., Colloid and interface science in the oil industry. Current Opinion in Colloid & Interface Science 1996, 1 (4), 535-539.

25. Whitehouse, B. G.; Yeats, P. A.; Strain, P. M., Cross-flow filtration of colloids from aquatic environments. Limnology and Oceanography 1990, 35 (6), 1368-1375.

26. Neal, C.; Jarvie, H.; Rowland, P.; Lawler, A.; Sleep, D.; Scholefield, P., Titanium in UK rural, agricultural and urban/industrial rivers: Geogenic and anthropogenic colloidal/sub-colloidal sources and the significance of within-river retention. Sci Total Environ 2011, 409 (10), 1843-1853.

27. Verwey, E. J. W.; Overbeek, J. T. G., Theory of the stability of lyophobic colloids. Elsevier Publishing Company 1948.

28. Moore, T. L.; Rodriguez-Lorenzo, L.; Hirsch, V.; Balog, S.; Urban, D.; Jud, C.; Rothen-Rutishauser, B.; Lattuada, M.; Petri-Fink, A., Nanoparticle colloidal stability in cell culture media and impact on cellular interactions. Chemical Society Reviews 2015, 44 (17), 6287-6305.

29. Joanny, J. F.; Leibler, L.; Degennes, P. G., EFFECTS OF POLYMER-SOLUTIONS ON COLLOID STABILITY. Journal of Polymer Science Part B-Polymer Physics 1979, 17 (6), 1073-1084.

30. Heurtault, B.; Saulnier, P.; Pech, B.; Proust, J. E.; Benoit, J. P., Physico-chemical stability of colloidal lipid particles. Biomaterials 2003, 24 (23), 4283-4300.

31. Elimelech, M.; Gregory, J.; Jia, X.; Williams, R., Particle Deposition & Aggregation. Butterworth-Heinemann Ltd 1995.

32. Tufenkji, N.; Elimelech, M., Breakdown of colloid filtration theory: Role of the secondary energy minimum and surface charge heterogeneities. Langmuir 2005, 21 (3), 841-852.

33. Tufenkji, N.; Elimelech, M., Deviation from the classical colloid filtration theory in the presence of repulsive DLVO interactions. Langmuir 2004, 20 (25), 10818-10828.

34. Harvey, R. W.; Garabedian, S. P., USE OF COLLOID FILTRATION THEORY IN MODELING MOVEMENT OF BACTERIA THROUGH A CONTAMINATED SANDY AQUIFER. Environ Sci Technol 1991, 25 (1), 178-185.

35. Zhou, Z.; Tao, Y.; Zhang, S.; Xiao, Y.; Meng, F.; Stuckey, D. C., Size-dependent microbial diversity of sub-visible particles in a submerged anaerobic membrane bioreactor (SAnMBR): Implications for membrane fouling. Water Res 2019, 159, 20-29.

36. Kunacheva, C.; Soh, Y. N. A.; Stuckey, D. C., Effect of feed pH on reactor performance and production of soluble microbial products (SMPs) in a submerged anaerobic membrane bioreactor. Chem Eng J 2017, 320, 135-143.

37. Zhou, Z.; Meng, F.; Chae, S.-R.; Huang, G.; Fu, W.; Jia, X.; Li, S.; Chen, G.-H., Microbial Transformation of Biomacromolecules in a Membrane Bioreactor: Implications for Membrane Fouling Investigation. Plos One 2012, 7 (8).

38. Song, W.; Lee, L. Y.; You, H.; Shi, X.; Ng, H. Y., Microbial community succession and its correlation with reactor performance in a sponge membrane bioreactor coupled with fiber-bundle anoxic bio-filter for treating saline mariculture wastewater. Bioresource Technology 2020, 295.

39. Elander, R. P., Industrial production of beta-lactam antibiotics. Appl Microbiol Biot 2003, 61 (5-6), 385-392.

40. Takiguchi, Y.; Mishima, H.; Okuda, M.; Terao, M., MILBEMYCINS, A NEW FAMILY OF MACROLIDE ANTIBIOTICS - FERMENTATION, ISOLATION AND PHYSICOCHEMICAL PROPERTIES. Journal of Antibiotics 1980, 33 (10), 1120-1127.

41. Sehgal, S. N.; Baker, H.; Vezina, C., RAPAMYCIN (AY-22,989), A NEW ANTIFUNGAL ANTIBIOTIC .2. FERMENTATION, ISOLATION AND CHARACTERIZATION. Journal of Antibiotics 1975, 28 (10), 727-732.

42. Erguder, T. H.; Tezel, U.; Guven, E.; Demirer, G. N., Anaerobic biotransformation and methane generation potential of cheese whey in batch and UASB reactors. Waste Management 2001, 21 (7), 643-650.

43. Castello, E.; Garcia y Santos, C.; Iglesias, T.; Paolino, G.; Wenzel, J.; Borzacconi, L.; Etchebehere, C., Feasibility of biohydrogen production from cheese whey using a UASB reactor: Links between microbial community and reactor performance. International Journal of Hydrogen Energy 2009, 34 (14), 5674-5682.

44. Smogrovicova, D.; Domeny, Z.; Gemeiner, P.; Malovikova, A.; Sturdik, E., Reactors for continuous primary beer fermentation using immobilised yeast. Biotechnology Techniques 1997, 11 (4), 261-264.

45. Parawira, W.; Kudita, I.; Nyandoroh, M. G.; Zvauya, R., A study of industrial anaerobic treatment of opaque beer brewery wastewater in a tropical climate using a full-scale UASB reactor seeded with activated sludge. Process Biochemistry 2005, 40 (2), 593-599.

46. Branyik, T.; Silva, D. P.; Vicente, A. A.; Lehnert, R.; Silva, J. B. A. E.; Dostalek, P.; Teixeira, J. A., Continuous immobilized yeast reactor system for complete beer fermentation using spent grains and corncobs as carrier materials. Journal of Industrial Microbiology & Biotechnology 2006, 33 (12), 1010-1018.

47. Najafpour, G.; Younesi, H.; Ismail, K. S. K., Ethanol fermentation in an immobilized cell reactor using Saccharomyces cerevisiae. Bioresource Technology 2004, 92 (3), 251-260.

48. Ren, N. Q.; Wang, B. Z.; Huang, J. C., Ethanol-type fermentation from carbohydrate in high rate acidogenic reactor. Biotechnology and Bioengineering 1997, 54 (5), 428-433.

49. Pan, X.; Fan, Z.; Chen, W.; Ding, Y.; Luo, H.; Bao, X., Enhanced ethanol production inside carbon-nanotube reactors containing catalytic particles. Nature Materials 2007, 6 (7), 507-511.

50. Wargacki, A. J.; Leonard, E.; Win, M. N.; Regitsky, D. D.; Santos, C. N. S.; Kim, P. B.; Cooper, S. R.; Raisner, R. M.; Herman, A.; Sivitz, A. B.; Lakshmanaswamy, A.; Kashiyama, Y.; Baker, D.; Yoshikuni, Y., An Engineered Microbial Platform for Direct Biofuel Production from Brown Macroalgae. Science 2012, 335 (6066), 308-313.

51. Peralta-Yahya, P. P.; Zhang, F.; del Cardayre, S. B.; Keasling, J. D., Microbial engineering for the production of advanced biofuels. Nature 2012, 488 (7411), 320-328.

52. Li, Q.; Du, W.; Liu, D., Perspectives of microbial oils for biodiesel production. Appl Microbiol Biot 2008, 80 (5), 749-756.

53. Heidebrecht, A.; Scheibel, T., Recombinant Production of Spider Silk Proteins. Advances in Applied Microbiology, Vol 82 2013, 82, 115-153.

54. Fahnestock, S. R.; Yao, Z.; Bedzyk, L. A., Microbial production of spider silk proteins. Journal of biotechnology 2000, 74 (2), 105-19.

55. Singh, R. S.; Saini, G. K.; Kennedy, J. F., Pullulan: Microbial sources, production and applications. Carbohydrate Polymers 2008, 73 (4), 515-531.

56. Jonas, R.; Farah, L. F., Production and application of microbial cellulose. Polymer Degradation and Stability 1998, 59 (1-3), 101-106.

57. Chawla, P. R.; Bajaj, I. B.; Survase, S. A.; Singhal, R. S., Microbial Cellulose: Fermentative Production and Applications. Food Technology and Biotechnology 2009, 47 (2), 107-124.

58. Suopajarvi, T.; Liimatainen, H.; Hormi, O.; Niinimaki, J., Coagulation-flocculation treatment of municipal wastewater based on anionized nanocelluloses. Chem Eng J 2013, 231, 59-67.

59. Hargreaves, A. J.; Vale, P.; Whelan, J.; Alibardi, L.; Constantino, C.; Dotro, G.; Cartmell, E.; Campo, P., Impacts of coagulation-flocculation treatment on the size distribution and bioavailability of trace metals (Cu, Pb, Ni, Zn) in municipal wastewater. Water Res 2018, 128, 120-128.

60. Chan, Y. J.; Chong, M. F.; Law, C. L.; Hassell, D. G., A review on anaerobic-aerobic treatment of industrial and municipal wastewater. Chem Eng J 2009, 155 (1-2), 1-18.

61. Beltran-Heredia, J.; Sanchez-Martin, J., Municipal wastewater treatment by modified tannin flocculant agent. Desalination 2009, 249 (1), 353-358.

62. Tu, X.; Song, Y.; Yu, H.; Zeng, P.; Liu, R., Fractionation and characterization of dissolved extracellular and intracellular products derived from floccular sludge and aerobic granules. Bioresource Technology 2012, 123, 55-61.

63. Shak, K. P. Y.; Wu, T. Y., Coagulation-flocculation treatment of high-strength agro-industrial wastewater using natural Cassia obtusifolia seed gum: Treatment efficiencies and flocs characterization. Chem Eng J 2014, 256, 293-305.

64. Peppas, N. A., Hydrogels in Medicine and Pharmacy: Fundamentals. CRC Press: 2019.

65. Menut, P.; Seiffert, S.; Sprakel, J.; Weitz, D. A., Does size matter? Elasticity of compressed suspensions of colloidal- and granular-scale microgels. Soft Matter 2012, 8 (1), 156-164.

66. Benjamin, A. D.; Abbasi, R.; Owens, M.; Olsen, R. J.; Walsh, D. J.; LeFevre, T. B.; Wilking, J. N., Light-based 3D printing of hydrogels with high-resolution channels. Biomedical Physics & Engineering Express 2019, 5 (2).

67. Farjami, T.; Madadlou, A., An overview on preparation of emulsion-filled gels and emulsion particulate gels. Trends Food Sci. Technol. 2019, 86, 85-94.

68. Mason, T. G.; Bibette, J.; Weitz, D. A., Elasticity of Compressed Emulsions. Physical Review Letters 1995, 75 (10), 2051-2054.

69. Mason, T. G., New fundamental concepts in emulsion rheology. Current Opinion in Colloid & Interface Science 1999, 4 (3), 231-238.

70. Brummer, R., Rheology Essentials of Cosmetic and Food Emulsions. Springer Berlin Heidelberg: 2006.

71. Fryd, M. M.; Mason, T. G., Advanced Nanoemulsions. In Annual Review of Physical Chemistry, Vol 63, Johnson, M. A.; Martinez, T. J., Eds. Annual Reviews: Palo Alto, 2012; Vol. 63, pp 493-518.

72. Lee, G.; Han, S.-B.; Lee, J.-H.; Kim, H.-W.; Kim, D.-H., Cancer Mechanobiology: Microenvironmental Sensing and Metastasis. ACS Biomaterials Science & Engineering 2019, 5 (8), 3735-3752.

73. Verbruggen, S., Mechanobiology in Health and Disease. Elsevier Science: 2018.

74. Hu, R. Q.; Li, F.; Lv, J. Q.; He, Y.; Lu, D. T.; Yamada, T.; Ono, N., Microfluidic analysis of pressure drop and flow behavior in hypertensive micro vessels. Biomedical Microdevices 2015, 17 (3).

75. von Smoluchowski, M., Experiments on a mathematical theory of kinetic coagulation of coloid solutions. Zeitschrift Fur Physikalische Chemie--Stochiometrie Und Verwandtschaftslehre 1917, 92 (2), 129-168.

76. Doob, J. L., The Brownian movement and stochastic equations. Annals of Mathematics 1942, 43, 351-369.

77. Brown, R., A brief account of microscopical observations on the particles contained in the pollen of plants. 1827.

78. Einstein, A., The theory of the Brownian Motion. Annalen Der Physik 1906, 19 (2), 371-381.

79. Perrin, J., Brownian motion and molecular reality. Annales De Chimie Et De Physique 1909, 18, 5-114.

80. Israelachvili, J. N., Intermolecular and Surface Forces, 3rd Edition. Intermolecular and Surface Forces, 3rd Edition 2011, 1-674.

81. Duncan, G. A.; Gerecht, S.; Fairbrother, D. H.; Bevan, M. A., Diffusing Colloidal Probes of kT-Scale Biomaterial-Cell Interactions. Langmuir 2016, 32 (46), 12212-12220.

82. Bevan, M. A.; Eichmann, S. L., Optical microscopy measurements of kT-scale colloidal interactions. Current Opinion in Colloid & Interface Science 2011, 16 (2), 149-157.

83. Sutherland, W., A dynamical theory of diffusion for non-electrolytes and the molecular mass of albumin. Philosophical Magazine 1905, 9 (49-54), 781-785.

84. Langevin, M. P., Sur la the´orie du mouvement brownien. C. R. Acad. Sci. 1908, 146, 530–533.

85. Einstein, A., Über die von der molekularkinetischen Theorie der Wärme geforderte Bewegung von in ruhenden Flüssigkeiten suspendierten Teilchen. Annalen der Physik 1905, 322 (8), 549-560.

86. Derjaguin, B.; Landau, L., THEORY OF THE STABILITY OF STRONGLY CHARGED LYOPHOBIC SOLS AND OF THE ADHESION OF STRONGLY CHARGED-PARTICLES IN SOLUTIONS OF ELECTROLYTES. Prog. Surf. Sci. 1993, 43 (1-4), 30-59.

87. Verwey, E. J. W., THEORY OF THE STABILITY OF LYOPHOBIC COLLOIDS. Journal of Physical and Colloid Chemistry 1947, 51 (3), 631-636.

88. Israelachvilli, J. N., Intermolecular & Surface Forces, 2nd Edition. 1985, 1-674.

89. Hamaker, H. C., The London - Van Der Waals attraction between spherical particles. Physica 1937, 4, 1058-1072.

90. Lipomi, D., Van der Waals forces between surfaces, Derjaguin approximation. In NANO 202, YouTube: University of California San Diego, 2017.

91. Mo, S.; Shao, X.; Chen, Y.; Cheng, Z., Increasing entropy for colloidal stabilization. Sci Rep-Uk 2016, 6.

92. van Roij, R., Defying gravity with entropy and electrostatics: sedimentation of charged colloids. Journal of Physics-Condensed Matter 2003, 15 (48), S3569-S3580.

93. Swendsen, R. H., Statistical mechanics of colloids and Boltzmann's definition of the entropy. American Journal of Physics 2006, 74 (3), 187-190.

94. Speck, T.; Blickle, V.; Bechinger, C.; Seifert, U., Distribution of entropy production for a colloidal particle in a nonequilibrium steady state. Epl 2007, 79 (3).

95. Royall, C. P.; van Roij, R.; van Blaaderen, A., Extended sedimentation profiles in charged colloids: the gravitational length, entropy, and electrostatics. Journal of Physics-Condensed Matter 2005, 17 (15), 2315-2326.

96. Manoharan, V. N., Colloidal matter: Packing, geometry, and entropy. Science 2015, 349 (6251).

97. Overbeek, J. T. G., THE ROLE OF ENERGY AND ENTROPY IN THE ELECTRICAL DOUBLE-LAYER. Colloids and Surfaces 1990, 51, 61-75.

98. Frenkel, D., Why colloidal systems can be described by statistical mechanics: some not very original comments on the Gibbs paradox. Molecular Physics 2014, 112 (17), 2325-2329.

99. Gregory, J., Interaction of Unequal Double Layers at Constant Charge. J Colloid and Interface Sci 1974, 51, 44-51.

100. Assemi, S.; Nalaskowski, J.; Johnson, W. P., Direct force measurements between carboxylate-modified latex microspheres and glass using atomic force microscopy. Colloid Surf. A-Physicochem. Eng. Asp. 2006, 286 (1-3), 70-77.

101. Chen, C.; Liu, K. S.; Shang, J. Y., Effects of ionic strength, electrolyte type, pH, and flow rate on transport and retention of atmospheric deposition particles in saturated porous media. Journal of Soils and Sediments 2018, 18 (3), 1066-1075.

102. Liang, Y.; Hilal, N.; Langston, P.; Starov, V., Interaction forces between colloidal particles in liquid: Theory and experiment. Advances in Colloid and Interface Science 2007, 134-35, 151-166.

103. Trefalt, G.; Palberg, T.; Borkovec, M., Forces between colloidal particles in aqueous solutions containing monovalent and multivalent ions. Current Opinion in Colloid & Interface Science 2017, 27, 9-17.

104. Gosse, C.; Croquette, V., Magnetic tweezers: Micromanipulation and force measurement at the molecular level. Biophys. J. 2002, 82 (6), 3314-3329.

105. Wilson, L.; Matsudaira, P. T.; Sheetz, M. P., Laser Tweezers in Cell Biology. Elsevier Science: 1997.

106. Grier, D. G., Optical tweezers in colloid and interface science. Current Opinion in Colloid & Interface Science 1997, 2 (3), 264-270.

107. Kegler, K.; Salomo, M.; Kremer, F., Forces of Interaction between DNA-Grafted Colloids: An Optical Tweezer Measurement. Physical Review Letters 2007, 98 (5), 058304.

108. LeFevre, T. B.; Bikos, D. A.; Chang, C. B.; Wilking, J. N., Measuring colloid-surface interaction forces in parallel using fluorescence centrifuge force microscopy. Soft Matter 2021, 17 (26), 6326-6336.

109. Butt, H. J.; Berger, R.; Bonaccurso, E.; Chen, Y.; Wang, J., Impact of atomic force microscopy on interface and colloid science. Advances in Colloid and Interface Science 2007, 133 (2), 91-104.

110. Butt, H. J.; Cappella, B.; Kappl, M., Force measurements with the atomic force microscope: Technique, interpretation and applications. Surf. Sci. Rep. 2005, 59 (1-6), 1-152.

111. van Oene M, D. L., Cross B, Pedaci F, Lipfert J, Dekker N, Applying torque to the Escherichia coli flagellar motor using magnetic tweezers. Nature Scientific Reports 2017, 7, 1-11.

112. Halvorsen, K.; Wong, W. P., Massively Parallel Single-Molecule Manipulation Using Centrifugal Force. Biophys. J. 2010, 98 (11), L53-L55.

113. Hoang, T.; Patel, D. S.; Halvorsen, K., A wireless centrifuge force microscope (CFM) enables multiplexed single-molecule experiments in a commercial centrifuge. Rev Sci Instrum 2016, 87 (8), 083705.

114. Yang, D.; Ward, A.; Halvorsen, K.; Wong, W. P., Multiplexed single-molecule force spectroscopy using a centrifuge. Nat. Commun. 2016, 7, 7.

115. Kou, L.; Jin, L.; Lei, H.; Hu, C.; Li, H.; Hu, X., Real-time parallel 3D multiple particle tracking with single molecule centrifugal force microscopy. J. Microsc. 2019, 273 (3), 178-188.

116. Punnoose, J. A.; Hayden, A.; Zhou, L. F.; Halvorsen, K., Wi-Fi Live-Streaming Centrifuge Force Microscope for Benchtop Single-Molecule Experiments. Biophys. J. 2020, 119 (11), 2231-2239.

117. Kirkness, M. W. H.; Forde, N. R., Single-Molecule Assay for Proteolytic Susceptibility: Force-Induced Collagen Destabilization. Biophys. J. 2018, 114 (3), 570-576.

118. Saiki, R. K.; Scharf, S.; Faloona, F.; Mullis, K. B.; Horn, G. T.; Erlich, H. A.; Arnheim, N., ENZYMATIC AMPLIFICATION OF BETA-GLOBIN GENOMIC SEQUENCES AND RESTRICTION SITE ANALYSIS FOR DIAGNOSIS OF SICKLE-CELL ANEMIA. Science 1985, 230 (4732), 1350-1354.

119. Saiki, R. K.; Gelfand, D. H.; Stoffel, S.; Scharf, S. J.; Higuchi, R.; Horn, G. T.; Mullis, K. B.; Erlich, H. A., PRIMER-DIRECTED ENZYMATIC AMPLIFICATION OF DNA WITH A THERMOSTABLE DNA-POLYMERASE. Science 1988, 239 (4839), 487-491.

120. Mullis, K. B.; Faloona, F. A., SPECIFIC SYNTHESIS OF DNA INVITRO VIA A POLYMERASE-CATALYZED CHAIN-REACTION. Methods in Enzymology 1987, 155, 335-350.

121. Mullis, K. B., THE UNUSUAL ORIGIN OF THE POLYMERASE CHAIN-REACTION. Scientific American 1990, 262 (4), 56-&.

122. Mullis, K.; Faloona, F.; Scharf, S.; Saiki, R.; Horn, G.; Erlich, H., SPECIFIC ENZYMATIC AMPLIFICATION OF DNA INVITRO - THE POLYMERASE CHAIN-REACTION. Cold Spring Harbor Symposia on Quantitative Biology 1986, 51, 263-273.

123. Notomi, T.; Okayama, H.; Masubuchi, H.; Yonekawa, T.; Watanabe, K.; Amino, N.; Hase, T., Loop-mediated isothermal amplification of DNA. Nucleic Acids Research 2000, 28 (12).

124. Parida, M.; Sannarangaiah, S.; Dash, P. K.; Rao, P. V. L.; Morita, K., Loop mediated isothermal amplification (LAMP): a new generation of innovative gene amplification technique; perspectives in clinical diagnosis of infectious diseases. Reviews in Medical Virology 2008, 18 (6), 407-421.

125. Mori, Y.; Kitao, M.; Tomita, N.; Notomi, T., Real-time turbidimetry of LAMP reaction for quantifying template DNA. Journal of Biochemical and Biophysical Methods 2004, 59 (2), 145-157.

126. Mori, Y.; Nagamine, K.; Tomita, N.; Notomi, T., Detection of loop-mediated isothermal amplification reaction by turbidity derived from magnesium pyrophosphate formation. Biochemical and Biophysical Research Communications 2001, 289 (1), 150-154.

127. Ignatov, K. B.; Barsova, E. V.; Fradkov, A. F.; Blagodatskikh, K. A.; Kramarova, T. V.; Kramarov, V. M., A strong strand displacement activity of thermostable DNA polymerase markedly improves the results of DNA amplification. Biotechniques 2014, 57 (2), 81-87.

128. Ririe, K. M.; Rasmussen, R. P.; Wittwer, C. T., Product differentiation by analysis of DNA melting curves during the polymerase chain reaction. Anal Biochem 1997, 245 (2), 154-160.

129. Owen, R. J.; Hill, L. R.; Lapage, S. P., DETERMINATION OF DNA BASE COMPOSITIONS FROM MELTING PROFILES IN DILUTE BUFFERS. Biopolymers 1969, 7 (4), 503-&.

130. Viet Loan Dao, T.; Herbst, K.; Boerner, K.; Meurer, M.; Kremer, L. P. M.; Kirrmaier, D.; Freistaedter, A.; Papagiannidis, D.; Galmozzi, C.; Stanifer, M. L.; Boulant, S.; Klein, S.; Chlanda, P.; Khalid, D.; Miranda, I. B.; Schnitzler, P.; Kraeusslich, H.-G.; Knop, M.; Anders, S., A colorimetric RT-LAMP assay and LAMP-sequencing for detecting SARS-CoV-2 RNA in clinical samples. Science Translational Medicine 2020, 12 (556).

131. Chow, F. W.-N.; Chan, T. T.-Y.; Tam, A. R.; Zhao, S.; Yao, W.; Fung, J.; Cheng, F. K.-K.; Lo, G. C.-S.; Chu, S.; Aw-Yong, K. L.; Tang, J. Y.-M.; Tsang, C.-C.; Luk, H. K.-H.; Wong, A. C.-P.; Li, K. S.-M.; Zhu, L.; He, Z.; Tam, E. W. T.; Chung, T. W.-H.; Wong, S. C. Y.; Que, T.-L.; Fung, K. S.-C.; Lung, D. C.; Wu, A. K.-L.; Hung, I. F.-N.; Woo, P. C.-Y.; Lau, S. K.-P., A Rapid, Simple, Inexpensive, and Mobile Colorimetric Assay COVID-19-LAMP for Mass On-Site Screening of COVID-19. Int. J. Mol. Sci. 2020, 21 (15).

132. Clune, T.; Anstey, S.; Kasimov, V.; Jacobson, C.; Jelocnik, M., Real-Time Fluorometric Isothermal LAMP Assay for Detection of Chlamydia pecorum in Rapidly Processed Ovine Abortion Samples: A Veterinary Practitioner's Perspective. Pathogens 2021, 10 (9).

133. Gibson, J., Loop-mediated isothermal amplification (LAMP) - a fast-growing technology with a wide range of applications [white paper]. New England Biolabs, Inc. 2020.

134. Schenkels, L.; Veerman, E. C. I.; Amerongen, A. V. N., BIOCHEMICAL-COMPOSITION OF HUMAN SALIVA IN RELATION TO OTHER MUCOSAL FLUIDS. Critical Reviews in Oral Biology and Medicine 1995, 6 (2), 161-175.

135. Humphrey, S. P.; Williamson, R. T., A review of saliva: Normal composition, flow, and function. Journal of Prosthetic Dentistry 2001, 85 (2), 162-169.

136. Iorgulescu, G., Saliva between normal and pathological. Important factors in determining systemic and oral health. Journal of medicine and life 2009, 2 (3), 303-7.

137. Oncescu, V.; O'Dell, D.; Erickson, D., Smartphone based health accessory for colorimetric detection of biomarkers in sweat and saliva. Lab on a Chip 2013, 13 (16), 3232-3238.

138. Michael, A.; Bajracharya, S. D.; Yuen, P. S. T.; Zhou, H.; Star, R. A.; Illei, G. G.; Alevizos, I., Exosomes from human saliva as a source of microRNA biomarkers. Oral Diseases 2010, 16 (1), 34-38.

139. Kinney, J. S.; Morelli, T.; Braun, T.; Ramseier, C. A.; Herr, A. E.; Sugai, J. V.; Shelburne, C. E.; Rayburn, L. A.; Singh, A. K.; Giannobile, W. V., Saliva/Pathogen Biomarker Signatures and Periodontal Disease Progression. Journal of Dental Research 2011, 90 (6), 752-758.

140. Jokerst, J. V.; Raamanathan, A.; Christodoulides, N.; Floriano, P. N.; Pollard, A. A.; Simmons, G. W.; Wong, J.; Gage, C.; Furmaga, W. B.; Redding, S. W.; McDevitt, J. T., Nano-bio-chips for high performance multiplexed protein detection: Determinations of cancer biomarkers in serum and saliva using quantum dot bioconjugate labels. Biosens Bioelectron 2009, 24 (12), 3622-3629.

141. Musso, D.; Roche, C.; Tu-Xuan, N.; Robin, E.; Teissier, A.; Cao-Lormeau, V.-M., Detection of Zika virus in saliva. Journal of Clinical Virology 2015, 68, 53-55.

142. Groopman, J. E.; Salahuddin, S. Z.; Sarngadharan, M. G.; Markham, P. D.; Gonda, M.; Sliski, A.; Gallo, R. C., HTLV-III IN SALIVA OF PEOPLE WITH AIDS-RELATED COMPLEX AND HEALTHY HOMOSEXUAL MEN AT RISK FOR AIDS. Science 1984, 226 (4673), 447-449.

143. Dubrulle, M.; Mousson, L.; Moutailler, S.; Vazeille, M.; Failloux, A.-B., Chikungunya Virus and Aedes Mosquitoes: Saliva Is Infectious as soon as Two Days after Oral Infection. Plos One 2009, 4 (6).

144. Wyllie, A. L.; Fournier, J.; Casanovas-Massana, A.; Campbell, M.; Tokuyama, M.; Vijayakumar, P.; Warren, J. L., Saliva or Nasopharyngeal Swab Specimens for Detection of SARS-CoV-2. New England Journal of Medicine 2020, 383 (13), 1283-1286.

145. To, K. K.-W.; Tsang, O. T.-Y.; Leung, W.-S.; Tam, A. R.; Wu, T.-C.; Lung, D. C.; Yip, C. C.-Y.; Cai, J.-P.; Chan, J. M.-C.; Chik, T. S.-H.; Lau, D. P.-L.; Choi, C. Y.-C.; Chen, L.-L.; Chan, W.-M.; Chan, K.-H.; Ip, J. D.; Ng, A. C.-K.; Poon, R. W.-S.; Luo, C.-T.; Cheng, V. C.-C.; Chan, J. F. W.; Hung, I. F.-N.; Chen, Z.; Chen, H.; Yuen, K.-Y., Temporal profiles of viral load in posterior oropharyngeal saliva samples and serum antibody responses during infection by SARS-CoV-2: an observational cohort study. Lancet Infectious Diseases 2020, 20 (5), 565-574.

146. Azzi, L.; Carcano, G.; Gianfagna, F.; Grossi, P.; Dalla Gasperina, D.; Genoni, A.; Fasano, M.; Sessa, F.; Tettamanti, L.; Carinci, F.; Maurino, V.; Rossi, A.; Tagliabue, A.; Baj, A., Saliva is a reliable tool to detect SARS-CoV-2. Journal of Infection 2020, 81 (1), E45-E50.

147. Pedrosa, M. d. S.; Sipert, C. R.; Nogueira, F. N., Salivary Glands, Saliva and Oral Findings in COVID-19 Infection. Pesquisa Brasileira Em Odontopediatria E Clinica Integrada 2020, 20.

148. Fini, M. B., Oral saliva and COVID-19. Oral Oncology 2020, 108.

149. Eichel, H. J.; Conger, N.; Chernick, W. S., ACID + ALKALINE RIBONUCLEASES OF HUMAN PAROTID SUBMAXILLARY + WHOLE SALIVA. Archives of Biochemistry and Biophysics 1964, 107 (2), 197-&.

150. Eichen Chemical Co., L. The principle of LAMP method.

151. Mugambi, R. M.; Agola, E. L.; Mwangi, I. N.; Kinyua, J.; Shiraho, E. A.; Mkoji, G. M., Development and evaluation of a Loop Mediated Isothermal Amplification (LAMP) technique for

the detection of hookworm (Necator americanus) infection in fecal samples. Parasites & Vectors 2015, 8.

152. Isayev, A. I.; Hieber, C. A., TOWARD A VISCOELASTIC MODELING OF THE INJECTION-MOLDING OF POLYMERS. Rheologica Acta 1980, 19 (2), 168-182.

153. Chang, R. Y.; Yang, W. H., Numerical simulation of mold filling in injection molding using a three-dimensional finite volume approach. International Journal for Numerical Methods in Fluids 2001, 37 (2), 125-148.

154. Kamal, M. R.; Kenig, S., INJECTION MOLDING OF THERMOPLASTICS .1. THEORETICAL MODEL. Polymer Engineering and Science 1972, 12 (4), 294-&.

155. Huang, M. C.; Tai, C. C., The effective factors in the warpage problem of an injection-molded part with a thin shell feature. Journal of Materials Processing Technology 2001, 110 (1), 1-9.

156. Ozcelik, B.; Erzurumlu, T., Comparison of the warpage optimization in the plastic injection molding using ANOVA, neural network model and genetic algorithm. Journal of Materials Processing Technology 2006, 171 (3), 437-445.

157. Fujiyama, M.; Wakino, T.; Kawasaki, Y., STRUCTURE OF SKIN LAYER IN INJECTION-MOLDED POLYPROPYLENE. Journal of Applied Polymer Science 1988, 35 (1), 29-49.

158. Chiang, H. H.; Hieber, C. A.; Wang, K. K., A UNIFIED SIMULATION OF THE FILLING AND POSTFILLING STAGES IN INJECTION-MOLDING .1. FORMULATION. Polymer Engineering and Science 1991, 31 (2), 116-124.

159. Tadmor, Z., MOLECULAR-ORIENTATION IN INJECTION MOLDING. Journal of Applied Polymer Science 1974, 18 (6), 1753-1772.

160. Lipshitz, S. D.; Lavie, R.; Tadmor, Z., MELTING MODEL FOR RECIPROCATING SCREW INJECTION-MOLDING MACHINES. Polymer Engineering and Science 1974, 14 (8), 553-559.

161. Donovan, R. C.; Thomas, D. E.; Leversen, L. D., EXPERIMENTAL STUDY OF PLASTICATING IN A RECIPROCATING-SCREW INJECTION MOLDING MACHINE. Polymer Engineering and Science 1971, 11 (5), 353-&.

162. Donovan, R. C., THEORETICAL MELTING MODEL FOR A RECIPROCATING-SCREW INJECTION MOLDING MACHINE. Polymer Engineering and Science 1971, 11 (5), 361-&.

163. Bi, C.; Jiang, B., Study of residence time distribution in a reciprocating single-screw pin-barrel extruder. Journal of Materials Processing Technology 2009, 209 (8), 4147-4153.

164. Xie, L.; Shen, L.; Jiang, B.-y. In Modelling and Simulation for Micro Injection Molding Process, 2011.

165. Chen, J. Y.; Liu, C. Y.; Huang, M. S., Enhancement of Injection Molding Consistency by Adjusting Velocity/Pressure Switching Time Based on Clamping Force. International Polymer Processing 2019, 34 (5), 564-572.

166. Pantani, R.; Coccorullo, I.; Speranza, V.; Titomanlio, G., Morphology evolution during injection molding: Effect of packing pressure. Polymer 2007, 48 (9), 2778-2790.

167. Kurt, M.; Kamber, O. S.; Kaynak, Y.; Atakok, G.; Girit, O., Experimental investigation of plastic injection molding: Assessment of the effects of cavity pressure and mold temperature on the quality of the final products. Mater Design 2009, 30 (8), 3217-3224.

168. Mavridis, H.; Hrymak, A. N.; Vlachopoulos, J., THE EFFECT OF FOUNTAIN FLOW ON MOLECULAR-ORIENTATION IN INJECTION-MOLDING. Journal of Rheology 1988, 32 (6), 639-663.

169. Mavridis, H.; Hrymak, A. N.; Vlachopoulos, J., FINITE-ELEMENT SIMULATION OF FOUNTAIN FLOW IN INJECTION-MOLDING. Polymer Engineering and Science 1986, 26 (7), 449-454.

170. Lafleur, P. G.; Kamal, M. R., A STRUCTURE-ORIENTATED COMPUTER-SIMULATION OF THE INJECTION-MOLDING OF VISCOELASTIC CRYSTALLINE POLYMERS .1. MODEL WITH FOUNTAIN FLOW, PACKING, SOLIDIFICATION. Polymer Engineering and Science 1986, 26 (1), 92-102.

171. Kamal, M. R.; Goyal, S. K.; Chu, E., SIMULATION OF INJECTION MOLD FILLING OF VISCOELASTIC POLYMER WITH FOUNTAIN FLOW. Aiche Journal 1988, 34 (1), 94-106.

172. Gogos, C. G.; Huang, C. F.; Schmidt, L. R., THE PROCESS OF CAVITY FILLING INCLUDING THE FOUNTAIN FLOW IN INJECTION-MOLDING. Polymer Engineering and Science 1986, 26 (20), 1457-1466.

173. Coyle, D. J.; Blake, J. W.; Macosko, C. W., THE KINEMATICS OF FOUNTAIN FLOW IN MOLD-FILLING. Aiche Journal 1987, 33 (7), 1168-1177.

174. Kamal, M. R.; Chu, E.; Lafleur, P. G.; Ryan, M. E., COMPUTER-SIMULATION OF INJECTION MOLD FILLING FOR VISCOELASTIC MELTS WITH FOUNTAIN FLOW. Polymer Engineering and Science 1986, 26 (3), 190-196.

175. Chang, Y. H.; Wei, T. H.; Chen, S. C.; Lou, Y. F., The investigation onPVTcontrol method establishment for scientific injection molding parameter setting and its quality control. Polymer Engineering and Science 2020, 60 (11), 2895-2907.

176. Chen, Z. B.; Giacomin, A. J.; Turng, L. S., Flash. Polymer Engineering and Science 2006, 46 (3), 241-247.

177. Weinstein, M.; Manoochehri, S., Optimum parting line design of molded and cast parts for manufacturability. Journal of Manufacturing Systems 1997, 16 (1), 1-12.

178. Schmidt, L. R., SPECIAL MOLD AND TRACER TECHNIQUE FOR STUDYING SHEAR AND EXTENSIONAL FLOWS IN A MOLD CAVITY DURING INJECTION MOLDING. Polymer Engineering and Science 1974, 14 (11), 797-800.

179. Zhou, Y.; Yu, F.; Deng, H.; Huang, Y.; Li, G.; Fu, Q., Morphology Evolution of Polymer Blends under Intense Shear During High Speed Thin-Wall Injection Molding. Journal of Physical Chemistry B 2017, 121 (25), 6257-6270.

180. Zhang, S. X.; Khayat, R. E., A low-dimensional description of transient shear-thinning free-surface flow in thin cavities, as applied to injection molding. International Journal for Numerical Methods in Fluids 2004, 44 (1), 91-114.

181. Li, Y.; Huang, B.; Qu, X., Viscosity and melt rheology of metal injection moulding feedstocks. Powder Metallurgy 1999, 42 (1), 86-90.

182. Koszkul, J.; Nabialek, J., Viscosity models in simulation of the filling stage of the injection molding process. Journal of Materials Processing Technology 2004, 157, 183-187.

183. Hieber, C. A.; Chiang, H. H., SHEAR-RATE-DEPENDENCE MODELING OF POLYMER MELT VISCOSITY. Polymer Engineering and Science 1992, 32 (14), 931-938.

184. Sorgato, M.; Babenko, M.; Lucchetta, G.; Whiteside, B., Investigation of the influence of vacuum venting on mould surface temperature in micro injection moulding. Int J Adv Manuf Tech 2017, 88 (1-4), 547-555.

185. Yao, D. G.; Kim, B., Development of rapid heating and cooling systems for injection molding applications. Polymer Engineering and Science 2002, 42 (12), 2471-2481.

186. Sachs, E.; Wylonis, E.; Allen, S.; Cima, M.; Guo, H. L., Production of injection molding tooling with conformal cooling channels using the three dimensional printing process. Polymer Engineering and Science 2000, 40 (5), 1232-1247.

187. Xu, X. R.; Sachs, E.; Allen, S., The design of conformal cooling channels in injection molding tooling. Polymer Engineering and Science 2001, 41 (7), 1265-1279.

188. Dimla, D. E.; Camilotto, M.; Miani, F., Design and optimisation of conformal cooling channels in injection moulding tools. Journal of Materials Processing Technology 2005, 164, 1294-1300.

189. Gnielinski, V., NEW EQUATIONS FOR HEAT AND MASS-TRANSFER IN TURBULENT PIPE AND CHANNEL FLOW. International Chemical Engineering 1976, 16 (2), 359-368.

190. Ahlers, G.; Grossmann, S.; Lohse, D., Heat transfer and large scale dynamics in turbulent Rayleigh-Benard convection. Rev. Mod. Phys. 2009, 81 (2), 503-537.

191. Shen, Y.-K.; Wu, C.-W.; Yu, Y.-F.; Chung, H.-W., Analysis for optimal gate design of thin-walled injection molding. International Communications in Heat and Mass Transfer 2008, 35 (6), 728-734.

192. Pandelidis, I.; Zou, Q., OPTIMIZATION OF INJECTION-MOLDING DESIGN .1. GATE LOCATION OPTIMIZATION. Polymer Engineering and Science 1990, 30 (15), 873-882.

193. Lee, B. H.; Kim, B. H., Automated selection of gate location based on desired quality of injection-molded part. Polymer-Plastics Technology and Engineering 1996, 35 (2), 253-269.

194. Kim, I. H.; Park, S. J.; Chung, S. T.; Kwon, T. H., Numerical modeling of injection/compression molding for center-gated disk: Part I. Injection molding with viscoelastic compressible fluid model. Polymer Engineering and Science 1999, 39 (10), 1930-1942.

195. Cabrera-Rios, M.; Zuyev, K. S.; Chen, X.; Castro, J. M.; Straus, E. J., Optimizing injection gate location and cycle time for the in-mold coating (IMC) process. Polymer Composites 2002, 23 (5), 723-738.

196. Lee, B. H.; Kim, B. H., OPTIMIZATION OF PART WALL THICKNESSES TO REDUCE WARPAGE OF INJECTION-MOLDED PARTS BASED ON THE MODIFIED COMPLEX METHOD. Polymer-Plastics Technology and Engineering 1995, 34 (5), 793-811.

197. Injection molding design guidelines. In Stratasys.

198. Wall Thickness Guide For Plastic Part Design. https://www.xcentricmold.com/how-wall-thickness-impacts-injection-mold-part-design/.

199. How to Improve Injection Molding Design With Uniform Wall Thickness.

200. Harris, R.; Hopkinson, N.; Newlyn, H.; Hague, R.; Dickens, P., Layer thickness and draft angle selection for stereolithography injection mould tooling. International Journal of Production Research 2002, 40 (3), 719-729.

201. Draft Angle Guidelines for Injection Molding. https://www.protolabs.com/resources/design-tips/improving-part-moldability-with-draft/.

202. Draft Angles in Injection Molded Plastics. https://www.natechplastics.com/draft_angles/.

203. Ho, K. H.; Newman, S. T., State of the art electrical discharge machining (EDM). International Journal of Machine Tools & Manufacture 2003, 43 (13), 1287-1300.

204. Abbas, N. M.; Solomon, D. G.; Bahari, M. F., A review on current research trends in electrical discharge machining (EDM). International Journal of Machine Tools & Manufacture 2007, 47 (7-8), 1214-1228.

205. Lin, J. L.; Lin, C. L., The use of the orthogonal array with grey relational analysis to optimize the electrical discharge machining process with multiple performance characteristics. International Journal of Machine Tools & Manufacture 2002, 42 (2), 237-244.

206. Ho, K. H.; Newman, S. T.; Rahimifard, S.; Allen, R. D., State of the art in wire electrical discharge machining (WEDM). International Journal of Machine Tools & Manufacture 2004, 44 (12-13), 1247-1259.

207. Dibitonto, D. D.; Eubank, P. T.; Patel, M. R.; Barrufet, M. A., THEORETICAL-MODELS OF THE ELECTRICAL-DISCHARGE MACHINING PROCESS .1. A SIMPLE CATHODE EROSION MODEL. J Appl Phys 1989, 66 (9), 4095-4103.

208. Boothroyd, G., PRODUCT DESIGN FOR MANUFACTURE AND ASSEMBLY. Computer-Aided Design 1994, 26 (7), 505-520.

209. Daoud, M.; Lyle, S. N.; Williams, C. E., Soft Matter Physics. Springer Berlin Heidelberg: 2013.

210. Chaikin, P. M.; Lubensky, T. C., Principles of Condensed Matter Physics. Cambridge University Press: 2000.

211. Rubinstein, M. C., Ralph Polymer Physics. Oxford University Press: 2003.

212. Kokubo, T.; Kim, H. M.; Kawashita, M., Novel bioactive materials with different mechanical properties. Biomaterials 2003, 24 (13), 2161-2175.

213. Marchetti, M. C.; Joanny, J. F.; Ramaswamy, S.; Liverpool, T. B.; Prost, J.; Rao, M.; Simha, R. A., Hydrodynamics of soft active matter. Rev. Mod. Phys. 2013, 85 (3), 47.

214. Mezzenga, R.; Schurtenberger, P.; Burbidge, A.; Michel, M., Understanding foods as soft materials. Nature Materials 2005, 4 (10), 729-740.

215. Donald, A., Food for thought. Nature Materials 2004, 3 (9), 579-581.

216. Fung, Y. C., Biomechanics: Mechanical Properties of Living Tissues. Springer New York: 2013.

217. Lu, P. J.; Weitz, D. A., Colloidal Particles: Crystals, Glasses, and Gels. Annual Review of Condensed Matter Physics 2013, 4 (1), 217-233.

218. Vlassopoulos, D.; Cloitre, M., Tunable rheology of dense soft deformable colloids. Current Opinion in Colloid & Interface Science 2014, 19 (6), 561-574.

219. Adamczyk, Z.; Warszynski, P., Role of electrostatic interactions in particle adsorption. Advances in Colloid and Interface Science 1996, 63, 41-149.

220. Wilking, J. N.; Angelini, T. E.; Seminara, A.; Brenner, M. P.; Weitz, D. A., Biofilms as complex fluids. MRS Bull. 2011, 36 (5), 385-391.

221. Larson, R. G., The Structure and Rheology of Complex Fluids. OUP USA: 1999.

222. Erhart-Hledik, J. C.; Chehab, E. F.; Asay, J. L.; Favre, J.; Chu, C. R.; Andriacchi, T. P., Longitudinal changes in tibial and femoral cartilage thickness are associated with baseline ambulatory kinetics and cartilage oligomeric matrix protein (COMP) measures in an asymptomatic aging population. Osteoarthritis and cartilage 2021.

223. Zignego, D. L.; Hilmer, J. K.; June, R. K., Mechanotransduction in primary human osteoarthritic chondrocytes is mediated by metabolism of energy, lipids, and amino acids. Journal of biomechanics 2015, 48 (16), 4253-61.

224. Mason, T. G.; Weitz, D. A., Linear Viscoelasticity of Colloidal Hard Sphere Suspensions near the Glass Transition. Physical Review Letters 1995, 75 (14), 2770-2773.

225. Leite, F. L.; Bueno, C. C.; Da Roz, A. L.; Ziemath, E. C.; Oliveira, O. N., Theoretical Models for Surface Forces and Adhesion and Their Measurement Using Atomic Force Microscopy. Int. J. Mol. Sci. 2012, 13 (10), 12773-12856.

226. Meyers, M. A.; Chen, P. Y.; Lin, A. Y. M.; Seki, Y., Biological materials: Structure and mechanical properties. Progress in Materials Science 2008, 53 (1), 1-206.

227. Yang, D.; Ward, A.; Halvorsen, K.; Wong, W. P., Multiplexed single-molecule force spectroscopy using a centrifuge. Nat Commun 2016, 7, 11026.

228. Parthasarathy, R., Rapid, accurate particle tracking by calculation of radial symmetry centers. Nat. Methods 2012, 9 (7), 724-U291.

229. Behrens, S. H.; Grier, D. G., The charge of glass and silica surfaces. J. Chem. Phys. 2001, 115 (14), 6716-6721.

230. Folkersma, R.; van Diemen, A. J. G.; Stein, H. N., Electrophoretic properties of polystyrene spheres. Langmuir 1998, 14 (21), 5973-5976.

231. Ohsawa, K. M., M.; and Ohshima, H., Zeta potential and surface charge density of polystyrene-latex; comparison with synaptic vesicle and brush border membrane vesicle. Colloid & Polymer Science 1986, 264, 1005-1009.

232. Garg, A.; Cartier, C. A.; Bishop, K. J. M.; Velegol, D., Particle Zeta Potentials Remain Finite in Saturated Salt Solutions. Langmuir 2016, 32 (45), 11837-11844.

233. Adamczyk, Z.; Bratek-Skicki, A.; Dabrowska, P.; Nattich-Rak, M., Mechanisms of Fibrinogen Adsorption on Latex Particles Determined by Zeta Potential and AFM Measurements. Langmuir 2012, 28 (1), 474-485.

234. Yan, E. C. Y.; Liu, Y.; Eisenthal, K. B., New method for determination of surface potential of microscopic particles by second harmonic generation. Journal of Physical Chemistry B 1998, 102 (33), 6331-6336.

235. El-Gholabzouri, O.; Cabrerizo, M. A.; Hidalgo-Alvarez, R., The surface charge density influence on the electrokinetic properties of model colloids: Solvent composition effect. Journal of Colloid and Interface Science 1999, 214 (2), 243-250.

236. Tabata, Y.; Ikada, Y., Effect of the size and surface-charge of polymer microspheres on their phagocytosis by macrophage. Biomaterials 1988, 9 (4), 356-362.

237. Brouwer, W. M.; Zsom, R. L. J., Polystyrene latex particle surface characteristics. Colloids and Surfaces 1987, 24 (2-3), 195-208.

238. Luthi, Y.; Ricka, J.; Borkovec, M., Colloidal particles at water-glass interface: Deposition kinetics and surface heterogeneity. Journal of Colloid and Interface Science 1998, 206 (1), 314-321.

239. Schrader, A. M.; Monroe, J. I.; Sheil, R.; Dobbs, H. A.; Keller, T. J.; Li, Y. X.; Jain, S.; Shell, M. S.; Israelachvili, J. N.; Han, S. G., Surface chemical heterogeneity modulates silica surface hydration. PNAS 2018, 115 (12), 2890-2895.

240. Cras, J. J.; Rowe-Taitt, C. A.; Nivens, D. A.; Ligler, F. S., Comparison of chemical cleaning methods of glass in preparation for silanization. Biosens Bioelectron 1999, 14 (8-9), 683-688.

241. Warszynski, P. a. A., Z, Calculations of Double-Layer Electrostatic Interactions for the Sphere/Plane Geometry. J Colloid and Interface Sci 1996, 1878, 283-295.

242. Pashley, R. M.; McGuiggan, P. M.; Ninham, B. W.; Evans, D. F., Attractive forces between uncharged hydrophobic surfaces - direct measurements in aqueous-solution. Science 1985, 229 (4718), 1088-1089.

243. Rabinovich, Y. I.; Adler, J. J.; Ata, A.; Singh, R. K.; Moudgil, B. M., Adhesion between nanoscale rough surfaces - I. Role of asperity geometry. Journal of Colloid and Interface Science 2000, 232 (1), 10-16.

244. Cooper, K.; Ohler, N.; Gupta, A.; Beaudoin, S., Analysis of contact interactions between a rough deformable colloid and a smooth substrate. Journal of Colloid and Interface Science 2000, 222 (1), 63-74.

245. Cooper, K.; Gupta, A.; Beaudoin, S., Substrate morphology and particle adhesion in reacting systems. Journal of Colloid and Interface Science 2000, 228 (2), 213-219.

246. Wu, L.; Feng, H.; Guo, D.; Zheng, B., Measuring the adhesion strength of a thin film to a substrate by centrifugation. RSC Adv. 2014, 4 (104), 60002-60006.

247. Israelachvilli, J., Intermolecular & Surface Forces. 1985.

248. Gregory, J., Approximate expressions for retarded vanderwaals interaction. Journal of Colloid and Interface Science 1981, 83 (1), 138-145.

249. Bevan, M. A. a. P., D. C., Direct Measurement of Retarded van der Waals Attraction. Langmuir 1999, 15, 7925-7936.

250. Tsaur, S. L.; Fitch, R. M., Preparation and properties of polystyrene model colloids .1. Preparation of surface-active monomer and model colloids derived therefrom. Journal of Colloid and Interface Science 1987, 115 (2), 450-462.

251. Lyklema, J.; Overbeek, J. T., On interpretation of electrokinetic potentials. Journal of Colloid Science 1961, 16 (5), 501-&.

252. Rimsza, J. M.; Jones, R. E.; Criscenti, L. J., Interaction of NaOH solutions with silica surfaces. Journal of Colloid and Interface Science 2018, 516, 128-137.

253. Elassy, K. S.; Rahman, M. A.; Yama, N. S.; Shiroma, W. A.; Ohta, A. T., Complex Permittivity of NaOH Solutions Used in Liquid-Metal Circuits. IEEE Access 2019, 7, 150150-150156.

254. Gu, Y. G.; Li, D. Q., The zeta-potential of glass surface in contact with aqueous solutions. Journal of Colloid and Interface Science 2000, 226 (2), 328-339.

255. Kirby, B. J.; Hasselbrink, E. F., Zeta potential of microfluidic substrates: 1. Theory, experimental techniques, and effects on separations. Electrophoresis 2004, 25 (2), 187-202.

256. Erickson, D.; Li, D. Q.; Werner, C., An improved method of determining the zeta-potential and surface conductance. Journal of Colloid and Interface Science 2000, 232 (1), 186-197.

257. Rabinovich, Y. I.; Adler, J. J.; Ata, A.; Singh, R. K.; Moudgil, B. M., Adhesion between nanoscale rough surfaces - II. Measurement and comparison with theory. Journal of Colloid and Interface Science 2000, 232 (1), 17-24.

258. Munster, V. J.; Koopmans, M.; van Doremalen, N.; van Riel, D.; de Wit, E., A novel coronavirus emerging in China — Key questions for impact assessment. New England Journal of Medicine 2020, 382 (8), 692-694.

259. Mina, M. J.; Andersen, K. G., COVID-19 testing: One size does not fit all. 2021, 371 (6525), 126-127.

260. Jain, K. K., Nanotechnology in clinical laboratory diagnostics. Clin Chim Acta 2005, 358 (1-2), 37-54.

261. Janda, J. M.; Abbott, S. L., 16S rRNA gene sequencing for bacterial identification in the diagnostic laboratory: Pluses, perils, and pitfalls. Journal of Clinical Microbiology 2007, 45 (9), 2761-2764.

262. Gao, Y.; Li, T.; Han, M.; Li, X.; Wu, D.; Xu, Y.; Zhu, Y.; Liu, Y.; Wang, X.; Wang, L., Diagnostic utility of clinical laboratory data determinations for patients with the severe COVID-19. Journal of Medical Virology 2020, 92 (7), 791-796.

263. Chiappin, S.; Antonelli, G.; Gatti, R.; De Palo, E. F., Saliva specimen: A new laboratory tool for diagnostic and basic investigation. Clin Chim Acta 2007, 383 (1-2), 30-40.

264. Yager, P.; Domingo, G. J.; Gerdes, J., Point-of-care diagnostics for global health. Annual Review of Biomedical Engineering 2008, 10, 107-144.

265. Hu, J.; Wang, S.; Wang, L.; Li, F.; Pingguan-Murphy, B.; Lu, T. J.; Xu, F., Advances in paper-based point-of-care diagnostics. Biosens Bioelectron 2014, 54, 585-597.

266. Gubala, V.; Harris, L. F.; Ricco, A. J.; Tan, M. X.; Williams, D. E., Point of Care Diagnostics: Status and Future. Analytical Chemistry 2012, 84 (2), 487-515.

267. Craw, P.; Balachandran, W., Isothermal nucleic acid amplification technologies for point-of-care diagnostics: a critical review. Lab on a Chip 2012, 12 (14), 2469-2486.

268. Chin, C. D.; Linder, V.; Sia, S. K., Commercialization of microfluidic point-of-care diagnostic devices. Lab on a Chip 2012, 12 (12), 2118-2134.

269. Ahn, C. H.; Choi, J. W.; Beaucage, G.; Nevin, J. H.; Lee, J. B.; Puntambekar, A.; Lee, J. Y., Disposable Smart lab on a chip for point-of-care clinical diagnostics. Proceedings of the Ieee 2004, 92 (1), 154-173.

270. Yetisen, A. K.; Akram, M. S.; Lowe, C. R., Paper-based microfluidic point-of-care diagnostic devices. Lab on a Chip 2013, 13 (12), 2210-2251.

271. Wang, J., Electrochemical biosensors: Towards point-of-care cancer diagnostics. Biosens Bioelectron 2006, 21 (10), 1887-1892.

272. Yang, S.; Rothman, R. E., PCR-based diagnostics for infectious diseases: uses, limitations, and future applications in acute-care settings. Lancet Infectious Diseases 2004, 4 (6), 337-348.

273. Reed, G. H.; Kent, J. O.; Wittwer, C. T., High-resolution DNA melting analysis for simple and efficient molecular diagnostics. Pharmacogenomics 2007, 8 (6), 597-608.

274. Huggett, J. F.; Cowen, S.; Foy, C. A., Considerations for Digital PCR as an Accurate Molecular Diagnostic Tool. Clinical Chemistry 2015, 61 (1), 79-88.

275. Elnifro, E. M.; Ashshi, A. M.; Cooper, R. J.; Klapper, P. E., Multiplex PCR: Optimization and application in diagnostic virology. Clin Microbiol Rev 2000, 13 (4), 559-+.

276. Porte, L.; Legarraga, P.; Vollrath, V.; Aguilera, X.; Munita, J. M.; Araos, R.; Pizarro, G.; Vial, P.; Iruretagoyena, M.; Dittrich, S.; Weitzel, T., Evaluation of a novel antigen-based rapid detection test for the diagnosis of SARS-CoV-2 in respiratory samples. International Journal of Infectious Diseases 2020, 99, 328-333.

277. Mak, G. C. K.; Cheng, P. K. C.; Lau, S. S. Y.; Wong, K. K. Y.; Lau, C. S.; Lam, E. T. K.; Chan, R. C. W.; Tsang, D. N. C., Evaluation of rapid antigen test for detection of SARS-CoV-2 virus. Journal of Clinical Virology 2020, 129.

278. Hirotsu, Y.; Maejima, M.; Shibusawa, M.; Nagakubo, Y.; Hosaka, K.; Amemiya, K.; Sueki, H.; Hayakawa, M.; Mochizuki, H.; Tsutsui, T.; Kakizaki, Y.; Miyashita, Y.; Yagi, S.; Kojima, S.; Omata, M., Comparison of automated SARS-CoV-2 antigen test for COVID-19 infection with quantitative RT-PCR using 313 nasopharyngeal swabs, including from seven serially followed patients. International Journal of Infectious Diseases 2020, 99, 397-402.

279. Dinnes, J.; Deeks, J. J.; Adriano, A.; Berhane, S.; Davenport, C.; Dittrich, S.; Emperador, D.; Takwoingi, Y.; Cunningham, J.; Beese, S.; Dretzke, J.; di Ruffano, L. F.; Harris, I. M.; Price, M. J.; Taylor-Phillips, S.; Hooft, L.; Leeflang, M. M. G.; Spijker, R.; Van den Bruel, A.; Cochrane, C.-D. T. A., Rapid, point-of-care antigen and molecular-based tests for diagnosis of SARS-CoV-2 infection (Review). Cochrane Database of Systematic Reviews 2020, (8).

280. Mackay, I. M., Real-time PCR in the microbiology laboratory. Clinical Microbiology and Infection 2004, 10 (3), 190-212.

281. Johnston, S. P.; Pieniazek, N. J.; Xayavong, M. V.; Slemenda, S. B.; Wilkins, P. P.; da Silva, A. J., PCR as a confirmatory technique for laboratory diagnosis of malaria. Journal of Clinical Microbiology 2006, 44 (3), 1087-1089.

282. Geha, D. J.; Uhl, J. R.; Gustaferro, C. A.; Persing, D. H., MULTIPLEX PCR FOR IDENTIFICATION OF METHICILLIN-RESISTANT STAPHYLOCOCCI IN THE CLINICAL LABORATORY. Journal of Clinical Microbiology 1994, 32 (7), 1768-1772.

283. Espy, M. J.; Uhl, J. R.; Sloan, L. M.; Buckwalter, S. P.; Jones, M. F.; Vetter, E. A.; Yao, J. D. C.; Wengenack, N. L.; Rosenblatt, J. E.; Cockerill, F. R.; Smith, T. F., Real-time PCR in clinical microbiology: Applications for a routine laboratory testing. Clin Microbiol Rev 2006, 19 (1), 165-+.

284. Petralia, S.; Conoci, S., PCR Technologies for Point of Care Testing: Progress and Perspectives. Acs Sensors 2017, 2 (7), 876-891.

285. Park, S.; Zhang, Y.; Lin, S.; Wang, T.-H.; Yang, S., Advances in microfluidic PCR for point-of-care infectious disease diagnostics. Biotechnol Adv 2011, 29 (6), 830-839.

286. Lee, S. H.; Kim, S.-W.; Kang, J. Y.; Ahn, C. H., A polymer lab-on-a-chip for reverse transcription (RT)-PCR based point-of-care clinical diagnostics. Lab on a Chip 2008, 8 (12), 2121-2127.

287. Tomita, N.; Mori, Y.; Kanda, H.; Notomi, T., Loop-mediated isothermal amplification (LAMP) of gene sequences and simple visual detection of products. Nature Protocols 2008, 3 (5), 877-882.

288. Nagamine, K.; Hase, T.; Notomi, T., Accelerated reaction by loop-mediated isothermal amplification using loop primers. Molecular and Cellular Probes 2002, 16 (3), 223-229.

289. Cutting Corners on Injection-Molded Parts. https://www.protolabs.com/resources/design-tips/cutting-corners-on-injection-molded-parts/.

290. What's the Average Hand Size for Men, Women, and Children? https://www.healthline.com/health/average-hand-size#adults.

291. Mahinroosta, M.; Farsangi, Z. J.; Allahverdi, A.; Shakoori, Z., Hydrogels as intelligent materials: A brief review of synthesis, properties and applications. Mater Today Chem 2018, 8, 42-55.

292. Li, H. J.; Tan, C.; Li, L., Review of 3D printable hydrogels and constructs. Mater Design 2018, 159, 20-38.

293. Ahmed, E. M., Hydrogel: Preparation, characterization, and applications: A review. J Adv Res 2015, 6 (2), 105-121.

294. Saroia, J.; Wang, Y. E.; Wei, Q. H.; Zhang, K.; Lu, T. L.; Zhang, B., A review on biocompatibility nature of hydrogels with 3D printing techniques, tissue engineering application and its future prospective. Bio-Des Manuf 2018, 1 (4), 265-279.

295. Rosiak, J. M.; Yoshii, F., Hydrogels and their medical applications. Nucl Instrum Meth B 1999, 151 (1-4), 56-64.

296. Saul, J. M.; Williams, D. F., Hydrogels in Regenerative Medicine. Pdl Handb Ser 2014, 279-302.

297. Calo, E.; Khutoryanskiy, V. V., Biomedical applications of hydrogels: A review of patents and commercial products. Eur Polym J 2015, 65, 252-267.

298. Chai, Q. Y.; Jiao, Y.; Yu, X. J., Hydrogels for Biomedical Applications: Their Characteristics and the Mechanisms behind Them. Gels-Basel 2017, 3 (1).

299. Sidar, B.; Jenkins, B. R.; Huang, S.; Spence, J. R.; Walk, S. T.; Wilking, J. N., Long-term flow through human intestinal organoids with the gut organoid flow chip (GOFlowChip). Lab on a Chip 2019, 19 (20), 3552-3562.

300. Chueh, B. H.; Zheng, Y.; Torisawa, Y. S.; Hsiao, A. Y.; Ge, C. X.; Hsiong, S.; Huebsch, N.; Franceschi, R.; Mooney, D. J.; Takayama, S., Patterning alginate hydrogels using light-directed release of caged calcium in a microfluidic device. Biomedical Microdevices 2010, 12 (1), 145-151.

301. Grigoryan, B.; Paulsen, S. J.; Corbett, D. C.; Sazer, D. W.; Fortin, C. L.; Zaita, A. J.; Greenfield, P. T.; Calafat, N. J.; Gounley, J. P.; Ta, A. H.; Johansson, F.; Randles, A.; Rosenkrantz, J. E.; Louis-Rosenberg, J. D.; Galie, P. A.; Stevens, K. R.; Miller, J. S., BIOMEDICINE Multivascular networks and functional intravascular topologies within biocompatible hydrogels. Science 2019, 364 (6439), 458-+.

302. Goy, C. B.; Chaile, R. E.; Madrid, R. E., Microfluidics and hydrogel: A powerful combination. React Funct Polym 2019, 145.

303. Zhou, Y. F., The recent development and applications of fluidic channels by 3D printing. J Biomed Sci 2017, 24.

304. Koo, H. J.; Velev, O. D., Design and characterization of hydrogel-based microfluidic devices with biomimetic solute transport networks. Biomicrofluidics 2017, 11 (2).

305. Xia, C. G.; Fang, N. X., 3D microfabricated bioreactor with capillaries. Biomedical Microdevices 2009, 11 (6), 1309-1315.

306. Dhariwala, B.; Hunt, E.; Boland, T., Rapid prototyping of tissue-engineering constructs, using photopolymerizable hydrogels and stereolithography. Tissue Eng 2004, 10 (9-10), 1316-1322.

307. Spicer, C. D., Hydrogel scaffolds for tissue engineering: the importance of polymer choice. Polym Chem-Uk 2020, 11 (2), 184-219.

308. Schaffner, M.; Ruhs, P. A.; Coulter, F.; Kilcher, S.; Studart, A. R., 3D printing of bacteria into functional complex materials. Sci Adv 2017, 3 (12).

309. Ogawa, M.; Higashi, K.; Miki, N., Microbial Production inside Microfabricated Hydrogel Microtubes. 2015 Transducers - 2015 18th International Conference on Solid-State Sensors, Actuators and Microsystems (Transducers) 2015, 1692-1694.

310. Bertassoni, L. E.; Cecconi, M.; Manoharan, V.; Nikkhah, M.; Hjortnaes, J.; Cristino, A. L.; Barabaschi, G.; Demarchi, D.; Dokmeci, M. R.; Yang, Y. Z.; Khademhosseini, A., Hydrogel bioprinted microchannel networks for vascularization of tissue engineering constructs. Lab on a Chip 2014, 14 (13), 2202-2211.

311. Sooppan, R.; Paulsen, S. J.; Han, J.; Ta, A. H.; Dinh, P.; Gaffey, A. C.; Venkataraman, C.; Trubelja, A.; Hung, G.; Miller, J. S.; Atluri, P., In Vivo Anastomosis and Perfusion of a Three-Dimensionally-Printed Construct Containing Microchannel Networks. Tissue Eng Part C Methods 2016, 22 (1), 1-7.

312. Kinstlinger, I. S.; Miller, J. S., 3D-printed fluidic networks as vasculature for engineered tissue. Lab Chip 2016, 16 (11), 2025-43.

313. Miller, J. S.; Stevens, K. R.; Yang, M. T.; Baker, B. M.; Nguyen, D. H. T.; Cohen, D. M.; Toro, E.; Chen, A. A.; Galie, P. A.; Yu, X.; Chaturvedi, R.; Bhatia, S. N.; Chen, C. S., Rapid casting of patterned vascular networks for perfusable engineered three-dimensional tissues. Nature Materials 2012, 11 (9), 768-774.

314. Nie, J.; Fu, J. Z.; He, Y., Hydrogels: The Next Generation Body Materials for Microfluidic Chips? Small 2020, 16 (46).

315. Wong, A. P.; Perez-Castillejos, R.; Love, J. C.; Whitesides, G. M., Partitioning microfluidic channels with hydrogel to construct tunable 3-D cellular microenvironments. Biomaterials 2008, 29 (12), 1853-1861.

316. Christensen, A. M.; Chang-Yen, D. A.; Gale, B. K., Characterization of interconnects used in PDMS microfluidic systems. J Micromech Microeng 2005, 15 (5), 928-934.

317. Chang, W. J.; Akin, D.; Sedlak, M.; Ladisch, M. R.; Bashir, R., Poly(dimethylsiloxane) (PDMS) and silicon hybrid biochip for bacterial culture. Biomedical Microdevices 2003, 5 (4), 281-290.

318. Faley, S. L.; Baer, B. B.; Larsen, T. S. H.; Bellan, L. M., Robust fluidic connections to freestanding microfluidic hydrogels. Biomicrofluidics 2015, 9 (3).

319. Patel, J. N.; Kaminska, B.; Gray, B. L.; Gates, B. D., PDMS as a sacrificial substrate for SU-8-based biomedical and microfluidic applications. J Micromech Microeng 2008, 18 (9).

320. Ravetz, J. R., The Rational Mechanics of Flexible or Elastic Bodies - Truesdell,C. Isis 1962, 53 (172), 263-266.

321. Yanez-Soto, B.; Liliensiek, S. J.; Murphy, C. J.; Nealey, P. F., Biochemically and topographically engineered poly(ethylene glycol) diacrylate hydrogels with biomimetic characteristics as substrates for human corneal epithelial cells. Journal of Biomedical Materials Research Part A 2013, 101 (4), 1184-1194.

322. Seymour, R. S.; Blaylock, A. J., The principle of laplace and scaling of ventricular wall stress and blood pressure in mammals and birds. Physiol Biochem Zool 2000, 73 (4), 389-405.

323. Bhargava, K. C.; Thompson, B.; Malmstadt, N., Discrete elements for 3D microfluidics. P Natl Acad Sci USA 2014, 111 (42), 15013-15018.

324. Loskill, P.; Marcus, S. G.; Mathur, A.; Reese, W. M.; Healy, K. E., mu Organo: A Lego (R)-Like Plug & Play System for Modular Multi-Organ-Chips. Plos One 2015, 10 (10).

325. Ong, L. J. Y.; Ching, T.; Chong, L. H.; Arora, S.; Li, H.; Hashimoto, M.; DasGupta, R.; Yuen, P. K.; Toh, Y. C., Self-aligning Tetris-Like (TILE) modular microfluidic platform for mimicking multi-organ interactions. Lab on a Chip 2019, 19 (13), 2178-2191.

326. Miserendino, S.; Tai, Y. C., Modular microfluidic interconnects using photodefinable silicone microgaskets and MEMS O-rings. Sensor Actuat a-Phys 2008, 143 (1), 7-13.

327. Justin, A. W.; Brooks, R. A.; Markaki, A. E., Multi-casting approach for vascular networks in cellularized hydrogels. J R Soc Interface 2016, 13 (125).

328. Golden, A. P.; Tien, J., Fabrication of microfluidic hydrogels using molded gelatin as a sacrificial element. Lab on a Chip 2007, 7 (6), 720-725.

329. Nie, J.; Gao, Q.; Wang, Y. D.; Zeng, J. H.; Zhao, H. M.; Sun, Y.; Shen, J.; Ramezani, H.; Fu, Z. L.; Liu, Z. J.; Xiang, M. X.; Fu, J. Z.; Zhao, P.; Chen, W.; He, Y., Vessel-on-a-chip with Hydrogel-based Microfluidics. Small 2018, 14 (45).

330. LaFratta, C. N.; Li, L. J., Making Two-Photon Polymerization Faster. Micro Nano Technol 2016, 221-241.

331. LaFratta, C. N.; Baldacchini, T.; Farrer, R. A.; Fourkas, J. T.; Teich, M. C.; Saleh, B. E. A.; Naughton, M. J., Replication of two-photon-polymerized structures with extremely high aspect ratios and large overhangs. Journal of Physical Chemistry B 2004, 108 (31), 11256-11258.

332. Markert, C. D.; Guo, X. Y.; Skardal, A.; Wang, Z.; Bharadwaj, S.; Zhang, Y. Y.; Bonin, K.; Guthold, M., Characterizing the micro-scale elastic modulus of hydrogels for use in regenerative medicine. J Mech Behav Biomed 2013, 27, 115-127.

333. Fairbanks, B. D.; Schwartz, M. P.; Bowman, C. N.; Anseth, K. S., Photoinitiated polymerization of PEG-diacrylate with lithium phenyl-2,4,6-trimethylbenzoylphosphinate: polymerization rate and cytocompatibility. Biomaterials 2009, 30 (35), 6702-6707.

334. Della Sala, F.; Biondi, M.; Guarnieri, D.; Borzacchiello, A.; Ambrosio, L.; Mayol, L., Mechanical behavior of bioactive poly(ethylene glycol) diacrylate matrices for biomedical application. J Mech Behav Biomed 2020, 110.

335. Xu, C. C.; Dai, G. H.; Hong, Y., Recent advances in high-strength and elastic hydrogels for 3D printing in biomedical applications. Acta Biomaterialia 2019, 95, 50-59.

336. Ahearne, M.; Yang, Y.; El Haj, A. J.; Then, K. Y.; Liu, K. K., Characterizing the viscoelastic properties of thin hydrogel-based constructs for tissue engineering applications. J R Soc Interface 2005, 2 (5), 455-463.

337. Sun, M. Y.; Sun, X. T.; Wang, Z. Y.; Guo, S. Y.; Yu, G. J.; Yang, H. Z., Synthesis and Properties of Gelatin Methacryloyl (GelMA) Hydrogels and Their Recent Applications in Load-Bearing Tissue. Polymers-Basel 2018, 10 (11).

338. Stammen, J. A.; Williams, S.; Ku, D. N.; Guldberg, R. E., Mechanical properties of a novel PVA hydrogel in shear and unconfined compression. Biomaterials 2001, 22 (8), 799-806.

339. Raman, R.; Bhaduri, B.; Mir, M.; Shkumatov, A.; Lee, M. K.; Popescu, G.; Kong, H.; Bashir, R., High-Resolution Projection Microstereolithography for Patterning of Neovasculature. Adv Healthc Mater 2016, 5 (5), 610-9.

340. Jacobs, P. F., Rapid Prototyping & Manufacturing: Fundamentals of StereoLithography. 1992.

341. Drury, J. L.; Mooney, D. J., Hydrogels for tissue engineering: scaffold design variables and applications. Biomaterials 2003, 24 (24), 4337-4351.

342. Peppas, N. A.; Bures, P.; Leobandung, W.; Ichikawa, H., Hydrogels in pharmaceutical formulations. European Journal of Pharmaceutics and Biopharmaceutics 2000, 50 (1), 27-46.

343. Qiu, Y.; Park, K., Environment-sensitive hydrogels for drug delivery. Adv Drug Deliver Rev 2001, 53 (3), 321-339.

344. Zhu, J. M., Bioactive modification of poly(ethylene glycol) hydrogels for tissue engineering. Biomaterials 2010, 31 (17), 4639-4656.

345. Bowman, C. N.; Kloxin, C. J., Toward an enhanced understanding and implementation of photopolymerization reactions. AIChE Journal 2008, 54 (11), 2775-2795.

346. Zhu, W.; Li, J.; Leong, Y. J.; Rozen, I.; Qu, X.; Dong, R.; Wu, Z.; Gao, W.; Chung, P. H.; Wang, J.; Chen, S., 3D-Printed Artificial Microfish. Adv Mater 2015.

347. Slaughter, B. V.; Khurshid, S. S.; Fisher, O. Z.; Khademhosseini, A.; Peppas, N. A., Hydrogels in regenerative medicine. Adv Mater 2009, 21 (32-33), 3307-29.

348. Bae, M.; Divan, R.; Suthar, K. J.; Mancini, D. C.; Gemeinhart, R. A., Fabrication of Poly(ethylene glycol) Hydrogel Structures for Pharmaceutical Applications using Electron beam and Optical Lithography. J Vac Sci Technol B Microelectron Nanometer Struct Process Meas Phenom 2010, 28 (6), C6P24-C6P29.

349. Qu, X.; Gou, M.; Zaidan, J.; Zhang, K.; Chen, S., Challenges and opportunities in developing nanoparticles for detoxification. Nanomedicine (Lond) 2014, 9 (16), 2437-2439.

350. Waheed, S.; Cabot, J. M.; Macdonald, N. P.; Lewis, T.; Guijt, R. M.; Paull, B.; Breadmore, M. C., 3D printed microfluidic devices: enablers and barriers. Lab Chip 2016, 16 (11), 1993-2013.

351. Floren, M.; Migliaresi, C.; Motta, A., Processing Techniques and Applications of Silk Hydrogels in Bioengineering. J Funct Biomater 2016, 7 (3).

352. Billiet, T.; Vandenhaute, M.; Schelfhout, J.; Van Vlierberghe, S.; Dubruel, P., A review of trends and limitations in hydrogel-rapid prototyping for tissue engineering. Biomaterials 2012, 33 (26), 6020-41.

353. Ma, X.; Qu, X.; Zhu, W.; Li, Y. S.; Yuan, S.; Zhang, H.; Liu, J.; Wang, P.; Lai, C. S.; Zanella, F.; Feng, G. S.; Sheikh, F.; Chien, S.; Chen, S., Deterministically patterned biomimetic human iPSC-derived hepatic model via rapid 3D bioprinting. Proc Natl Acad Sci U S A 2016, 113 (8), 2206-11.

354. A.Liu, V.; Bhatia, S. N., Three-Dimensional Photopatterning of Hydrogels Containing Living Cells. Biomedical Microdevices 2002, 4 (4), 257-266.

355. El-Sherbiny, I. M.; Yacoub, M. H., Hydrogel scaffolds for tissue engineering: Progress and challenges. Glob Cardiol Sci Pract 2013, 2013 (3), 316-42.

356. Ling, Y.; Rubin, J.; Deng, Y.; Huang, C.; Demirci, U.; Karp, J. M.; Khademhosseini, A., A cell-laden microfluidic hydrogel. Lab on a Chip 2007, 7 (6), 756-762.

357. Ziaie, B.; Baldi, A.; Lei, M.; Gu, Y.; Siegel, R. A., Hard and soft micromachining for BioMEMS: review of techniques and examples of applications in microfluidics and drug delivery. Adv Drug Deliver Rev 2004, 56 (2), 145-172.

358. Warner, J.; Soman, P.; Zhu, W.; Tom, M.; Chen, S., Design and 3D Printing of Hydrogel Scaffolds with Fractal Geometries. ACS Biomaterials Science & Engineering 2016, 2 (10), 1763-1770.

359. Do, A. V.; Khorsand, B.; Geary, S. M.; Salem, A. K., 3D Printing of Scaffolds for Tissue Regeneration Applications. Adv Healthc Mater 2015, 4 (12), 1742-62.

360. Shi, W.; He, R.; Liu, Y., 3D printing scaffolds with hydrogel materials for biomedical applications. European Journal of BioMedical Research 2015, 1 (3).

361. Melchels, F. P.; Feijen, J.; Grijpma, D. W., A review on stereolithography and its applications in biomedical engineering. Biomaterials 2010, 31 (24), 6121-30.

362. Tumbleston, J. R.; Shirvanyants, D.; Ermoshkin, N.; Janusziewicz, R.; Johnson, A. R.; Kelly, D.; Chen, K.; Pinschmidt, R.; Rolland, J. P.; Ermoshkin, A.; Samulski, E. T.; DeSimone, J. M., Continuous liquid interface production of 3D objects. Science 2015, 347 (6228), 1349.

363. Zhang, A. P.; Qu, X.; Soman, P.; Hribar, K. C.; Lee, J. W.; Chen, S.; He, S., Rapid fabrication of complex 3D extracellular microenvironments by dynamic optical projection stereolithography. Adv Mater 2012, 24 (31), 4266-70.

364. Gauvin, R.; Chen, Y. C.; Lee, J. W.; Soman, P.; Zorlutuna, P.; Nichol, J. W.; Bae, H.; Chen, S.; Khademhosseini, A., Microfabrication of complex porous tissue engineering scaffolds using 3D projection stereolithography. Biomaterials 2012, 33 (15), 3824-34.

365. Zhang, R.; Larsen, N. B., Stereolithographic hydrogel printing of 3D culture chips with biofunctionalized complex 3D perfusion networks. Lab on a Chip 2017, 17 (24), 4273-4282.

366. Arcaute, K.; Mann, B. K.; Wicker, R. B., Stereolithography of Three-Dimensional Bioactive Poly(Ethylene Glycol) Constructs with Encapsulated Cells. Annals of Biomedical Engineering 2006, 34 (9), 1429-1441.

367. Lu, Y.; Mapili, G.; Suhali, G.; Chen, S.; Roy, K., A digital micro-mirror device-based system for the microfabrication of complex, spatially patterned tissue engineering scaffolds. Journal of biomedical materials research. Part A 2006, 77 (2), 396-405.

368. Chan, V.; Zorlutuna, P.; Jeong, J. H.; Kong, H.; Bashir, R., Three-dimensional photopatterning of hydrogels using stereolithography for long-term cell encapsulation. Lab Chip 2010, 10 (16), 2062-70.

369. R., S. K.; S., M. J.; L., B. B.; S., C. C.; N., B. S., Degradable hydrogels derived from PEG-diacrylamide for hepatic tissue engineering. Journal of Biomedical Materials Research Part A 2015, 103 (10), 3331-3338.

370. Suntornnond, R.; Tan, E. Y. S.; An, J.; Chua, C. K., A highly printable and biocompatible hydrogel composite for direct printing of soft and perfusable vasculature-like structures. Sci Rep-Uk 2017, 7 (1), 16902.

371. Seo, H.; Heo, S. G.; Lee, H.; Yoon, H., Preparation of PEG materials for constructing complex structures by stereolithographic 3D printing. RSC Adv. 2017, 7 (46), 28684-28688.

372. Sambrook, J., Molecular cloning : a laboratory manual. Third edition. Cold Spring Harbor, N.Y. : Cold Spring Harbor Laboratory Press, [2001] ©2001: 2001.

373. Jones, C. A.; Huberman, E.; Cunningham, M. L.; Peak, M. J., Mutagenesis and Cytotoxicity in Human Epithelial Cells by Far- and Near-Ultraviolet Radiations: Action Spectra. Radiation Research 1987, 110 (2), 244-254.

374. Wells, R. L.; Han, A., Action spectra for killing and mutation of Chinese hamster cells exposed to mid- and near-ultraviolet monochromatic light. Mutation Research/Fundamental and Molecular Mechanisms of Mutagenesis 1984, 129 (2), 251-258.

375. M., T. R.; P., W.; C., M. E., LETHAL ACTION OF ULTRAVIOLET AND VISIBLE (BLUE-VIOLET) RADIATIONS AT DEFINED WAVELENGTHS ON HUMAN LYMPHOBLASTOID CELLS: ACTION SPECTRA AND INTERACTION SITES. Photochemistry and Photobiology 1984, 39 (2), 183-189.

376. Andley, U. P.; Lewis, R. M.; Reddan, J. R.; Kochevar, I. E., Action spectrum for cytotoxicity in the UVA- and UVB-wavelength region in cultured lens epithelial cells. Investigative ophthalmology & visual science 1994, 35 (2), 367-73.

377. Browning, M. B.; Cereceres, S. N.; Luong, P. T.; Cosgriff-Hernandez, E. M., Determination of the in vivo degradation mechanism of PEGDA hydrogels. Journal of biomedical materials research. Part A 2014, 102 (12), 4244-51.

378. Majiama, T.; Schnabel, W., Phenyl-2,4,6-trimethylbenzoylphosphinates as water-soluble photoinitiators. Generation and reactivity of O=P(C6H5)(O-) radical anions. Makromol. Chem. 1991, 192 (10), 2307-2315.

379. Han, D.; Lu, Z.; Chester, S. A.; Lee, H., Micro 3D Printing of a Temperature-Responsive Hydrogel Using Projection Micro-Stereolithography. Sci Rep-Uk 2018, 8 (1), 1963.

380. Oster, G.; Broyde, S. B.; Bellin, J. S., Spectral Properties of Chlorophyllin a. Journal of the American Chemical Society 1964, 86 (7), 1309-1313.

381. Sikorski, Z., Caris-Veyrat, C., Pintea, A., Wurtzel, E., Otles, S., Giusti, M., Marquez, U., During, A., Mercandante, A., Luning, P., Dufosse, L., Stintzing, F., Amiot, M., Brat, P., Matthews, P., Diehl, H., Carle, R., Sinnecker, P., Bobbio, F., Jing, P., Laurent, C., Tourniaire, F. , Food Colorants. CRC Press: Boca Raton, 2008.

382. Miller, G. A.; Gou, L.; Narayanan, V.; Scranton, A. B., Modeling of Photobleaching for the Photoinitiation of Thick Polymerization Systems. Journal of Polymer Science Part A: Polymer Chemistry 2001, 40 (6), 793-808.

383. Reyes, D. R.; Iossifidis, D.; Auroux, P.-A.; Manz, A., Micro total analysis systems. 1. Introduction, theory, and technology. Analytical chemistry 2002, 74 (12), 2623-2636.

384. Stone, H. A.; Stroock, A. D.; Ajdari, A., Engineering flows in small devices: microfluidics toward a lab-on-a-chip. Annu. Rev. Fluid Mech. 2004, 36, 381-411.

385. Dittrich, P. S.; Manz, A., Lab-on-a-chip: microfluidics in drug discovery. Nature reviews Drug discovery 2006, 5 (3), 210-218.

386. Andersson, H.; Van den Berg, A., Microfluidic devices for cellomics: a review. Sensors and actuators B: Chemical 2003, 92 (3), 315-325.

387. Dusny, C.; Grünberger, A., Microfluidic single-cell analysis in biotechnology: from monitoring towards understanding. Current opinion in biotechnology 2020, 63, 26-33.

388. McCalla, S. E.; Tripathi, A., Microfluidic reactors for diagnostics applications. Annual review of biomedical engineering 2011, 13, 321-343.

389. Miralles, V.; Huerre, A.; Malloggi, F.; Jullien, M.-C., A review of heating and temperature control in microfluidic systems: techniques and applications. Diagnostics 2013, 3 (1), 33-67.

390. Jung, W.; Han, J.; Choi, J.-W.; Ahn, C. H., Point-of-care testing (POCT) diagnostic systems using microfluidic lab-on-a-chip technologies. Microelectron Eng 2015, 132, 46-57.

391. Kaminski, T.; Garstecki, P., Controlled droplet microfluidic systems for multistep chemical and biological assays. Chemical Society Reviews 2017, 46 (20), 6210-6226.

392. Bruijns, B.; Van Asten, A.; Tiggelaar, R.; Gardeniers, H., Microfluidic devices for forensic DNA analysis: A review. Biosensors 2016, 6 (3), 41.

393. Zheng, B.; Roach, L. S.; Ismagilov, R. F., Screening of protein crystallization conditions on a microfluidic chip using nanoliter-size droplets. Journal of the American chemical society 2003, 125 (37), 11170-11171.

394. Beer, N. R.; Hindson, B. J.; Wheeler, E. K.; Hall, S. B.; Rose, K. A.; Kennedy, I. M.; Colston, B. W., On-chip, real-time, single-copy polymerase chain reaction in picoliter droplets. Analytical chemistry 2007, 79 (22), 8471-8475.

395. Srivannavit, O.; Gulari, M.; Hua, Z.; Gao, X.; Zhou, X.; Hong, A.; Zhou, T.; Gulari, E., Microfluidic reactor array device for massively parallel in situ synthesis of oligonucleotides. Sensors and Actuators B: Chemical 2009, 140 (2), 473-481.

396. Geertz, M.; Shore, D.; Maerkl, S. J., Massively parallel measurements of molecular interaction kinetics on a microfluidic platform. Proceedings of the National Academy of Sciences 2012, 109 (41), 16540-16545.

397. Burns, M. A.; Johnson, B. N.; Brahmasandra, S. N.; Handique, K.; Webster, J. R.; Krishnan, M.; Sammarco, T. S.; Man, P. M.; Jones, D.; Heldsinger, D., An integrated nanoliter DNA analysis device. Science 1998, 282 (5388), 484-487.

398. Lamprou, D. A., Emerging technologies for diagnostics and drug delivery in the fight against COVID-19 and other pandemics. Expert review of medical devices 2020, 1-6.

399. Chen, T.; Gomez-Escoda, B.; Munoz-Garcia, J.; Babic, J.; Griscom, L.; Wu, P.-Y. J.; Coudreuse, D., A drug-compatible and temperature-controlled microfluidic device for live-cell imaging. Open biology 2016, 6 (8), 160156.

400. Jähnisch, K.; Hessel, V.; Löwe, H.; Baerns, M., Chemistry in microstructured reactors. Angewandte Chemie International Edition 2004, 43 (4), 406-446.

401. Demello, A. J., Control and detection of chemical reactions in microfluidic systems. Nature 2006, 442 (7101), 394-402.

402. Woolley, A. T.; Hadley, D.; Landre, P.; deMello, A. J.; Mathies, R. A.; Northrup, M. A., Functional integration of PCR amplification and capillary electrophoresis in a microfabricated DNA analysis device. Analytical Chemistry 1996, 68 (23), 4081-4086.

403. Casquillas, G. V.; Fu, C.; Le Berre, M.; Cramer, J.; Meance, S.; Plecis, A.; Baigl, D.; Greffet, J.-J.; Chen, Y.; Piel, M., Fast microfluidic temperature control for high resolution live cell imaging. Lab on a Chip 2011, 11 (3), 484-489.

404. Angione, S. L.; Chauhan, A.; Tripathi, A., Real-time droplet DNA amplification with a new tablet platform. Analytical chemistry 2012, 84 (6), 2654-2661.

405. Amasia, M.; Cozzens, M.; Madou, M. J., Centrifugal microfluidic platform for rapid PCR amplification using integrated thermoelectric heating and ice-valving. Sensors and Actuators B: Chemical 2012, 161 (1), 1191-1197.

406. Bu, M.; Perch-Nielsen, I. R.; Sørensen, K. S.; Skov, J.; Sun, Y.; Bang, D. D.; Pedersen, M. E.; Hansen, M. F.; Wolff, A., A temperature control method for shortening thermal cycling time to achieve rapid polymerase chain reaction (PCR) in a disposable polymer microfluidic device. J Micromech Microeng 2013, 23 (7), 074002.

407. Kimura, Y.; Ikeuchi, M.; Inoue, Y.; Ikuta, K., 3D microdevices that perform sample purification and multiplex qRT-PCR for early cancer detection with confirmation of specific RNAs. Sci Rep-Uk 2018, 8 (1), 1-10.

408. Selck, D. A.; Ismagilov, R. F., Instrument for real-time digital nucleic acid amplification on custom microfluidic devices. PLoS One 2016, 11 (10).

409. Mendoza-Gallegos, R. A.; Rios, A.; Garcia-Cordero, J. L., An affordable and portable thermocycler for real-time PCR made of 3D-printed parts and off-the-shelf electronics. Analytical chemistry 2018, 90 (9), 5563-5568.

410. Wade, H., Trial and error: An organized procedure. InTech 2005, 52 (5), 38-42.

411. Duffy, D. C.; McDonald, J. C.; Schueller, O. J.; Whitesides, G. M., Rapid prototyping of microfluidic systems in poly (dimethylsiloxane). Analytical chemistry 1998, 70 (23), 4974-4984.

412. Schneider, C. A.; Rasband, W. S.; Eliceiri, K. W., NIH Image to ImageJ: 25 years of image analysis. Nat. Methods 2012, 9 (7), 671.

413. Klein, D., Quantification using real-time PCR technology: applications and limitations. Trends in molecular medicine 2002, 8 (6), 257-260.

414. Schweiz, M. V., Table of Emissivity of various surfaces. Schaffhausen: Mikron Instrument, nd Print 2012.

415. Shah, J. J.; Gaitan, M.; Geist, J., Generalized temperature measurement equations for rhodamine B dye solution and its application to microfluidics. Analytical chemistry 2009, 81 (19), 8260-8263.

416. Temiz, Y.; Lovchik, R. D.; Kaigala, G. V.; Delamarche, E., Lab-on-a-chip devices: How to close and plug the lab? Microelectron Eng 2015, 132, 156-175.

417. Olliaro, P.; Torreele, E.; Vaillant, M., COVID-19 vaccine efficacy and effectiveness-the elephant (not) in the room. Lancet Microbe 2021.

418. Thompson, R. N.; Hill, E. M.; Gog, J. R., SARS-CoV-2 incidence and vaccine escape. Lancet Infect Dis 2021.

419. Castillo, J. C.; Ahuja, A.; Athey, S.; Baker, A.; Budish, E.; Chipty, T.; Glennerster, R.; Kominers, S. D.; Kremer, M.; Larson, G.; Lee, J.; Prendergast, C.; Snyder, C. M.; Tabarrok, A.; Tan, B. J.; Wiecek, W., Market design to accelerate COVID-19 vaccine supply. Science 2021, 371 (6534), 1107-1109.

420. Chia, W. N.; Zhu, F.; Ong, S. W. X.; Young, B. E.; Fong, S. W.; Le Bert, N.; Tan, C. W.; Tiu, C.; Zhang, J.; Tan, S. Y.; Pada, S.; Chan, Y. H.; Tham, C. Y. L.; Kunasegaran, K.; Chen, M. I.; Low, J. G. H.; Leo, Y. S.; Renia, L.; Bertoletti, A.; Ng, L. F. P.; Lye, D. C.; Wang, L. F., Dynamics of SARS-CoV-2 neutralising antibody responses and duration of immunity: a longitudinal study. Lancet Microbe 2021.

421. Kirby, T., When should the UK lift its lockdown? Lancet Respir Med 2021, 9 (4), e44-e45.

422. Head, J. R.; Andrejko, K. L.; Cheng, Q.; Collender, P. A.; Phillips, S.; Boser, A.; Heaney, A. K.; Hoover, C. M.; Wu, S. L.; Northrup, G. R.; Click, K.; Bardach, N. S.; Lewnard, J. A.; Remais, J. V., School closures reduced social mixing of children during COVID-19 with implications for transmission risk and school reopening policies. J R Soc Interface 2021, 18 (177), 20200970.

423. Trotta, J. Why qPCR is the gold standard for COVID-19 testing. https://www.thermofisher.com/blog/ask-a-scientist/why-qpcr-is-the-gold-standard-for-covid-19-testing/.

424. COVID-19 and PCR Testing. https://my.clevelandclinic.org/health/diagnostics/21462-covid-19-and-pcr-testing.

425. Rogers, W.; Ruiz-Aravena, M.; Hansen, D.; Madden, W.; Kessler, M.; Fields, M. W.; Ferrari, M. J.; Chang, C. B.; Morrow, J.; Hoegh, A.; Plowright, R. K., High-frequency screening combined with diagnostic testing for control of SARS-CoV-2 in high-density settings: an economic evaluation of resources allocation for public health benefit. 2021, 2021.03.04.21252949.

426. Curtis, K. A.; Rudolph, D. L.; Owen, S. M., Rapid detection of HIV-1 by reverse-transcription, loop-mediated isothermal amplification (RT-LAMP). Journal of Virological Methods 2008, 151 (2), 264-270.

427. Parida, M.; Posadas, G.; Inoue, S.; Hasebe, F.; Morita, K., Real-time reverse transcription loop-mediated isothermal amplification for rapid detection of West Nile virus. Journal of Clinical Microbiology 2004, 42 (1), 257-263.

428. Bhadra, S.; Maranhao, A. C.; Paik, I.; Ellington, A. D., A one-enzyme RT-qPCR assay for SARS-CoV-2, and procedures for reagent production. Bio-protocol 2021, 11 (2), e3898.

429. Buck, M. D.; Poirier, E. Z.; Cardoso, A.; Frederico, B.; Canton, J.; Barrell, S.; Beale, R.; Byrne, R.; Caidan, S.; Crawford, M.; Cubitt, L.; Gamblin, S.; Gandhi, S.; Goldstone, R.; Grant, P. R.; Gulati, K.; Hindmarsh, S.; Howell, M.; Hubank, M.; Instrell, R.; Jiang, M.; Kassiotis, G.; Lu, W.-T.; MacRae, J. I.; Martini, I.; Miller, D.; Moore, D.; Nastouli, E.; Nicod, J.; Nightingale, L.; Olsen, J.; Oomatia, A.; O'Reilly, N.; Rideg, A.; Song, O.-R.; Strange, A.; Swanton, C.; Turajlic, S.; Walker, P. A.; Wu, M.; Sousa, C. R. e., Standard operating procedures for SARS-CoV-2 detection by a clinical diagnostic RT-LAMP assay. medRxiv 2020, 2020.06.29.20142430.

430. Esbin, M. N.; Whitney, O. N.; Chong, S.; Maurer, A.; Darzacq, X.; Tjian, R., Overcoming the bottleneck to widespread testing: a rapid review of nucleic acid testing approaches for COVID-19 detection. RNA (New York, N.Y.) 2020, 26 (7), 771-783.

431. Kashir, J.; Yaqinuddin, A., Loop mediated isothermal amplification (LAMP) assays as a rapid diagnostic for COVID-19. Medical Hypotheses 2020, 141, 109786.

432. Yan, C.; Cui, J.; Huang, L.; Du, B.; Chen, L.; Xue, G.; Li, S.; Zhang, W.; Zhao, L.; Sun, Y.; Yao, H.; Li, N.; Zhao, H.; Feng, Y.; Liu, S.; Zhang, Q.; Liu, D.; Yuan, J., Rapid and visual detection of 2019 novel coronavirus (SARS-CoV-2) by a reverse transcription loop-mediated isothermal amplification assay. Clin Microbiol Infect 2020, 26 (6), 773-779.

433. Lamb, L. E.; Bartolone, S. N.; Ward, E.; Chancellor, M. B., Rapid detection of novel coronavirus/Severe Acute Respiratory Syndrome Coronavirus 2 (SARS-CoV-2) by reverse transcription-loop-mediated isothermal amplification. PLoS One 2020, 15 (6), e0234682.

434. Tan, S. H.; Allicock, O.; Armstrong-Hough, M.; Wyllie, A. L., Saliva as a gold-standard sample for SARS-CoV-2 detection. The Lancet Respiratory Medicine.

435. Moisset, X.; Gautier, N.; Godet, T.; Parabere, S.; Pereira, B.; Meunier, E.; Gerbaud, L.; Lesens, O.; Henquell, C.; Beytout, J.; Clavelou, P., Nasopharyngeal swab-induced pain for SARS-CoV-2 screening: A randomised controlled trial of conventional and self-swabbing. European Journal of Pain 2021.

436. Koenig, D. Brain Scraper: Why Do Some COVID Tests Hurt So Much?

437. Mahony, J.; Chong, S.; Bulir, D.; Ruyter, A.; Mwawasi, K.; Waltho, D., Multiplex loop-mediated isothermal amplification (M-LAMP) assay for the detection of influenza A/H1, A/H3 and influenza B can provide a specimen-to-result diagnosis in 40 min with single genome copy sensitivity. Journal of Clinical Virology 2013, 58 (1), 127-131.

438. Aoki, M. N.; Coelho, B. d. O.; Bentim Goes, L. G.; Minoprio, P.; Durigon, E. L.; Morello, L. G.; Marchini, F. K.; Riediger, I. N.; Debur, M. d. C.; Nakaya, H. I.; Blanes, L., Colorimetric RT-LAMP SARS-CoV-2 diagnostic sensitivity relies on color interpretation and viral load. Sci Rep-Uk 2021, 11 (1).

439. Scherf, U. A new process that can be used in place of the extraction method when materials for the current method are limited. https://www.fda.gov/media/138931/download.

440. Diseases, C. D. N. D. o. V., CDC 2019-Novel Coronavirus (2019-nCoV) Real-Time RT-PCR Diagnostic Panel. CDC-006-00019, Revision: 06 ed.; Prevention, C. f. D. C. a., Ed. 12/01/2020.

441. Efron, B.; Tibshirani, R., An introduction to the bootstrap. Chapman & Hall: New York, 1993; p xvi, 436 p.

442. Zhu, J.; Guo, J.; Xu, Y.; Chen, X., Viral dynamics of SARS-CoV-2 in saliva from infected patients. J Infect 2020, 81 (3), e48-e50.

443. Corstjens, P. L. A. M.; Abrams, W. R.; Malamud, D., Saliva and viral infections. Periodontol 2000 2016, 70 (1), 93-110.

444. Wyllie, A. L.; Fournier, J.; Casanovas-Massana, A.; Campbell, M.; Tokuyama, M.; Vijayakumar, P.; Warren, J. L.; Geng, B.; Muenker, M. C.; Moore, A. J.; Vogels, C. B. F.; Petrone, M. E.; Ott, I. M.; Lu, P.; Venkataraman, A.; Lu-Culligan, A.; Klein, J.; Earnest, R.; Simonov, M.; Datta, R.; Handoko, R.; Naushad, N.; Sewanan, L. R.; Valdez, J.; White, E. B.; Lapidus, S.; Kalinich, C. C.; Jiang, X.; Kim, D. J.; Kudo, E.; Linehan, M.; Mao, T.; Moriyama, M.; Oh, J. E.; Park, A.; Silva, J.; Song, E.; Takahashi, T.; Taura, M.; Weizman, O. E.; Wong, P.; Yang, Y.; Bermejo, S.; Odio, C. D.; Omer, S. B.; Dela Cruz, C. S.; Farhadian, S.; Martinello, R. A.; Iwasaki, A.; Grubaugh, N. D.; Ko, A. I., Saliva or nasopharyngeal swab specimens for detection of SARS-CoV-2. N Engl J Med 2020, 383 (13), 1283-1286.

445. Adaway, J. E.; Hawley, J. M.; Lockhart, S. J.; Keevil, B. G., Heat inactivation of saliva samples for the analysis of cortisol and cortisone during the COVID-19 pandemic. The Journal of Applied Laboratory Medicine 2020, 5 (6), 1413-1416.

446. Bujang, M. A.; Adnan, T. H., Requirements for Minimum Sample Size for Sensitivity and Specificity Analysis. J Clin Diagn Res 2016, 10 (10), YE01-YE06.

447. 2019: American Community Survey 5-Year Estimates Data Profiles. 2019.

448. Nickbakhsh, S.; Ho, A.; Marques, D. F. P.; McMenamin, J.; Gunson, R. N.; Murcia, P. R., Epidemiology of Seasonal Coronaviruses: Establishing the Context for the Emergence of Coronavirus Disease 2019. The Journal of Infectious Diseases 2020, 222 (1), 17-25.

449. Reese, H.; Iuliano, A. D.; Patel, N. N.; Garg, S.; Kim, L.; Silk, B. J.; Hall, A. J.; Fry, A.; Reed, C., Estimated Incidence of Coronavirus Disease 2019 (COVID-19) Illness and Hospitalization—United States, February–September 2020. Clinical Infectious Diseases 2020, 72 (12), e1010-e1017.

450. Kapoor, P.; Chowdhry, A.; Kharbanda, O. P.; Popli, D. B.; Gautam, K.; Saini, V., Exploring salivary diagnostics in COVID-19: a scoping review and research suggestions. Bdj Open 2021, 7 (1).

451. Benn, A. M.; Thomson, W. M., Saliva: an overview. The New Zealand dental journal 2014, 110 (3), 92-6.

452. Subramanian, S.; Gomez, R. D., An Empirical Approach for Quantifying Loop-Mediated Isothermal Amplification (LAMP) Using Escherichia coli as a Model System. Plos One 2014, 9 (6).

453. Loveday, E. K.; Hain, K. S.; Kochetkova, I.; Hedges, J. F.; Robison, A.; Snyder, D. T.; Brumfield, S. K.; Young, M. J.; Jutila, M. A.; Chang, C. B.; Taylor, M. P., Effect of Inactivation Methods on SARS-CoV-2 Virion Protein and Structure. Viruses-Basel 2020, 13 (4).

454. Rogers, A. A.; Baumann, R. E.; Borillo, G. A.; Kagan, R. M.; Batterman, H. J.; Galdzicka, M. M.; Marlowe, E. M., Evaluation of Transport Media and Specimen Transport Conditions for the Detection of SARS-CoV-2 by Use of Real-Time Reverse Transcription-PCR. Journal of Clinical Microbiology 2020, 58 (8).

455. Grishin, A. M.; Dolgova, N. V.; Harms, S.; Pickering, I. J.; George, G. N.; Falzarano, D.; Cygler, M., Spike protein disulfide disruption as a potential treatment for SARS-CoV-2. bioRxiv 2021, 2021.01.02.425099.

456. Thompson, D.; Lei, Y., Mini review: Recent progress in RT-LAMP enabled COVID-19 detection. Sensors and Actuators Reports 2020, 2 (1).

457. Sabiiti, W.; Azam, K.; Esmeraldo, E.; Bhatt, N.; Rachow, A.; Gillespie, S. H., Heat Inactivation Renders Sputum Safe and Preserves Mycobacterium tuberculosis RNA for Downstream Molecular Tests. J Clin Microbiol 2019, 57 (4).

458. Rabe, B. A.; Cepko, C., SARS-CoV-2 detection using isothermal amplification and a rapid, inexpensive protocol for sample inactivation and purification. Proceedings of the National Academy of Sciences 2020, 117 (39), 24450-24458.

459. Ranoa, D. R. E.; Holland, R. L.; Alnaji, F. G.; Green, K. J.; Wang, L.; Brooke, C. B.; Burke, M. D.; Fan, T. M.; Hergenrother, P. J., Saliva-Based Molecular Testing for SARS-CoV-2 that Bypasses RNA Extraction. bioRxiv 2020, 2020.06.18.159434.

460. Ott, I. M.; Strine, M. S.; Watkins, A. E.; Boot, M.; Kalinich, C. C.; Harden, C. A.; Vogels, C. B. F.; Casanovas-Massana, A.; Moore, A. J.; Muenker, M. C.; Nakahata, M.; Tokuyama, M.; Nelson, A.; Fournier, J.; Bermejo, S.; Campbell, M.; Datta, R.; Dela Cruz, C. S.; Farhadian, S. F.; Ko, A. I.; Iwasaki, A.; Grubaugh, N. D.; Wilen, C. B.; Wyllie, A. L., Simply saliva: stability of SARS-CoV-2 detection negates the need for expensive collection devices. medRxiv : the preprint server for health sciences 2020, 2020.08.03.20165233.

461. Lalli, M. A.; Langmade, J. S.; Chen, X.; Fronick, C. C.; Sawyer, C. S.; Burcea, L. C.; Wilkinson, M. N.; Fulton, R. S.; Heinz, M.; Buchser, W. J.; Head, R. D.; Mitra, R. D.; Milbrandt, J., Rapid and Extraction-Free Detection of SARS-CoV-2 from Saliva by Colorimetric Reverse-Transcription Loop-Mediated Isothermal Amplification. Clinical Chemistry 2020, 67 (2), 415-424.

462. Pastorino, B.; Touret, F.; Gilles, M.; de Lamballerie, X.; Charrel, R. N., Heat Inactivation of Different Types of SARS-CoV-2 Samples: What Protocols for Biosafety, Molecular Detection and Serological Diagnostics? Viruses 2020, 12 (7), 735.

463. Loveday, E. K.; Hain, K. S.; Kochetkova, I.; Hedges, J. F.; Robison, A.; Snyder, D. T.; Brumfield, S. K.; Young, M. J.; Jutila, M. A.; Chang, C. B.; Taylor, M. P., Effects of inactivation method on SARS-CoV-2 virion protein and structure. bioRxiv 2020, 2020.11.14.383026.

464. Park, N. J.; Li, Y.; Yu, T.; Brinkman, B. M. N.; Wong, D. T., Characterization of RNA in saliva. Clinical chemistry 2006, 52 (6), 988-994.

465. Arons, M. M.; Hatfield, K. M.; Reddy, S. C.; Kimball, A.; James, A.; Jacobs, J. R.; Taylor, J.; Spicer, K.; Bardossy, A. C.; Oakley, L. P.; Tanwar, S.; Dyal, J. W.; Harney, J.; Chisty, Z.; Bell, J. M.; Methner, M.; Paul, P.; Carlson, C. M.; McLaughlin, H. P.; Thornburg, N.; Tong, S.; Tamin, A.; Tao, Y.; Uehara, A.; Harcourt, J.; Clark, S.; Brostrom-Smith, C.; Page, L. C.; Kay, M.; Lewis, J.; Montgomery, P.; Stone, N. D.; Clark, T. A.; Honein, M. A.; Duchin, J. S.; Jernigan, J. A., Presymptomatic SARS-CoV-2 Infections and Transmission in a Skilled Nursing Facility. New England Journal of Medicine 2020, 382 (22), 2081-2090.

466. Ravi, N.; Cortade, D. L.; Ng, E.; Wang, S. X., Diagnostics for SARS-CoV-2 detection: A comprehensive review of the FDA-EUA COVID-19 testing landscape. Biosens Bioelectron 2020, 165, 112454-112454.

467. Wang, W.; Xu, Y.; Gao, R.; Lu, R.; Han, K.; Wu, G.; Tan, W., Detection of SARS-CoV-2 in Different Types of Clinical Specimens. JAMA 2020, 323 (18), 1843-1844.

468. Mallett, S.; Allen, A. J.; Graziadio, S.; Taylor, S. A.; Sakai, N. S.; Green, K.; Suklan, J.; Hyde, C.; Shinkins, B.; Zhelev, Z.; Peters, J.; Turner, P. J.; Roberts, N. W.; di Ruffano, L. F.; Wolff, R.; Whiting, P.; Winter, A.; Bhatnagar, G.; Nicholson, B. D.; Halligan, S., At what times during infection is SARS-CoV-2 detectable and no longer detectable using RT-PCR-based tests? A systematic review of individual participant data. BMC Medicine 2020, 18 (1), 346.

469. Roy, K. M.; Bagg, J.; McCarron, B., The effect of saliva specimen collection, handling and storage protocols on hepatitis C virus (HCV) RNA detection by PCR. Oral Dis 1999, 5 (2), 123-7.

470. Gomes-Keller, M. A.; Gönczi, E.; Tandon, R.; Riondato, F.; Hofmann-Lehmann, R.; Meli, M. L.; Lutz, H., Detection of Feline Leukemia Virus RNA in Saliva from Naturally Infected

Cats and Correlation of PCR Results with Those of Current Diagnostic Methods. Journal of Clinical Microbiology 2006, 44 (3), 916-922.

471. Choi, J. E.; Lyons, K. M.; Kieser, J. A.; Waddell, N. J., Diurnal variation of intraoral pH and temperature. Bdj Open 2017, 3 (1), 17015.

472. Nunes, L. A. S.; Macedo, D. V. d., Saliva as a diagnostic fluid in sports medicine: potential and limitations. Jornal Brasileiro de Patologia e Medicina Laboratorial 2013, 49, 247-255.

473. Zhang, J. M.; Hu, Q. P.; Wang, S.; Tao, J.; Gou, M. L., Digital Light Processing Based Three-dimensional Printing for Medical Applications. Int J Bioprinting 2020, 6 (1), 12-27.